Geodätisch-geophysikalische Arbeiten in der Schweiz

(Fortsetzung der Publikationsreihe
«Astronomisch-geodätische Arbeiten in der Schweiz»)

herausgegeben von der

Schweizerischen Geodätischen Kommission
(Organ der Akademie der Naturwissenschaften Schweiz)

Siebenundsechzigster Band
Volume 67

GPS based Determination of the Integrated and Spatially Distributed Water Vapor in the Troposphere

Marc Troller

2004

Adresse der Schweizerischen Geodätischen Kommission:

Institut für Geodäsie und Photogrammetrie
Eidg. Technische Hochschule Zürich
ETH Hönggerberg
CH-8093 Zürich, Switzerland

Internet: http://www.sgc.ethz.ch

ISBN 3-908440-10-6

Redaktion des 67. Bandes:
Dr. M. Troller, Dr. B. Bürki

Druck: Print-Atelier E. Zingg, Zürich

VORWORT

Hochpräzise geodätische Anwendungen des Globalen Positionierungssystems GPS mit Anforderungen im cm-Genauigkeitsbereich sind aufgrund verschiedener systematischer Fehlereinflüsse limitiert. Das heutige Forschungsinteresse konzentriert sich auf die Reduktion systematischer Fehler, die vor allem mit den Übertragungsmedien zusammenhängen. Ein zentrales Problem ist der Troposphäreneinfluss. Im vorliegenden Band werden die neuesten Methoden zur Wasserdampfbestimmung vorgestellt und einer sorgfältigen Fehleruntersuchung unterzogen. Umfangreiche Vergleiche zwischen den boden- und satellitengestützten Verfahren zeigen die Machbarkeit der GPS-basierten Schätzverfahren auf. Dabei werden auch Möglichkeiten zur Bestimmung der Höhenverteilung des Wasserdampfes erarbeitet und in Messkampagnen erfolgreich getestet.

Einer der Datensätze zur Ermittlung des Wasserdampfes ist durch 72 Bodenstationen des automatischen Meteo-Netzes ANETZ gegeben, welches durch den Schweizerischen Wetterdienst MeteoSchweiz unterhalten wird. Zusätzlich hält MeteoSchweiz Ballonsondierungen in Payerne aufrecht. Herr Troller hat die Programmsysteme COMEDIE und COITROPA erfolgreich weiter entwickelt, bzw. neu konzipiert. Als besonders geeignetes Testfeld bietet sich das nationale automatische GPS Netz (AGNES) der Schweiz an, deren 29 Stationen von der Swisstopo unterhalten werden. Vierjährige Zeitreihen für die Stationen Zimmerwald und Locarno zeigen die Leistungsfähigkeit des neuen Programmsystems COITROPA auf.

Herr Troller hat zudem die Bestimmung der Höhenverteilung des Wasserdampfes bearbeitet, die auf der Grundlage eines tomographischen Ansatzes beruht. Herr Troller hat hierzu das Softwarepaket “Atmospheric Water Vapor Tomography Software (AWATOS)” erfolgreich weiter entwickelt und in gezielten Experimenten getestet. Unabhängige Referenzdaten liefert das numerische Wettervorhersagemodell von MeteoSchweiz (Alpines Modell (aLMo)). Ein ausführlicher Vergleich von aLMo mit den integralen Schätzmethoden sowie den AWATOS-Auswertungen von mehr als 7000 Refraktivitätsprofilen, basierend auf dem AGNES GPS Netz, erlaubte es Herrn Troller, die verschiedenen Methoden systematisch zu beurteilen.

Die entwickelten Algorithmen haben sich in der Schweizerischen Landesvermessung bestens bewährt. Im Rahmen der Ressortforschung der Swisstopo bestehen konkrete Pläne für deren Weiterentwicklung. Da der Wasserdampf und seine räumliche Verteilung für Wettervorhersage-Modelle von grosser Bedeutung sind, beginnen nun auch Wetterdienste, Laufzeitänderungen von GPS-Radiowellen in ihre Berechnungen einzubeziehen.

Mit den erzielten Ergebnissen und potentiellen Anwendungsmöglichkeiten hat Herr Troller einen wichtigen wissenschaftlichen Beitrag der schweizerischen Geodäsie auf dem Gebiet der GPS-Meteorologie geleistet. Ihre Bedeutung kann sehr gut mit den Zielsetzungen des Kyoto-Protokolls in Beziehung gesetzt werden. Internationale Beteiligungen an Projekten der Umweltforschung (ESCOMPTE) sowie im Rahmen des Prix du Jeune Entrepreneur de la Section Suisse des Conseillers du Commerce Extérieur de la France belegen das internationale Interesse an diesem Forschungsgebiet. Die Schweizerische Geodätische Kommission SGK dankt Herrn Marc Troller für seinen hochgeschätzten Beitrag. Das Projekt wurde von der ETH Zürich und der SGK gefördert. Der Schweizerischen Akademie für Naturwissenschaften SANW danken wir für die Übernahme der Druckkosten.

Prof. Dr. H.-G. Kahle
Institut für Geodäsie und Photogrammetrie,
ETH Zürich

Prof. Dr. A. Geiger
ETH Zürich
Präsident der SGK

PREFACE

Les applications géodésiques du GPS de haute précision requérant des précisions du centimètre sont limitées par plusieurs sources d'erreurs systématiques. Les recherches actuelles se sont focalisées sur l'atténuation des erreurs causées par le milieu de propagation. Les méthodes courantes sont présentées et discutées en termes de leurs budgets d'erreurs. D'intensives comparaisons entre méthodes terrestres et spatiales fournissent des preuves sur la faisabilité des procédures d'estimation basées sur le GPS. Des possibilités pour l'estimation des profils verticaux de la vapeur d'eau troposphérique sont investiguées et testées à l'aide de campagnes de mesures.

Un important jeu de données utilisant la détermination de la vapeur d'eau troposphérique est fourni par le réseau météorologique automatique ANETZ du service météorologique suisse (MétéoSuisse). De plus des radio-sondes sont journellement lancées à Payerne par MétéoSuisse. Monsieur M. Troller a raffiné et développé les paquets de programmes COMEDIE et COTRPA respectivement. Un réseau de test approprié, mis en oeuvre par Swisstopo, forme le réseau GPS automatique national AGNES consistant en 29 stations. Des séries temporelles des stations de Zimmerwald et de Locarno compilées sur une période de 4 ans démontrent la capacité du nouveau paquet de programmes COITROPA.

Monsieur M. Troller a investigué la possibilité de déterminer la distribution verticale de la vapeur d'eau en utilisant une approche tomographique. Pour cela il a raffiné le paquet de programmes AWATOS et testé ce paquet à l'aide d'une expérience spécifique. Des données de références indépendantes ont été fournies par le modèle numérique de prévisions du temps aLMo, développé par MétéoSuisse. Une comparaison étendue des données aLMo avec la méthode intégrale du GPS et avec les résultats fournis par AWATOS de plus de 7000 profils a permis d'évaluer systématiquement l'efficacité des méthodes présentées.

Les algorithmes développés ont prouvés leurs hautes valeurs dans le cadre des levés nationaux suisses, ils seront raffinés et appliqués dans le futur par Swisstopo. Du fait que la vapeur d'eau et sa distribution spatiale jouent un grand rôle dans les modèles de provisions du temps, les services météorologiques nationaux ont commencés à intégrer les retards de propagation des ondes GPS dans leurs calculs.

Avec les résultats obtenus et en considérant le haut potentiel d'applications Monsieur M. Troller a fourni une contribution significative à la géodésie suisse dans le domaine de la météorologie par GPS. Son importance peut être mise en relation avec les buts formulés par le protocole de Kyoto. Une coopération avec des projets environnementaux internationaux (ESCOMPTE) dans le cadre du " Prix du Jeune Entrepreneur" de la section suisse des conseillers du commerce extérieur de la France, révèle l'intérêt international de ce sujet de recherche. La Commission Suisse de Géodésie (SGC) exprime sa gratitude à Monsieur M. Troller pour cette contribution de haute valeur. Ce projet a été supporté financièrement par l'ETH Zürich et par la commission suisse de géodésie. Nous sommes de plus reconnaissant à l'Académie Suisse des Sciences Naturelles d'avoir couvert les coûts d'impression du présent fascicule.

Prof. Dr. H.-G. Kahle
Institut de Géodésie et Photogrammetrie,
ETH Zürich

Prof. Dr. A. Geiger
ETH Zürich
Président de la CGS

FOREWORD

High-precision geodetic applications of the Global Positioning System GPS requiring cm accuracy are limited due to several systematic error sources. Current interest of research is focused on the mitigation of errors, which are caused by the propagation media. The current methods are being presented and discussed in terms of their error budgets. Extensive comparisons between terrestrial and space-borne methods provide proof for the feasibility of GPS based estimation procedures. Possibilities for estimating height profiles of the tropospheric water vapor are also being investigated and tested in measuring campaigns.

One of the major data sets used for the determination of tropospheric water vapor is made available by the automatic ground-based Meteo network ANETZ, run by the Swiss National Weather Office MeteoSwiss. Moreover daily radiosondes at the city of Payerne are being conducted by MeteoSwiss. Marc Troller has refined and developed the program systems COMEDIE and COITRPA, respectively.

An appropriate test network, run by swisstopo, is the national automatic GPS network AGNES which consists of 29 stations. Time series for the stations Zimmerwald and Locarno compiled over a period of 4 years point out the capability of the new program package COITROPA.
Moreover, Marc Troller has investigated the possibility of determining the height distribution of water vapor, using a tomographic approach. For this he refined the program system AWATOS and tested it in dedicated experiments. Independent reference data were provided by the numerical weather forecast model aLMo, developed by MeteoSwiss. An extensive comparison of the aLMo data with both the integral GPS method as well as with the AWATOS results of more than 7000 profiles allowed to systematically evaluate the effectiveness of the methods presented.

The algorithms developed have proven of high value in the frame of Swiss National Surveying and they will be further refined and applied in the future by swisstopo. Since the water vapor and its spatial distribution play an important role for models of weather forecast, National Meteorological Services have commenced to integrate path delays of GPS radiowaves in their calculations.

With the results achieved and considering the high potential of applications Marc Troller has provided a significant body of work of Swiss Geodesy in the field of GPS meteorology. Its importance can be related to the goals formulated in the Kyoto Protocol. Cooperation in international projects of environmental research (ESCOMPTE) and in the frame of the Prix du Jeune Entrepreneur de la Section Suisse des Conseillers du Commerce Extérieur de la France reveal the international interest in the research topic pursued. The Swiss Geodetic Commission (SGC) expresses its gratitude to Marc Troller for his much valued contribution. The project was supported by ETH Zurich and the SGC. We are also grateful to the Swiss Academy of Sciences for covering the printing costs of this volume.

Prof. Dr. H-G. Kahle
Institute of Geodesy and Photogrammetry,
ETH Zürich

Prof. Dr. A. Geiger
ETH Zürich
President of SGC

Abstract

Climate change and global warming have become a major challenge for the sustainable development of our Earth and its environment. Intensive research is carried out to understand atmospheric processes and their implications. In this content, water vapor plays a key role. It is an important component of the global energy balance and is involved in many chemical reactions. In microwave measurements, the tropospheric refractivity causes a delay in the arrival of the signal propagating through the atmosphere. This refraction effect is one of the limiting factors in accurate GPS positioning. The tropospheric path delay can be decomposed into a dry and wet part, where the latter part is coupled with the integrated precipitable water vapor above the GPS receiver.

On the one hand, the refraction effect has to be corrected for GPS measurements, on the other hand, it is a valuable signal to determine the spatial distribution of the water vapor. This study investigates both aspects. For the first part, two basic approaches are looked into: One method is based on meteorological measurements. Thereby, the integrated amount of water vapor and its temporal variation are the prime target. The other concept makes use of long-term GPS measurements. The arrival delay of the GPS signals are used, to estimate the integrated amount of water vapor. This result can then be the basis to determine its spatial distribution and temporal behavior. The investigation is based on a tomographic approach and forms the main content of part 2 of this work.

In part 1, an extension of the software package COMEDIE is developed and applied to determine tropospheric path delays. COMEDIE allows a four-dimensional modeling (in space and time) of the meteorological parameters air pressure, temperature and water vapor pressure using a collocation approach. Integrating the meteorological parameters, tropospheric path delays are obtained. Evaluations and comparisons in Switzerland show the performance of this method. An overall good agreement was achieved compared to GPS-estimated path delays. The accuracy depends on the season, and is in the range of 1-2 cm for the tropospheric path delay.

Continuous GPS measurements allow to estimate tropospheric path delays in the GPS processing. In a second approach of part 1, a method based on such GPS-estimated path delays is developed. It uses - like COMEDIE - a four-dimensional model and a collocation adjustment to estimate tropospheric path delays at desired locations. Evaluations are carried out in the area of Switzerland using the permanent GPS network AGNES. Long-term time series of cross-correlations are analyzed. An accuracy of 0.5 - 1.5 cm is obtained.

To resolve the GPS-estimated water vapor in the vertical, a tomographic approach is investigated in part 2 of this study. It is based on the assimilation of GPS double-difference observations. The wet refractivity field is determined applying a least-squares adjustment. To test the performance of the software, different weather conditions are simulated. Various stochastically constrained models are applied and discussed in terms of inversion stability. Results from real data gathered during a dedicated measurement campaign in the high density GPS network of the Big Island of Hawaii are analyzed. Compared to radiosondes, an accuracy of about 10 ppm (refractivity units) is achieved.

To compare the potential and limits of the investigated methods, independent data must be available. An extensive study is performed in the area of Switzerland to evaluate and compare all presented methods with each other. For the validation, data of the numerical weather model aLMo are used. Seven days of data in a high spatial distribution and on an hourly basis are investigated. The tropospheric path delays resulting from the various methods are compared and analyzed. An overall good agreement with the aLMo data was observed. To evaluate the spatial distribution of water vapor, 7680 refractivity profiles are determined with the tomographic method and compared with the numerical weather data. The analysis contains four tomographic approaches including different types of constraints. The results are statistically evaluated and compared. A correlation between the accuracy and the weather situation was found. Overall, an agreement of 5-7 ppm (refractivity units) was achieved compared to aLMo.

In conclusion, it can be stated that the determination of the integrated amount of water vapor in the troposphere was successfully performed. For the main geodetic application, the correction of GPS measurements, the estimation of path delays in the GPS processing is recommended, provided long-term GPS phase observations are available. For the determination of the spatial distribution and the temporal variation of the integrated amount of water vapor, modeling of the GPS-estimated path delays is a successful method. Moreover, the principal feasibility to resolve the vertical distribution of the water vapor applying the tomographic approach was demonstrated. However, further investigations concerning constraints or the introduction of additional information are required.

Zusammenfassung

Klimaveränderung und globale Erderwärmung bilden heutzutage eine grosse Herausforderung für die nachhaltige Entwicklung unseres Planeten Erde und die Umwelt. Mit intensiver Forschungstätigkeit wird versucht, die atmosphärischen Prozesse und deren Auswirkungen zu verstehen. In diesem Zusammenhang bildet der Wasserdampf eine Schlüsselfunktion. Er ist in vielen chemischen Reaktionen involviert und bildet damit eine wichtige Grösse für die globale Energiebilanz. Das durch die Atmosphäre laufende Mikrowellen-Signal wird aufgrund der Refraktion verzögert. Dieser Effekt verursacht einen bedeutenden Genauigkeitsverlust von GPS. Troposphärische Weglängenverzögerungen können in einen trockenen und feuchten Anteil separiert werden, wobei letzterer mit dem gesamten (integrierten) ausfällbaren Wasserdampf oberhalb des GPS-Empfängers zusammenhängt.

Der Refraktivitätseffekt muss einerseits als Korrektur bei den GPS Messungen angebracht werden, andererseits kann er als Signal zur Bestimmung der räumlichen Verteilung des Wasserdampfes aufgefasst werden. In dieser Arbeit werden beide Aspekte untersucht. Im ersten Teil werden zwei grundlegende Ansätze zur Korrektur des troposphärischen Effektes erforscht. Einerseits wird die Refraktivität mit Hilfe von meteorologischen Daten modelliert. Dabei ist das Hauptziel die Bestimmung des integralen Wasserdampfgehaltes und dessen zeitliche Veränderung. Andererseits wird mit langen GPS-Messreihen die Zeitverzögerung des Signals ermittelt und der integrale Wasserdampfgehalt geschätzt. Letzterer kann im zweiten Teil dieser Arbeit dazu benutzt werden, um die räumliche Verteilung und das zeitliche Verhalten des Wasserdampfes zu bestimmen. Diese Untersuchungen basieren auf einem tomographischen Ansatz.

Im ersten Teil dieser Arbeit wird eine Erweiterung der Software COMEDIE zur Bestimmung von troposphärischen Weglängenverzögerungen untersucht. COMEDIE erlaubt eine vierdimensionale Modellierung (Raum und Zeit) der meteorologischen Parameter Luftdruck, Temperatur und Wasserdampfdruck mittels eines Kollokationsansatzes. Durch die Integration der meteorologischen Parameter entlang des Signalweges lassen sich die troposphärischen Weglängenverzögerungen bestimmen. Auswertungen und Vergleiche im Gebiet der Schweiz zeigen die Qualität dieser Methode auf. Im Allgemeinen konnten gute Übereinstimmungen mit den Weglängenverzögerungen, welche mit GPS geschätzt wurden, erreicht werden. Die Genauigkeit ist jahreszeitabhängig und erreicht eine Grössenordnung von 1-2 cm für die troposphärischen Weglängenverzögerungen.

Kontinuierliche GPS-Messungen erlauben die Schätzung der troposphärischen Weglängenverzögerungen mit einer GPS-Auswertesoftware. Im nächsten Teil dieser Arbeit wird eine Methode entwickelt, die auf aus GPS geschätzten Weglängenverzögerungen basiert. Es wird - wie bei COMEDIE - eine vierdimensionale Modellierung und eine Kollokationsausgleichung zur Bestimmung von troposphärischen Weglängenverzögerungen an beliebigen Orten verwendet. In der Schweiz wurden Daten

des GPS-Permanentnetzes AGNES ausgewertet. Mit Hilfe der Kreuzkorrelationsmethode wurden Zeitserien analysiert. Dabei konnte eine Genauigkeit von 0.5-1.5 cm erreicht werden.

Um die Höhenverteilung des mit GPS geschätzten Wasserdampfes bestimmen zu können, wird ein tomographischer Ansatz untersucht. Dieser basiert auf GPS-Doppeldifferenz-Beobachtungen. Der Feuchtanteil des Refraktivitätsfeldes wird mit der Methode der kleinsten Quadrate bestimmt. Um die Leistungsfähigkeit der Software zu untersuchen, wurden unterschiedliche Witterungsverhältnisse simuliert. Modelle mit verschiedenen stochastischen Nebenbedingungen wurden benutzt und bezüglich der Inversionsstabilität untersucht. Dazu wurden auch Auswertungen einer Messkampagne im dichten GPS-Netz von Hawaii analysiert. Der Vergleich zu Radiosonden ergab eine Genauigkeit von ca. 10 ppm (Refraktivitätseinheiten).

Um das Potential und die Grenzen der untersuchten Methoden bestimmen zu können, wurden alle oben vorgestellten Ansätze in einer ausgedehnten Studie auf dem Gebiet der Schweiz miteinander verglichen. Als Referenz wurden Daten des numerischen Wettermodells aLMo benutzt. Die Untersuchungen basieren auf stündlichen Zeitserien während sieben Tagen mit hoher räumlicher Auflösung im ganzen Gebiet der Schweiz. Die resultierenden troposphärischen Weglängenverzögerungen wurden miteinander verglichen und analysiert. Im Allgemeinen konnte eine gute Übereinstimmung mit den aLMo-Daten festgestellt werden. Um die räumliche Verteilung des Wasserdampfes zu untersuchen, wurden 7680 Refraktivitätsprofile mit der tomographischen Methode bestimmt und mit den numerischen Wetterdaten verglichen. Die Analyse beinhaltet vier tomographische Lösungen mit verschiedenen Nebenbedingungen. Die Auswertungen wurden statistisch analysiert und verglichen. Dabei wurde eine Korrelation zwischen der erreichten Genauigkeit und der Wettersituation festgestellt. Generell konnte im Vergleich mit aLMo eine Genauigkeit von 5-7 ppm (Refraktivitätseinheiten) erreicht werden.

Als Fazit dieser Arbeit kann zusammenfassend festgestellt werden, dass die Bestimmung des integralen Wasserdampfgehaltes in der Troposphäre erfolgreich demonstriert wurde. Für die geodätische Hauptanwendung, die Korrektur von GPS Messungen, wird aufgrund der gezeigten Ergebnisse weiterhin die Schätzung der Weglängenverzögerungen mit der GPS-Auswertesoftware empfohlen. Vorausgesetzt ist allerdings, dass GPS-Phasenmessungen mit langen Messzeiten vorliegen. Für die Bestimmung der räumlichen Verteilung und der zeitlichen Variation des integralen Wasserdampfgehaltes kann die Modellierung der mit GPS geschätzten Weglängenverzögerungen erfolgreich eingesetzt werden. Zudem wurde die Machbarkeit des tomographischen Ansatzes zur Bestimmung der Höhenauflösung des Wasserdampfes aufgezeigt. In diesem Zusammenhang sind noch weitere Untersuchungen bezüglich der Verwendung von Modellzwängen und auch weiterer zusätzlicher Informationen notwendig.

Contents

Abbreviations

AGNES	Automated GPS Network of Switzerland
aLMo	Alpine Model (numerical weather model of Switzerland)
ANETZ	Automated Meteorological Network of Switzerland
AWATOS	Atmospheric Water Vapor Tomography Software
COITROPA	Collocation and Interpolation of Tropospheric Path Delays
COMEDIE	Collocation of Meteorological Data for Interpolation and Estimation of Tropospheric Path Delays
EUREF	European Reference Frame
GPS	Global Positioning System
GRTI00	Swisstopo GPS densitiy campaign *Graubünden Tessin 2000*
IGS	International GPS Service
ITRF97	International Terrestrial Reference Frame 1997
MAGIC	Meteorological Applications of GPS Integrated Column Water Vapor Measurements in the Western Mediterranean
PW or IPW	(Integrated) Precipitable Water Vapor
rms	Root mean square
RTK	Real Time Kinematics
SVD	Singular Value Decomposition
ZWD	Zenith Wet Delay

1. Introduction

1.1. Water Vapor in the Atmosphere

Recently, climate change has become one of the most important challenges for the sustainable development of the earth and its population. At political level, an international agreement - the *Kyoto Protocol* - has been formulated for climate protection. Atmospheric processes and their implications such as global warming and the greenhouse effect are subject of intensive scientific research.

Water vapor takes part in the water cycle of the earth. It is condensated and precipitated in the form of rain or snow and originates again by evaporation, sublimation and transpiration. Although, only 0.001% of the total amount of water on the earth is located in the atmosphere, water vapor plays a fundamental role in atmospheric processes. It is the most variable parameter of the major constituents of the atmosphere, both, in space and time. Water vapor influences or causes many chemical processes in the atmosphere. It is a major greenhouse gas and is involved in the decomposition of the ozone layer. Water vapor is constantly circulating in the atmospheric system and is coupled to the formation and distribution of clouds and rainfall as well as air pollution and acid rain. The distribution of water vapor plays a crucial role in the vertical stability of the atmosphere and, therefore, in the evolution of atmospheric storms. Moreover, water vapor is the carrier of latent heat and an important component of the global energy balance as well as the transportation medium of energy in the atmosphere. Therefore, it is a fundamental quantity for climatological studies over short and long periods as well as for weather forecasting. Time series of atmospheric water vapor content as well as its spatial distribution is the basis for successful research in many climatic coherences and atmospheric processes.

1.2. Space Geodesy and Water Vapor

The Global Positioning System GPS was developed by the US Department of Defense (DoD) to allow positioning with an accuracy of better than 10 m over the whole world. Soon, many civil navigation applications began to use the GPS system for positioning at the accuracy level of 1 - 50 m, such as in traffic navigation systems (car, ship, plane), or GPS handheld devices for pedestrians, sometimes in combination with a geographical information system (GIS). On the other hand, high accuracy applications, mainly in the field of geodesy, became popular. Differential phase measurements reached an accuracy sufficient for ordnance survey and engineering geodesy work but also for very high accuracy applications such as realizing geodetic reference systems or monitoring recent crustal movements of the earth.

However, several corrections of the measurements are necessary to reach a sufficient accuracy level. The error sources can be divided into three types; errors originating from the satellite, errors of the antenna of the receiver and errors of the transmission medium, the atmosphere. Latter is divided in the ionosphere and the troposphere. If measurements are taken at two frequencies, a so called ionosphere-free linear combination can be composed, which eliminates the error originating from the ionosphere. One of the most important error sources remains the tropospheric path delay. It is caused by the varying density of the air. The GPS signal propagates with a varying speed and direction causing an arrival delay compared to a signal traveling with the speed of light in vacuum. This path delay causes a positioning error in the height component mainly, which is approximately 2-3 times larger than the excess path (Geiger, 1987). The effect is strongly correlated with the ground height. For the Swiss flat area, the total delay is about 2 m. It can be decomposed into a so-called dry ($\sim$ 90% of the total amount) and wet ($\sim$ 10% of the total amount) part. The dry part is mainly dependent on the moderately varying air pressure. The wet part of the path delay is primarily dependent on the water vapor amount of the troposphere which is varying strongly in space and time. Furthermore, a contribution to the wet path delay is caused of condensated water, such as clouds and rain. However, for usual conditions, this effect can be neglected. Only during extreme rainfall, this influence gets relevant (Elgered, 1993).

Several methods have been recently investigated to obtain an accurate tropospheric refractivity correction. The types of approaches can be divided into three groups: estimation of path delays by GPS measurements, assimilation of (mostly) meteorological measurements including water vapor radiometers and solar spectrometers, and modeling. Figure 1.1 gives an overview of the main methods applied.

The oldest possibility of modeling path delays is to use standard approaches like Saastamoinen (1972) or Hopfield (1969). Usually, only ground meteorological data can be assimilated to these models. Such an approach works well, if common atmospheric conditions apply: exponential decrease of pressure and water vapor pressure with height, and linear decrease of temperature with height up to the tropopause. The pressure-dependent dry part of the path delay can mostly be determined with high accuracy using standard models like Saastamoinen. The wet part of the path delay which depends primarily on the amount of water vapor in the troposphere is varying strongly in space and time. Standard models can not account for this effect.

Other types of methods determine the path delay directly with meteorological measurements:

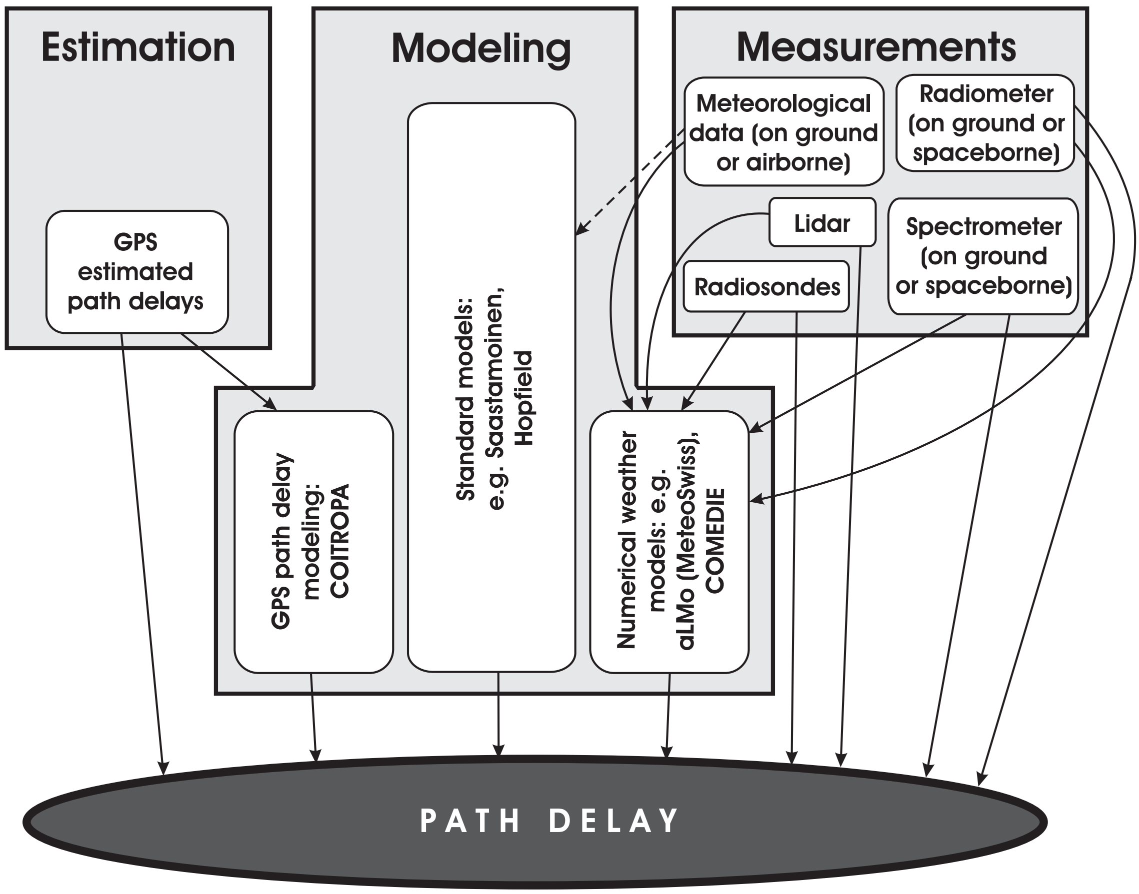

Figure 1.1.: Overview of main methods to determine tropospheric path delays, including COMEDIE and COITROPA which are presented in the following chapters.

- Water vapor radiometers measure the radiation intensity of the atmosphere which is proportional to the amount of water vapor in the line of sight (e.g. Kruse, 2001; Somieski et al., 2002)
- Solar spectrometers measure the absorption of the solar radiation due to water molecules which depends on the amount of tropospheric water vapor (Somieski et al., 2003).
- Radiosondes measure the pressure, temperature and relative humidity along the line of the sounding, which allows to calculate the respective path delay.
- Lidars use narrow band tunable lasers to transmit a short light pulse into the atmosphere at one (Raman lidar) or two (differential absorption lidar, DIAL) wavelengths. The light is backscattered by the atmosphere and measured to determine the water vapor concentration (Bock et al., 2001).

Another method estimates path delays from GPS measurements. Nowadays, this method yields the most accurate path delays. However, GPS-estimated path delays as well as path delays obtained directly from meteorological measurements can only be determined in the line of sight (or zenith direction) of the respective measurement system.

To account for a whole region using only a minimum of measurements, path delay models are inevitable. Models can be based on meteorological and/or GPS data. The present work investigates the potential and limits of modeling both types of base data.

1.3. GPS Meteorology

Apart from its importance in geodesy, GPS signals are also a highly valuable information for atmospheric research. The integrated amount of water vapor in the zenith direction is called *precipitable water vapor (PW)*. It is approximately proportional to the tropospheric path delay which can be estimated from GPS measurements. This relatively new research field is commonly called GPS meteorology (Bevis et al., 1992).

An overview of methods to determine atmospheric water vapor is given in Table 1.1. In difference to conventional methods, existing GPS permanent stations are able to estimate tropospheric water vapor continuously at nearly no further costs. For meteorology, two main data types are of importance:

- The wet path delay estimates can be used to determine the precipitable water vapor (PW). So far, this data is gained from radiosondes and meteorological satellites. Latter have a large noise, and consequently only a low resolution in accuracy can be achieved. The use of radiosondes is expensive and, therefore, the number of launches and stations is limited. Automated GPS networks can complement and fill this lack of data at low cost.

- An even larger benefit is gained from 4D spatial and temporal information of water vapor. So far, these data are determined using radiosondes. A new technique called GPS tomography is basically using GPS measurements. Applying a tomographic approach, spatial and temporal water vapor data are estimated at a high 4D resolution depending on the GPS network resolution. This method is investigated in detail. The performance and limits are presented and discussed.

measurements of the amount of water vapor	***in situ measurements of water vapor***
water vapor radiometer	ground sensor
solar spectrometer	radiosonde
lidar	airborne
spaceborne (METEOSAT)	
GPS	

Table 1.1.: Techniques to determine the atmospheric water vapor. GPS - as a new technique - is able to estimate the tropospheric amount of water vapor continuously.

1.4. Goals and Outline of Work

The goal of this thesis is to determine and model the tropospheric refractivity, especially the wet part. Furthermore, the application of tropospheric path delays from GPS and meteorological data is investigated in practical studies. Its behavior and variation are examined with particular emphasis on geodetic and meteorological applications.

Chapter 2 gives a short overview of the theoretical background. The basic definitions and equations of atmospheric propagation are presented.

The development of correction models for GPS measurements is described and discussed in Chapter 3 and 4. Chapter 3 investigates the use of meteorological base data in combination with a tropospheric model. Water vapor pressure is measured and transformed into wet path delays. Chapter 4 uses GPS estimated data preferably from continuous GPS networks to model tropospheric corrections. In both methods, special attention is paid to the accuracy and reliability of the wet path delay determination.

GPS measurements can also be used on its own or in combination with the method described in Chapter 4 to determine the spatial amount of water vapor for applications in atmospheric sciences.

The method of GPS tomography to determine the spatial and temporal distribution of water vapor in the atmosphere is presented in Chapter 5. Results of simulations and real data comparisons are presented.

In Chapter 6, a case study has been performed on the Swiss territory. The path delays have been determined with the methods presented in Chapter 3 and 4 and are compared with data of a numerical weather model.

In the second part of Chapter 6, the distribution of water vapor has been estimated applying GPS tomography. The results are analyzed based on data of a numerical weather model as well.

Chapter 7 gives a concluding evaluation of the discussed methods, its possibilities and limitations. As outlook, an outline of promising further research in the field of atmospheric water vapor determination is presented.

2. Propagation Characteristics of the Atmosphere

2.1. Propagation of GPS Signals

GPS signals emitted from the satellite are significantly influenced by the atmosphere along the entire path to the GPS antenna. The GPS satellites transmit at two different carrier frequencies of 1575.42 MHz (L1 signal) and 1227.60 MHz (L2 signal). The upper part of the atmosphere, called ionosphere, is a dispersive medium for frequencies in the radio band. That means, the delay depends on the frequency of the signal. Provided that the measurements are taken at two frequencies, a so-called ionosphere-free linear combination of the two signals can be composed, which allows to eliminate the ionospheric effects. The lower part of the atmosphere, called troposphere, is neutral and non-dispersive for radio frequencies. Hence, the tropospheric delay is independent from the carrier frequency and, therefore, can not be eliminated with multi-frequency measurements. The tropospheric influence can be separated into two physical effects. Primarily, due to the non-vacuum nature of the atmosphere, the propagating signal is delayed, according to the refractivity of the atmosphere. Secondly, the GPS signal is bent. It propagates along a curved path. Both effects generate an excessive path.

The basic methods of tropospheric refractivity modeling are introduced in this chapter, and the relation to atmospheric water vapor is outlined. Current techniques and formulas used are presented and explained.

2.2. Definition of the Tropospheric Path Delay

The tropospheric path delay is defined as the delay of the signal propagating through the troposphere compared to a signal propagating with the speed of light in the vacuum. The troposphere is a non-dispersive medium for radio frequencies up to 15 GHz, i.e. the refractivity is frequency-independent and the signals are equally delayed. This delay is a function of the tropospheric refractive index (Seeber, 1993; Kaplan, 1996).

Looking at Figure 2.1, the geometry of the ray can be formulated. The time difference between the emission of the signal and its arrival at the receiver is defined as:

$$\Delta t = t_R - t_S = \int_{t_S}^{t_R} dt = \int_W \frac{1}{v} ds \tag{2.1}$$

where:

t_S	:	emitting time of the ray at the GPS satellite
t_R	:	arriving time of the ray at the GPS receiver
W	:	propagation line of the GPS ray
v	:	propagation velocity of the GPS ray dependent on the propagation line W

Considering the refractive index n as

$$n = \frac{c}{v} \tag{2.2}$$

c : velocity of light in the vacuum

the time difference Δt is then given as:

$$\Delta t = t_R - t_S = \frac{1}{c} \cdot \int_W n(s) ds \tag{2.3}$$

The radio distance RD is written as

$$RD = c \cdot (t_R - t_S) = \int_W n(s) ds \tag{2.4}$$

whereas the Euclidean distance ED is (Figure 2.1):

$$ED = \int_{W_0} ds_0 \tag{2.5}$$

The excess path length or path delay Δ^{PD} is defined as the difference between the radio and Euclidean distance:

$$\begin{aligned} \Delta^{PD} &= \int_W n(s) ds - \int_{W_0} ds_0 & (2.6) \\ &= \int_W [n(s) - 1] ds + \{\int_W ds - \int_{W_0} ds_0\} & (2.7) \end{aligned}$$

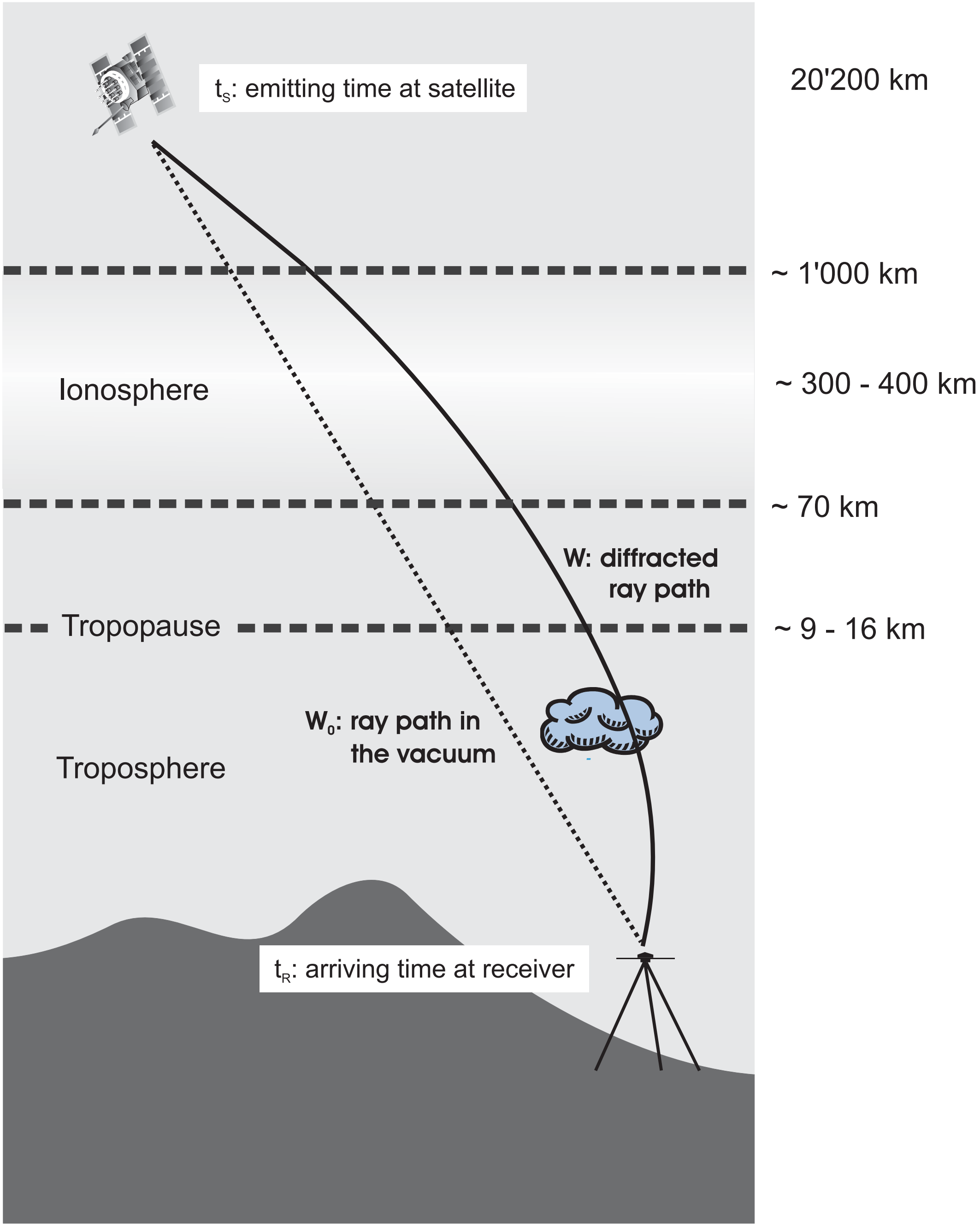

Figure 2.1.: Propagation of a GPS signal through the atmosphere. Diffraction in the troposphere causes a delayed and bent ray. The distance traveled along W can be determined. The dotted line shows the Euclidean distance as if the signal propagates through the vacuum.

The excess path length is caused by two atmospheric effects: the propagation delay (first term of (2.7)) and the bending (term in braces of (2.7)) of the ray. The size of the path delay is mainly dependent on the elevation angle of the arriving ray. Considering an elevation angle of 5 degrees, ray bending causes a delay of around 10 cm, regarding an elevation angle of 15 degrees, the delay caused by bending decreases to 1 mm and if the zenith direction is focused, the bending effect is no longer observable (Mendes, 1999). Therefore, the ray bending term is often neglected and the relation (2.7) can be simplified as follows:

$$\Delta^{PD} = \int_W [n(s) - 1] ds \tag{2.8}$$

Often the path delay is expressed in terms of refractivity N:

$$\Delta^{PD} = 10^{-6} \int_W N ds \tag{2.9}$$

whereby the refractivity is defined as:

$$N = 10^6 \cdot (n - 1) \tag{2.10}$$

2.3. Modeling of Refractivity

The refractivity N is mainly determined by the three meteorological parameters air pressure p, temperature T and water vapor pressure e. The general formula has been developed empirically (e.g. Essen and Froome, 1951):

$$N = (n-1) \cdot 10^6 = k_1 \frac{p_d}{T} \cdot Z_d^{-1} + k_2 \frac{e}{T} \cdot Z_w^{-1} + k_3 \frac{e}{T^2} \cdot Z_w^{-1} \tag{2.11}$$

where:

$$\begin{aligned}
p_d &= \text{partial pressure of dry gases} \\
T &: \text{temperature} \\
e &: \text{water vapor pressure} \\
k_1, k_2, k_3 &= \text{empirically determined constants} \\
Z_d^{-1} &= \text{inverse compressibility of dry air} \\
Z_w^{-1} &= \text{inverse compressibility of wet air}
\end{aligned}$$

The partial pressure of dry gases p_d can be expressed with the total pressure of the moist air p and the water vapor pressure e (Boudouris, 1963):

$$p_d = p - e \tag{2.12}$$

The values of the constants k_1, k_2, k_3 are published by Essen and Froome (1951), Smith and Weintraub (1953), Owens (1967) and Thayer (1974). A summary of the individual constants can be found in Hartmann and Leitinger (1984). In the present study, the values published by Thayer (1974) for microwave refractivity are used, since they are considered to have the highest accuracy (Table 2.1).

	$k_1[K/hPa]$	$k_2[K/hPa]$	$k_3[K^2/hPa]$
value	77.60	64.8	$3.776 \cdot 10^5$
std. error	0.014	0.08	$0.004 \cdot 10^5$

Table 2.1.: Constants for the equation of the radio refractive index (2.11) according to Thayer (1974).

The compression factors Z_d and Z_w account for the correction of non-ideal gas behavior (Owens, 1967). Assuming that the atmosphere behaves like an ideal gas, we get

$$Z_d^{-1} = Z_w^{-1} = 1 \tag{2.13}$$

Introducing the values of constants of Thayer (1974), along with (2.12) and (2.13), relation (2.11) can be rewritten as:

$$\begin{aligned} N &= k_1 \frac{p-e}{T} + k_2 \frac{e}{T} + k_3 \frac{e}{T^2} && (2.14) \\ &= 77.60 \frac{p-e}{T} + 64.8 \frac{e}{T} + 3.776 \cdot 10^5 \cdot \frac{e}{T^2} && (2.15) \\ &= 77.60 \frac{p-e}{T} + 64.8 \frac{e}{T}\left(1 + \frac{5827}{T}\right) && (2.16) \end{aligned}$$

Often, the refractivity is separated into a dry and a wet component (e.g. Hopfield, 1969).

$$N_{total} = N_{dry} + N_{wet} \tag{2.17}$$

The separation is commonly used, because modeling of the two parts requires different height-dependent functions. In doing so, the dry component contains the dry atmosphere, whereas the wet component describes the part associated to water vapor. According to (2.17), the path delay determination (2.9) can be rewritten as:

$$\Delta^{PD} = 10^{-6} \int_W N_{dry}\, ds + 10^{-6} \int_W N_{wet}\, ds \tag{2.18}$$

Looking at (2.16), the separate parts of the refractivity N can be expressed in meteorological terms.

$$N_{dry} = \quad k_1 \frac{p-e}{T} \quad = 77.60 \frac{p-e}{T} \tag{2.19}$$

$$N_{wet} = \quad k_2 \frac{e}{T} + k_3 \frac{e}{T^2} \quad = 64.8 \frac{e}{T}\left(1 + \frac{5827}{T}\right) \tag{2.20}$$

Davis et al. (1985) proposed to separate the equation of the radio refractive index (2.11) in a way, that a term nearly independent of the wet-dry mixing ratio is created. Relation (2.14) is converted to:

$$N \quad = \quad k_1 \frac{R}{M_d}\rho + k_2^{'} \frac{e}{T} + k_3 \frac{e}{T^2} \tag{2.21}$$

where:

$R =$	$8.3145\ J\ mol^{-1}\ K^{-1}$	: universal gas constant
$M_d =$	$28.9644\ kg\ kmol^{-1}$	: molar mass of dry air
ρ		: density for dry air
$k_2^{'} =$	$17\ K\ hPa^{-1}$	: derived constant (Davis et al., 1985)

The first term of (2.21) is often called hydrostatic refractivity. The remaining two term are wet terms. Sometimes they are referred to as wet refractivity. However they are not equal to the wet refractivity of (2.20). Therefore, in this work the terms are named as non-hydrostatic refractivity.

2.4. Mapping Functions

The path delay introduced in (2.9) corresponds to a slant delay from the station to the satellite. Often a zenithal path delay pointing to the zenith is used as reference and for comparison purposes. The mapping function describes the transformation from the delay at zenith direction to a slant delay at different elevation angles:

$$\Delta^{PD} = MF(z) \cdot \Delta_0^{PD} \tag{2.22}$$

where:

Δ^{PD}	:	slant path delay
Δ_0^{PD}	:	zenithal path delay
$MF(z)$	:	mapping function
z	:	zenith distance

The simplest mapping function is the inverse cosinus function:

$$MF(z) = \frac{1}{cosz} \tag{2.23}$$

This mapping function assumes a horizontally layered atmosphere and does not take into account the earth's curvature. This fact obviously results in an error increasing with increasing zenith distance z. In the last couple of decades, a number of scientists were engaged in developing more accurate mapping functions. Marini (1972) proposed the most popular mapping function $MF(z)$:

$$MF(z) = \cfrac{1}{cosz + \cfrac{a}{cosz + \cfrac{b}{cosz + \cfrac{c}{cosz + ...}}}} \tag{2.24}$$

This basic form of continuous fraction describes the geometrical approximation of the elevation dependence of the delay. Several researchers improved the constants a, b, c with only small changes on the base formula (2.24) (e.g. Chao, 1973; Davis et al., 1985; Ifadis, 1986, 1987). Due to the different type of behavior of the dry and wet refractivity, Davis et al. (1985) and Rothacher (1992) proposed different mapping functions for the dry and wet parts. (2.22) becomes:

$$\Delta^{PD} = \Delta^{PD}_{dry} + \Delta^{PD}_{wet} = MF_{dry}(z) \cdot \Delta^{PD}_{0,dry} + MF_{wet}(z) \cdot \Delta^{PD}_{0,wet} \tag{2.25}$$

Herring (1992) enhanced the usual form of (2.24) by introducing a numerator:

$$MF(z) = \frac{1 + \cfrac{a}{1 + \cfrac{b}{1 + c}}}{cosz + \cfrac{a}{cosz + \cfrac{b}{cosz + c}}} \tag{2.26}$$

So far, all mapping functions are based on meteorological parameters. Because of the different behavior of the lower compared to the higher atmosphere, Niell (1996) developed a mapping function completely independent of meteorological parameters but dependent on the season and geographic location (Table 2.2).

Furthermore, Niell (1996) introduced a height correction term. The complete formula reads now:

$$MF(z) \quad = \quad \frac{1 + \cfrac{a}{1 + \cfrac{b}{1 + c}}}{cosz + \cfrac{a}{cosz + \cfrac{b}{cosz + c}}} + H \cdot 10^{-3} \cdot M_h \tag{2.27}$$

mapping function	minimum elevation	coefficient dry	wet
Marini (1972)	10	(tabulated)	-
Chao (1973)	10	(tabulated)	-
Davis et al. (1985)	5	p, e, T, β, h_t	p, e, T, β, h_t
Ifadis (1986)	2	T, p, e	T, p, e
Herring (1992)	3	T, φ, H	T, φ, H
Niell (1996)	3	DOY, φ, H	φ

Table 2.2.: Parameterization of the main mapping functions and the minimum elevation of validity. The first approaches used tabulated constants, in the following, meteorological parameters are mainly used. Recent mapping functions are dependent on the season (DOY) and geographic location but independent of meteorological parameters. Abbreviations are p: total surface pressure; T: surface temperature; e: surface water vapor pressure; β: lapse rate; h_T: height of the tropopause; φ: latitude; H: station height; DOY: day of year in UTC.

where for the dry mapping function:

$$M_h = \frac{1}{cosz} - \frac{1 + \cfrac{a_{ht}}{1 + \cfrac{b_{ht}}{1 + c_{ht}}}}{cosz + \cfrac{a_{ht}}{cosz + \cfrac{b_{ht}}{cosz + c_{ht}}}}$$

$$\begin{aligned}
a &= a_{avg}(\varphi) + a_{amp}(\varphi) \cdot cos\left(2\pi\frac{t - T_0}{365.25}\right) \\
b &= b_{avg}(\varphi) + b_{amp}(\varphi) \cdot cos\left(2\pi\frac{t - T_0}{365.25}\right) \\
c &= c_{avg}(\varphi) + c_{amp}(\varphi) \cdot cos\left(2\pi\frac{t - T_0}{365.25}\right)
\end{aligned}$$

$a_{avg}, a_{amp}, b_{avg}, b_{amp}, c_{avg}, c_{amp}$: tabulated average values and annual amplitudes depending on the latitude φ

a_{ht}, b_{ht}, c_{ht} : tabulated height correction values

t : time from January 0.0 [in UT days]

T_0 : adopted phase [DOY 28]

and for the wet mapping function:

$$\begin{aligned} M_h &= 0 \\ a, b, c &: \text{tabulated values} \end{aligned}$$

The accuracy of all mapping functions is 1 cm or better. The main difference is the elevation angle range for which this accuracy is valid (Table 2.2). A detailed description of the individual mapping functions, their accuracy and characteristics can be found in Niell (1996) or Ifadis (2000).

Because of the small differences between the individual mapping functions, common GPS processing software packages usually have only few functions implemented. The Bernese Processing Software Version 4.2 (Beutler et al., 2001) includes the simple $cosz$ mapping function (2.23) (Saastamoinen, 1972), the Hopfield model (Hopfield, 1969) and the dry and wet Niell formula (Niell, 1996).

2.5. Models of Path Delay Calculation

Calculating the path delay according to the integrals described in (2.18) requires the determination of the refractivity along the whole propagation ray. This method is time-consuming and usually not feasible. Thus, several models were developed, which allow the calculation of the path delay using just a few parameters. Basic work was done by Hopfield (1969), who found a representation of the dry refractivity as a function of height. In a further step the modified Hopfield model (Hopfield, 1971) was developed. It depends on the direction of the refracted ray instead of the height.

Currently, the model proposed by Saastamoinen (1972), which is deduced from the gas laws is often used. This approach requires the ground temperature T, pressure p and water vapor pressure e as well as the elevation angle as input. In case of absence of meteorological measurements, it is possible to use the standardized values of the atmosphere. For GPS processing, common values for station height $H = 0$ are (e.g. Rothacher, 1992):

$$p = 1013.25 \ hPa \tag{2.28}$$

$$T = 291.16 \ K \tag{2.29}$$

$$\text{Humidity} = 50 \ \% \tag{2.30}$$

The detailed derivation of the Saastamoinen model is published in Saastamoinen (1972): Starting with the integration equation of the refractive index (2.8), the inverse cosinus mapping function (2.23) and applying the formula of Essen and Froome (1951), a numerical form for the tropospheric path delay results:

$$\Delta^{PD}_{saas} = \frac{0.002277}{cosz} \cdot \left[p + \left(\frac{1255}{T} + 0.05 \right) \cdot e - B \cdot tan^2 z \right] + \delta_R \tag{2.31}$$

The variables B and δ_R are correction quantities. B is a pressure correction which mainly depends on the station height. δ_R is a range correction term depending primarily on the zenith distance and secondly on the station height. Both values are tabulated (e.g. Saastamoinen, 1973; Hofmann-Wellenhof et al., 2001). For the sake of completeness, the tables are also given in Appendix A.1.

According to the derivation of (2.31), it is possible to calculate the dry Δ_{dry} and wet path delay Δ_{wet}. The detailed derivation is described in Appendix A.2.

$$\Delta_{dry} = \frac{0.002277}{cos z} \cdot \left(p - 0.155471\ e - B \cdot tan^2 z\right) + \delta_R \tag{2.32}$$

$$\Delta_{wet} = \frac{0.002277}{cos z} \cdot \left(\frac{1255}{T} + 0.205471\right) \cdot e \tag{2.33}$$

2.6. Path Delay and Precipitable Water Vapor

A commonly used quantity of atmospheric water vapor is the *(integrated) precipitable water vapor (PW)*. It contains the amount of water potentially available in the atmosphere for precipitation. PW is usually measured in a vertical column that extends from the earth's surface to the upper edge of the troposphere (PG.net, 2004; Askne and Nordius, 1987).

$$PW[m] = \frac{1}{\rho_l} \int \rho_w ds \tag{2.34}$$

where:

ρ_l	$= 1000\ kgm^{-3}$	: density of liquid water
ρ_w		: mass density of water vapor $[kgm^{-3}]$

In some cases the precipitable water vapor is expressed as the vertically integrated mass of water vapor per unit area in $[kgm^{-2}]$:

$$PW[kgm^{-2}] = \int \rho_w ds \tag{2.35}$$

Obviously, the relationship between $PW\ [m]$ and $PW\ [kgm^{-2}]$ is given as:

$$PW[m] = \frac{PW[kgm^{-2}]}{\rho_l} \tag{2.36}$$

Recalling (2.18), the dry and wet components of the path delay are caused by different physical effects. The dry delay is mainly caused by the atmospheric condition itself and depends strongly on the pressure. The variation of the dry delay is relatively small. In contrast, the wet delay is mainly caused by the water vapor which changes rapidly both in space and time. The formula for the wet path delay can be expressed as follows (2.18 and 2.20):

$$\Delta_{wet}^{PD} = 10^{-6} \int_W \Big(k_2 \frac{e}{T} + k_3 \frac{e}{T^2}\Big) ds \tag{2.37}$$

A relationship between the tropospheric wet path delay Δ_{wet}^{PD} and the precipitable water vapor PW can be found (Askne and Nordius, 1987). By introducing a mean temperature T_m (Davis et al., 1985)

$$T_m = \frac{\int \frac{e}{T} ds}{\int \frac{e}{T^2} ds}, \tag{2.38}$$

(2.37) yields:

$$\Delta_{wet}^{PD} = 10^{-6} \Big(k_2 + \frac{k_3}{T_m}\Big) \int \frac{e}{T} ds \tag{2.39}$$

The equation of state for ideal gases can be used, as, under terrestrial conditions water vapor behaves approximately as an ideal gas.

$$e = \rho_w R_w T \tag{2.40}$$

where:

$R_w = \; 461.524 JK^{-1} kg^{-1}$: specific gas constant for water vapor

Combining (2.39) and (2.40), and, taking into account (2.35), the integral can be substituted:

$$\Delta_{wet}^{PD} = 10^{-6} \Big(k_2 + \frac{k_3}{T_m}\Big) \int \rho_w R_w ds \tag{2.41}$$

$$= \kappa' \cdot PW [kgm^{-2}] \tag{2.42}$$

where:

$$\kappa^{'} = 10^{-6} \cdot \Big(k_2 + \frac{k_3}{T_m}\Big) R_w$$

Often, the non-hydrostatic path delay is used instead of the wet path delay. Starting from (2.21), the relation (2.42) can be derived in a similar way as:

$$\Delta^{PD}_{non-hydrostatic} = 10^{-6}\Big(k_2^{'} + \frac{k_3}{T_m}\Big) R_w \cdot PW[kgm^{-2}] \tag{2.43}$$

Usually the relation is written as:

$$\Delta^{PD}_{non-hydrostatic} = \kappa \cdot PW[kgm^{-2}] \tag{2.44}$$

where:

$$\kappa = 10^{-6} \cdot \Big(k_2^{'} + \frac{k_3}{T_m}\Big) R_w \tag{2.45}$$

The constants $k_2^{'}$ and k_3 have to be expressed in the SI units $[K]$ and $[Pa]$.

Alternatively, the relation between the PW and the non-hydrostatic path delay can be stated as following:

$$\Delta^{PD}_{non-hydrostatic} = \kappa \cdot \rho_l \cdot PW[m] = Q \cdot PW[m] \tag{2.46}$$

Since both, the PW[m] and $\Delta^{PD}_{non-hydrostatic}$ have the same unit, the coefficient Q gets a dimensionless quantity. As approximation, the coefficient can be set to $Q \approx 6.5$.

A precise retrieval of the PW from $\Delta^{PD}_{non-hydrostatic}$ requires an accurate determination of the constant κ, thus of an accurate determination of T_m. The latter can be calculated by a statistical analysis of a large number of radiosonde observations. Analysis of 8718 radiosonde profiles during two years in the United States yield a linear relation between T_m and the surface temperature T_s (Bevis et al., 1992):

$$T_m \sim 70.2 + 0.72\ T_s \tag{2.47}$$

The relative error of this determination is stated as less than 2%. An investigation based on more than 120'000 radiosonde profiles in Europe was carried out by Emardson and Derks (2000). Four different models for the coefficient Q were studied, based on different combinations of surface temperature, latitude of the site and time of the year. The so-called *annual model* is given as:

$$Q = a_0 + a_1 \cdot \theta + a_2 \cdot sin\Big(2\pi\frac{t_D}{365}\Big) + a_3 \cdot cos\Big(2\pi\frac{t_D}{365}\Big) \tag{2.48}$$

where:

$$
\begin{aligned}
\theta &: \text{latitude of the station [in degree]} \\
t_D &: \text{day of year} \\
a_0 &= 5.882 \\
a_1 &= 0.01113 \\
a_2 &= 0.064 \\
a_3 &= 0.127
\end{aligned}
$$

The relative error of this function is stated as 1.43%. The relative error can be reduced to 1.14% if the so-called *hybrid model* is used, which includes the surface temperature. However, this reduction is only moderate, and it is normally not worth to get surface temperature values.

3. Path Delay Modeling Using Meteorological Input Data

3.1. Introduction

A promising method to determine the tropospheric path delay is to model meteorological observations. A commonly used model has been derived by Saastamoinen (1972) (2.31). Ground meteorological measurements are introduced to compute the tropospheric path delay of the GPS signal. Another approach is to obtain the tropospheric refractivity field using functional modeling. At the Geodesy and Geodynamics Lab (GGL), a software package COMEDIE (COllocation of MEteorological Data for Interpolation and Estimation of tropospheric path delays) was developed to model the refractivity field using meteorological data. The feasibility study was done using a three-dimensional refractivity field (Eckert et al., 1992). Subsequently, a four-dimensional modeling of the refractivity field was developed (Hirter, 1998). It allows to determine tropospheric path delays independently of the GPS technique.

3.2. Principle of the Software Package COMEDIE

3.2.1. Overview

In the frame of this research work, a completely new version of COMEDIE was developed (Troller et al., 2000, 2002b). Modeling and adjustment algorithms were taken over from previous versions (Eckert et al., 1992; Hirter, 1998) and were refined. The current version of COMEDIE is modularly programmed. The main calculation routines are based on the programming language C and the data exchange routines on the script language Perl.

COMEDIE allows a four-dimensional modeling of meteorological observations of pressure p, temperature t and water vapor pressure e in space and time. It is based on the method of least-squares collocation (Moritz, 1973), i.e., the model is described by a functional and a stochastic part. This approach allows the interpolation of each meteorological parameter individually, both, in space as well as in time. Using the formula of Essen and Froome (1951) (2.15), the wet refractivity throughout the atmosphere can be determined. In the last step, the refractivity is integrated along a ray in zenith direction (2.18). The integration yields the corresponding delay (Figure 3.1).

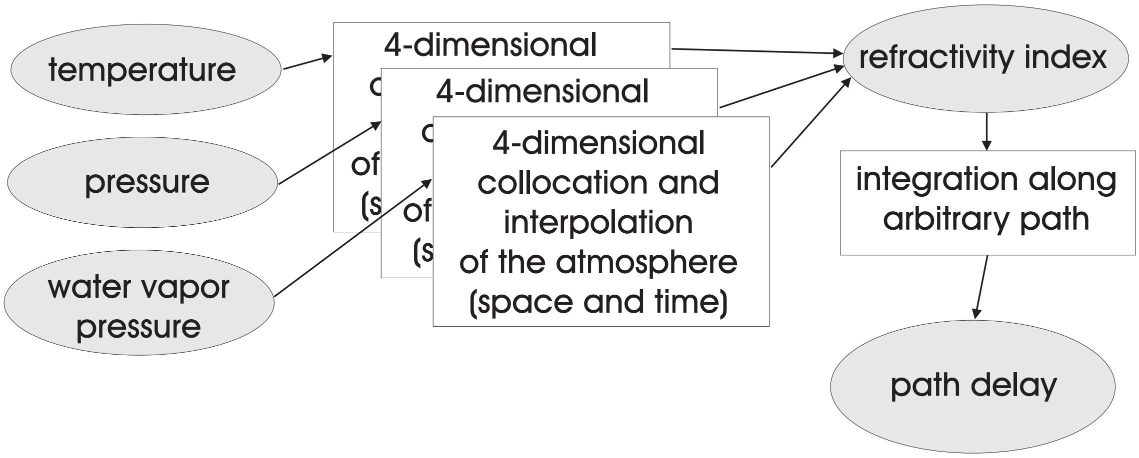

Figure 3.1.: Flow chart of the software package COMEDIE. The three parameters pressure, temperature and water vapor pressure are collocated and interpolated individually in the four-dimensional atmosphere. After calculating the refractivity, the integration along an arbitrary path can be achieved to determine the path delay.

Due to the large amount of ground meteorological observations, the collocation matrices get huge and the processing is time consuming. For the dry path delay, the Saastamoinen formula (Saastamoinen, 1972) achieves a similar accuracy level as COMEDIE. Therefore the dry tropospheric path delay is computed with the formula of Saastamoinen (1972) and only the wet tropospheric path delay is modeled using COMEDIE.

3.2.2. Collocation Approach

The atmosphere is an inhomogeneous medium. Traditional adjustment algorithms model functional parts which account only partly for the complexity of the atmosphere. Otherwise, the functional models would have a high complexity.

The collocation is an extended application of the traditional adjustment method. Apart from the use of common functional models, remaining systematic parts are determined and separated from measurement noise. Therefore, simple functional models - which describe the reality only partly - can be applied. Figure 3.2 illustrates the situation. The main equation of the collocation reads as follows:

$$l = A \cdot x + s' + n \tag{3.1}$$

where:

$$\begin{array}{rcl} l & : & \text{measurement} \\ A & : & \text{design matrix} \\ x & : & \text{vector of unknowns} \\ s' & : & \text{signal} \\ n & : & \text{noise} \end{array}$$

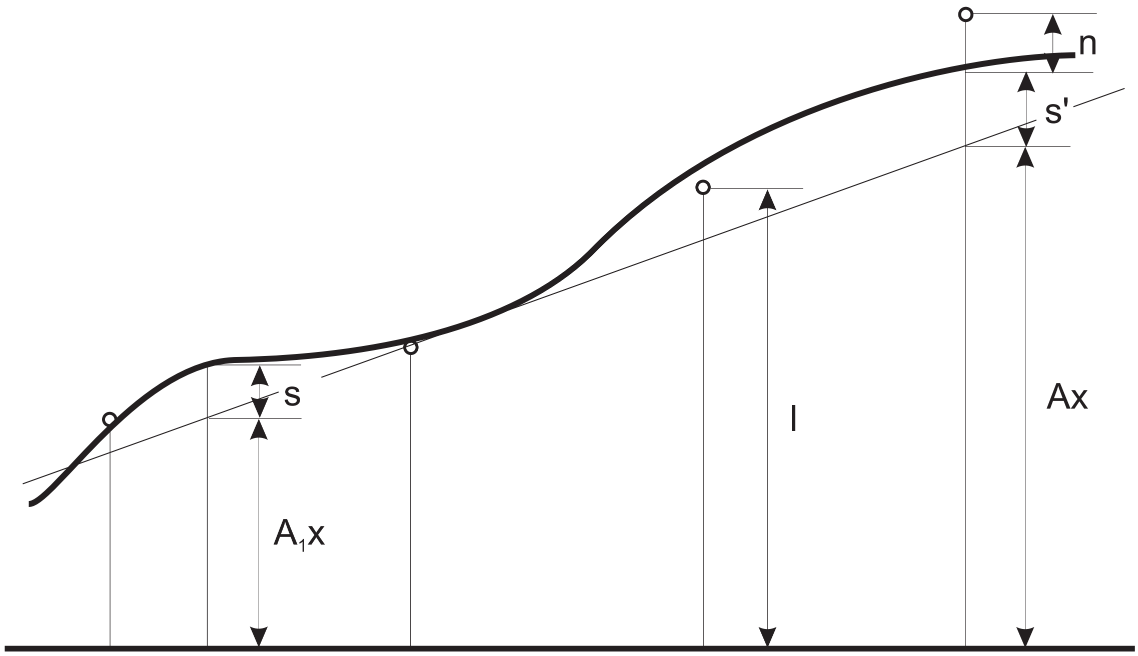

Figure 3.2.: Principle of the collocation approach in 1 dimension (Wirth, 1990). The measurement l is displayed with circles. Its value is composed of the functional part Ax, the signal part s' and the noise n. A point can be interpolated as summation of the functional part A_1x and the signal part s. Latter accounts for functional systematic parts.

The functional part is represented by the term Ax. The remaining of the observation is separated into a signal and noise part according to a chosen covariance function. As a major result of the collocation method, arbitrarily chosen observation points can be interpolated in the collocated area using the following equations:

$$t = A_1 \cdot x + s \tag{3.2}$$

$$s = C_{ss'} \cdot C_{ll}^{-1} \cdot (l - A \cdot x) \tag{3.3}$$

where:

$$\begin{array}{rcl} A_1 & : & \text{design matrix for the interpolated point} \\ s & : & \text{signal at the interpolated point} \\ C_{ss'} & : & \text{covariance matrix of the signal} \\ C_{ll} & : & \text{covariance matrix of the observation} \end{array}$$

Nowadays, the collocation is a widely used method for a variety of applications. For more information we refer to Moritz (1973) or Wirth (1990).

3.2.3. Functional Modeling

The functional models are selected based on physical realities. Simple functions are used, dependent on the height, the horizontal and temporal gradients. The systematic part, which cannot be represented by the functional model, will be assigned to the signal. In the following, the three meteorological parameters pressure, water vapor pressure and temperature are discussed in detail.

Pressure p

An exponential approach is chosen under the assumption of an isothermal atmosphere (Figure 3.3).

$$p(x, y, z, t) = (p_0 + a(x - x_0) + b(y - y_0) + c(t - t_0)) \cdot e^{-\frac{z - z_0}{H}} \tag{3.4}$$

where:

$$\begin{array}{rcl} p(x, y, z, t) & : & \text{pressure at point } P(x, y, z) \text{ at time } t \\ p_0 & : & \text{pressure at reference point } P_0(x_0, y_0, z_0) \text{ at time } t_0 \\ a, b, c & : & \text{coefficients of the horizontal and temporal gradients} \\ H & : & \text{scale height} \end{array}$$

The reference coordinates x_0, y_0 and t_0 are calculated as means of all measurement points and times, except the height is set to $z_0 = 0$.

Practical examinations have shown that an equally balanced distribution of measurements should be aimed at, specially in the height component. Otherwise the parameters of the model cannot be determined adequately.

Water Vapor Pressure e

Commonly, humidity is expressed in terms of relative humidity. Since the latter depends on the temperature and is not conservative, COMEDIE uses water vapor

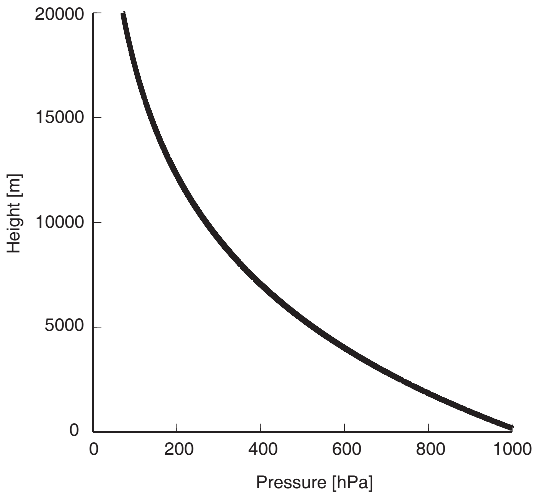

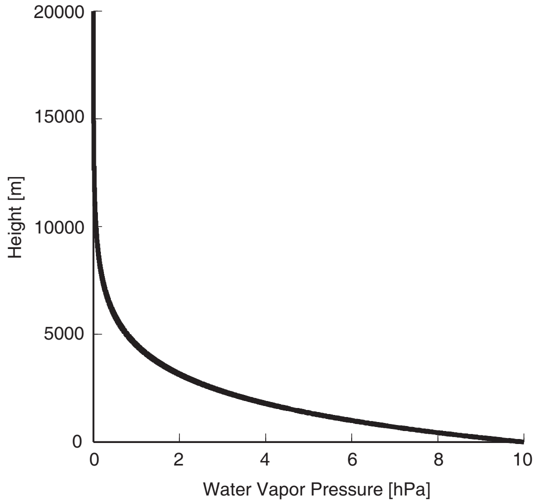

Figure 3.3.: Characteristics of the pressure function (left graph) and the water vapor pressure function (right graph). Both functions are based on an exponential approach. The pressure function has a scale height of approximately 7500 m whereas the scale height of the water vapor pressure is only around 2000 m. Typically, the amount of water vapor pressure decreases to zero at a height of 8000 m.

pressure instead. The relation between relative humidity H_r (in percent) and water vapor pressure e is defined as (e.g. Berg, 1948; Zuev and Komarov, 1987):

$$e = \frac{H_r}{100} \cdot E(T) \tag{3.5}$$

where:

E : saturation vapor pressure
T : temperature [Kelvin]

If the dew point temperature T_d is used, (3.5) can be simplified (e.g. Berg, 1948; Zuev and Komarov, 1987):

$$e = E(T_d) \tag{3.6}$$

Several formulas are available to calculate the saturation vapor pressure E (e.g. Richner et al., 1996). Today, the commonly used approach is given by Goff and Gratch (1946), and slightly revised by Goff (1965):

$$E(T) = 10^u \cdot e_1 \tag{3.7}$$

where:

$$
\begin{aligned}
u &= 10.79586 \cdot (1 - \frac{T_0}{T}) - 5.02808 \cdot \log_{10}(\frac{T}{T_0}) \\
&\quad +1.50474 \cdot 10^{-4} \cdot (1 - 10^{-8.29692 \cdot (\frac{T}{T_0} - 1)}) \\
&\quad +4.2873 \cdot 10^{-4} \cdot (10^{4.76955 \cdot (1 - \frac{T_0}{T})} - 1) - 2.2195983
\end{aligned} \tag{3.8}
$$

and:

T_0 : temperature of the triple point of water (=273.15 K)
e_1 : saturation water vapor pressure at the triple point (=1013.25 hPa)

Alternatively, a much simpler formula is often used to derive a function of the saturated water vapor (Richner et al., 1999; HMP243, 1996):

$$E(T) = 6.1078 \cdot 10^{\frac{7.5 \cdot (T - T_0)}{T - T_0 + 237.3}} \tag{3.9}$$

According to Zuev (1974) the water vapor pressure in the troposphere can be described using an exponential approach (Figure 3.3):

$$e(x, y, z, t) = (e_0 + a(x - x_0) + b(y - y_0) + c(t - t_0)) \cdot e^{-\frac{z - z_0}{H}} \tag{3.10}$$

where:

$e(x, y, z, t)$: water vapor pressure at point $P(x, y, z)$ at time t
e_0 : water vapor pressure at reference point $P_0(x_0, y_0, z_0)$ at time t_0
a, b, c : coefficients of the horizontal and temporal gradients
H : scale height

The reference coordinates are calculated as mean of all measurement points and times, except the height is set to $z_0 = 0$.

Temperature T

Evaluations of radio soundings show, that a linear model of the temperature holds true only, as long as the measurements are below the tropopause. However, an accurate COMEDIE modeling should exceed the tropopause and consider the lower stratosphere. Therefore, up to about 20 km height, a constant temperature is assumed (U. S. Standard Atmosphere, 1962). Linear model segments are chosen for the temperature. As the transition between the two segments depends on the weather

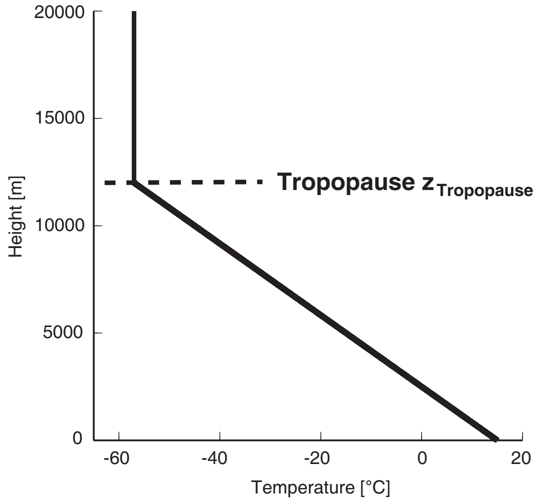

Figure 3.4.: Characteristics of the temperature function. It is fragmented into a linear and a constant part, intersected at the tropopause. As the height of the tropopause is dependent on the actual weather situation, an additional parameter $z_{Tropopause}$ is introduced.

situation, an additional parameter for the height of the transition $z_{Tropopause}$ is introduced (Figure 3.4).

$$\begin{aligned} T(x,y,z,t) &= T_0 + a(x-x_0) + b(y-y_0) + c(t-t_0) + \gamma(z-z_0) \quad (3.11) \\ & \qquad \text{for } z < z_{Tropopause} \\ T(x,y,z,t) &= T_1 + a(x-x_0) + b(y-y_0) + c(t-t_0) \quad (3.12) \\ & \qquad \text{for } z > z_{Tropopause} \end{aligned}$$

where:

$T(x,y,z,t)$	:	temperature at point $P(x,y,z)$ at time t
T_0	:	temperature at reference point $P_0(x_0,y_0,z_0)$ at time t_0
$z_{Tropopause}$	:	height of the tropopause
a,b,c	:	coefficients of the horizontal and temporal gradients
γ	:	temperature gradient with height
T_1	:	temperature above the tropopause up to 20 km height

Again, the reference coordinates are calculated as mean of all measurement points and times, except the height is set to $z_0 = 0$. Combining (3.11) and (3.12) by applying a Heavyside function (Bronstein et al., 1993), the description of the functional model of the temperature is given by the following equation:

$$\begin{aligned} T(x,y,z,t) &= (T_0 + \gamma z) \cdot (1 - S(z - z_{Tropopause})) + a(x-x_0) \\ & \quad + b(y-y_0) + c(t-t_0) + T_1 \cdot S(z - z_{Tropopause}) \quad (3.13) \end{aligned}$$

where:

$$S(z - z_{Tropopause}) = \frac{1}{\pi}\Big[\arctan(z - z_{Tropopause})\Big] + 0.5$$

To use this formula, sufficient measurements in the lower stratosphere are necessary to solve the collocation. Otherwise, if only measurements below the tropopause are available, (3.11) should be used, accepting the restriction that the interpolation area ranges only up to the tropopause.

3.2.4. Stochastic Modeling

The part not represented by the functional model is allocated to the stochastic modeling. It is decomposed into signal and noise according to the covariance function, which describes the weighting of the individual sampling points to each other. Normally, this is only an isotropic function. In the present case, anisotropy exists between the horizontal, the vertical and the time dimension, and because of the Swiss topography even in the horizontal dimension (Wehrli, 1986). Eckert et al. (1992) proposed a formula considering each dimension individually:

$$\Phi_{i,j} = \frac{\sigma_0^2}{1 + (\frac{x_i - x_j}{\Delta x_0})^2 + (\frac{y_i - y_j}{\Delta y_0})^2 + (\frac{z_i - z_j}{\Delta z_0})^2 + (\frac{t_i - t_j}{\Delta t_0})^2} \tag{3.14}$$

where:

$$\begin{aligned}
\Phi_{i,j} &: \text{ covariance function} \\
\sigma_0^2 &: \text{ a priori variance of the signal} \\
\overrightarrow{x_i} = \begin{pmatrix} x_i \\ y_i \\ z_i \\ t_i \end{pmatrix}, \overrightarrow{x_j} = \begin{pmatrix} x_j \\ y_j \\ z_j \\ t_j \end{pmatrix} &: \text{ space and time vector of point } i \text{ and } j \\
\Delta x_0, \Delta y_0, \Delta z_0, \Delta t_0 &: \text{ correlation length of the individual components}
\end{aligned}$$

Usually it is simple and inexpensive to obtain meteorological ground measurements, but difficult and expensive to get sampling points in the atmosphere. They can only be acquired by radiosonde launchings or expensive airborne measurements. Due to this fact, the covariance function has been complemented with a damping factor to assign an increased weight to the data in the higher atmosphere:

$$\Phi_{i,j} = \frac{\sigma_0^2}{1 + \left((\frac{x_i - x_j}{\Delta x_0})^2 + (\frac{y_i - y_j}{\Delta y_0})^2 + (\frac{z_i - z_j}{\Delta z_0})^2 + (\frac{t_i - t_j}{\Delta t_0})^2\right) \cdot e^{-\frac{z_i + z_j}{2 z_0}}} \tag{3.15}$$

where:

$$z_0 \quad : \quad \text{scaling height}$$

The choice of dedicated correlation lengths and variances depends strongly on the network of the meteorological input data. On the one hand, a suitable balance of signal and noise parameters should be achieved. On the other hand, the signal variance and individual correlation lengths should be defined in a way to allow a mutually matching signal. The main factors to determine the correlation lengths and variances are:

- The accuracy of the meteorological observation.
- The density of the meteorological network in the horizontal extension.
- The height distribution of the meteorological network and if so, the inclusion of other measurements to sustain the model in height.
- The sampling rate of measurements.

A set of correlation parameters and variances is given in Table 3.2. These apply to the refractivity field over the Swiss territory, and the introduction of meteorological measurements as described in Chapter 3.5.

3.3. Meteorological Input Data

3.3.1. Introduction

An accurate modeling of the refractivity field requires a dense network of meteorological measurements as well as a high accuracy of the measuring sensors used. Generally permanent weather stations are used for ground measurements and radiosondes for airborne measurements. The evaluation study (Chapter 3.5) was accomplished in the Swiss territory. The available meteorological data over the last few years allows to realize several investigations. Attention was given to analyze different time periods as well as different topographic areas.

3.3.2. Ground Measurements

The ground measurements of the Swiss automated meteorological network, called ANETZ, are used (SMA, 1985). ANETZ is operated by MeteoSwiss. A total of 72 well distributed stations covering Switzerland (Figure 3.5) are logging amongst other data, temperature and humidity every ten minutes and pressure every hour.

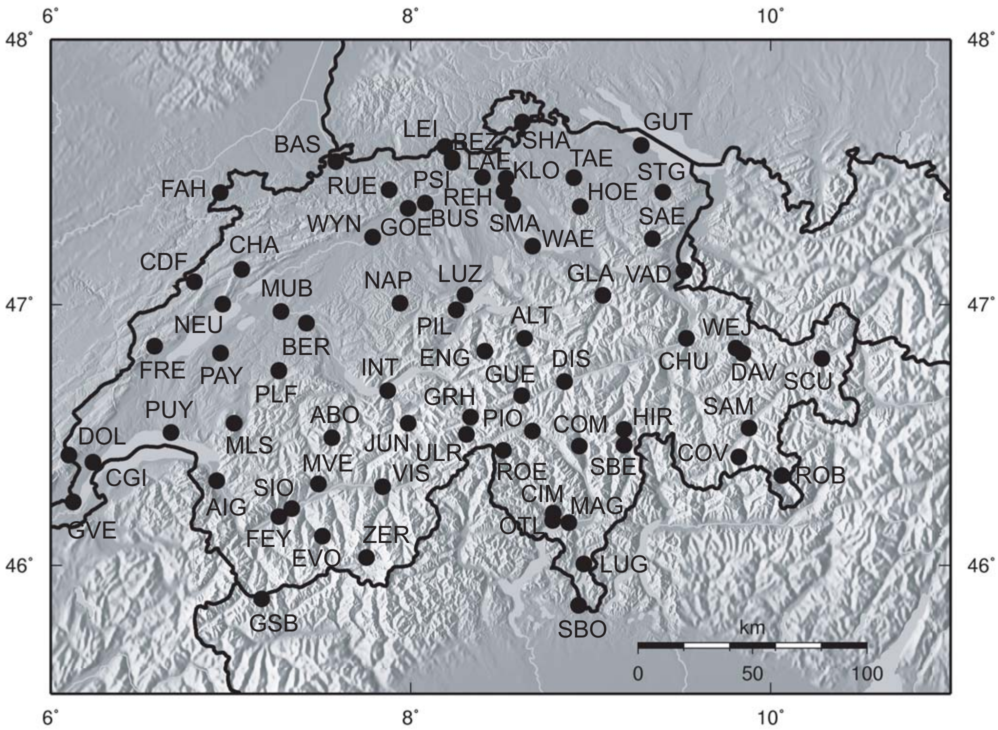

Figure 3.5.: The Automated Meteorological network (ANETZ) operated by MeteoSwiss. 72 stations are equally distributed over the Swiss territory. Pressure data are logged hourly, temperature and humidity data every ten minutes.

However, the height distribution of the network is not optimal (Figure 3.6). More than half of the stations are at an altitude below 1000 m. Only nine stations ($\sim$ 10%) are above 2000 m. Therefore, additional data from the upper layers of the atmosphere are essential for a good determination of the refractivity field.

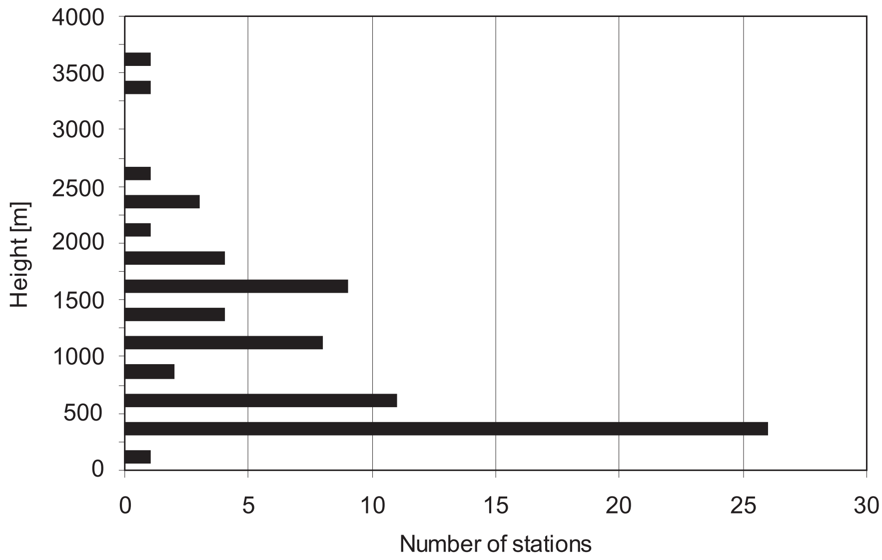

Figure 3.6.: Height distribution of the 72 ANETZ stations. 27 stations are at an altitude below 500 m, $\sim$ 90% of the stations are below 2000 m.

3.3.3. Radiosonde Observations

165 stations of radiosonde launchings are distributed all over Europe. They form the European Radiosonde Network. Sondes are typically launched once, twice or four times a day, measuring vertical profiles of pressure, temperature and humidity. Released from the surface, they provide data up to 20 to 30 km height. Measurements are taken at an interval of approximately 2 seconds. Even if the sonde is not ascending strictly vertical, the profiles can be assumed vertical without significant error (BADC, 2002). In the current study eight radiosonde stations are used; the station PAYERNE in Switzerland and seven stations in the surrounding countries (Figure 3.7).

3.3.4. Weighting of the Measurement Sets

A large imbalance in the number of data in each height layer is obtained by using the ground meteorological data of the 72 ANETZ stations and 8 radiosondes from the European radiosonde network. While ANETZ data is available on an hourly basis or each 10 minutes, radiosondes are only launched once, twice or four times a day. The situation is even worse due to circumstances that only $\sim$ 40% of the observed

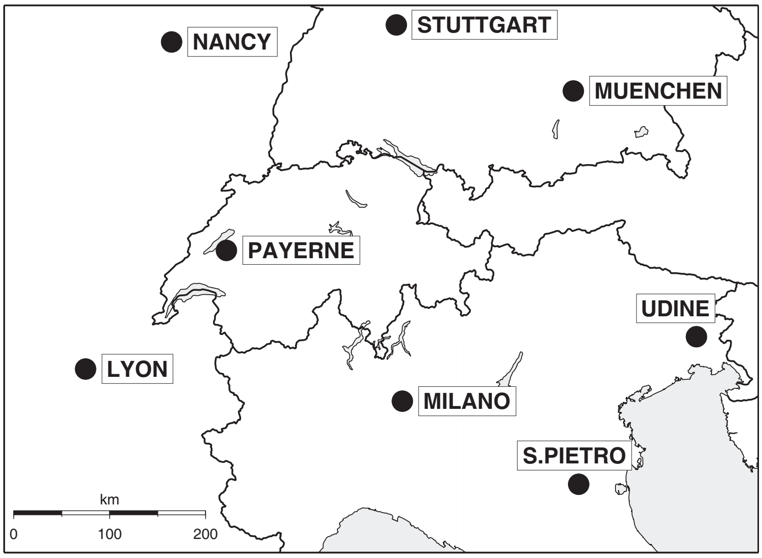

Figure 3.7.: The part of the European Radiosonde Network used in this study. Radiosondes are typically launched once, twice or four times a day at each station.

radiosonde measurements are usable for calculations. Table 3.1 gives an overview of the observed and usable number of measurements for all meteorological data. The approximate distribution of pressure data in the vertical component is plotted in Figure 3.8, the respective information for temperature and relative humidity in Figure 3.9.

measurements	Ground data (ANETZ)		Radiosonde data	
per day	theoretical	usable	theoretical	usable
pressure	24	~ 24	106	$\sim 40 - 60$
temperature	144	~ 140	106	$\sim 30 - 50$
water vapor pressure	144	~ 140	106	$\sim 30 - 50$

Table 3.1.: Theoretical and usable number of ground station and radiosonde data during one day. Almost 100% of the ground data is reliable for calculations, while only $\sim$ 40% of the radiosonde data are usable for calculations.

These circumstances make it necessary to use stochastic models applying a larger weighting for the data in higher layers (Section 3.2.4). The following analysis is using the stochastic model of (3.15).

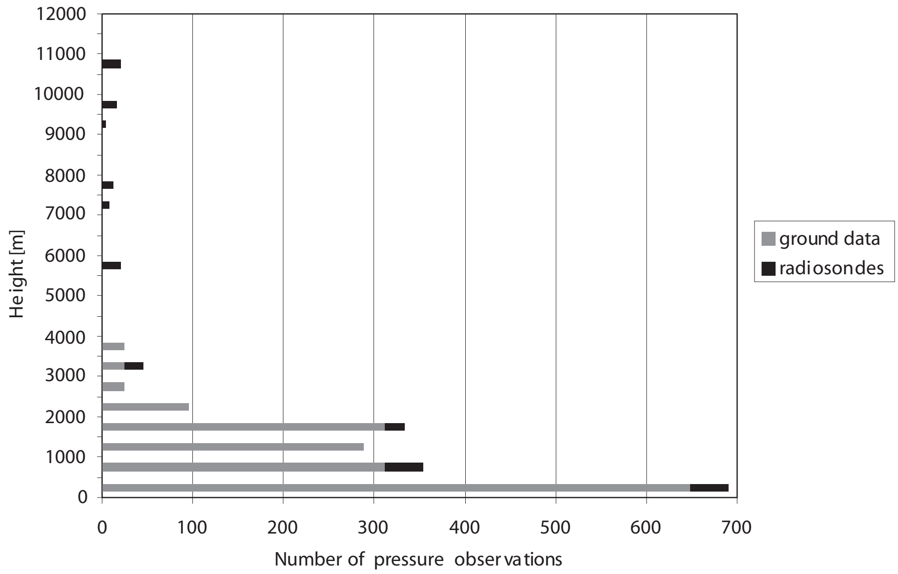

Figure 3.8.: Height distribution of usable ANETZ and radiosonde pressure data during one day. The height layers below 2000 m are characterized by a lot of ground meteorological data. In the higher layers, the deficiency is visible due to the small number of radiosonde observations.

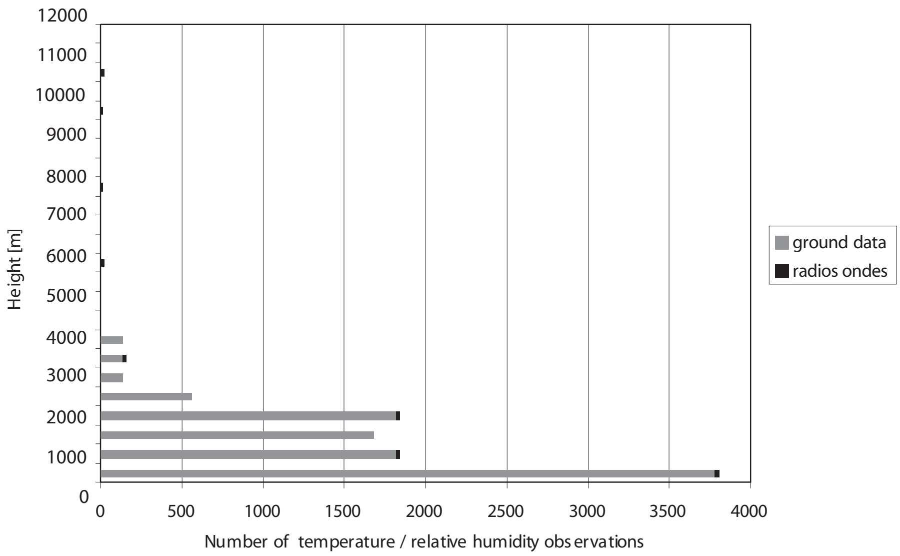

Figure 3.9.: Height distribution of ANETZ and radiosonde relative humidity and temperature data, respectively. Approximately the same amount of radiosonde data is available as in Figure 3.8, and also the distribution is similar. However, the amount of ground measurements is much higher, which strengthens the imbalance between ground and radiosonde data.

3.4. Error Investigation

The basis for an accurate path delay determination must be provided by a precise collocation and interpolation of the meteorological measurements. With COMEDIE, the dry part of the path delay is determined using the Saastamoinen formula. Geiger (1987) presented an appropriate error estimation. Assuming a zenith direction of the path delay ($z = 90°$) and neglecting the pressure correction B and the range correction δ_R, (2.31) gets:

$$\Delta_{saas}^{PD} = 0.002277 \cdot \left[p + \left(\frac{1255}{T} + 0.05 \right) \cdot e \right] \tag{3.16}$$

the partial derivations of p, T and e yields:

$$\frac{\partial \Delta_{saas}^{PD}}{\partial p} = 0.002277 \tag{3.17}$$

$$\frac{\partial \Delta_{saas}^{PD}}{\partial T} = -0.002277 \cdot \left(\frac{1255}{T^2} \right) \tag{3.18}$$

$$\frac{\partial \Delta_{saas}^{PD}}{\partial e} = 0.002277 \cdot \left(\frac{1255}{T} + 0.05 \right) \tag{3.19}$$

Inserting common values for $T = 288.16K$ and $e = 8.5hPa$ ($H_r = 50\%$), the error of the meteorological values gets to (Eckert et al., 1992):

$$\partial \Delta_{saas,p}^{PD} = 2mm/hPa \tag{3.20}$$

$$\partial \Delta_{saas,T}^{PD} = 0.3mm/K \tag{3.21}$$

$$\partial \Delta_{saas,e}^{PD} = 10mm/hPa \tag{3.22}$$

As humidity is measured at the ANETZ stations, Geiger (1987) proposed to express e by the humidity H_r:

$$e = \frac{H_r}{100} \cdot e^{-37.25 + 0.213166T - 0.000256988T^2} \tag{3.23}$$

This yields the following partial derivations:

$$
\begin{aligned}
\frac{\partial \Delta_{saas}^{PD}}{\partial p} &= 0.002277 && (3.24)\\
\frac{\partial \Delta_{saas}^{PD}}{\partial T} &= 0.002277 \cdot \Big(-\frac{1255}{T^2} + (\frac{1255}{T} + 0.05) && (3.25)\\
&\quad \cdot (0.213166 - 2 \cdot 0.000256988T) \Big) e \\
\frac{\partial \Delta_{saas}^{PD}}{\partial H_r} &= 0.002277 \cdot \big(\frac{1255}{T} + 0.05\big) \frac{e}{H_r} && (3.26)
\end{aligned}
$$

Applying the same values as in the example above, it results:

$$
\begin{aligned}
\partial \Delta_{saas,p}^{PD} &= 2mm/hPa && (3.27)\\
\partial \Delta_{saas,T}^{PD} &= 5mm/K && (3.28)\\
\partial \Delta_{saas,H_r}^{PD} &= 2mm/\% && (3.29)
\end{aligned}
$$

Hirter (1998) published an extended table of partial derivations using different meteorological conditions. In general, the temperature derivation is increasing significantly with increasing temperature. Therefore, the temperature has a major influence of the path delay error to be expected.

3.5. Evaluation Study

3.5.1. Collocation and Interpolation of Meteorological Parameters

To investigate the accuracy and reliability of COMEDIE, a cross-correlation analysis is performed. Additionally, comparisons between interpolations and other independent meteorological sensors are provided.

As simple functional models are used, the accuracy of the results depend strongly on the parameters chosen for the covariance function. They are mainly a function of the available number and the distribution of meteorological measurements. In Table 3.2, a set of correlation lengths and variances is presented, which is used for the subsequent investigations in the area of Switzerland. Figure 3.10 shows the behavior of the covariance function in the horizontal extension.

Interpolations of meteorological parameters are investigated on the basis of two time series in the year 2000. Figure 3.11 depicts a sample of collocated and interpolated temperature values compared to independent values obtained from the temperature sensor at the AGNES station ETHZ. A good agreement of the two data series is evident. The statistical evaluations of the time series is given in Table 3.3.

	σ_0 [hPa] or [°C]	Δx_0 [km]	Δy_0 [km]	Δz_0 [km]	Δt_0 [h]	z_0 [km]	$\sigma_0(noise)$ [hPa] or [°C]
p	0.5	200	200	1	6	3	0.5
t	0.7	200	200	1	6	3	0.5
e	0.6	50	50	0.2	2	4	0.5

Table 3.2.: Correlation of stochastic parameters and variances for the collocation of pressure p, temperature t and water vapor pressure e. The height variability of water vapor has to be taken into account with the choice of smaller correlation lengths in spatial as well as in temporal dimension. Abbreviations: σ_0: a priori standard deviation of the signal; $\sigma_0(noise)$: a priori standard deviation of the noise; $\Delta x_0, \Delta y_0, \Delta z_0, \Delta t_0$: correlation length of the individual components; z_0: scaling height.

a.) 9.-14. January 2000

	Zimmerwald			**Davos**		
	p	T	e	p	T	e
mean offset	-0.0 hPa	0.5 K	-0.1 hPa	-0.6 hPa	1.6 K	0.4 hPa
mean rms	0.2 hPa	1.3 K	0.5 hPa	0.8 hPa	2.1 K	0.5 hPa

b.) 20.-24. May 2000

	ETH Zürich			**Davos**		
	p	T	e	p	T	e
mean offset	0.0 hPa	0.4 K	-0.1 hPa	-0.2 hPa	-0.4 K	-0.1 hPa
mean rms	0.2 hPa	0.9 K	0.5 hPa	0.7 hPa	1.3 K	0.7 hPa

Table 3.3.: Statistical evaluation of two time series of meteorological interpolation in the year 2000. An overall good agreement is visible. For all investigations, the temperature interpolation shows the largest offsets and rms. Generally, the interpolation is more accurate for stations in the Swiss flat area (Zimmerwald, ETH Zürich) than for mountainous stations (Davos).

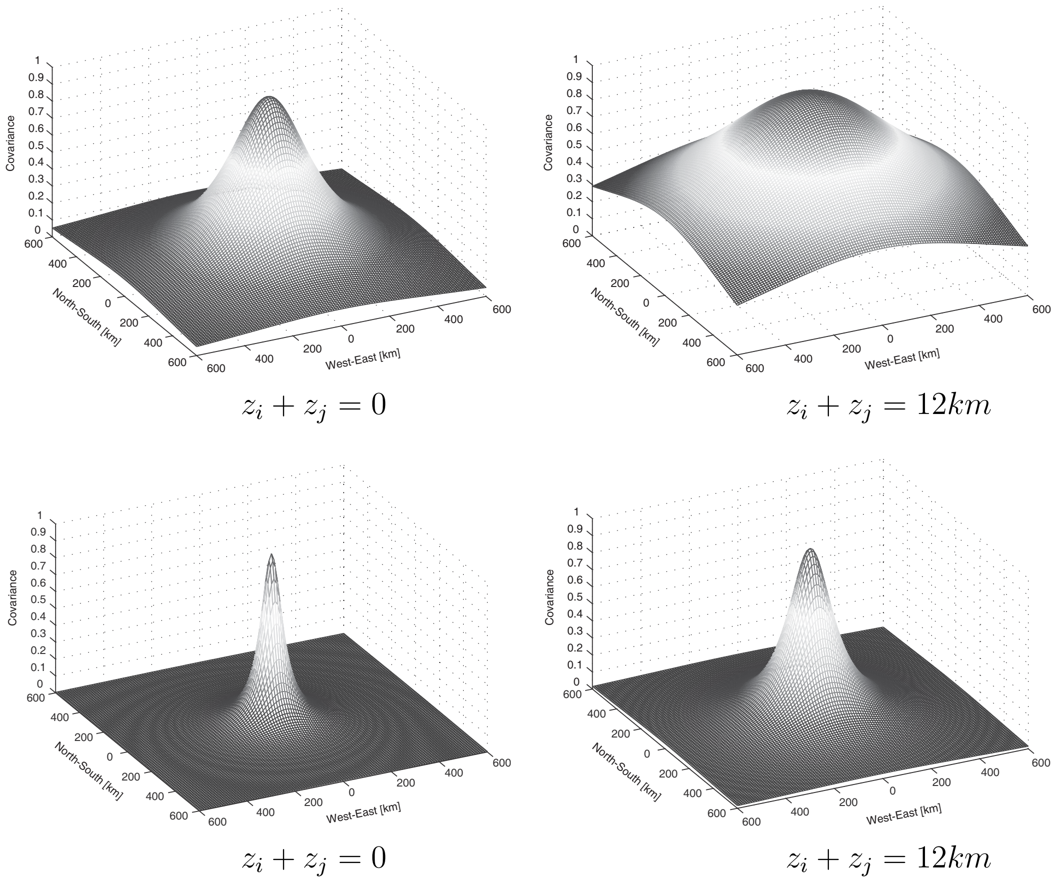

Figure 3.10.: Behavior of the covariance function Φ in the horizontal component. $z_i = z_j$ and $t_i = t_j$, $\sigma = 1$ to get a standardized illustration. The upper subfigures show the situation for pressure/temperature, the lower subfigures represent the situation for water vapor pressure. Because of the strong variation of water vapor pressure, the correlation takes effect in a limited local area, whereas the covariance function for pressure and temperature has a impact on a larger area. The effect of the damping factor is visible in the right subfigures. The area of impact is larger in both plots.

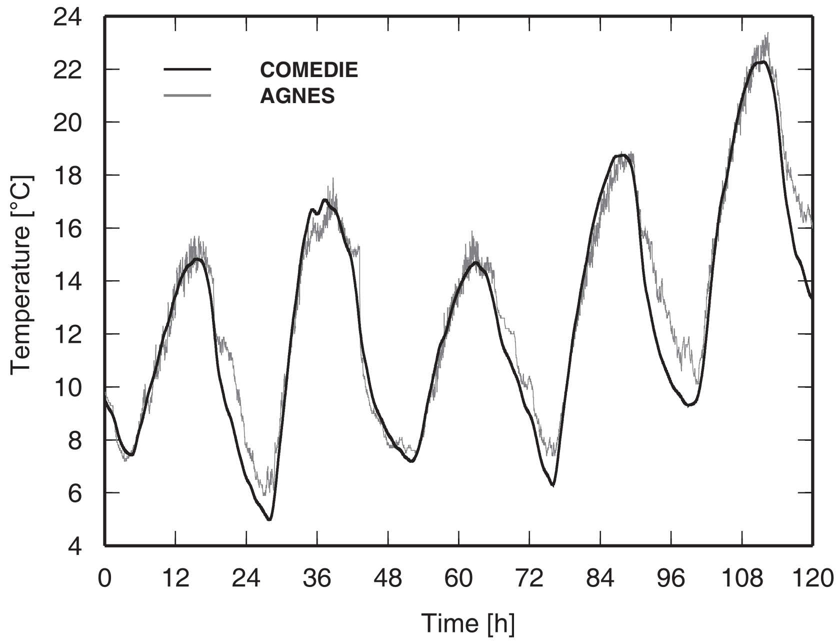

Figure 3.11.: Comparison of interpolated temperatures using COMEDIE and data from the temperature sensor at the AGNES station ETHZ. 120 hours are shown in the period of 20.-24.5.2000.

parameter	error of the parameter	error of the path delay
pressure	$0.2-1.0hPa$	$0.4-2mm$
temperature	$1.0-2.0K$	$5-10mm$
humidity	$2-5\%$ $(0.5-1.0hPa$ at $T=291.16K)$	$4-10mm$
total error of the path delay		$\approx \mathbf{9-22mm}$

Table 3.4.: Error budget of the path delay determination based on meteorological measurements of pressure, temperature and humidity and the formula of Saastamoinen. The errors are estimated using the values given in (3.27)-(3.29). The main errors stem from the temperature and humidity measurements whereas the pressure parameter has only a marginal influence.

Eckert et al. (1992) published a cross-correlation analysis of all ANETZ stations applying pressure, temperature and water vapor pressure. These results confirm the values given in Table 3.3. Summarizing, an error of around 2 cm for the path delay determination must be accepted using the Saastamoinen formula (Table 3.4).

To investigate the determination of the wet path delay, the functional model in the height component is analyzed. All ground meteorological data and the radiosondes in the nearby foreign countries are used to collocate and interpolate a height profile at the radiosonde station Payerne. This result is compared with radiosondes, ascending in Payerne. Figure 3.12 shows an example of a temperature profile. A statistical analysis of several profiles is given in Table 3.5.

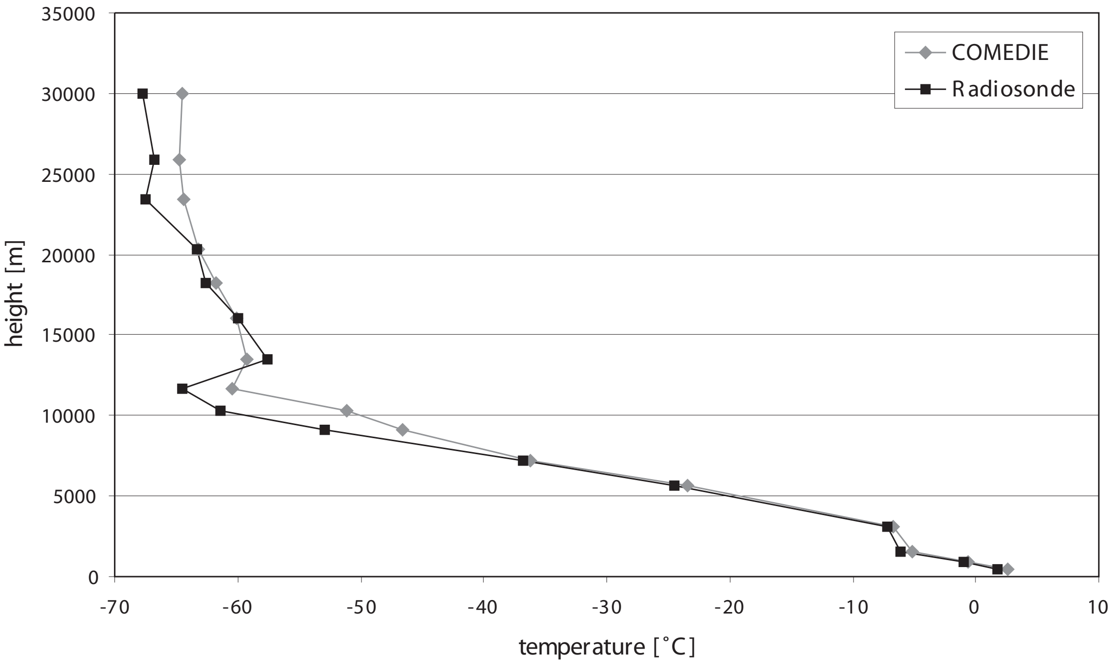

Figure 3.12.: Comparison of interpolated temperatures using COMEDIE and a radiosonde profile at station Payerne at January 11, 2000, 23h UT. Considering the lowest 20'000 m height, in overall, the COMEDIE interpolation reproduces the temperature profile accurately. However, modeling errors occur at the tropopause.

	9.-14. January 2000			**20.-24. May 2000**		
	p	T	e	p	T	e
mean offset	-0.1 hPa	1.9 K	0.1 hPa	1.9 hPa	-1.2 K	0.5 hPa
mean rms	1.2 hPa	3.5 K	0.3 hPa	3.0 hPa	4.6 K	0.8 hPa

Table 3.5.: Statistical evaluation of meteorological interpolation of radiosonde ascendings at station Payerne. The left subtable shows an analysis of 12, the right subtable of 10 ascendings. The water vapor pressure can be accurately interpolated. The temperature shows the largest offsets and represents the limitations of path delay modeling.

The wet path delay is mainly dependent on the temperature and water vapor pressure. While the water vapor pressure can be modeled accurately, the interpolated temperature profiles show relatively large rms. Specially the layer around the tropopause is difficult to reproduce.

3.5.2. Integration of Path Delays

The collocated and interpolated four-dimensional refractivity field enables to determine arbitrary path delays. So far, COMEDIE is restricted to zenith path delays. The dry and wet path delays are derived individually (2.18). Because of the sparse data distribution above the tropopause, the integration with COMEDIE using the described models and configurations is only accurate up to 12'000 m height. For the determination of the dry path delay above 12'000 m height, the Saastamoinen formula (2.32) achieves a better accuracy. In doing so, the accuracy of the entire dry path delay is similar to a dry path delay calculated completely by the Saastamoinen formula. Its calculation is much faster and, therefore, used as default in COMEDIE. Interpolated meteorological ground data forms the input for these calculations. Wet path delays are integrated with the refractivity model of COMEDIE.

Applying this procedure, the path delay can be calculated at any desired location within the area of the meteorological data. Figure 3.13 shows the total zenith path delay in Switzerland on January 12, 2000 at 12h UT. This result points out, that the path delay is correlated primarily with the topography. This is physically explainable since a longer distance through the atmosphere causes a larger path delay. As the largest part of the path delay can be allocated to the dry delay, the path delay describes - like the pressure - an exponential distribution. Also the wet path delay follows - like the water vapor pressure - an exponential function with the scaling height of about 2000 m. Figure 3.14 shows an example of a wet path delay during one day for different heights. It is clearly visible, that the wet path delay also depends on the time. The time variation is qualitatively identical at all height levels. Only a reduction of the variation is visible for the higher levels because of the smaller amount of wet path delay, i.e. water vapor.

3.6. Comparison Data

The capabilities of COMEDIE are analyzed by comparing the results for the zenith path delays with several series of GPS zenith delay estimates. They differ mainly in the GPS network used, the interval of the path delay estimates and the GPS processing strategy. The different topographic situations along with their weather conditions allow differentiated statements about the possibilities and limits of the method.

3.6.1. IGS Data

The *International GPS Service (IGS)* maintains around 200 GPS permanent stations distributed all over the world. The continuously recorded data are collected and processed at ten IGS analysis centers. The main activity of the analysis centers is

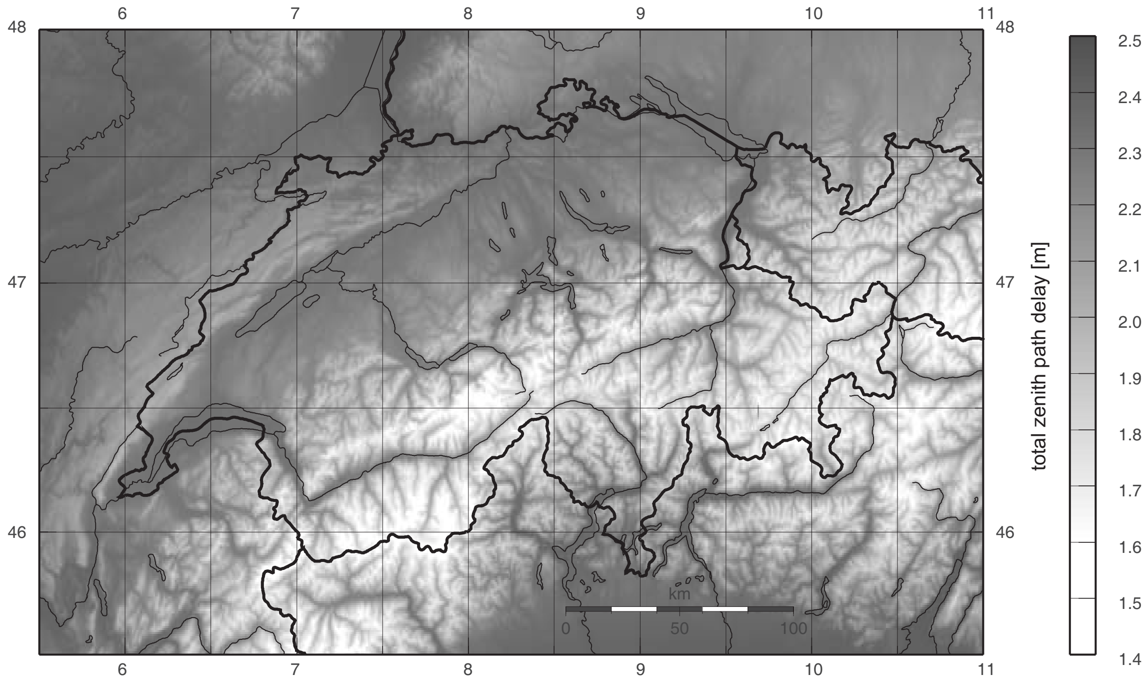

Figure 3.13.: Total zenith path delays calculated with COMEDIE in Switzerland on January 12, 2000 at 12h UT. A strong dependence of the path delay on the topography is obvious.

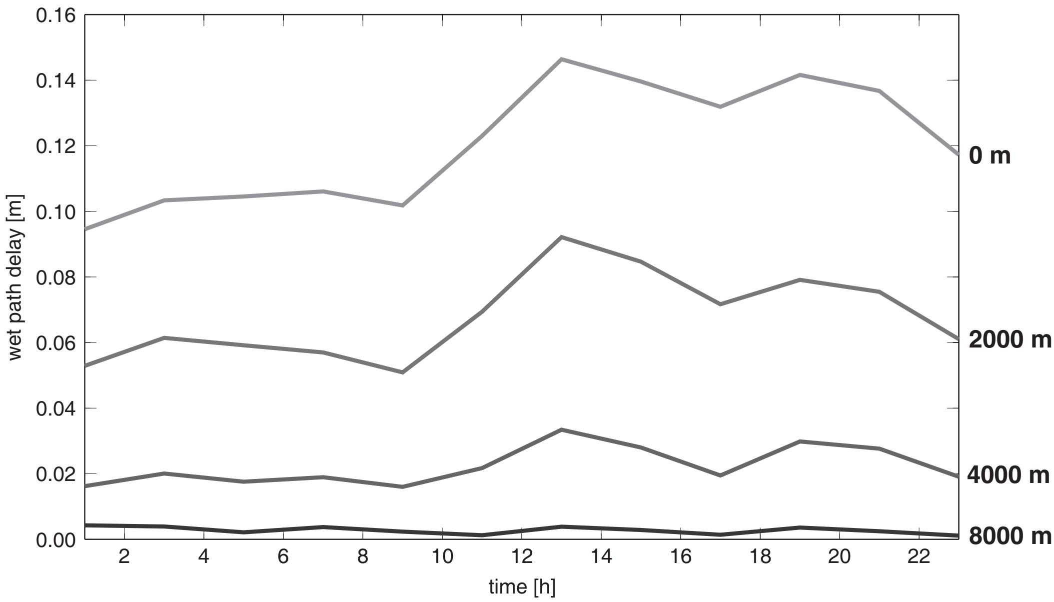

Figure 3.14.: Wet path delay variation on 21.5.2000 at four different height levels. Path delays are determined every two hours beginning at 1h UT and ending at 23h UT. The characteristics of the four graphs are similar. On the higher levels, the size and the temporal variation of the wet path delay is reduced.

to determine precise GPS orbits. However, several other *IGS products* including 2-hour means of GPS-derived tropospheric path delays are provided. In Switzerland, the AGNES station ZIMM (Zimmerwald) operated by Swisstopo belongs to the IGS network (Mervart, 1995).

3.6.2. AGNES Data

AGNES (Automatic GPS NEtwork of Switzerland) is a multi-functional permanent GPS network operated by Swisstopo. It serves various purposes in national geodetic surveying, ordnance surveying, geodynamics and scientific research. The Swisstopo analysis center is processing the GPS data in near real-time. To achieve better results, the data of 20 stations of the *EUropean REference Frame (EUREF)* (Brockmann and Wiget, 2001) are included in the processing. GPS-derived path delays are determined every two hours. Since September 2001, even hourly means are provided. In 2002, the AGNES network includes 30 stations totally. For further details on the AGNES network we refer to Section 4.3.1.

3.6.3. Data of the MAGIC Project

MAGIC (Meteorological Applications of GPS Integrated Column water vapor measurements in the Western Mediterranean) aims to derive and validate GPS-derived tropospheric path delays for meteorological applications (Haase et al., 2001). MAGIC consists of 51 permanent GPS stations in the Western Mediterranean area. The analysis centers are estimating 15-minute means of tropospheric path delays. The AGNES station ZIMM is part of the MAGIC network.

3.7. Evaluation Analysis and Comparison

Several comparisons have been performed in the entire area of Switzerland. They show an overall good agreement of the COMEDIE solution with the GPS-derived path delays. COMEDIE calculations using just a part of the meteorological input data show deficiencies. If no radiosondes are used, the size of the path delay is generally overestimated. An example of COMEDIE-based path delays compared to IGS and MAGIC values is shown in Figure 3.15. This COMEDIE determination was made with ground meteorological and radiosonde data but no damping function was used to increase the weighting for the data in higher altitudes and only one linearly decreasing temperature function is used to model the whole collocation area. The jumps are clearly visible. In general, an accurate result is achieved every 12 hours during the radiosonde launches. Figure 3.16 shows the same time series as in Figure 3.15 but with a COMEDIE solution applying the damping factor as introduced in (3.15) and two functions for the temperature modeling as described in (3.11) and

(3.12). The agreement of the COMEDIE solution with the GPS-derived path delays is much better. The jumps could be eliminated.

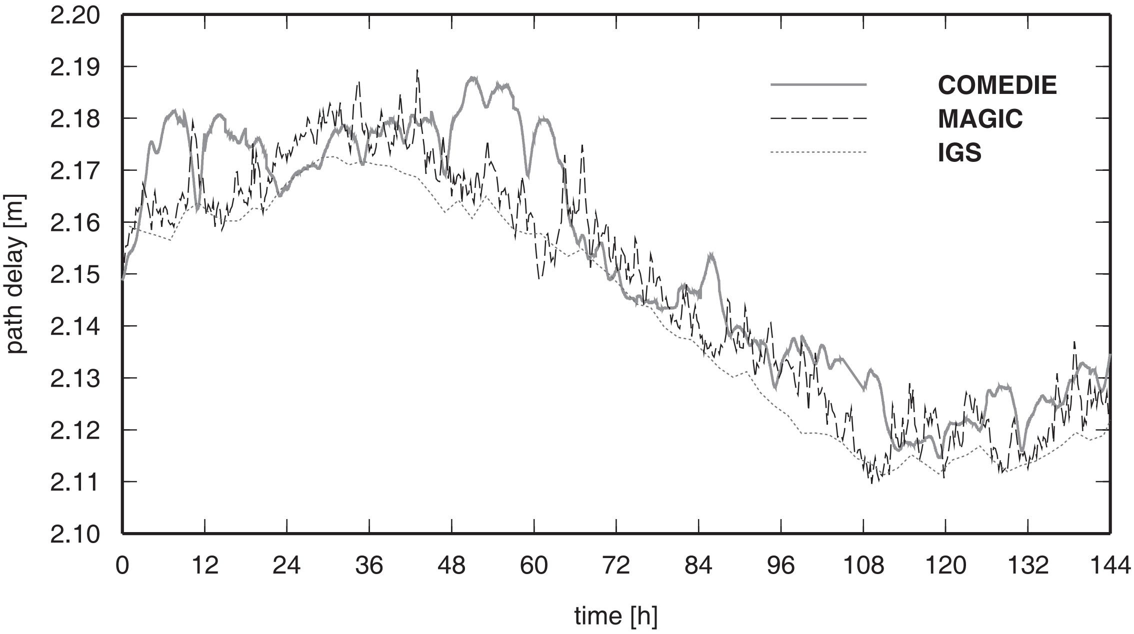

Figure 3.15.: Comparison of zenith path delays obtained from COMEDIE and GPS-derived path delays for the station Zimmerwald from January 9 - 15, 2000. The COMEDIE solution fits the IGS and MAGIC solution at the radiosonde launching times (every 12 hours at 11h and 23h UT). The functional model for the temperature is assumed to decrease linearly in the whole collocation area and no damping factor in the stochastic modeling is used within the COMEDIE solution. This leads to a miss-modeling of the temperature above the tropopause and results usually in an over-estimated amount of the path delay between the radiosonde launchings. The IGS curve is smoothed because of the two hour mean values, whereas the 15-minute means of the MAGIC solution have naturally stronger variations.

However, also an offset between the two GPS-derived path delays is visible. This indicates, that the determination is extremely sensitive to the chosen stations and the site coordinates used for the network as well as the GPS analysis strategy. The rapidly changing behavior of the MAGIC solution is an effect of the 15-minute means of the tropospheric path delays in contrast to the 2-hour means of the smoothed IGS solution. Figure 3.17 depicts the difference of each data series to the mean of all three series. Since true time series are not available in reality, the mean is chosen as reference. The statistical evaluation is given in Table 3.6. Furthermore, the statistical analysis of the individual pairs of series is displayed in Table 3.7. (The calculation of the statistical data is described in Appendix B).

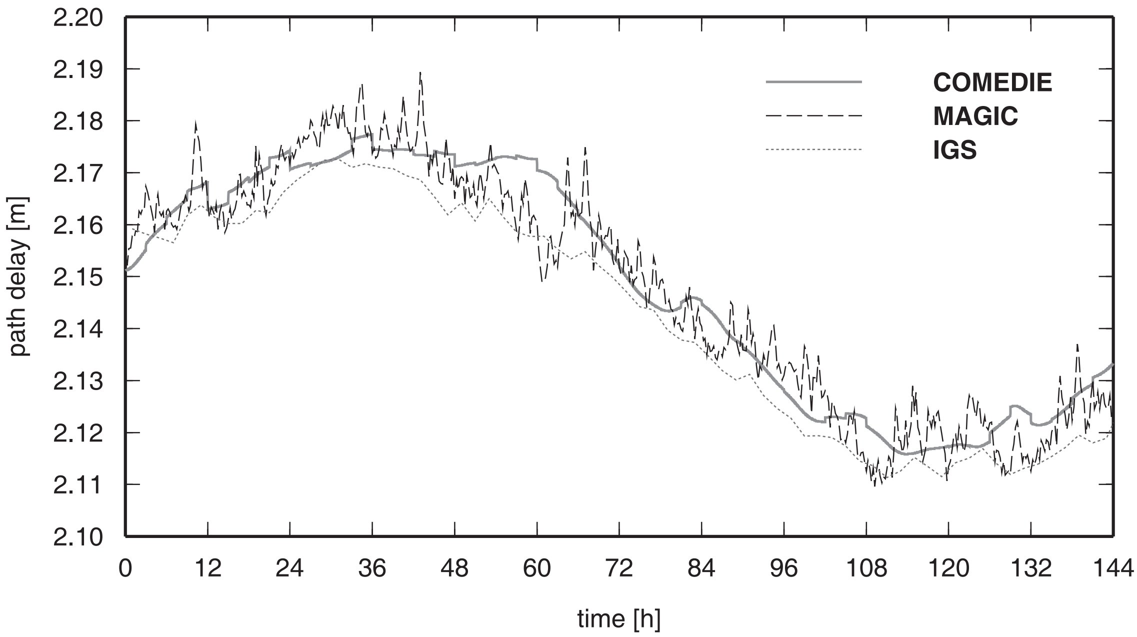

Figure 3.16.: Comparison of COMEDIE-determined path delays and GPS-derived path delays at the same station and for the same interval as in Figure 3.15. In contrary to Figure 3.15, a constant function for modeling the temperature above the tropopause is added to the COMEDIE determination and a damping factor is used to increase the weighting for the data in higher layers. It is clearly seen, that the jumps between radiosonde launchings are no more existing.

[mm]	COMEDIE	IGS	MAGIC
offset	2.1	-3.8	1.7
rms	3.7	4.2	3.6
σ	3.1	1.8	3.1

Table 3.6.: Statistical analysis of the data series presented in Figures 3.16 and 3.17. The offset values confirm the visual impression of Figure 3.17, i.e., the COMEDIE and MAGIC solutions are on the same offset level whereas the IGS solution has a negative offset. As 2-hour means of path delays are used at the IGS solution, the values are smoothed and, consequently, the standard deviation is smaller than of the 15-minutes means of the MAGIC solution. The formulas for the statistical calculations are described in Appendix B.

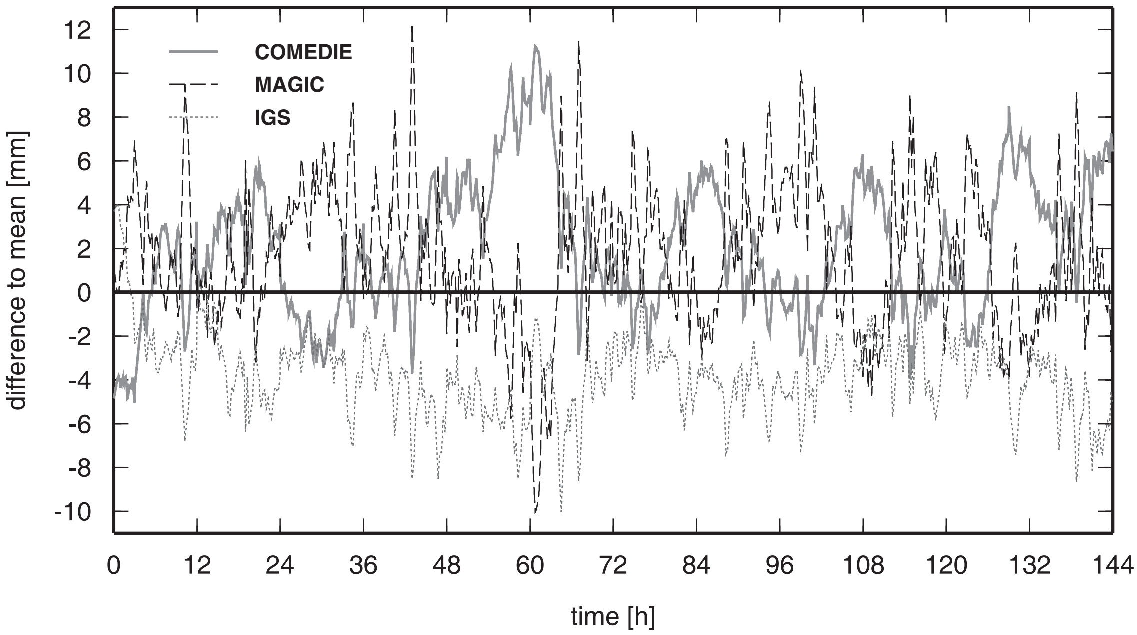

Figure 3.17.: Difference of COMEDIE-determined and GPS-estimated path delays to the mean of the three determinations at station Zimmerwald from January, 9-15, 2000 (see also Figure 3.16). The IGS series is generally lower than the COMEDIE and MAGIC values.

[mm]	COMEDIE-IGS	COMEDIE-MAGIC	MAGIC-IGS
offset	5.9	0.3	5.6
rms	7.1	5.9	6.9
σ	3.9	5.9	4.1

Table 3.7.: Statistical analysis of the pairs of series presented in Figures 3.16 and 3.17. Again, the IGS data show an offset compared to COMEDIE and MAGIC. However, the rms of the three pairs of series are on the same order of magnitude.

To consolidate the statistical statement, four additional evaluations are provided from the year 2000. Each evaluation comprises 5-10 days of path delay determination. The evaluations in the second part of the year 2000 are made using the AGNES data instead of the MAGIC data (Table 3.8).

a.) 20.-24. February 2000

[mm]	COMEDIE	IGS	MAGIC
offset	6.2	-0.2	-6.0
rms	7.7	2.4	6.8
σ	4.5	2.4	3.2

b.) 20.-25. August 2000

[mm]	COMEDIE	IGS	AGNES
offset	18.1	-10.9	-7.3
rms	20.7	11.5	10.5
σ	10.1	3.9	7.5

c.) 16.-25. October 2000

[mm]	COMEDIE	IGS	AGNES
offset	10.5	-4.7	-5.8
rms	12.7	6.0	7.4
σ	7.1	3.7	4.6

d.) 20.-25. November 2000

[mm]	COMEDIE	IGS	AGNES
offset	2.2	-3.3	1.1
rms	5.2	4.7	3.6
σ	4.7	3.3	3.4

Table 3.8.: Statistical analysis of four time series in the year 2000 at station Zimmerwald. COMEDIE is compared with IGS and MAGIC (first part of the year 2000) or IGS and AGNES (second part of the year 2000), respectively. It is visible, that the large and small amounts of rms and offsets are coupled together. The most accurate values are achieved in winter time, the accuracy decreases in summer time.

The statistics demonstrate that the achieved rms lies between 0.5 to 2.0 cm. In summer time, the rms is higher than in winter time. Reminding, that the air is more humid in summer time than in winter time, the amount of path delay is larger in summer time. The larger the amount is, the larger the rms is. The offset shows a similar seasonal behavior, also in the same range as the rms. In the following section, the dependence of the rms on station height is discussed.

3.8. Approach of an Improvement

Swisstopo organized a GPS campaign (GRTI00) from August, 21 to 31, 2000, in order to densify the Swiss high precision network in the Cantons Ticino and Graubünden (Santschi et al., 2000). In the frame of this project, an error diagnosis was performed. This campaign is specially suited as it took place in the summer time, when the path delay rms is usually at a maximum. The comparison and evaluation of the data calculated with COMEDIE is done with path delays estimated from GPS.

A total of 23 stations were occupied during the time period of ten days in August 2000. At each station, measurements were performed continuously during 12 hours. In addition, data from the eight stations of the continuously operating AGNES network were integrated in the analysis. All GPS stations are shown in Figure 3.18. Two sets of GPS-derived path delays were calculated for the evaluation:

- AGNES: The automated post-processing of all AGNES stations including 15 EUREF stations. Thereafter the campaign measurements of all 23 stations were processed in a separate run. 2-hour means of zenith total delays have been determined for all AGNES stations and 1-hour means for all campaign stations.

- GRTI00: The 23 campaign stations along with the eight AGNES stations are processed as autonomous network without the EUREF sites. 1-hour means of zenith total delays have been determined.

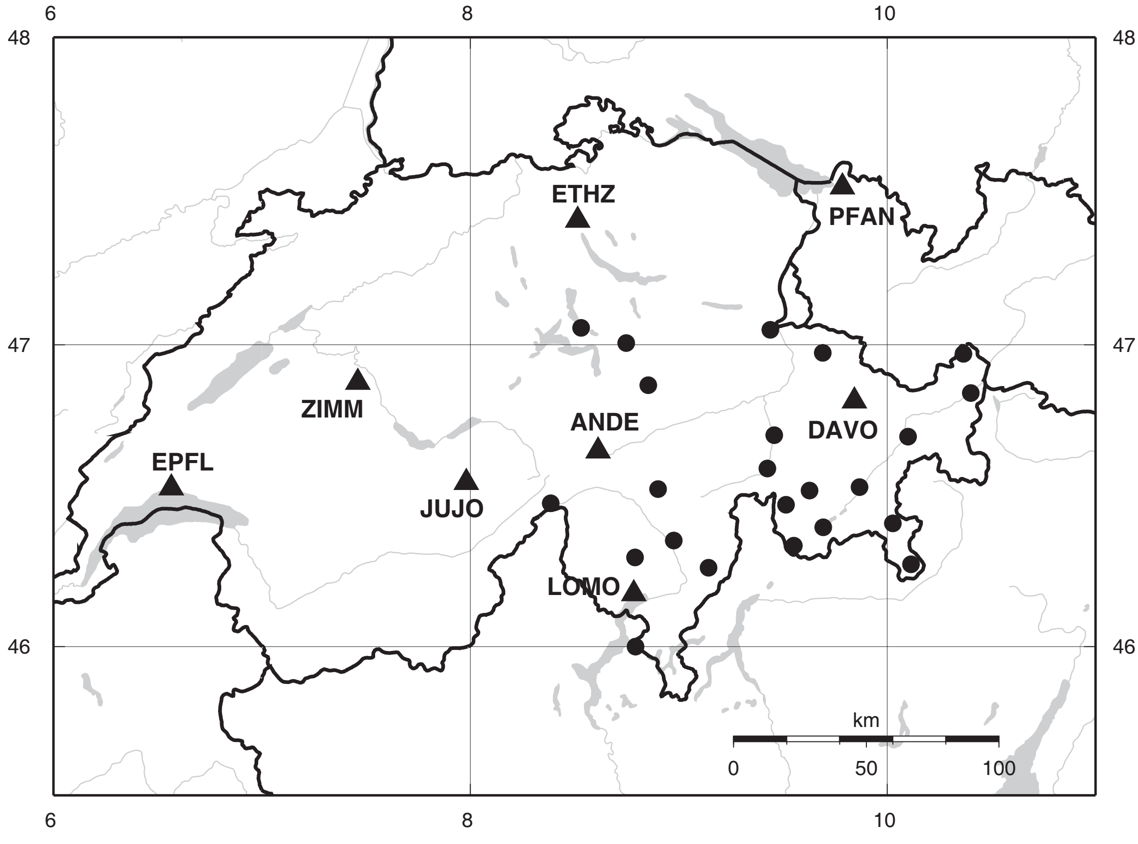

Figure 3.18.: 8 AGNES stations (labeled) and 23 stations of the campaign GRTI00 (dots), mainly distributed in the south-eastern part of Switzerland.

Path delays have been calculated for all 31 stations ranging from 438 m to 3635 m height (Troller and Brockmann, 2001). Figures 3.19 and 3.20 show two representative plots and Table 3.9 the corresponding statistical analysis for the stations

Andermatt (ANDE, 2368 m height) and ETH Zürich (ETHZ, 595 m height). The evaluation shows an accuracy similar to the results in Section 3.7. The discrepancy between COMEDIE and the GPS-derived path delays is visible.

Furthermore, differences between the AGNES and GRTI00 solutions are visible. Due to the small geographic extension of the stations included in the GRTI00 solution, one has to speak of *relative* troposphere estimates (Beutler et al., 2001). The path delays of the AGNES solutions can be referred to as *absolute* estimates, as the geographic extension of the GPS stations used, reaches over continental Europe.

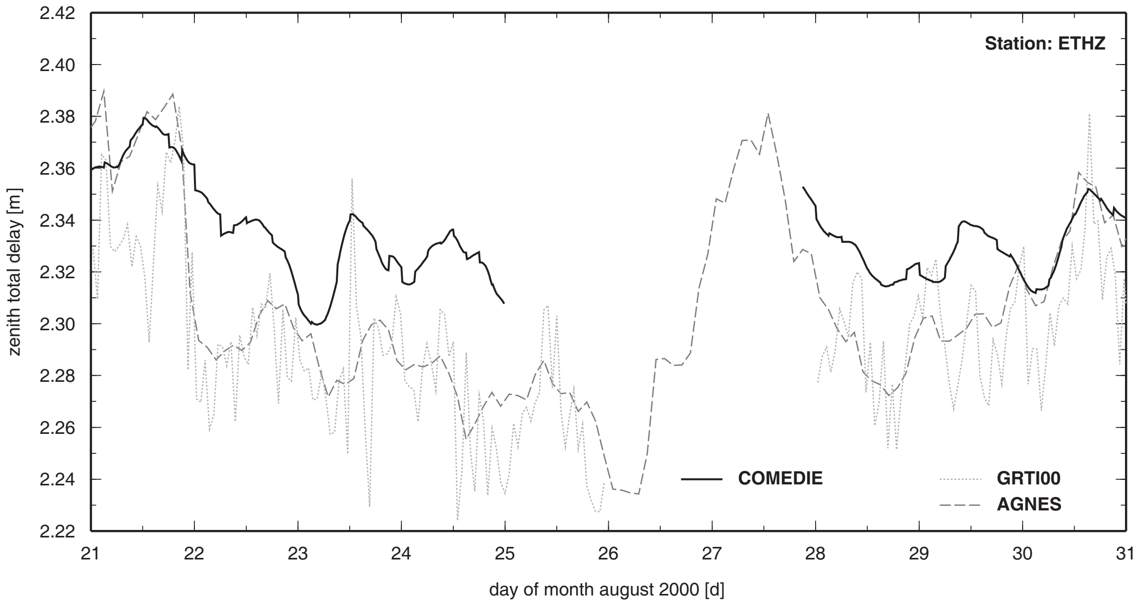

Figure 3.19.: Total zenith path delay at station ETH Zürich (ETHZ). The COMEDIE solution shows an overall good agreement with the two GPS-derived solutions AGNES and GRTI00. However, the COMEDIE solution has usually larger values than the GPS solutions.

Comparing the analysis of all stations, the increase of the offset and the rms seems to be proportional to the decrease of the station height. This behavior can be understood as the total path delay decreases primarily with height. Figure 3.21 shows a plot of the mean offset of the path delay versus the station height including all 31 GPS stations. A small correlation between the mean rms and the station height is visible on the COMEDIE-AGNES and COMEDIE-GRTI00 data series. Considering the differences of the mean offset of COMEDIE with respect to GRTI00, a logarithmic regression was statistically verified. However, the stability index of $R^2 = 0.18$ indicates just a marginal significance of the coefficients. A similar result was found for the data series COMEDIE-AGNES. Table 3.10 shows the effect of correcting this systematic influence. In the same step, the GRTI00 data series with respect to AGNES are corrected using a mean offset of around 7 mm (Table 3.10). The rms decreased around 25% to the level of the standard deviation σ. Latter,

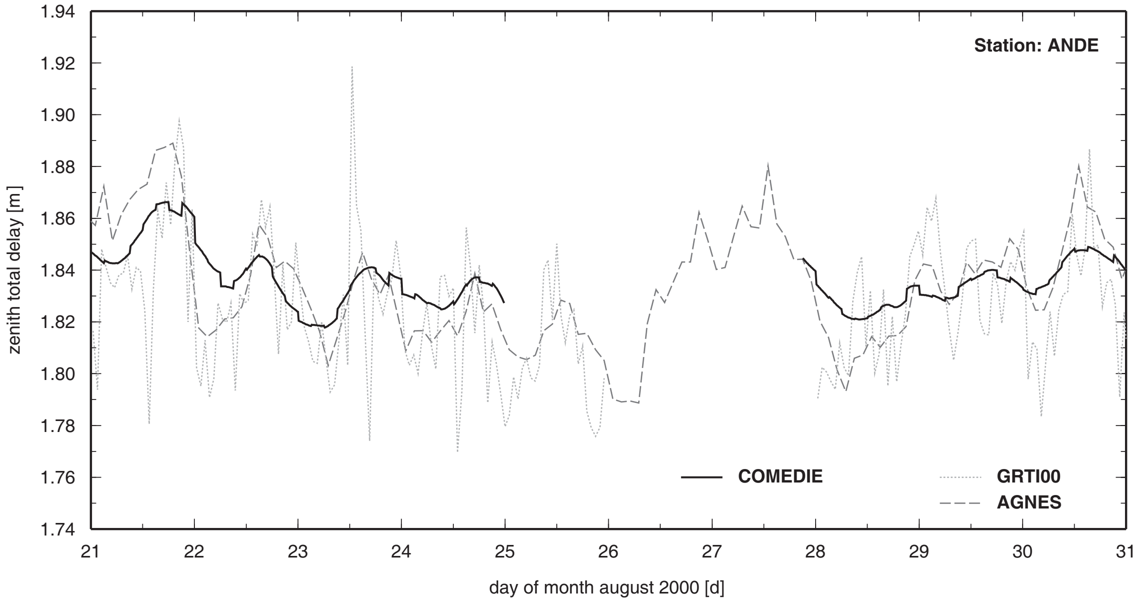

Figure 3.20.: Total zenith path delay at station Andermatt (ANDE). The COMEDIE solution agrees better with the two GPS solutions AGNES and GRTI00 than in the case of the station ETHZ (Figure 3.19). Offsets between the series are practically zero in this example.

Station: ETHZ	Number of points: 10464		
[mm]	COMEDIE	AGNES	GRTI00
offset	20.1	-4.3	-15.7
rms	24.1	12.4	19.8
σ	13.3	11.6	12.0
Station: ANDE	Number of points: 10445		
[mm]	COMEDIE	AGNES	GRTI00
offset	3.0	2.7	-5.7
rms	9.8	9.2	13.7
σ	9.4	8.8	12.5

Table 3.9.: Statistical evaluation of station ETHZ and ANDE. Station ETHZ has a relatively large offset as well as rms. Station ANDE has a much smaller offset and rms. It is assumed, that this fact results due to the different station height of ETHZ (595 m) and ANDE (2368 m).

which is independent from the offset, remains approximately the same.

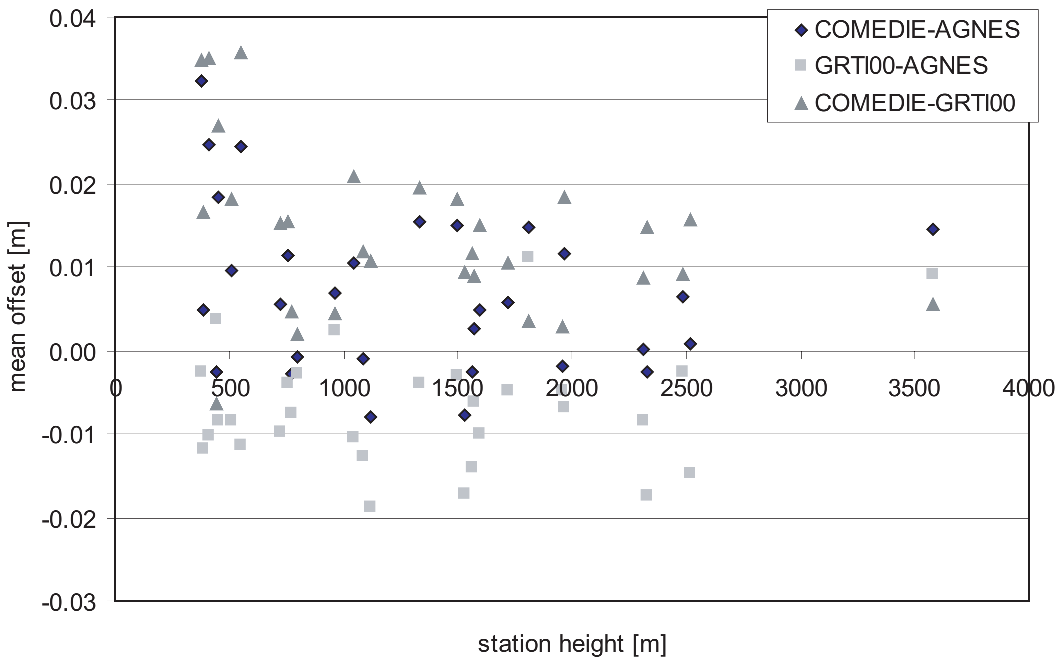

Figure 3.21.: The plot shows the offsets of the COMEDIE, AGNES and GRTI00 series with respect to each other. The plot includes all 31 GPS stations of the campaign GRTI00. A slight exponential increase of the offsets with decreasing station height is visible in the plot.

[mm]	**PD comparison**			**using corr. function**		
	COMEDIE - AGNES	COMEDIE -GRTI00	GRTI00 - AGNES	COMEDIE - AGNES	COMEDIE -GRTI00	GRTI00 - AGNES
offset	7.1	13.9	-6.9	0.0	0.0	0.0
rms	12.0	17.0	9.8	9.0	8.8	7.0
σ	9.9	9.9	7.1	9.4	9.0	7.1

Table 3.10.: Statistical evaluation before and after applying the correction function. As a consequence of this procedure, the offset is reduced to zero. The standard deviation σ stays approximately the same. The rms decreases well below one centimeter.

3.9. Discussion

The improved version of COMEDIE was successfully applied. The modifications in the modeling of the temperature and the covariance function lead to more accurate results. Due to the structured programming of the actual version of COMEDIE, further modeling developments and independent measurements such as those from radiometers or spectrometers can be introduced very easily.

The numerous evaluations and comparisons with GPS-derived path delays have been performed and revealed the accuracy which can be achieved using COMEDIE. In winter time, the difference to the GPS-derived path delays reaches an accuracy of less than one centimeter. This accuracy level is usually satisfactory to correct kinematic GPS measurements. Whereas in summer time the accuracy is only partially satisfactory. Adding a height-dependent correction function allows to slightly improve the results. The achieved path delay accuracy of 1-2 cm allows a GPS height accuracy of about 3-6 cm.

The main part of the error is caused by modeling the temperature. The used functional model is a simple formula. However, the complex layers near the tropopause can only partially be modeled with a sufficient accuracy. Special weather conditions such as temperature inversions intensify the deficiency.

However, for deriving path delays from meteorological input data, COMEDIE is a relatively accurate and convenient method. Alternatively, two other methods to estimate path delays should be mentioned:

- Simplified path delay calculation formulas with meteorological ground measurements as the only input data (detailed description in Chapter 2.5): Nowadays, the formula of Saastamoinen (1972) is commonly used. This procedure is simple and fast, as only ground pressure, temperature and water vapor pressure are necessary. The resulting dry path delay is satisfactory. But water vapor, which influences mainly the wet path delay, rapidly changes in space as well as in time and often does not behave according to the atmospheric standard model. Therefore, the estimation of wet path delays is often inaccurate (detailed evaluations are presented in Chapter 6.4).

- Path delays derived from numerical weather forecast models: Several successful approaches have been made to derive path delays from numerical weather models. An evaluation in Switzerland using the AGNES network and the Swiss *local model LM* achieved an accuracy similar to the COMEDIE accuracy (e.g. Brockmann et al., 2001; Guerova et al., 2003). In winter time, the rms compared to GPS-derived path delays ranges between 0.8 - 1.2 centimeter, in the summer period the accuracy decreases to about 2 centimeters.

To improve the accuracy, the modeling of the temperature and the water vapor pressure should be revised. Another possibility is to determine the path delay without meteorological data. Such an approach is presented in the following chapter.

4. Modeling of Zenith Path Delay Using GPS-Estimated Delays

4.1. Introduction

Due to the increasing number of permanent GPS stations in the last years, a new approach to model the path delay is becoming more and more applicable. As input data, GPS-estimated path delays are used, gained from a GPS permanent network. Preliminary investigations were done in the framework of testing the accuracy of COMEDIE (Troller and Brockmann, 2001). The results yielded an overall good agreement. Therefore, this new approach was investigated in more detail. A software package called COITROPA (COllocation and Interpolation of TROpospheric PAth delays) was developed. It is based on COMEDIE. The calculation routines applying a 4-dimensional collocation adjustment have been adopted.

A GPS processing software estimates path delays in zenith direction at selectable time intervals. In recent years, 2-hour time intervals were reasonable, but nowadays, an interval of one hour or even 30 minutes has been achieved for permanent GPS processing. For campaign treatment even time intervals of 15 minutes are used (Haase et al., 2001). Applying this time interval, COITROPA is able to account for the rapid temporal variation of the water vapor and the path delay, respectively (Troller and Brockmann, 2002; Troller et al., 2003).

4.2. Principles of the COITROPA Software Package

4.2.1. Overview

GPS-estimated zenith path delays are introduced in COITROPA along with the associated 3-dimensional coordinates and the time information. A least-squares collocation adjustment and interpolation (Moritz, 1973; Wirth, 1990) is done with the appropriate functional and stochastic model, described in the following chapters (Figure 4.1).

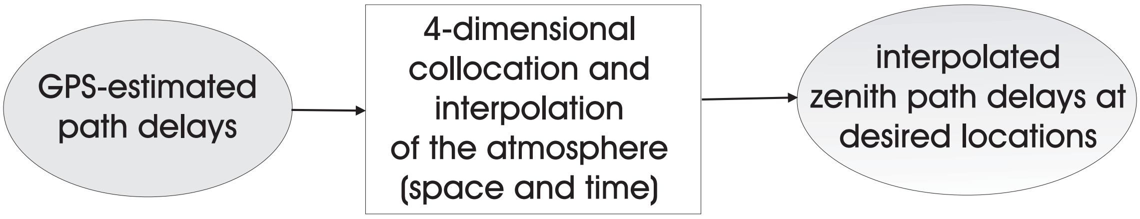

Figure 4.1.: Flow chart of the software package COITROPA. GPS-estimated path delays are the input data. Applying a four-dimensional collocation of the atmosphere, interpolated path delays can be obtained.

4.2.2. Functional Modeling

The functional model should give an accurate picture of the reality. However, since a collocation approach is used, the model is chosen as simple as possible. Unmodeled systematic parts will be assigned to the signal.

Under the assumption of an isotherm atmosphere, an exponential approach is chosen for the functional modeling of the air pressure (Chapter 3.2.3). The main part of the path delay depends directly on the current air pressure. Therefore, the same exponential function is used to model the path delay.

$$\Delta^{PD}(x,y,z,t) = \Big(\Delta_0^{PD} + a(x-x_0) + b(y-y_0) + c(t-t_0)\Big) \cdot e^{-\frac{z-z_0}{H}} \tag{4.1}$$

where:

$\Delta^{PD}(x,y,z,t)$	:	path delay at point $P(x,y,z)$ at time t
Δ_0^{PD}	:	path delay at reference point $P_0(x_0,y_0,z_0)$ at time t_0
a,b,c	:	coefficients for the horizontal and temporal gradients
H	:	scale height

The reference coordinates (x_0,y_0) and the reference time t_0 are calculated as mean of all measurement points and times, except the height is set to $z_0 = 0$.

4.2.3. Stochastic Modeling

The stochastic modeling is defined by a signal and a noise part. The connection between the two parts is given by the covariance function. The consideration of dedicated covariance functions corresponds to the implementation in the software package COMEDIE (Chapter 3.2.4). Usually, (3.14) is used. The other proposed function applying an increased weight in the higher atmospheric layers (3.15) is normally not suitable because of the lack of measurements in these atmospheric layers.

To get a high quality of the interpolated path delays, it is important to choose the correlation lengths and the variances properly. The criteria are discussed in Section 3.2.4. In Table 4.1, reasonable values are presented for the Swiss AGNES network, i.e., an approximately consistent network with distances from station to station of about 30-50 km, a height range of the GPS stations from nearly sea level to about 3600 m and a determination of GPS-estimated path delay means every 1-2 hours.

σ_0 $[m]$	Δx_0 $[km]$	Δy_0 $[km]$	Δz_0 $[km]$	Δt_0 $[h]$	$\sigma_0(noise)$ $[m]$
0.01	100	100	1	6	1)

1) The $\sigma_0(noise)$ is given by the GPS processing.

Table 4.1.: Correlation parameters and variances for the covariance function (3.14) used to interpolate path delays with COITROPA. The parameters apply to a GPS network density of around 10 stations per $100 \cdot 100\ km^2$ and path delay intervals of 1-2 hours. Abbreviations: σ_0: a priori standard deviation of the signal; $\Delta x_0, \Delta y_0, \Delta z_0, \Delta t_0$: correlation lengths of the individual components; $\sigma_0(noise)$: formal error of the GPS-derived path delay.

4.2.4. Input Data

Various kinds of GPS-estimated path delays can be used as input data. They can stem from permanent networks or episodic measurement campaigns as well as from combined networks. It is important that the density of the GPS stations is adapted to the topography. Furthermore, the GPS post-processing should be carefully analyzed to obtain the best possible accuracy of the GPS-estimated path delays.

4.3. Data Evaluation and Comparisons

4.3.1. The AGNES Network and Processing

To evaluate the performance of this approach, an investigation has been carried out in the area of Switzerland, which is particularly suited, due to the topographic variances from flat to mountainous alpine areas. Furthermore, the *Automated GPS NEtwork of Switzerland (AGNES)* allows a precise and reliable study. The set-up of the AGNES network started in August 1998 with the station Zimmerwald (ZIMM). The number of operational sites increased permanently (Figure 4.2). In 2002, AGNES consisted of 30 stations, equally distributed over the entire country (Figure 4.3). The height distribution reaches from 329 m (station FHBB) to 3584 m (station JUJO). Due to the topography in Switzerland, the lower layers up to 1000 m have much more stations than the upper layers (Figure 4.4).

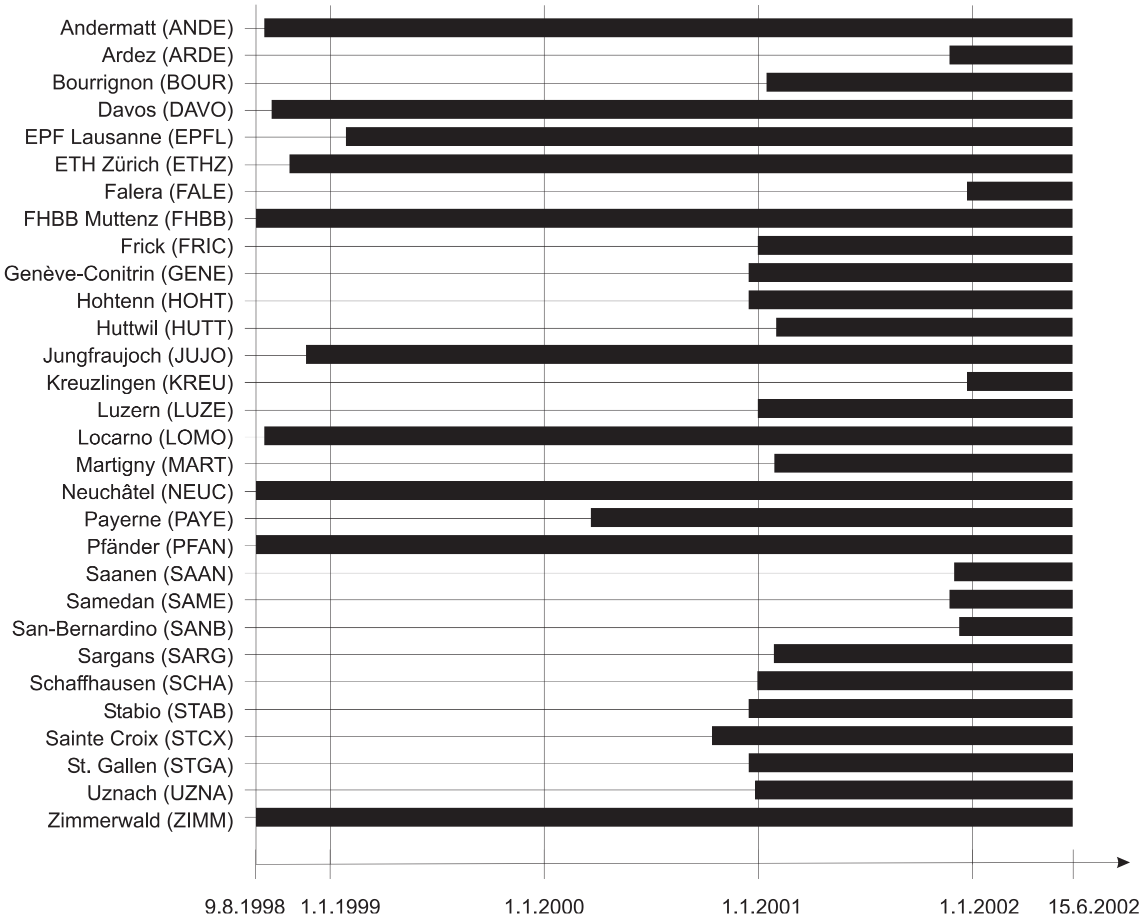

Figure 4.2.: Evolution of the AGNES network in Switzerland. The start of AGNES is set to the 9.8.1998. During the first two years a consistent distribution in Switzerland is realized with approximately 10 stations. End of 2000, a substantial network densification was initiated and was completed in 2002 with totally 30 stations.

The data of all AGNES stations are automatically processed using the Bernese GPS Processing Engine (Beutler et al., 2001). Additionally, the data of 20 EUREF stations are used to enlarge the station network in order to achieve better results (Brockmann and Troller, 2002). In the starting time of AGNES, 2-hour means of GPS-estimated path delays were available. Since September 2001, 1-hour means are estimated. The precision of the GPS-derived path delays is usually smaller than 1 cm, however, outliers are sporadically possible and require a quality check before another processing of the data can be commenced.

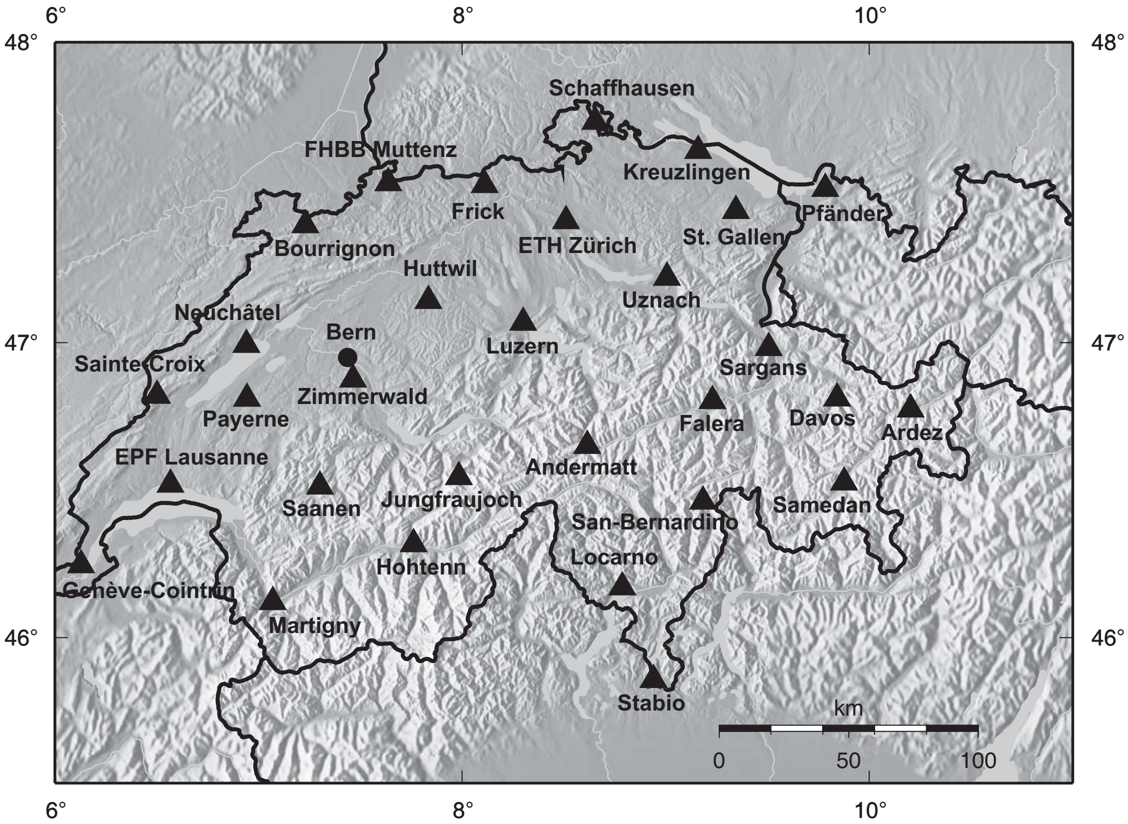

Figure 4.3.: GPS stations of the AGNES processing in Switzerland operated by Swisstopo. The whole processing network contains 30 AGNES stations (triangles), 20 EUREF stations and 23 stations from other networks (circles). The figure shows the stations in the Swiss territory only.

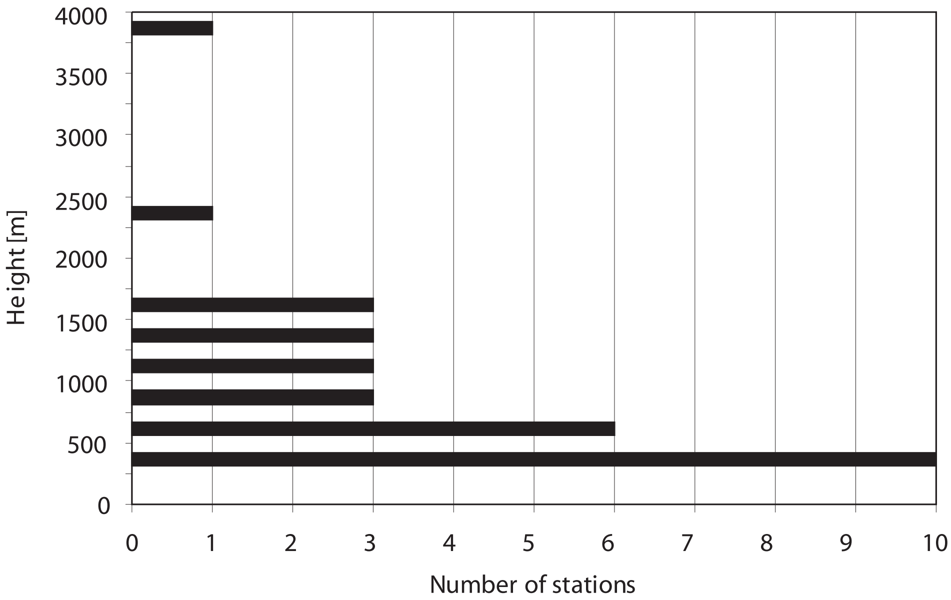

Figure 4.4.: Height distribution of the AGNES stations. 93% of the stations are located below 2000 m. Only Andermatt (2366 m) and Jungfraujoch (3634 m) are situated above 2000 m.

4.3.2. Data Treatment and Analysis

The potential and limits of COITROPA are shown on the basis of cross-correlations. Investigations are performed at station Zimmerwald (ZIMM). The station representing the reference of the Swiss national geodetic survey was put into operation as the first station in August, 1998. The time series of the coordinates show a very accurate repeatability during the whole time range. The north and east components differ in the range of 1 mm, the height component has a variance of around 10 mm in the beginning reducing to 3-4 mm in the last two years. The path delay of the station ZIMM is interpolated with all available AGNES stations except ZIMM itself. Due to the central location in the Swiss area and its station height (907m), a high accuracy and reliability of the interpolation can be expected. A general improvement of the GPS-derived path delays is visible as of April 20, 2000 due to a modification in the Saastamoinen a priori model of the GPS processing. Furthermore, the variation of accuracy in combination with the number of AGNES stations can be studied.

The reference for the comparisons is given by the GPS-estimated path delays at the station Zimmerwald, obtained from the Bernese GPS processing. The comparison to the COITROPA interpolation shows a good agreement over all. Figure 4.5 shows a comparison sample of the month of April 2002. The time series analysis from August 1998 to June 2002 is displayed in Figure 4.6 and Figure 4.7, respectively. Also the statistical analyses are placed in the figures (The calculation of the statistical data is described in Appendix B). A satisfactory result is shown. In Figure 4.5 for instance, the mean offset is below 5 mm and also the mean rms is only 6 mm. The annual time series in Figure 4.6 and Figure 4.7 show small mean rms as well. Furthermore a decrease in the zenith path delay rms over the years is detected.

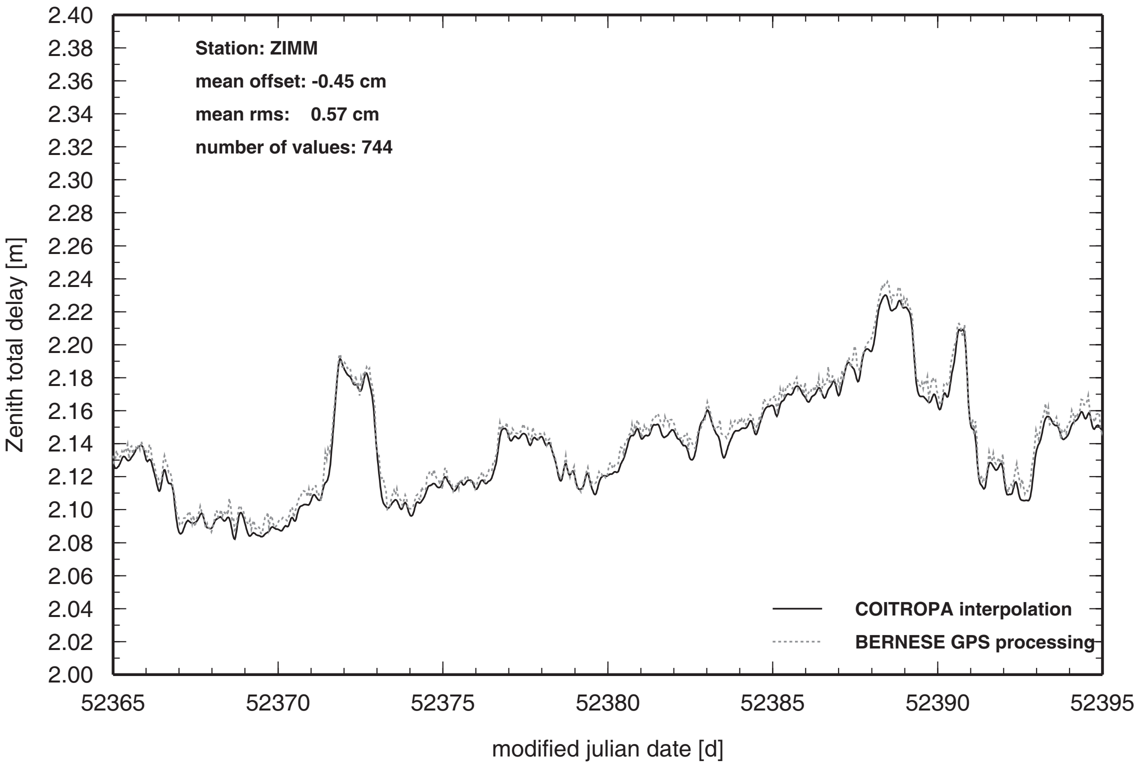

Figure 4.5.: Comparison of GPS-estimated path delays to values obtained by COITROPA at station ZIMM in April 2002. The two graphs fit accurately, the mean rms is well below one centimeter.

To analyze this behavior, monthly evaluated statistical data have been plotted with respect to time (Figure 4.8). The large offset and rms values are clearly visible during the initiation period in 1998. The jump in the mean offset in August 2000 can be traced back to a modification of the AGNES processing method. While coordinates are fixed to ITRF values of Zimmerwald until then, the subsequent evaluations estimated those coordinates as well. The definition of the datum is realized with two EUREF stations. A continuous decrease of the mean rms during the time period is visible. This is due to the increasing number of GPS stations. Since 1999 the mean rms is smaller than 1 cm.

It has to be noted, that the Zimmerwald station is an ideal station because of its location in the Swiss flat area. In the following paragraph, the cross-validation of the station Locarno (LOMO) is presented. Locarno is located south of the Alps with a strongly changing topography and a smaller number of neighboring AGNES stations. Until 2001, LOMO was the only station south of the Alps. Figure 4.9 shows a sample for the evaluation in March 2002. The time series analysis from August 1998 to June 2002 are displayed in Figure 4.10 and Figure 4.11.

The COITROPA interpolation fits the GPS-derived path delays precisely, i.e. within

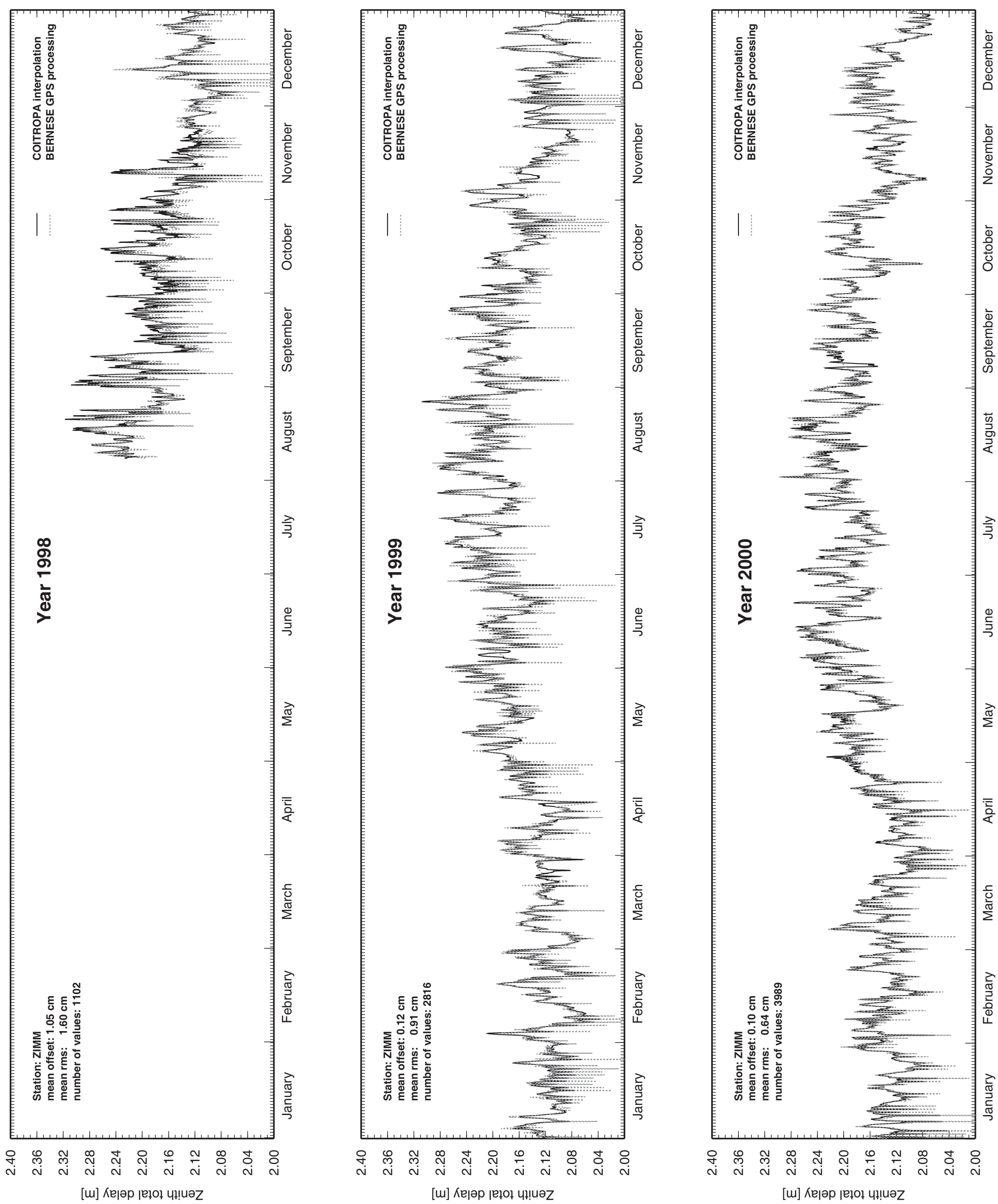

Figure 4.6.: Time series of GPS-estimated path delays and the solution obtained by COITROPA at station Zimmerwald in the years 1998 - 2000. The two series show a good agreement. The mean rms is decreasing during these three years due to the increasing number of GPS stations. Additionally, a seasonal influence is visible. Since April 20, 2000, a general improvement of the GPS-derived path delays is visible. This is due to a slight modification of the Saastamoinen a priori model in the residual screening step of the GPS processing.

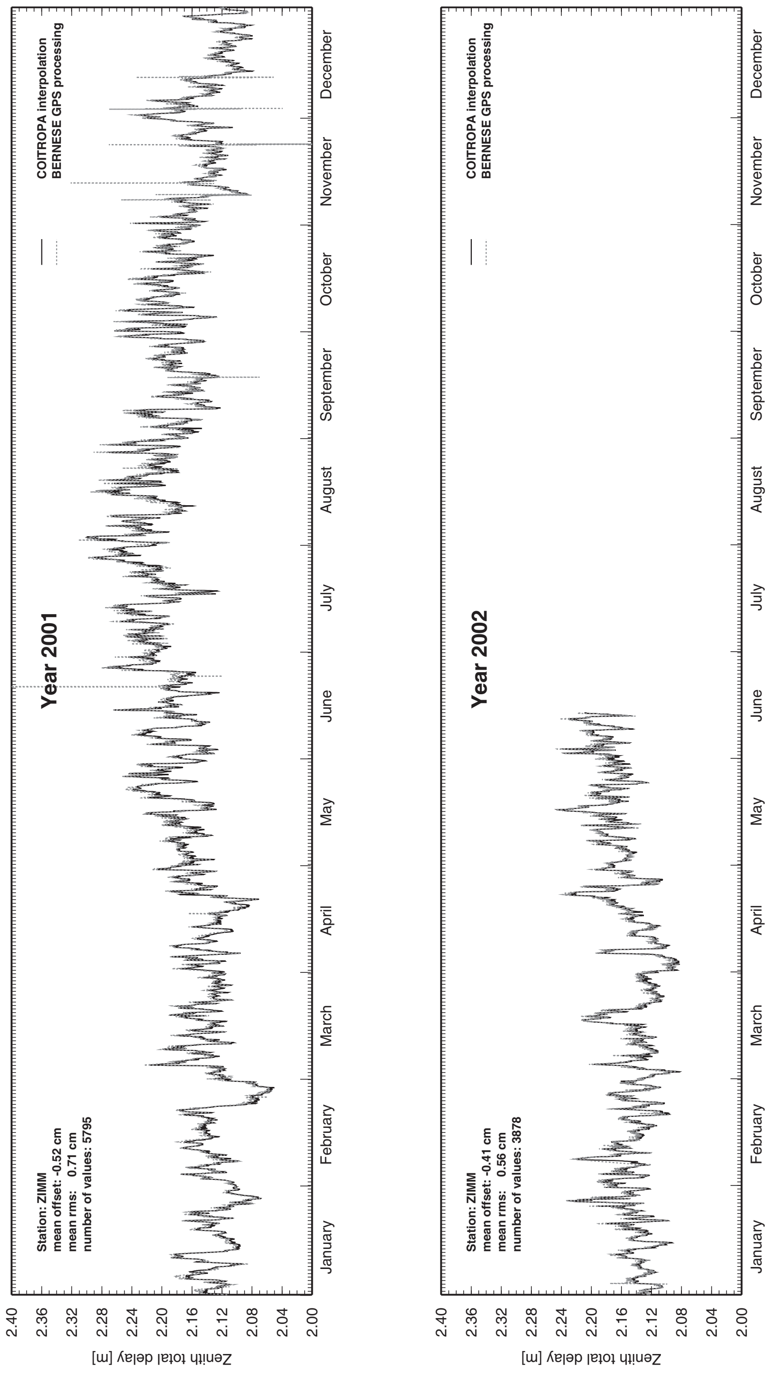

Figure 4.7.: Time series of GPS-estimated path delays and the solution obtained by COITROPA at station Zimmerwald in the years 2001 - 2002. In contrast to Figure 4.6, the rms stays at the same accuracy level during the years 2001 - 2002.

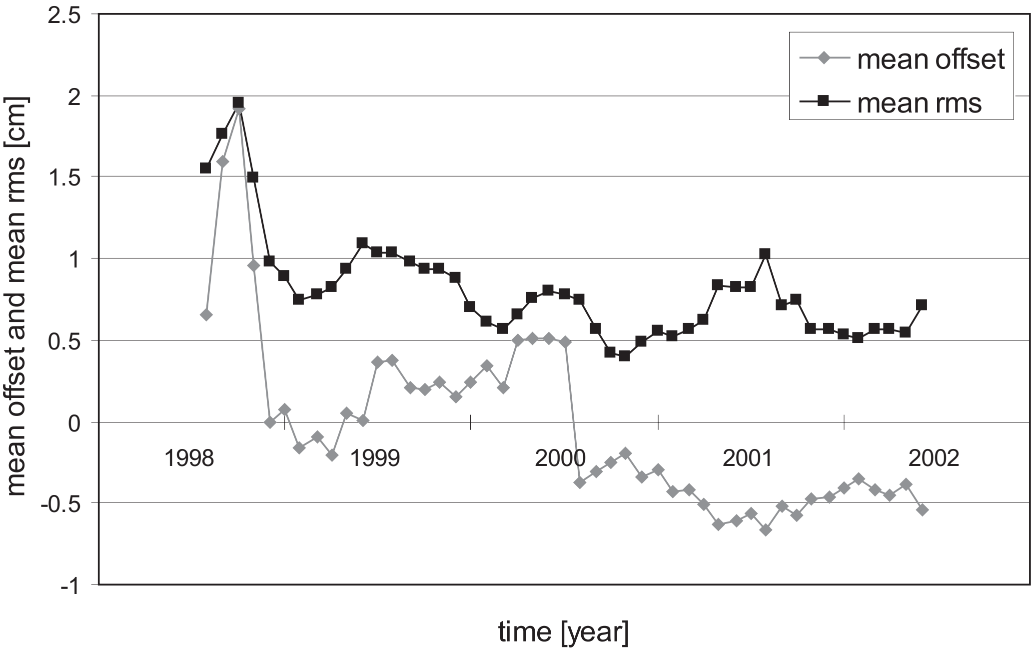

Figure 4.8.: Time series of the statistical evaluations at station Zimmerwald. While the mean offset is rapidly changing in the years 1998 and 1999, it stays constant from the year 2000 onward. The large jump on August, 2000 is due to a change of the reference system in the GPS processing. The reason for the bias of approximately 5 mm from the year 2000 onward, is assumed in defects of the deterministic modeling. The mean rms decreased from around 2 cm (1998) to less than 1 cm in 2002.

the cm range. However, the accuracy is lower than the results gained at the Zimmerwald station. During the installation of the first AGNES stations, the four months in 1998 and the year 1999, many outliers are present. From 2000 onward, the time series are overall consistent. A general seasonal increase of the path delays in the summer months is clearly seen on the time series plots (Figure 4.10 and Figure 4.11). Figure 4.12 shows the statistical evaluation of the station Locarno. In contrast to the Zimmerwald evaluation, the variations of the mean offset and the mean rms is much larger. More homogeneous evaluations are available since the end of 2001. In this year, two additional AGNES stations in Ticino were put into operation. This had an impact on the absolute level of the rms as well. The rms is now constantly below the value of 2 cm.

4.3.3. Statistical Evaluation

Beneath Zimmerwald and Locarno, cross-validations of several additional stations are calculated to estimate whether the results are representative. Figure 4.13 con-

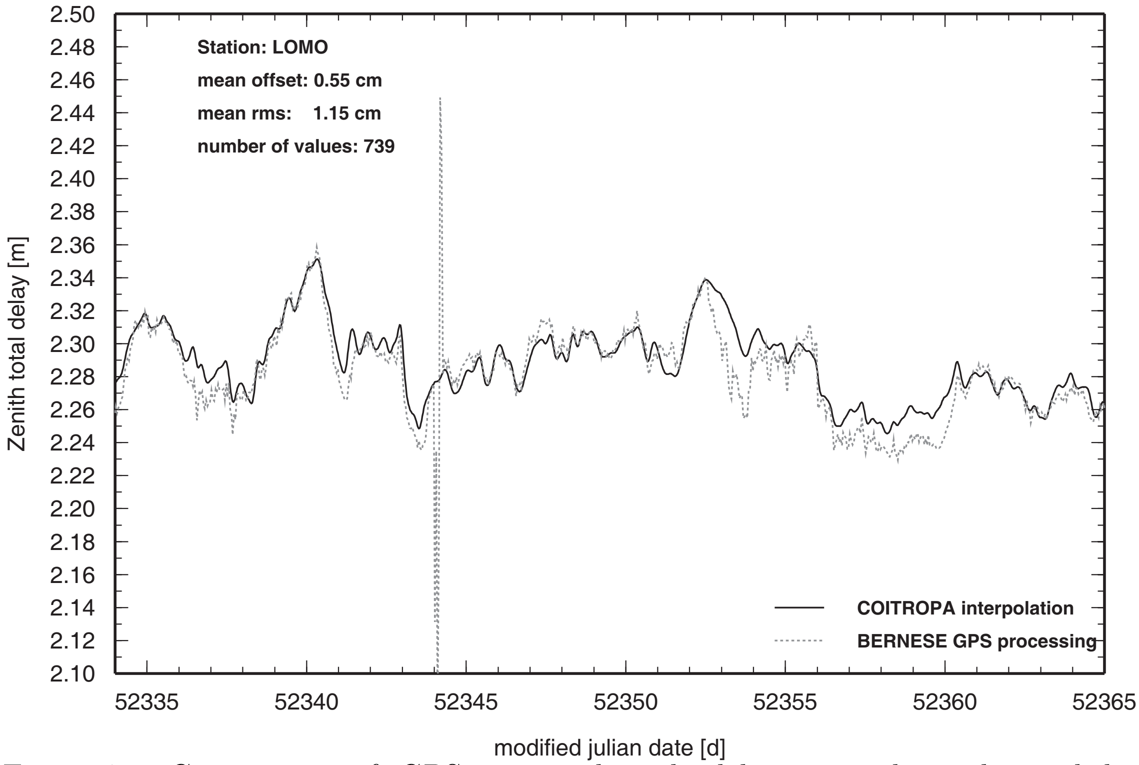

Figure 4.9.: Comparison of GPS-estimated path delays to values obtained by COITROPA for station Locarno in March 2002. The two time series show an overall good agreement. However, outliers are present. As a result, the rms is higher than for the station Zimmerwald (Figure 4.5).

tains the statistical evaluation of Zimmerwald (ZIMM), Locarno (LOMO), San Bernardino (SANB) and St. Gallen (STGA). One can assume, that the rms is getting higher with decreasing station height and, subsequently, the increase of the path delay. But this is just one factor of influence. The spatial distribution of GPS stations in the AGNES network as well as the total number of stations in the same meteorological region have a significant impact on the rms, too.

The stations Zimmerwald and St. Gallen are both located in the Swiss flat area. They show a similar behavior of accuracy of less than 1 cm. The stations Locarno and San Bernardino are located in a mountainous area in the southern part of Switzerland. There is only one more AGNES station located in this meteorological region. COITROPA needs to include also stations from the northern part to interpolate Locarno and San Bernardino. As in the southern part of Switzerland the weather is often differing from the atmospheric conditions in the northern part, the rms of the Locarno and San Bernardino time series is generally higher than time series in the northern flat area.

A linear regression for the stations Zimmerwald and Locarno points out a continuous decrease of the rms of about 0.8 mm/year in Zimmerwald and 2.9 mm/year in Locarno. This behavior depends on the increasing number of GPS stations as shown in Figure 4.2. Furthermore, a seasonal dependence of the rms is visible in Figure

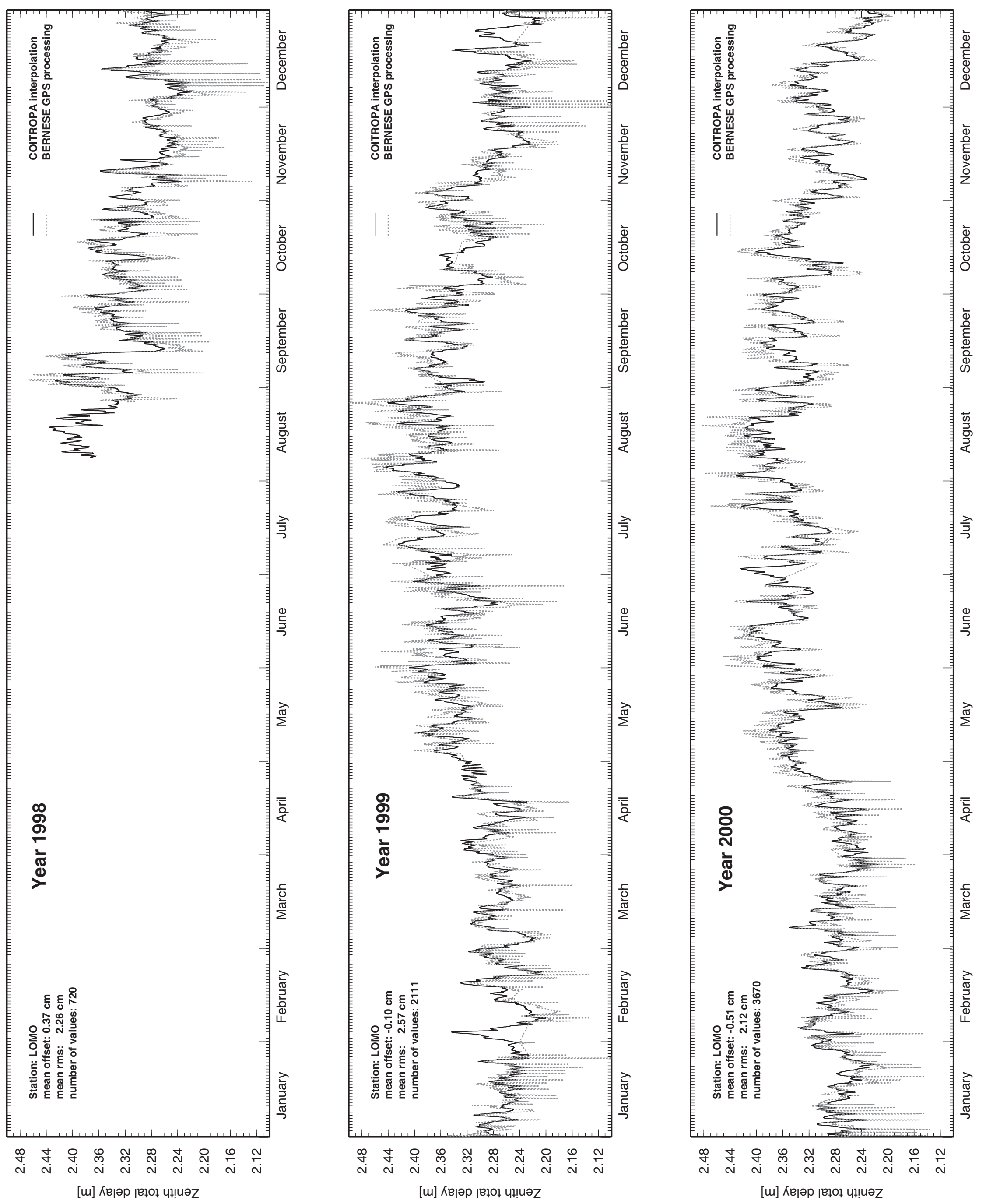

Figure 4.10.: Time series of GPS-estimated path delays and the solution obtained by COITROPA at station Locarno in the years 1998 - 2000. A seasonal influence is seen. Several discrepancies are present due to the fact, that LOMO is the only GPS station in Ticino in this particular time period. Since April 20, 2000, a general improvement of the GPS-derived path delays is visible. This is due to a slight modification of the Saastamoinen a priori model in the residual screening step of the GPS processing.

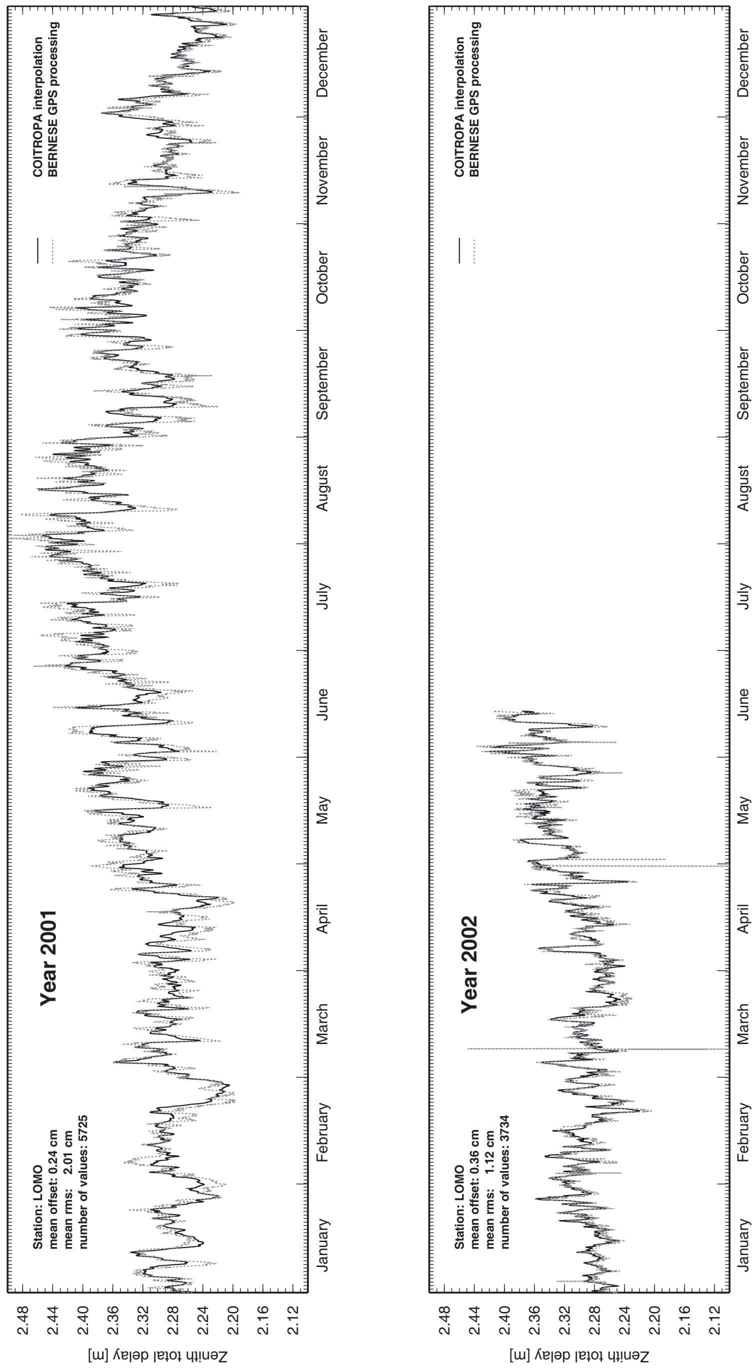

Figure 4.11.: Time series of GPS-estimated path delays and the solution obtained by COITROPA at station Locarno in the years 2001 - 2002. The accuracy in 2002 is increasing significantly compared to the years 1998 - 2001 (Figure 4.10). This is due to the starting-up of additional AGNES stations in Ticino.

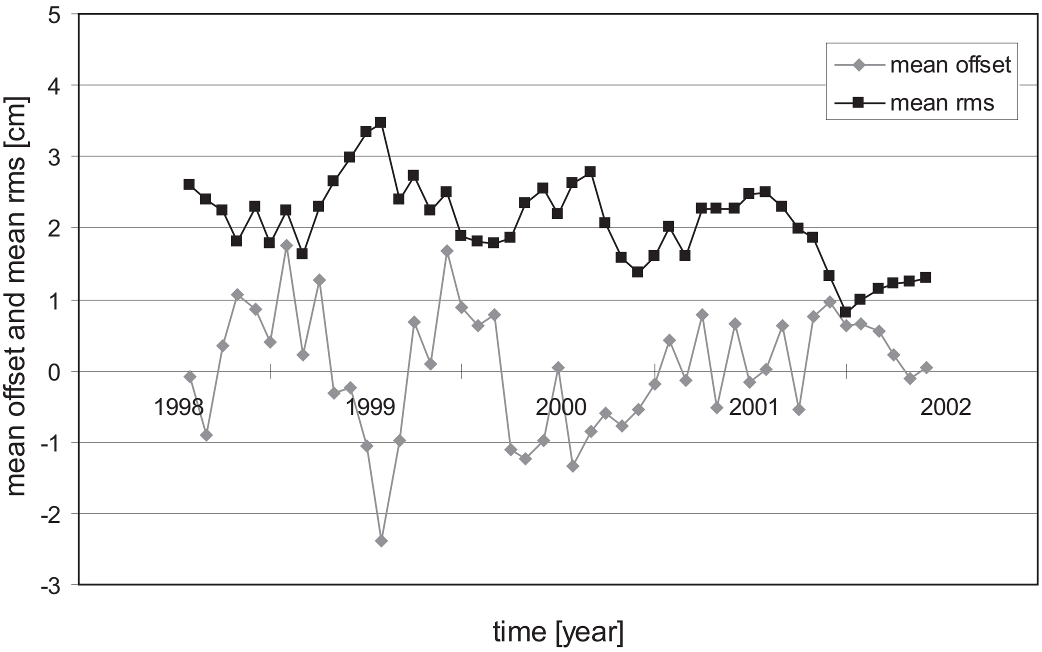

Figure 4.12.: Time series of statistical evaluations at the station Locarno. The values are changing rapidly, however, an improvement is seen in the course of the series. With the startup of a third AGNES station in Ticino at the end of 2001, the mean offset was stabilized. Since then, the mean rms is usually below two centimeters.

4.6, 4.7, 4.10 and 4.11. A frequency analysis (Fourier) of the rms after removing the linear regression result is provided to analyze this fact. Figure 4.14 displays the power spectrum density from the station Locarno (left) and Zimmerwald (right). The station Locarno shows a strong periodicity of one year. Zimmerwald has also an annual periodicity. Furthermore, a smaller periodicity of a half year is visible, for which no explanation can be given. However, the maximal amplitude of the Zimmerwald power spectral density is around fifteen times smaller then that of Locarno.

4.4. Discussion

Within this work, the software package COITROPA has been successfully developed. Applying it to the AGNES network, with very few exceptions, the interpolated path delays agree accurately with these estimated by GPS. The rms is usually smaller than one centimeter, for stations in the Swiss flat area it reaches nearly half a centimeter. Therefore, the accuracy required for applications in Switzerland was achieved.

In general, the accuracy is mainly dependent on the number of GPS stations in the

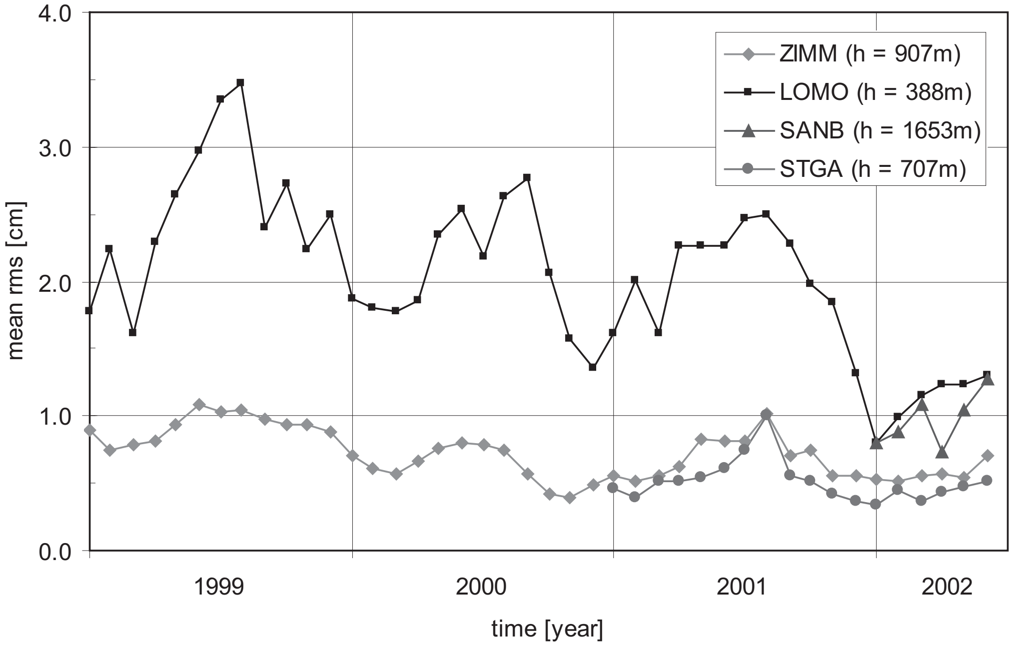

Figure 4.13.: Rms of path delay determination with COITROPA. Time series of four AGNES stations. The stations ZIMM and STGA are located in Central Switzerland, the stations LOMO and SANB in the Alps. Latter stations show generally a larger rms than the stations in Central Switzerland because of the AGNES network distribution.

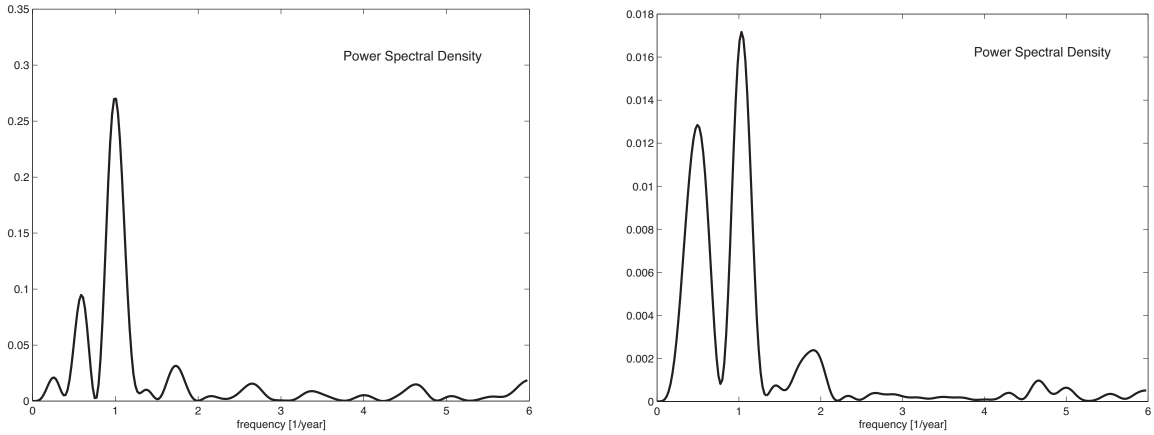

Figure 4.14.: Power spectral density of the mean rms for the station Locarno (left) and Zimmerwald (right). For Locarno a strong periodicity of one year is visible whereas two periodic parts (with considerably smaller significance) appear for the station Zimmerwald.

same meteorological area. Besides, the rms is also a function of the season. The higher values of the path delay in summer lead to a larger rms than in the winter months.

In a further study, the use of interpolated zenith total delays for the determination of precise station heights was investigated. The impact on the station height is smaller than 2 cm (Troller and Brockmann, 2002; Brockmann et al., 2003). The station density of AGNES is high enough to allow interpolations based on COITROPA with a sufficient accuracy for RTK applications.

If continuous GPS measurements are available at least during one hour, estimation using a GPS processing software still represents the preferred method to obtain GPS path delays. Otherwise, the interpolation of GPS-estimated path delays has currently turned out as the most accurate method.

In terms of accuracy, it has to be mentioned, that the GPS measurements influence the interpolated path delays. If latter are introduced to correct other GPS measurements, this procedure is not independent, i.e., systematic errors of GPS would not be recognized. Methods to determine path delays using meteorological input data such as COMEDIE yields a benefit as regards to the accuracy, however, COITROPA allows a higher consistency.

5. GPS Tomography

5.1. Introduction

In contrast to the methods described before, the tomographic approach allows to determine the height profile of the precipitable water vapor (PW). Several meteorological applications and studies require time series of atmospheric water vapor, e.g. for the assimilation in meteorological forecast models. Therefore, tomographic approaches, which enable to resolve the spatial and temporal distribution of the PW in the atmosphere have been investigated. A recent extensive theoretical study has been carried out by MacDonald et al. (2002). Three major methods have been realized so far:

- Flores (1999) developed a software package called LOTTOS (Local Tropospheric Tomographic Software). It uses wet slant delays from the GIPSY-OASIS II (GOA II) GPS processing software (Webb and Zumberge, 1997) as input. In addition several constraints are introduced in the adjustment system. Various simulations and real-data comparisons have been presented (e.g. Flores et al., 2000).
- A second approach was carried out in the framework of a GPS meteorology project in Japan (Hirahara, 2000; Seko et al., 2000). Its main goal was to monitor rapid changes of water vapor in order to predict Asian Monsoon and other atmospheric turbulences. Wet slant delays obtained from GPS processing using the GAMIT software (King and Bock, 1999) were introduced in conjunction with other measurements such as wind profiles of radiosondes and radiometer data (Seko et al., 2000).
- A third approach which uses double difference residuals from the Bernese GPS Processing Software (Beutler et al., 2001) has been pursued at ETH Zürich. Kruse (2001) developed a first version of a software package called AWATOS (Atmospheric Water Vapor Tomography).

Here, we present a refined version of AWATOS. On the basis of several simulation studies, the performance of the software package is discussed. Chapter 5.7 presents the analysis of real-data acquired during a field campaign (Troller et al., 2002a).

5.2. Tomographic Principle Applied to the Atmosphere

The satellite signal is influenced by the atmosphere along the entire path s from the satellite to the GPS antenna. The total slant path delay Δ^{PD} is obtained by integrating the refractivity N along the ray path from the receiving antenna to the satellite (2.9). Ray bending can be ignored (Ichikawa et al., 1995).

In the tomographic approach a discretisation of the atmosphere with a 3-dimensional voxel model is used. For each voxel i, an unknown but constant refractivity N_i is introduced. The total slant path delay observation Δ_j^{PD} can then be expressed as a summation over each individual voxel i the GPS signal passes through (Figure 5.1):

$$\Delta_j^{PD} = 10^{-6} \cdot \sum_{i=1}^{k} N_i \, \Delta s_{i,j} \tag{5.1}$$

where:

$\Delta s_{i,j}$	:	length of the ray j in voxel i, i.e. $\Delta s_{i,j} = 0$ for voxels not passed through by the ray j
k	:	total number of voxels in the model

Considering several observations j, subsequently, the equation system can be written as:

$$\boldsymbol{\Delta^{PD}} = \boldsymbol{A} \cdot \boldsymbol{N} \tag{5.2}$$

$\boldsymbol{\Delta^{PD}}$ represents the vector including all path delay observations Δ_j^{PD}, $\boldsymbol{N}$ represents the vector of the unknown refractivity values N_i. The design matrix $\boldsymbol{A}$ contains the lengths $\Delta s_{i,j}$ of the observations Δ_j^{PD} traversed in voxels i as well as the conversion factor 10^{-6}.

5.3. Inversion of the Equation System

The main problem of the tomographic approach is to form a regular normal equation matrix which can be inverted. In medicine for example, the tomographic approach has been successfully established. Usually, measurements of the human body are made from all sides and as long as necessary to achieve a sufficiently determined normal equation matrix. This is a necessary condition, if the interior structure of a body should be determined only with measurements from outside the body. When applying GPS tomography, in contrast, measurements of the atmosphere are only possible from the satellite (top) to the receiver (earth). Horizontal measurements in

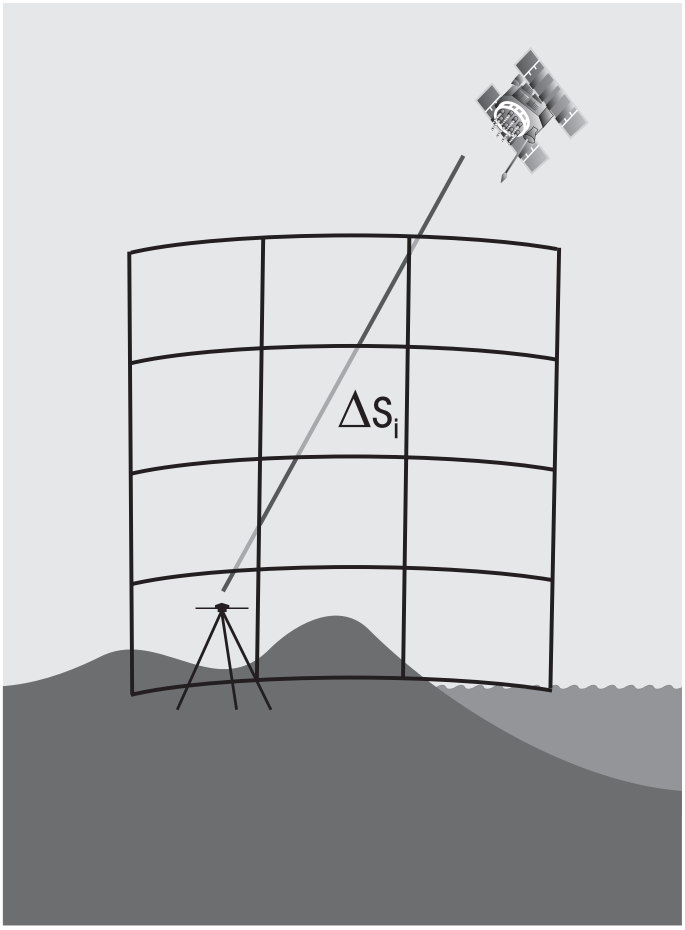

Figure 5.1.: Principle of GPS tomography. The observed ray traversing the atmosphere is delayed. The amount and distribution of water vapor in the atmosphere is one influence of this delay (2.9). To compute this effect mathematically, a 3-dimensional voxel model is introduced with a constant refractivity within each voxel. The rays are allocated in the chosen voxel model (5.1).

the atmosphere are usually not available. Additionally, the number of traversing rays per voxel depends on the resolution of the model given by the number of layers and the number of voxels per layer, as well as on the geometry defined by the distribution of the ground stations, the satellite constellation and the integration time. Therefore, it is usually not possible to have enough satellites and GPS ground stations to allocate enough measurements to each voxel. Consequently, GPS tomography yields an ill-posed problem. In fact, some voxels are over-determined, but others are under-determined. The whole equation system is mixed-determined (Menke, 1989) and the inversion may become singular.

To solve the equation system, the tomographic approach using GPS must fulfill some further conditions. They can be characterized as follow:

- In an ideal case, at least one GPS receiver would be present in each voxel. In that way, the inversion is solvable. Obviously, this network configuration is not possible. However, a topography which accounts for a good height distribution of the GPS stations contributes substantially to the quality of the solution.

- Zenith path delays on their own are not enough to construct a sufficiently determined equation system, no matter how many delays are available (except in the constellation described above). With slant delays indeed, it is possible to determine a voxel, even if no GPS receiver is inside this voxel (Menke, 1989). Therefore, a huge amount of slant delays with different elevation angles improves the quality of the solution significantly.

- If the inversion is partially under- and partially over-determined, a technique called *singular value decomposition (SVD)* can be applied to diagnose and separate the under-determined part in a way, that the over-determined part of the matrix can be inverted (Chapter 5.4.4).

- Supplementary voxel constraints can be used to sufficiently stabilize the equation system. It must be differentiated between two types of constraints. On the one hand, refractivity information obtained from independent sources can be used to constrain certain voxels. On the other hand, a determinability of a voxel can be assured, by constraining the refractivity between neighboring voxels (Chapter 5.4.5).

If one or several of these conditions are fulfilled, the equation system can be inverted. Various methods exist to check the quality of the normal equation matrix. It is dependent only on the network and observation geometry and the chosen voxel model. Therefore, an a priori variance-covariance analysis is useful. A common possibility is to determine the model resolution matrix (Menke, 1989). This method describes how well the model parameters can be determined compared to true parameters.

5.4. Tomographic Software Package AWATOS

5.4.1. Overview

The practical realization of the tomographic approach has been coded in the C++ software package AWATOS. It is able to handle several types of observations. A voxel model can be defined by the user. This allows to resolve the refractivity of each voxel using a least-squares adjustment (Figure 5.2).

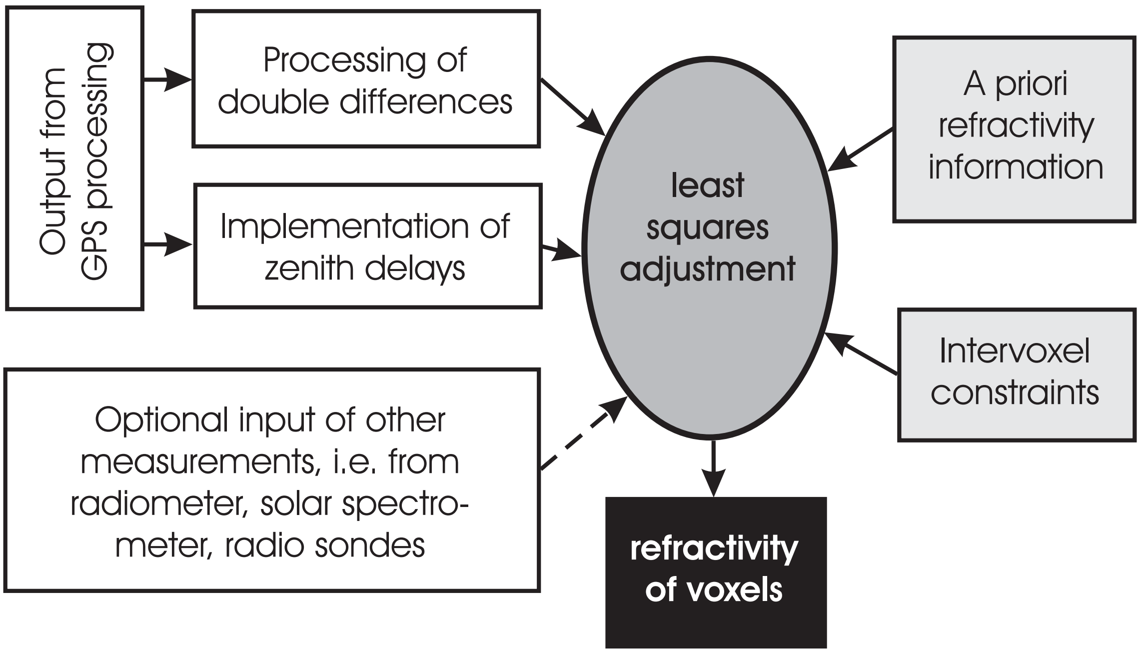

Figure 5.2.: Flow chart of the software package AWATOS. To perform the least squares adjustment, several types of input data can be used. On the left side, measurements from GPS and other techniques are shown. On the right side, additional artificial observations are listed.

5.4.2. Tomographic Voxel Model

The voxel model is defined by an arbitrary number of layers. Ellipsoidal boundary surfaces of the layers account for the earth's curvature. AWATOS allows an individual horizontal resolution of the voxels for each layer. At the horizontal boundaries of each layer open voxels are added, i.e., this voxels reach ad infinitum. Thus all rays are traversing voxels from the upper to the lower layers of the model. No rays pass completely or partially outside the model.

5.4.3. Observations

Several types of GPS path delays can be handled by AWATOS, namely zenith and double-difference slant delays. Additionally, observations from independent measurement systems such as radiometers or spectrometers can be included. However, the main type of observations used in our approach are GPS double-difference path delays.

Applying the tomographic approach, usually only the wet refractivity is of interest. Therefore, the observations must be corrected for the dry part of the refractivity prior to introducing them into the tomographic equation system.

Double-Difference Path Delays

The GPS data are first processed using a GPS software, e.g. the Bernese Software (Beutler et al., 2001). For the following steps, the GPS-estimated zenith path delays as well as the double-difference residuals are required. Furthermore, the information about which stations and satellites are used to compose the double-differences must be available together with their respective time information. First, the dry part of the path delay has to be subtracted. The standard approach is to use some meteorological ground data of hydrostatic pressure, temperature and water vapor pressure. They can be interpolated to the location of the GPS stations. Subsequently, using the formula of Saastamoinen (1972), the dry path delay can be computed with sufficient accuracy. Double-difference wet path delays can now be reconstructed. The total GPS-estimated zenith path delay is reduced by the corresponding dry delay to obtain the zenith wet delay $\overline{\rho}_p$. Latter is mapped to the respective elevation angle el_p^r applying the same mapping function $m(el_p^r)$ as used in the GPS processing. The double-difference $\Delta^2\overline{\rho}_{pq}^{rs}$ of the slant wet delays can now be formed. Finally, the double-difference phase residual $\Delta^2\Phi_{pq}^{rs}$ is added. The following equation describes the reconstruction of the double-difference wet path delay $\Delta^2\rho_{pq}^{rs}$:

$$\Delta^2\rho_{pq}^{rs} = (\rho_q^r - \rho_p^r) - (\rho_q^s - \rho_p^s) \tag{5.3}$$
$$= \Delta^2\overline{\rho}_{pq}^{rs} + \Delta^2\Phi_{pq}^{rs} \tag{5.4}$$

where:

$$\begin{aligned}\Delta^2\overline{\rho}_{pq}^{rs} &= (\overline{\rho}_q \cdot m(el_q^r) - \overline{\rho}_p \cdot m(el_p^r)) - \\ &\quad (\overline{\rho}_q \cdot m(el_q^s) - \overline{\rho}_p \cdot m(el_p^s))\end{aligned}$$

The main advantage of this approach is that satellite and receiver clock biases are already eliminated (Ware et al., 1997). However, the double-difference phase residual contains not only troposphere information but also other not-modeled information such as multipath, antenna phase center variations, clock errors and ionosphere information. Therefore, these effects may be interpreted as tropospheric effects as well.

The double-difference wet path delays are now allocated to the corresponding voxels (Figure 5.3). The path lengths $\Delta s_{i,j}$ are calculated and added to the first design matrix. One observation equation is formed as follows (the index j of the observation number is omitted to simplify matters):

$$\Delta^2 \rho_{pq}^{rs} = \left(\Delta s_1{}_{pq}^{rs} \quad \Delta s_2{}_{pq}^{rs} \quad \Delta s_3{}_{pq}^{rs} \quad \Delta s_4{}_{pq}^{rs} \quad \Delta s_5{}_{pq}^{rs} \quad ... \right) \cdot 10^{-6} \cdot \begin{pmatrix} N_1 \\ N_2 \\ N_3 \\ N_4 \\ N_5 \\ ... \end{pmatrix} \tag{5.5}$$

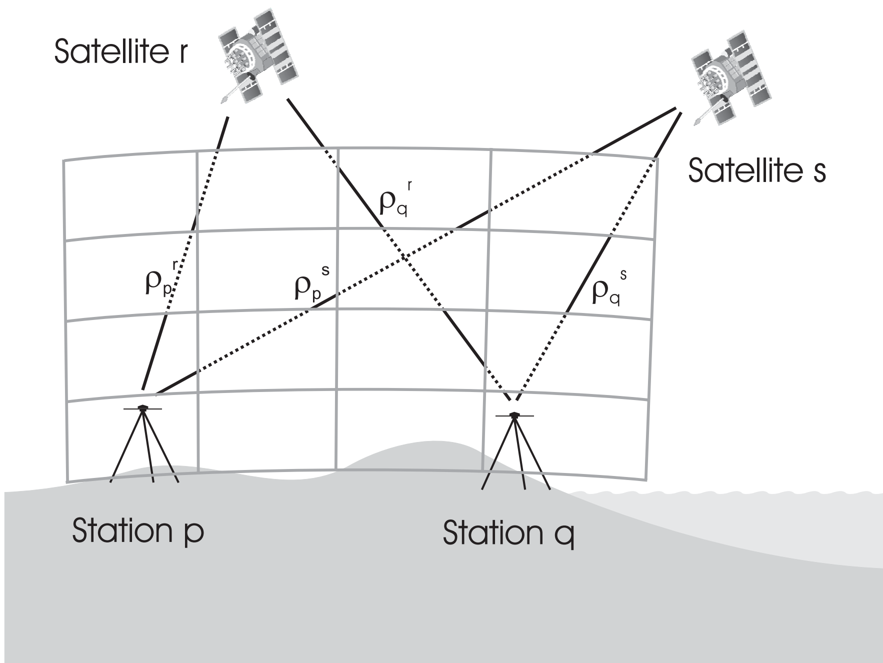

Figure 5.3.: Double-difference GPS tomography. The reconstructed double-difference observations are allocated to the corresponding voxels.

GPS-Derived Zenith Path Delays

Subsidiary to the import of double-difference delays, the GPS-estimated zenith delays can be introduced. First, again the GPS-estimated zenith path delay is reduced by the corresponding dry delay to obtain the zenith wet delay $\overline{\rho}_p$. Afterwards, the path lengths $\Delta s_{i,j}$ are allocated to the voxel model in the same way as in (5.5) (the index j of the observation number is omitted to simplify matters):

$$\overline{\rho}_p = \begin{pmatrix} \Delta s_{1p} & \Delta s_{2p} & \Delta s_{3p} & \Delta s_{4p} & \Delta s_{5p} & ... \end{pmatrix} \cdot 10^{-6} \cdot \begin{pmatrix} N_1 \\ N_2 \\ N_3 \\ N_4 \\ N_5 \\ ... \end{pmatrix} \tag{5.6}$$

Water Vapor Radiometer Data

The IPW of water vapor radiometers can also be included into the equation system. Both, zenith and pointed delays ΔL_o use the same observation equation (the index j of the observation number is omitted to simplify matters):

$$\Delta L_o = \begin{pmatrix} \Delta s_{1o} & \Delta s_{2o} & \Delta s_{3o} & \Delta s_{4o} & \Delta s_{5o} & ... \end{pmatrix} \cdot 10^{-6} \cdot \begin{pmatrix} N_1 \\ N_2 \\ N_3 \\ N_4 \\ N_5 \\ ... \end{pmatrix} \tag{5.7}$$

5.4.4. Applying a Singular Value Decomposition

The singular value decomposition (SVD) (Press et al., 1994) is a powerful technique to diagnose and sometimes solve the under-determined parts of a matrix to be inverted. The normal equation matrix M is separated into a column-orthogonal matrix U, a diagonal matrix W and the transpose of an orthogonal matrix V as followed:

$$M_{m,n} = U_{m,n} \cdot W_{n,n} \cdot V_{n,n}^T \tag{5.8}$$

The matrix W is a diagonal matrix whose elements are in descending order. Without loosing information, it is now possible to shorten the matrix W to the elements which are neither mathematically nor numerically zero. It is possible to invert the shortened matrix W, as well as the column-orthogonal matrix U and the orthogonal matrix V. Subsequently, the solution can be calculated. Obviously, this procedure can be applied to every kind of matrices. A numerical solution for the not under-determined unknowns is always given. But it has to be reviewed, whether the complete solution is also mathematically correct.

5.4.5. Additional Voxel Constraints

A Priori Information

Individual a priori information is used to constrain the refractivity to a given value in a specific voxel or layer. Generally, such constraints are applied to fix voxels and layers for which the refractivity value is known because of the atmospheric physics. In standard processing, the wet refractivity in the uppermost layer is usually constrained to zero. This allows to stabilize the inversion. The equation system is supplemented with constraints of the following type (pseudo-observation):

$$N_{a\ priori,i} = 1 \cdot N_i \tag{5.9}$$

where:

$$\begin{aligned} N_{a\ priori,i} &: \text{ a priori refractivity of voxel } i \\ N_i &: \text{ unkown refractivity of voxel } i \end{aligned}$$

For each pseudo-observation, a weight has to be introduced in the covariance matrix. If available, it can be useful to introduce a priori refractivity of ground meteorological stations in the lower-most layer of the tomographic voxel model. However, it may not be reasonable to use this method for the whole refractivity field. Even a small weighting of an imprecise a priori observation affects the solution in a negative way.

Inter-Voxel Constraints

The inter-voxel constraints limit the variation of the difference in the refractivity of neighboring voxels. As a result, under-determined voxels are constrained to the mean of the neighborhood and the refractivity at neighboring voxels may be smoothed. To reduce the smoothing effect, only the direct neighboring voxels in each dimension are taken into account. The weighting of the individual neighboring voxels is derived from the following covariance function $\Phi_{i,j}$ which is dependent on the distance (3.14):

$$\Phi_{i,j} = \frac{\sigma_0^2}{1 + \left[\left(\frac{x_i - x_j}{\Delta x_0}\right)^2 + \left(\frac{y_i - y_j}{\Delta y_0}\right)^2 + \left(\frac{z_i - z_j}{\Delta z_0}\right)^2\right]} \tag{5.10}$$

where:

$$\begin{aligned} \sigma_0^2 &: \text{ a priori variance of the signal} \\ \overrightarrow{x_i} = \begin{pmatrix} x_i \\ y_i \\ z_i \end{pmatrix}, \overrightarrow{x_j} = \begin{pmatrix} x_j \\ y_j \\ z_j \end{pmatrix} &: \text{ space vector of voxel centers i and j} \\ \Delta x_0, \Delta y_0, \Delta z_0 &: \text{ correlation lengths of the individual components} \end{aligned}$$

Assuming a 2-dimensional box model as shown in Figure 5.4, the constraints for box 9 can be formulated by set up the covariance function of each box relation, e.g. the relation for box 2 and 9 (based on 5.10):

$$\Phi_{9,2} = \frac{\sigma_0^2}{1 + \left[\left(\frac{x_9 - x_2}{\Delta x_0}\right)^2 + \left(\frac{y_9 - y_2}{\Delta y_0}\right)^2 + \left(\frac{z_9 - z_2}{\Delta z_0}\right)^2\right]} \tag{5.11}$$

25	26	27	28	29	30
19	20	21	22	23	24
13	14	15	16	17	18
7	8	9	10	11	12
1	2	3	4	5	6

Figure 5.4.: Example of a 2-dimensional box model. The boxes are numbered in a 1-dimension system. To constrain the refractivity of box 9, the mean of the refractivity values of the boxes 2, 3, 4, 8, 10, 14, 15 and 16 are used, weighted according to the distance to box 9.

Finally, the corresponding pseudo-observation equation for box 9 can be formulated:

$$0 = \begin{pmatrix} 0 & \frac{\Phi_{9,2}}{\Phi_{sum}} & \frac{\Phi_{9,3}}{\Phi_{sum}} & \frac{\Phi_{9,4}}{\Phi_{sum}} & 0 & 0 & 0 & \frac{\Phi_{9,8}}{\Phi_{sum}} & -1 & \frac{\Phi_{9,10}}{\Phi_{sum}} & 0 & 0 & ... \end{pmatrix} \begin{pmatrix} N_1 \\ N_2 \\ N_3 \\ N_4 \\ N_5 \\ N_6 \\ N_7 \\ N_8 \\ N_9 \\ N_{10} \\ N_{11} \\ N_{12} \\ ... \end{pmatrix} \tag{5.12}$$

where:

$$\Phi_{sum} = \sum_{j=1}^{30} \Phi_{9,j}$$

For each pseudo-observation, a weight has to be introduced in the covariance matrix of the equation system.

5.4.6. Equation System of AWATOS

All possible types of observation equations, measured observations as well as voxel constraints are combined to the total observation equation system:

$$\begin{array}{l} \text{Double difference observations:} \\ \text{Zenith path delay observations:} \\ \text{Radiometer observations:} \\ \text{A priori information:} \\ \text{Inter-voxel constraints:} \end{array} \begin{pmatrix} \Delta^2 \rho_{pq}^{rs} \\ \overline{\rho}_p \\ \Delta L_o \\ N_{a\ priori,i} \\ 0 \end{pmatrix} = A \cdot \begin{pmatrix} N_1 \\ N_2 \\ N_3 \\ N_4 \\ N_5 \\ N_6 \\ N_7 \\ N_8 \\ \cdots \end{pmatrix} \tag{5.13}$$

For the least-squares adjustment, a covariance matrix containing the weightings of the observations has to be defined as well. Usually, a weight is introduced for each type of observations, however, it is also possible to weight each observation individually.

5.5. The Campaign on the Island of Hawaii

5.5.1. Campaign Description

A dedicated field campaign was initiated to investigate the performance of GPS tomography. Optimal research conditions require a topography with large height changes in a relatively small area. The Big Island of Hawaii, USA, fits these requirements perfectly. Furthermore, a dense GPS permanent network had already been installed, associated with a nearly optimal station distribution. The height range extends from sea level up to nearly 4200 m on the Mauna Loa (Figure 5.5).

The permanent GPS network consists of 18 stations. 12 stations are operated by the Hawaiian Volcano Observatory (HVO) of the U.S. Geological Survey and 6 stations by the School of Ocean, Earth Science and Technology of the University of Hawaii (SOEST). During the campaign, the network was further densified by installing 6 additional GPS stations. Furthermore, two water vapor radiometers (Kruse, 2001) and a solar spectrometer (Sierk, 2001) were deployed. See Figure 5.6 for details.

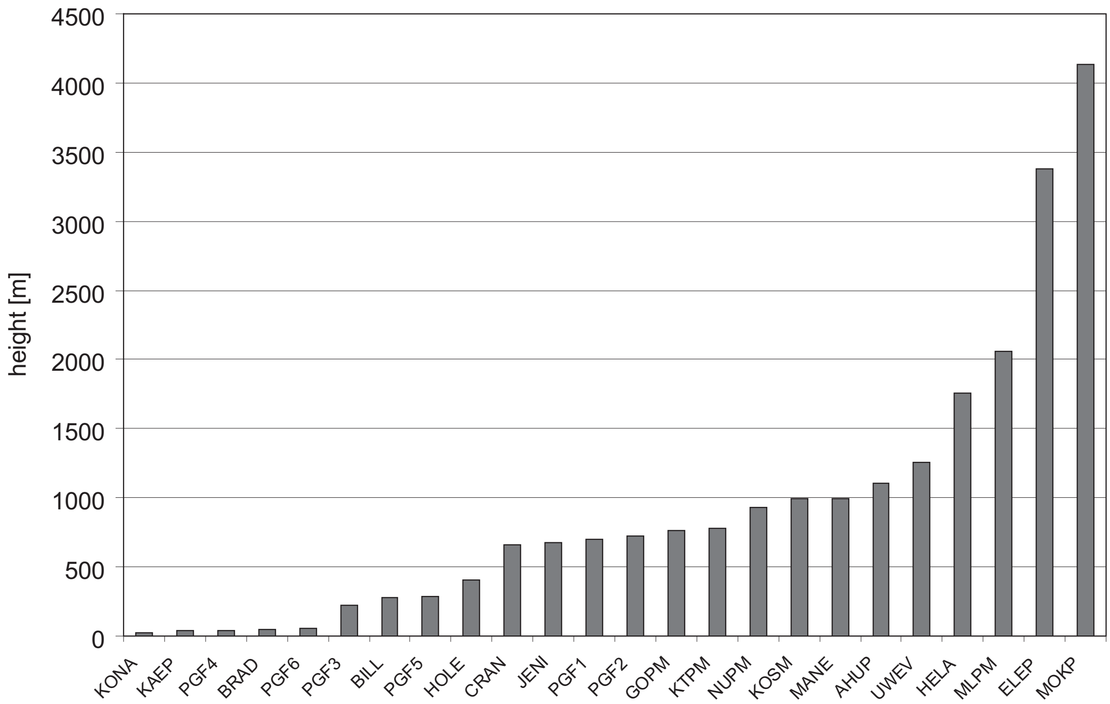

Figure 5.5.: Height distribution of the Hawaiian GPS network. The network is well-distributed from sea level up to the top of the mountain Mauna Loa (MOKP) at 4133 m. 25 % of the stations are higher than 1000 m.

To realize an independent comparison, ground meteorological measurements were recorded. Meteorological data are registered simultaneously at six permanent GPS stations, operated by SOEST. At the highest station MOKP, on top of Mauna Loa, a portable meteo logging unit was installed permanently during the campaign. Three additional recording units were installed temporarily at five different GPS locations in order to achieve a well-balanced distribution. The meteorological conditions in the higher atmospheric layers are measured by radiosondes. During the last two weeks of the campaign, 18 radiosondes were launched alternatively from four different locations (Figure 5.6). The meteorological measurements are described in detail in Figure 5.7. For a further description of the campaign we refer to Kruse (2001).

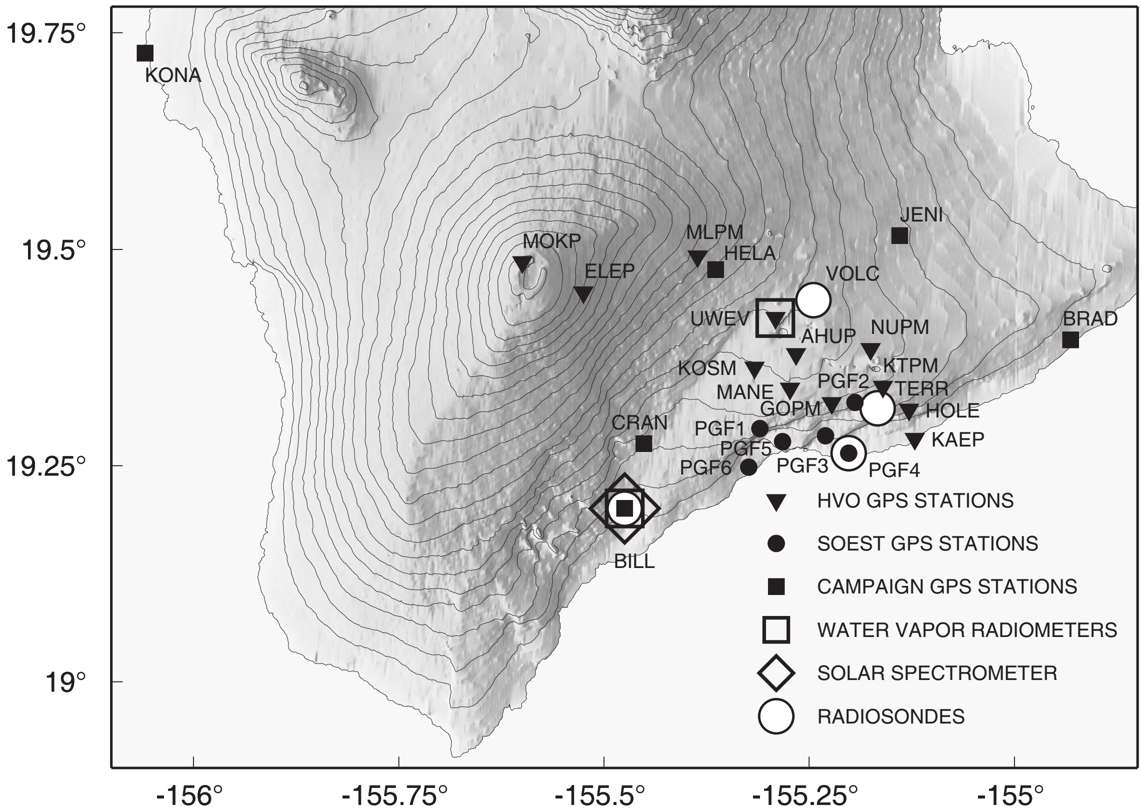

Figure 5.6.: Network of the Hawaiian campaign on the Big Island of Hawaii. 18 GPS stations belong to the permanent GPS network of the Hawaiian Volcano Observatory (HVO) of the U.S. Geological Survey and the School of Ocean, Earth Science and Technology of the University of Hawaii (SOEST). Furthermore, 6 campaign stations as well as 2 radiometers and 1 solar spectrometer were operated. In addition, 18 radiosondes were launched from four selected sites during the campaign. (Contour interval of topography = 200 m)

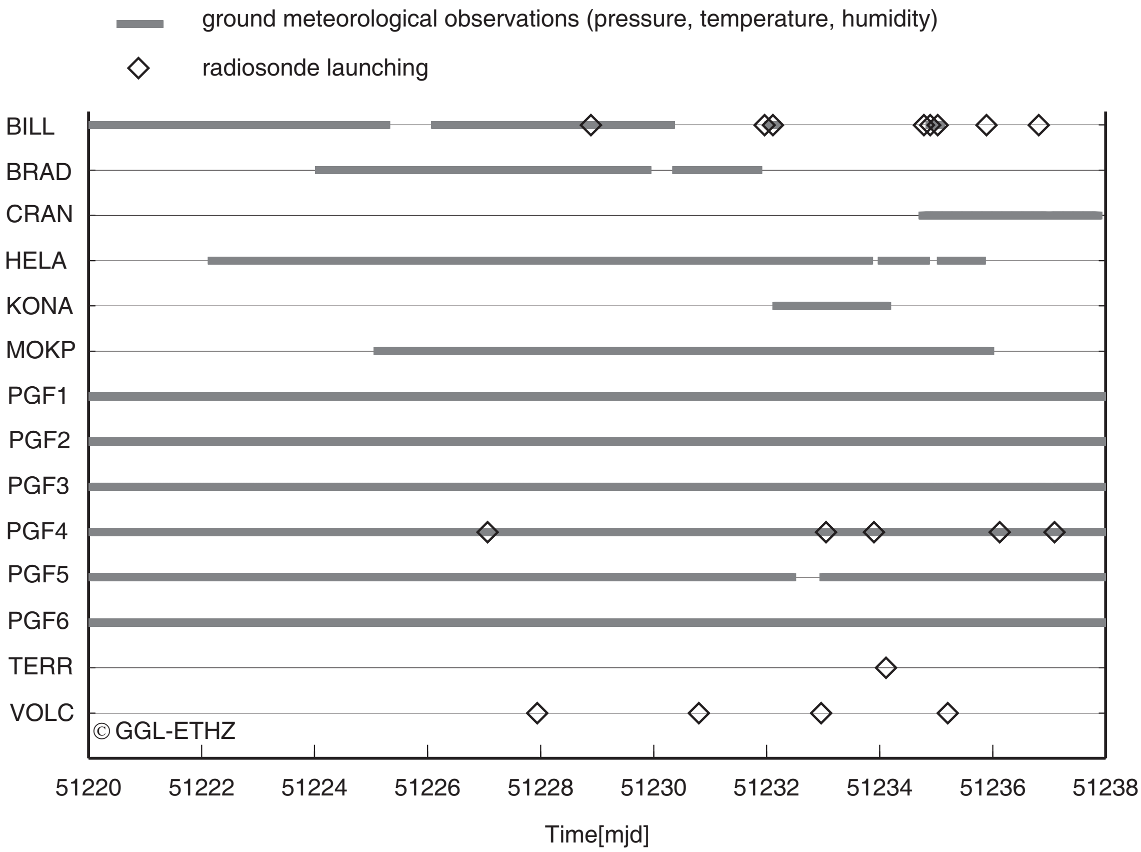

Figure 5.7.: Ground meteorological and radiosonde measurements during the Hawaiian campaign. The ground meteorological stations are equipped with pressure, temperature and humidity sensors. Because of a technical defect, no temperature and humidity measurements are available from station PGF4.

5.5.2. Meteorological Data Treatment

The ground pressure sensors are calibrated on the spot, while the manufacturer's calibration results for the dry-bulb and dew-point temperature sensors are taken into account. The humidity is calculated using the formula for saturated water vapor (3.9). The accuracy of the meteorological ground data is summarized in Table 5.1.

data type	pressure [hPA]	temperature [^{o}C]	relative humidity [%]
ground data	0.1 – 1.0	0.1	0.5 – 3
radiosonde	0.5	0.2	2.0

Table 5.1.: Accuracy of meteorological ground and radiosonde data according to Kruse (2001). The most precise meteorological ground stations are the six permanent stations PGF1 - PGF6 and the mobile station at MOKP.

The radiosondes consist of sensors for pressure, temperature and relative humidity. The radiosonde pressure is calibrated with accurate ground measurements directly before the launch. This procedure is very important to prevent large height errors of up to 800 m near the tropopause (Richner and Viatte, 1995). The calibration is given by:

$$p_{corr,sonde} = p_{mess,sonde} \cdot \frac{p_{0,ref}}{p_{0,sonde}} \tag{5.14}$$

where:

$p_{mess,sonde}$: pressure measurement of the radiosonde during launching

$p_{corr,sonde}$: corrected pressure measurement, applying the calibration

$p_{0,ref}$: pressure measurement of an accurate ground sonde

$p_{0,sonde}$: pressure measurement of the radiosonde on the ground at the same height than $p_{0,ref}$

Again, the calibration of the temperature and relative humidity sensors is given by the manufacturer. The accuracy of the radiosonde data is given in Table 5.1. The height difference between two measurement points is calculated applying the hydrostatic equation (Hann, 1901; Richner and Viatte, 1995):

$$\Delta H_{1,2} = -\frac{R}{g} \cdot T_v \cdot \int_{p_1}^{p_2} \frac{dp}{p} = \frac{R}{g} \cdot T_v \cdot \ln \frac{p_1}{p_2} \tag{5.15}$$

where:

$$\begin{aligned} p, p_1, p_2 &: \text{ pressure (general, at level } H_1\text{, at level } H_2) \\ \Delta H_{1,2} &: \text{ height difference of pressure level 1 and 2} \\ R &: \text{ universal gas constant of the air} \\ g &: \text{ acceleration due to earth's gravity} \\ T_v &: \text{ absolute virtual temperature} \end{aligned}$$

Inserting numerical values for the universal gas constant of the air R and the acceleration due to earth's gravity g and assuming further a water vapor pressure of $\sim$10 mbar, it follows (Chaperon and Elmiger, 1995):

$$\Delta H = 29.4mK^{-1} \cdot T_v \cdot \ln \frac{p_1}{p_2} \tag{5.16}$$

The radiosonde data is converted to wet refractivity applying the formula of Essen and Froome (1951). The resulting refractivity profiles can directly be compared to the solutions obtained with GPS tomography.

To evaluate the consistency of the meteorological measurements, the software package COMEDIE is used to process a 4-dimensional collocation of all meteorological measurements and to interpolate the wet refractivity. Figure 5.8 shows two representative refractivity plots of ground meteorological stations, interpolated with COMEDIE up to 2000 m and compared with the refractivity achieved from the radiosonde launchings. The refractivity comparisons of the other radiosonde launches are similar. It is evident that the ground meteorological measurements do not match the radiosonde data very well. This is most likely due to the small number of ground meteorological stations in this active atmospherically area. Nevertheless, the meteorological data is used to decompose GPS estimated path delays into its dry and wet parts.

5.5.3. GPS Data Processing

The GPS measurements are processed using the Bernese Processing Engine Version 4.2 (Beutler et al., 2001). Data sets of the permanent stations are available for the whole campaign period, whereas the campaign stations have recorded data only partially. In order to achieve better results and to embed the local network into a global system, seven IGS stations are used (Figure 5.9). They are introduced into the adjustment system with weak a priori constraints on the coordinate of 5 mm in each dimension. Thus, the high inner precision is kept. The coordinates of the campaign stations are treated unconstrained. The processing is done applying the reference system ITRF97. The use of post-processed precise orbits from the IGS allows a high accuracy.

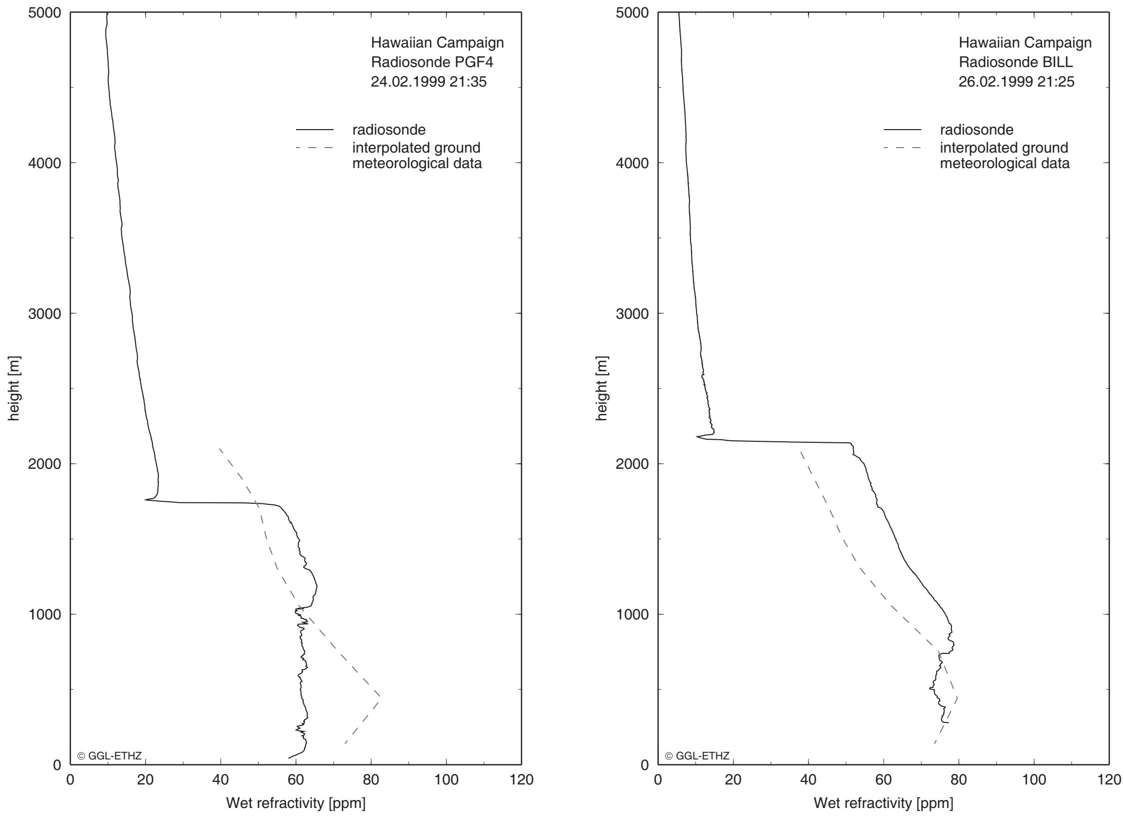

Figure 5.8.: Comparison of wet refractivity profiles. Ground meteorological measurements are collocated and interpolated up to around 2000 m. They are compared with the refractivity profile obtained from radiosonde launchings. Evidently, the two results do not agree very well. Trade wind inversions appears at 1750 and 2150 m height. The dry and warm trade wind causes a rapid decrease of the humidity and consequently the wet refractivity.

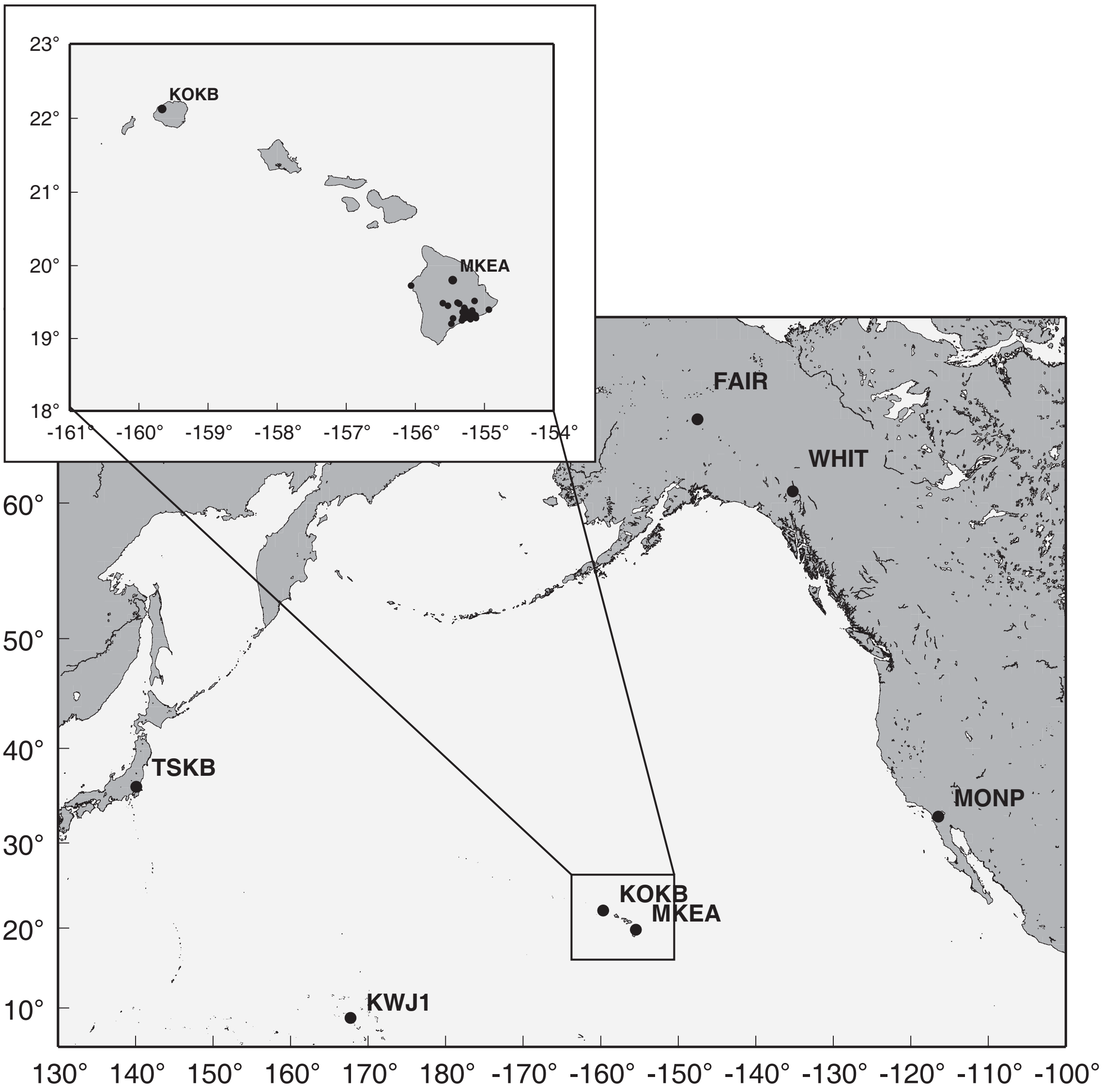

Figure 5.9.: IGS stations used in the GPS processing. The inset shows the Hawaiian Islands including the two respective IGS stations. The small black dots illustrate the locations of the GPS stations in the campaign area.

The baselines are constructed according to the strategy *OBS-MAX* (Beutler et al., 2001). If N receivers are used simultaneously, $N-1$ independent baselines can be formed. Using the strategy *OBS-MAX* means that the baselines are selected yielding the maximum number of observations. Particularly for campaign stations, the chosen strategy has the advantage, that the best baseline configuration is taken at each time and the influence of only partially working stations is kept to a minimum. The baseline length ranges from 5 to 100 km for campaign stations and up to 4000 km from campaign to IGS stations.

In the first step of the Bernese GPS processing, a code solution is calculated to get receiver clock corrections. Following, the baselines are built and a cycle-slip screening is performed. The adjustment is calculating double-difference phase solutions. The ambiguities are solved using the quasi ionospheric-free (QIF) ambiguity resolution strategy. The station coordinates are calculated along with the zenith path delays. Latter are estimated with the Niell dry mapping function (2.27). The resulting station coordinates of each day are analyzed. No significant coordinate differences are present. Therefore, in a last run, station coordinates of one day are introduced fixed and zenith path delays are determined again. This procedure prevents that imprecisely estimated station coordinates could affect the tropospheric path delays. However, no significant differences between the two solutions could be detected. Table 5.2 gives an overview of the achieved processing performance.

The result of the GPS treatment is used for the tomographic processing. Zenith delays are used as tomographic input data and also to reconstruct double-differences in combination with the double-difference residuals and the information of how the double-differences are built. For 95% of the zenith delays, a formal precision of better than 2 mm is achieved. The remaining 5% are detected as outliers and are eliminated.

5.5.4. Wet Path Delay Comparisons

Due to the different independent measurement sensors, it is possible to compare several determinations of zenith wet path delays:

1. *GPS-estimated path delays*: GPS-estimated total path delays obtained from the GPS processing, after removing the corresponding dry delays obtained by (2.32). The ground pressure and water vapor pressure are obtained from the meteorological measurement at the GPS station, or if no measurement sensor is available, from the COMEDIE interpolation.

2. *Radiosonde launchings*: The zenith wet path delays of the 38 radiosonde launches are calculated using the formula of Essen and Froome (1951) (2.11).

3. *Saastamoinen wet delays*: The wet path delays are calculated with (2.33). The pressure, temperature and water vapor pressure are available from the meteorological measurement at the GPS station or interpolated by COMEDIE.

DOY 1999	ambiguity resolution [%]	rms of the solution [mm]
41	*75.0*	1.5
42	68.8	1.3
43	62.5	1.4
44	65.5	1.3
45	62.3	1.5
46	68.1	1.3
47	66.0	1.2
48	63.8	1.2
49	61.8	1.2
50	61.7	1.3
51	59.9	1.5
52	64.3	1.3
53	62.6	*1.6*
54	*57.5*	1.5
55	68.9	1.2
56	74.1	1.2
57	70.6	1.2
58	72.6	*1.1*
59	72.3	*1.1*
mean	**66.2**	**1.3**

Table 5.2.: Performance of the Hawaiian GPS processing: Ambiguity resolution and rms of the solution. The rms corresponds to the a posteriori standard deviation of the unit weight (standard deviation of one-way L1 phase observable at zenith). The percentage of resolved ambiguities is acceptable considering that a quasi ionospheric-free strategy was chosen in combination with long baselines. The rms of the solution shows an overall good agreement. (Minimum and maximum values are italicized.)

4. *COMEDIE wet solutions*: The wet path delay is determined with the COMEDIE software package (Chapter 3).

5. *COMEDIE solution without radiosondes*: This solution is equivalent to the *COMEDIE wet solution* with the exception that no radiosonde observations are introduced for the collocation.

Figure 5.10, 5.11 and 5.12 show the zenith wet delay at the stations BILL, PGF4 and UWEV. The comparison of the path delay on UWEV is completed with radiosonde data of the nearby station VOLC. In the first part of the evaluated time range in Figure 5.10-5.12, the weather was rainy and windy. The remaining days were sunny and calm. The wet refractivity is thus smaller than in the first days.

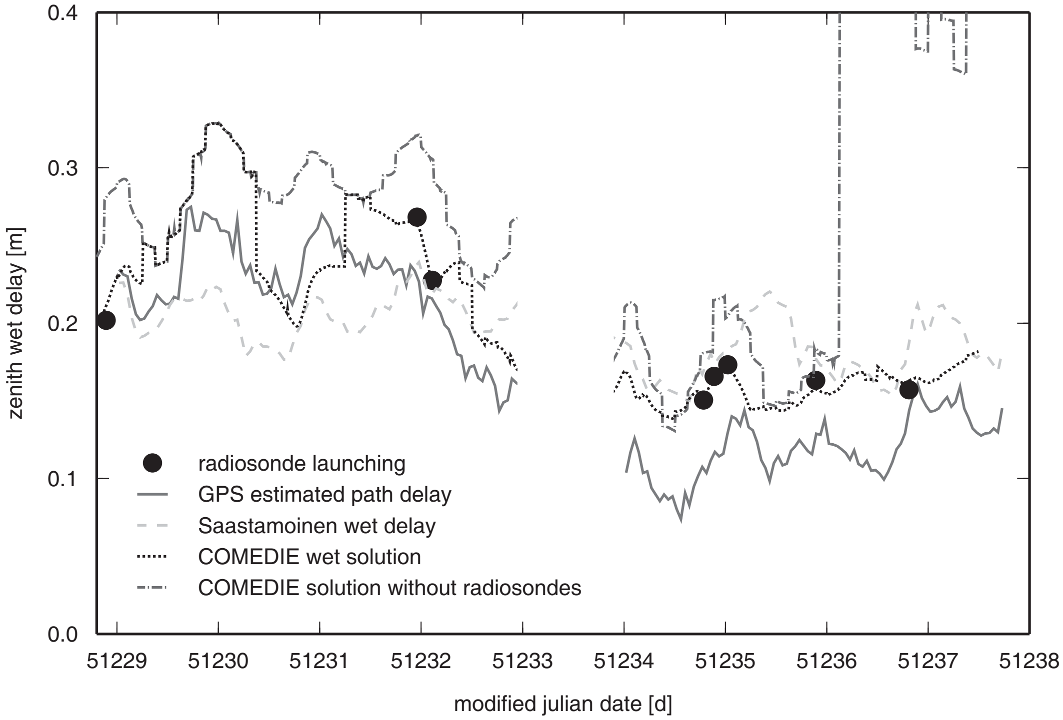

Figure 5.10.: Zenith wet delays at station BILL. The radiosonde solution fits the COMEDIE solution accurately. The COMEDIE solution without radiosondes generally over-estimates the wet delay. In the first part of the campaign, the GPS-estimated path delay as well as the Saastamoinen solution are at the same level as COMEDIE. In the second part of the time series, the GPS-estimated path delays has generally a lower and the Saastamoinen solution a higher wet delay than the other solutions.

The GPS-estimated wet path delay fits the radiosonde solution fairly accurately. The difference can be explained by the accuracy of the meteorological measurements and their interpolation. The COMEDIE solution fits the radio soundings perfectly because the latter data is integrated in this solution. The radiosonde data has even a strong influence on the whole network. The radiosonde on station VOLC on day

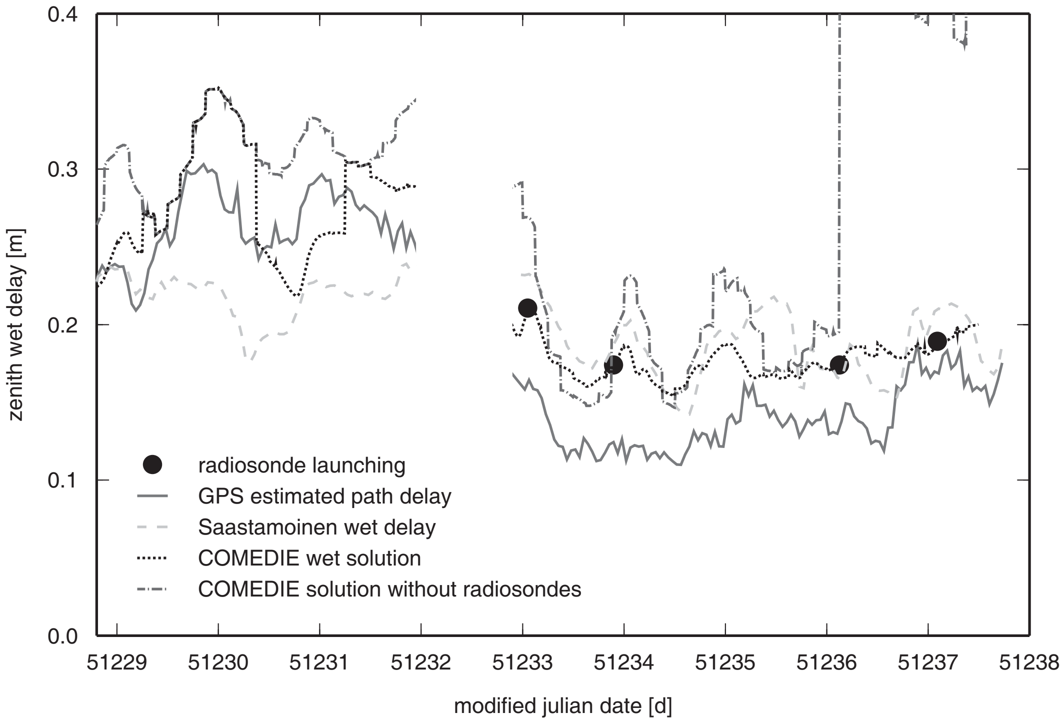

Figure 5.11.: Zenith wet delays at station PGF4. The time series show a similar behavior than on station BILL (Figure 5.10). However, the variation of the GPS estimated wet delay is smaller on this station.

51230 in the evening affects the COMEDIE solution on all stations. Between the radiosonde launches, specially on day 51230, the COMEDIE solution approaches the solution without radiosondes. The COMEDIE solution without radiosondes has generally an over-estimated wet delay. In the last two days, the only two meteorological stations higher than 1000 m were not operating any more. Because of the missing data in the higher area, strong outliers of the COMEDIE solution without radiosondes are resulting.

The Saastamoinen solution is calculated with the ground meteorological data only. The change of the weather cannot be reconstructed accurately by this solution. Usually, the wet delay is underestimated in a wet climate and overestimates in a dry climate.

In Table 5.3, a statistical comparison of the different kinds of path delays is given. The comparison is calculated with respect to the GPS-estimated solution and to the discrete radiosonde observations. The rms of around 4 cm between GPS-estimated path delays and the radiosonde solution shows that the best possible accuracy could not be reached. In others similar comparisons a rms of about 1-2 cm was achieved (see e.g. Chapter 6). Even though the GPS processing showed deficiencies which caused a worse GPS-estimated solution, the largest part of the discrepancies is assumably due to the quality of the meteorological measurements. The analysis showed that some of the ground meteorological sensors as well as the radiosondes do not

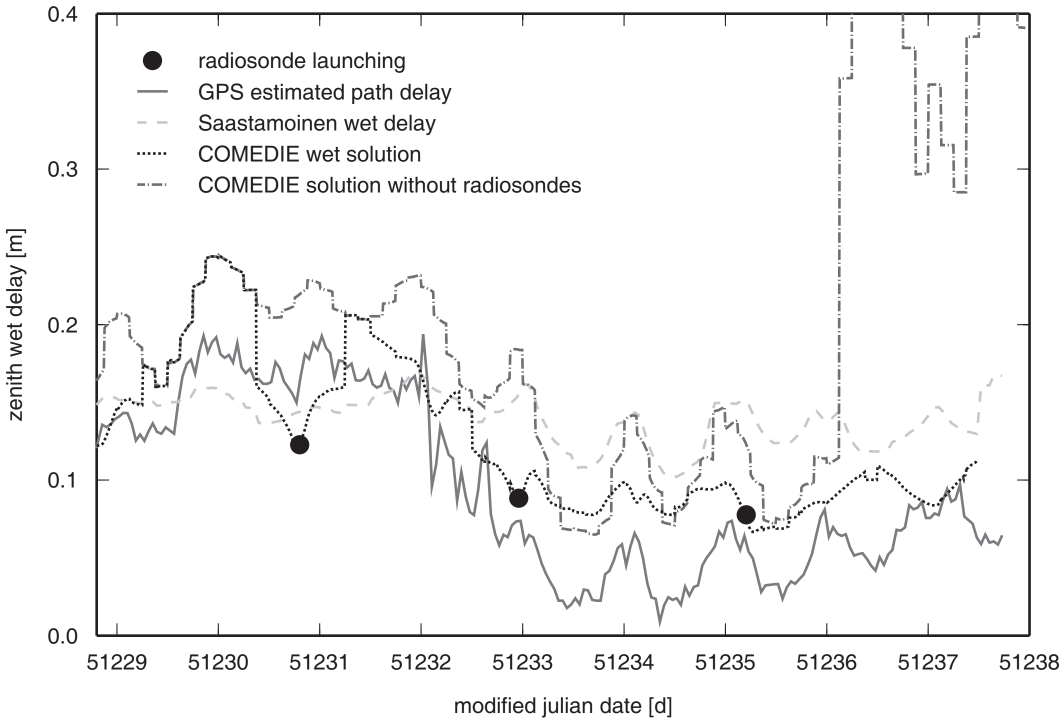

Figure 5.12.: Zenith wet delays at station UWEV. The radiosonde solution stems from the nearby station VOLC. As this station is higher than BILL and PGF4, the total amount of wet delay is smaller. The behavior and variation indeed, is similar.

provide the highest accuracy. The largest deficiency is probably the fact, that the meteorological network, especially in the last days of the campaign, is too weak to achieve an accurate refractivity distribution using COMEDIE.

5.6. Tomographic Simulations

The feasibility of the tomographic technique using AWATOS is first tested by simulations. These are based on the actual geometry of the Hawaiian network, using synthetically generated atmospheric conditions. The actual satellite constellation over a time span of 1 hour is used to derive synthetic double-differences applying several refractivity fields. The double-differences are used as main input to AWATOS.

The atmosphere over a central area of 30 x 30 km^2 at the Kilauea National Park has been subdivided into 16 layers spreading from 0 to 15'000 m in height. Each layer consists of 3 x 3 core voxels of around 10 km side length plus 16 outer voxels, which horizontally extend to infinity (Figure 5.13 and 5.14).

The resulting number of traversing rays per voxel is plotted in Figure 5.15. It is defined by the geometrical distribution of the ground stations and the visible satellites during the time span of one hour. This corresponds to the real conditions that oc-

Comparisons...	...with respect to GPS ZWD				...w.r.t. discrete radios. obs.			
	offset [m]	rms [m]	Std.dev. [m]	# obs.	offset [m]	rms [m]	Std.dev. [m]	# obs.
Station BILL								
GPS					-0.037	0.039	0.012	6
Saastamoinen	-0.013	0.051	0.050	146	-0.001	0.016	0.016	6
COMEDIE	-0.030	0.039	0.025	146	0.002	0.005	0.004	6
COMEDIE without radio-sonde data	-0.060	0.064	0.020	146	-0.044	0.048	0.019	6
Station PGF4								
GPS					0.047	0.047	0.002	3
Saastamoinen	-0.006	0.053	0.053	171	-0.009	0.015	0.012	3
COMEDIE	-0.029	0.040	0.028	171	0.001	0.001	0.000	3
COMEDIE without radio-sonde data	-0.055	0.062	0.030	171	-0.033	0.037	0.018	3
Station UWEV								
GPS					-0.005	0.028	0.028	3
Saastamoinen	-0.039	0.061	0.047	195	-0.055	0.059	0.024	3
COMEDIE	-0.029	0.039	0.026	195	-0.000	0.001	0.001	3
COMEDIE without radio-sonde data	-0.058	0.063	0.022	195	-0.080	0.083	0.023	3

Table 5.3.: Statistical comparison of the different methods of path delay determination. The statistical parameters are calculated with respect to the GPS-estimated solution and, additionally, with respect to the discrete radiosonde observations. The GPS-estimated path delays fit to the meteorologically determined path delays with an accuracy of around 3 cm. The rms of the Saastamoinen solution is usually higher.

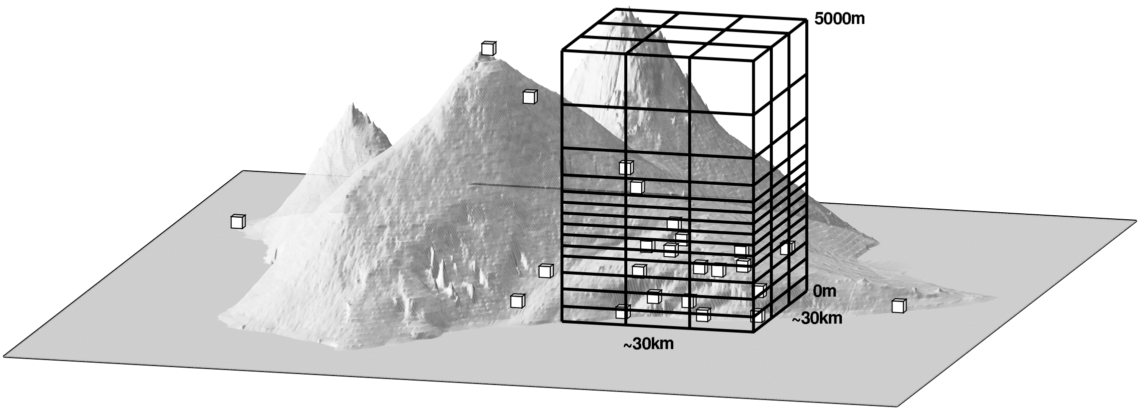

Figure 5.13.: Core of tomographic voxel model for the Hawaiian campaign. The model consists of 16 layers of 3 times 3 core voxels, plus 16 outer voxels per layer, which horizontally extend to infinity. The highest layer from 5'000 m up to 15'000 m is not shown on the figure. White boxes show the location of the GPS stations.

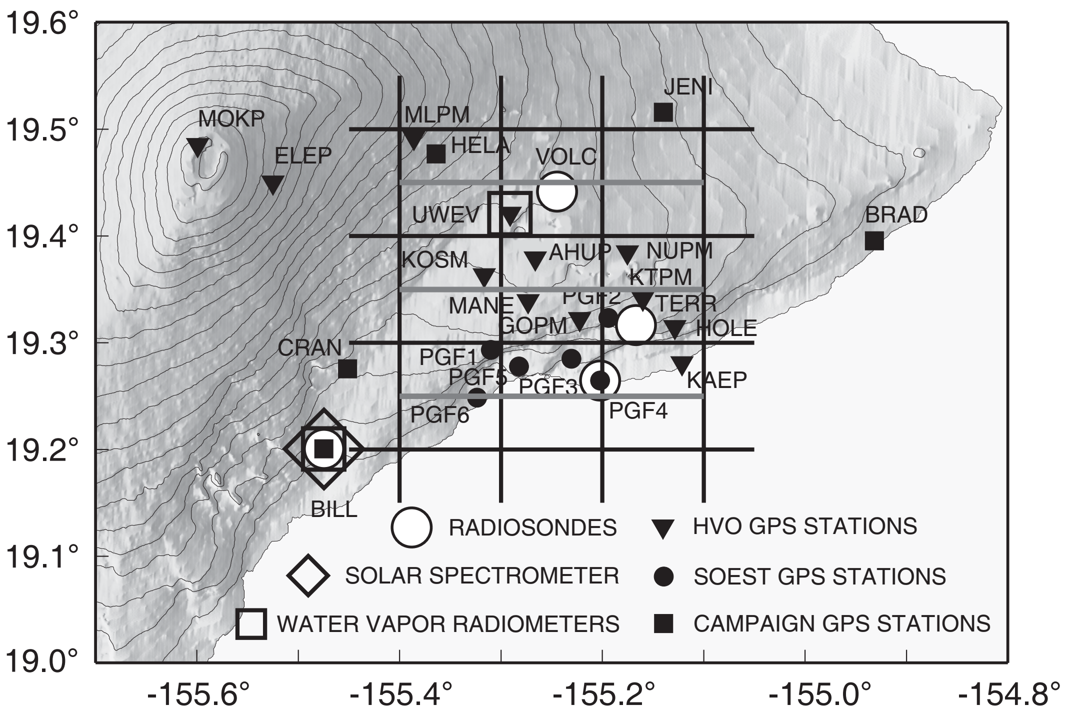

Figure 5.14.: Plan view of the campaign area on the Big Island of Hawaii. The voxel model is plotted in black. In the subsequent investigations, often three cross sections are used with constant latitude of 19.25°, 19.35° and 19.45°. These are indicated in gray.

curred on February 22, 1999, 22:35h until 23:35h. Synthetic atmospheric conditions are generated. Several simulation models are chosen to analyze the performance of the tomographic method. The first simulation model is composed of a consistently decreasing wet refractivity, following an exponential function. The layers are equally inclined with a refractivity decrease from south-east to north-west of 24 ppm (Figure 5.16).

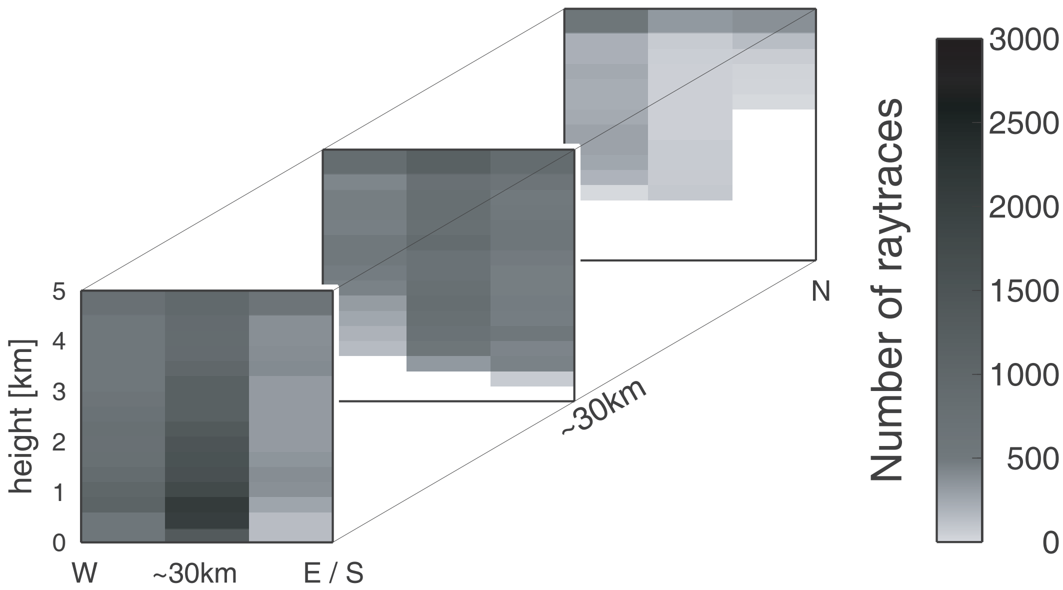

Figure 5.15.: Distribution of the number of ray traces through the core voxels. White voxels indicate areas without any ray traces. These are usually subterranean areas or voxels which are not covered by the GPS station distribution. A consistent coverage of rays in the two more southern located cross sections is clearly seen, compared to the northern cross section with only few ray traces.

Figure 5.17 shows slices of the tomographic evaluation at latitude 19.35^0. The evaluation using a singular value decomposition without any noise on the double-differences (Figure 5.17 b and c) indicates the proper working of the software package. The double-difference residuals are introduced without any other informations. Therefore a partially under-determined equation system results and a single value decomposition is necessary to achieve a result. This fact demonstrates the feasibility of the tomographic method.

In Figure 5.17 d) and e), a covariance function without any noise is applied to derive the tomographic solution. The constraints are only used to achieve a well-determined equation system. They are down-weighted by a factor of $100'000^2$ (regularization factor $= 100'000^{-2}$) compared to the simulated observations. The comparison of the model with the tomographic solution is even more accurate than the solution applying a singular value decomposition. However, both analyses prove the proper

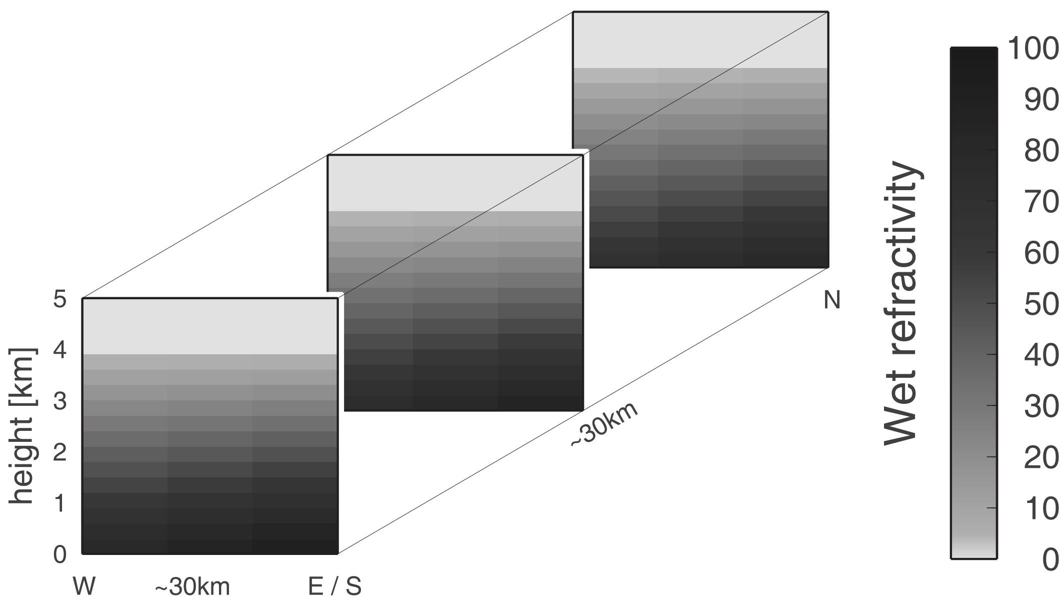

Figure 5.16.: Cross sections through the core voxels of the synthetically generated atmospheric model with inclined layers from SE to NW. The inclination angle is decreasing with increasing layer height.

calculation with the tomographic method. Admittedly, the observations are introduced error free here.

To simulate real conditions, a stochastic noise of 3 mm (Gaussian distributed) is added to the synthetic double-differences. A sample of the tomographic analysis using a singular value decomposition is shown in Figure 5.17 f) and g), and, using a covariance function in Figure 5.17 h) and i). Using a singular value decomposition, the noise level in combination with the partially under-determined equation system makes it impossible to achieve an accurate result. The differences between the tomographic solution and the model exceed several times 20 ppm. Therefore, it has been shown, that the singular value decomposition is a reliable method to solve a partially under-determined equation system only if the observations are error-free. The solution with a covariance function indeed, still produces an accurate result (Figure 5.17 h and i). However, it is necessary to adjust the regularization factor. The constraints are down-weighted in this example by a factor 1000^2. It can be concluded, that the optimized regularization factor depends mainly on the noise level. Increasing the noise level to 5 mm, the optimal regularization factor decreases to 200^{-2}. An example of this analysis is shown in Figure 5.17 j) and k). By optimizing the weighting of the constraints, again an accurate result can be achieved.

However, the possibilities of optimizing the weighting of the constraints are limited. This means, that the noise on the double-differences should be as small as possible. An accurate GPS treatment is a fundamental requirement to get reliable results with

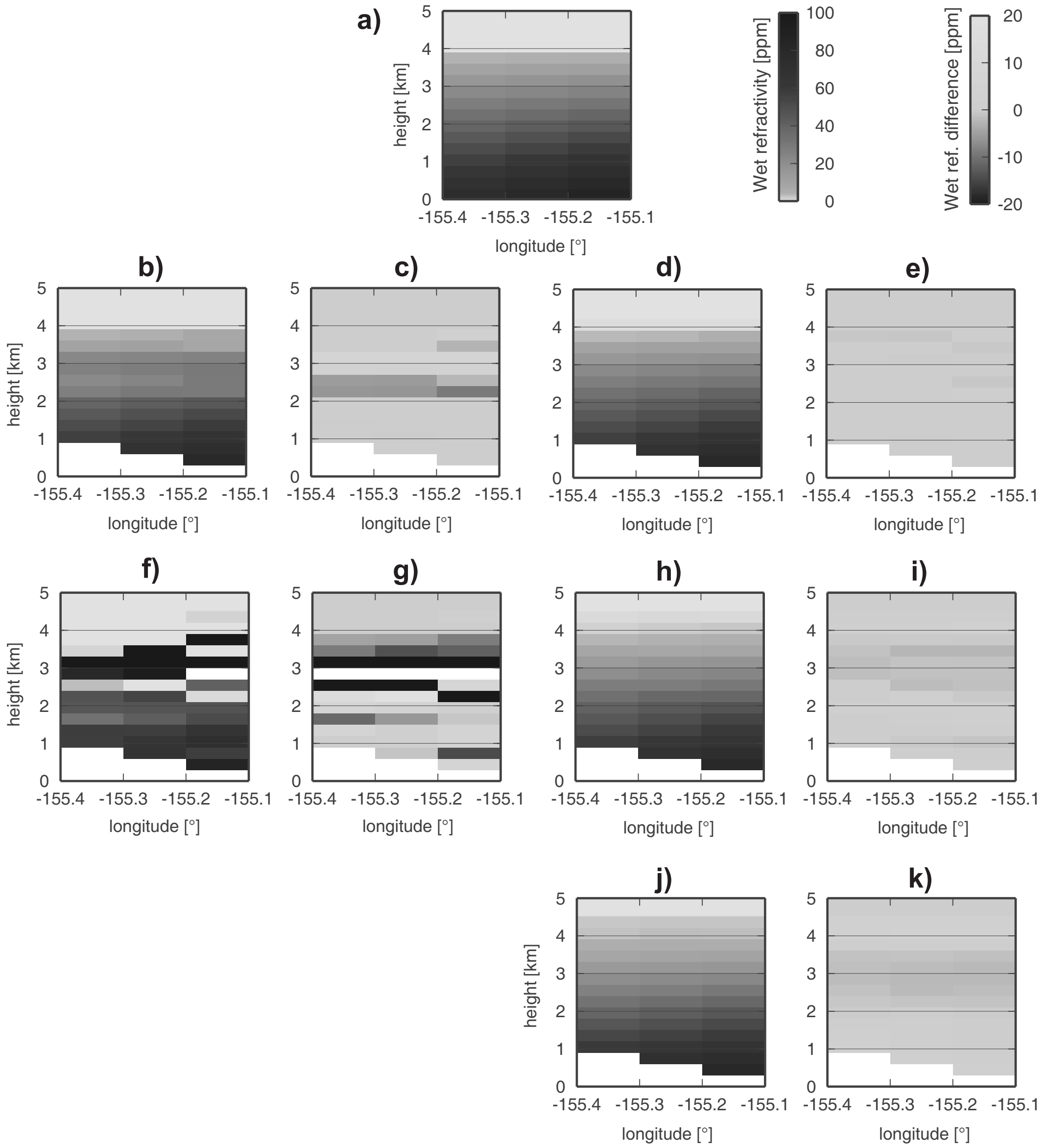

Figure 5.17.: Simulation with a synthetically generated inclined atmosphere. The figure shows cross sections at latitude 19.35°: The synthetically generated atmospheric model (a), the tomographic solution using a singular value decomposition with a noise of 0 mm (b) and 3 mm (f) on the double-difference observations and the differences between the model and the solution (c and g). The tomographic solution using a covariance function with a noise of 0 mm (d), 3 mm (h) and 5 mm (j) on the double-difference observations and its differences to the model (e, i and k). White voxels on the bottom indicate areas without any ray traces. These are usually areas below ground. Black and white voxels in the plots indicate values exceeding the range of the scale bar. The solutions applying a singular value decomposition show larger differences with an increasing noise whereas the application of the covariance function shows an overall good agreement independent of the noise level.

the tomographic method. According to experience, the noise level is smaller than 5 mm. This allows us to use the method as described above.

To check the sensitivity of the algorithm, an outlier is inserted in the synthetic model at latitude 19.45°, longitude -155.35° and height 2300 m. The true refractivity value of 30 ppm is replaced with the outlier value of 90 ppm. Figure 5.18 shows some results of this study. The analyses without noise show, that the model can be reproduced. This is illustrated in subfigures b) and c) using the singular value decomposition and in subfigures d) and e) using a covariance function. Differences are mainly seen when the singular value decomposition is used. The outlier causes a lack of refractivity in the whole layer. Furthermore, the thus missing refractivity is added to the layer at 3100 m height. The use of the covariance function strengthens the whole equation system and allows a better reproduction of the atmospheric model. The regularization factor is set again to $100'000^{-2}$. Adding noise requires an optimization of the regularization factor. In Figure 5.18 f) and g), a noise level of 5 mm is used and requires therefore to increase the factor to 200^{-2}. As a disadvantage, the increase of the factor enforces the smoothing effect between neighborhood voxels. Figure 5.18 f) and g) demonstrate that the outlier has been smoothed out completely. The missing amount of refractivity is allocated primarily to the voxels in the same column and secondarily to the voxel layers at 3800 - 4600 m height.

Often, the real atmospheric distribution of refractivity is not consistently decreasing as assumed in the recent examples. Rapid refractivity changes with height and even atmospheric inversions occur. Figure 5.19 illustrates a simulation applying an atmospheric model with a rapid refractivity change at a height of 2200 m. Both, the solution using singular value decomposition (subfigure c and d) as well as the solution applying a covariance function (subfigure e and f) are not able to reproduce the simulated refractivity field. The solutions detect a rapid decreasing of the wet refractivity but expect it already at a height of 1000 m. The same effect appears if a noise level of 5 mm is used together with a covariance function (subfigure g and h).

In an additional analysis, an atmospheric inversion model was chosen (Figure 5.20). The inversion was set to a height of 3000 m (subfigure a and b). All presented solutions are almost equal; the one using a singular value decomposition (subfigure c and d), the one applying a covariance function (subfigure e and f), and even the solution using a noise level of 5 mm (subfigure g) and h)). The atmospheric inversion cannot be reproduced. Compared to the simulation with rapid changes, this simulation shows even larger errors. Concluding, the above simulations clearly show, that the resolution of rapid changes and inversions in the atmosphere is usually not possible if only GPS data are used. GPS is sensitive to the integrated amount of water vapor. The height distribution is only given by the covariances and tomographic models. Usually, additional information is necessary. Such possibilities are discussed in the following sections.

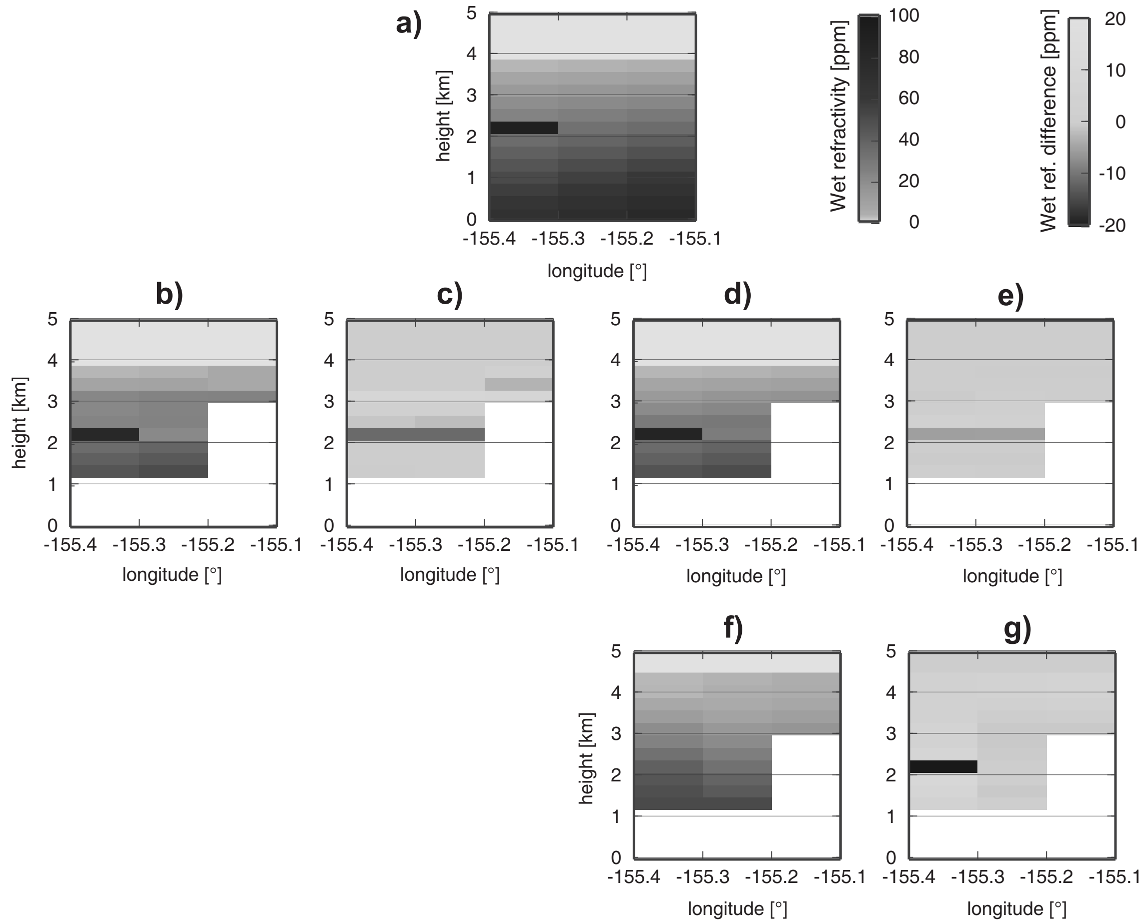

Figure 5.18.: Simulation with an outlier voxel of 90 ppm instead of 30 ppm at the height of 2300 m. Cross sections at latitude 19.45° are displayed: Synthetic atmospheric model with an outlier (a), tomographic solution (b) and difference (c) to the model applying a singular value decomposition with a noise of 0 mm on the double-differences. The tomographic solution and difference to the model applying a covariance function are displayed with a noise of 0 mm (d and e) and 5 mm (f and g) on the double-differences. White voxels on the bottom indicate areas without any ray traces. These are usually areas below ground. The black voxel on the plot of the wet refractivity differences indicates a value falling below the range of the scale bar. The solution applying a singular value decomposition reproduces the outlier relatively accurately. A value of 79.6 ppm is achieved for this voxel. A similar result is obtained with a covariance function and a noise level of 0 mm (85.5 ppm). If a noise level of 5 mm is introduced, the refractivity value of the outlier voxel decreases to 41.0 ppm.

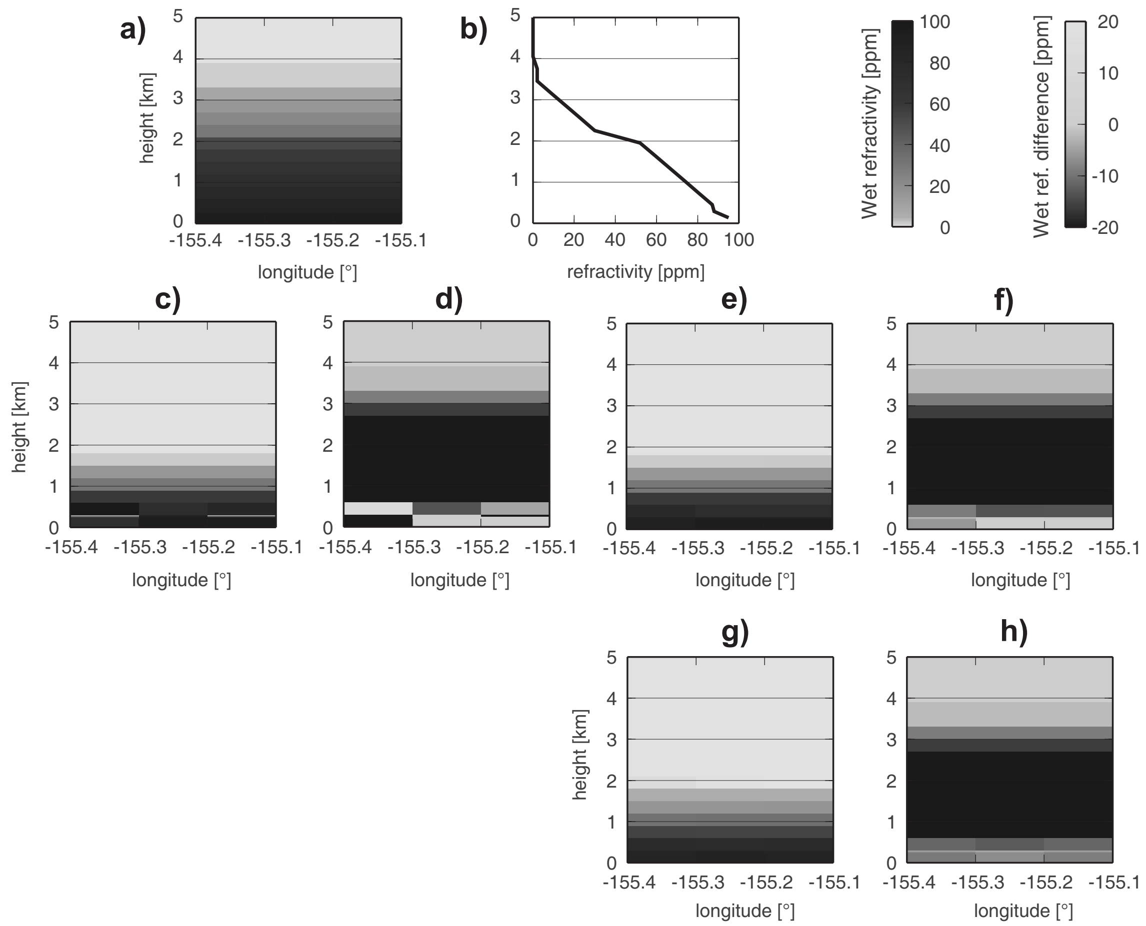

Figure 5.19.: Simulation of a rapid change in refractivity at the height of 2300 m. Cross sections at latitude 19.25° are displayed: Synthetic atmospheric model (a), profile of the synthetic atmospheric model (b), tomographic solution (c) and difference (d) to the model applying a singular value decomposition with a noise of 0 mm on the double-differences. The tomographic solution and difference to the model applying a covariance function are displayed with a noise of 0 mm (e and f) and 5 mm (g and h) on the double-differences. Black voxels on the plots of the wet refractivity differences indicate values falling below the range of the scale bar. Neither solution can account for the rapid refractivity change. However, using a covariance function, an increase of the noise on the double-differences does not affect the accuracy of the solution substantially. Applying a singular value decomposition, already the solution without noise is less accurate than the solutions using a covariance function.

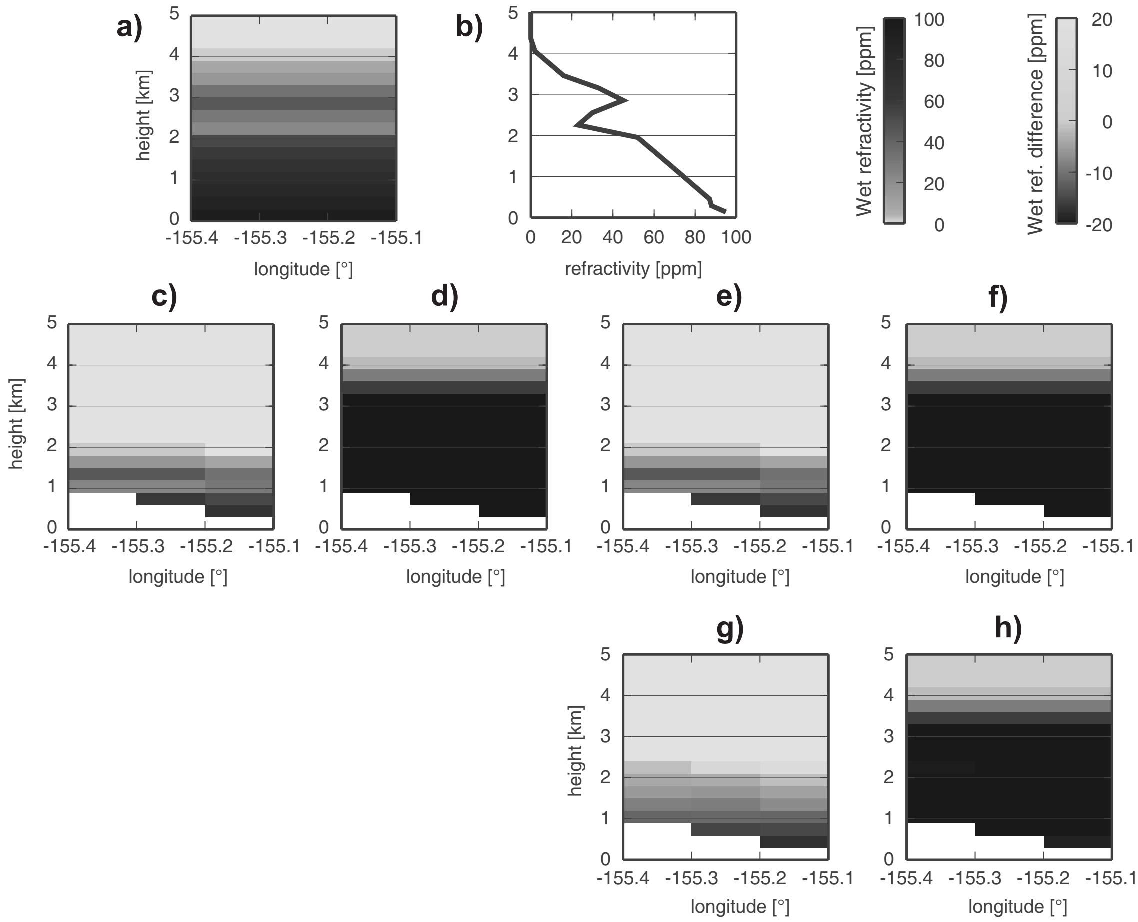

Figure 5.20.: Simulation with an atmospheric inversion at the height of 3000 m. Cross sections at latitude 19.35° are displayed: Synthetic atmospheric model (a), profile of the atmospheric inversion (b), tomographic solution (c) and difference (d) to the model applying a singular value decomposition with a noise of 0 mm on the double-differences. The tomographic solution and difference to the model applying a covariance function are displayed with a noise of 0 mm (e and f) and 5 mm (g and h) on the double-differences. White voxels indicate areas without any ray traces. These are usually areas below ground. Black voxels on the plots of the wet refractivity differences indicate values falling below the range of the scale bar. Neither solution can account for the atmospheric inversion. The three solutions are equally bad. In contrast to a rapid change in refractivity (Figure 5.19), in this simulation of an inversion, a larger number of layers cannot correctly be recovered.

5.7. Real Data Analysis

To analyze the overall performance of GPS tomography, real data analyses are presented. The Bernese Processing Software (Beutler et al., 2001) was used to determine double-difference wet path delays. One hour of observations was assimilated for the tomographic inversion. The refractivity of neighboring voxels was constrained using the same correlation function as in the simulations. The constraints were down-weighted by a factor of 60^2 compared to the observations. This value has been optimized for the given data set by comparing retrieved profiles with local balloon soundings. Additionally, the wet refractivity of the voxels in the uppermost layer was set to zero.

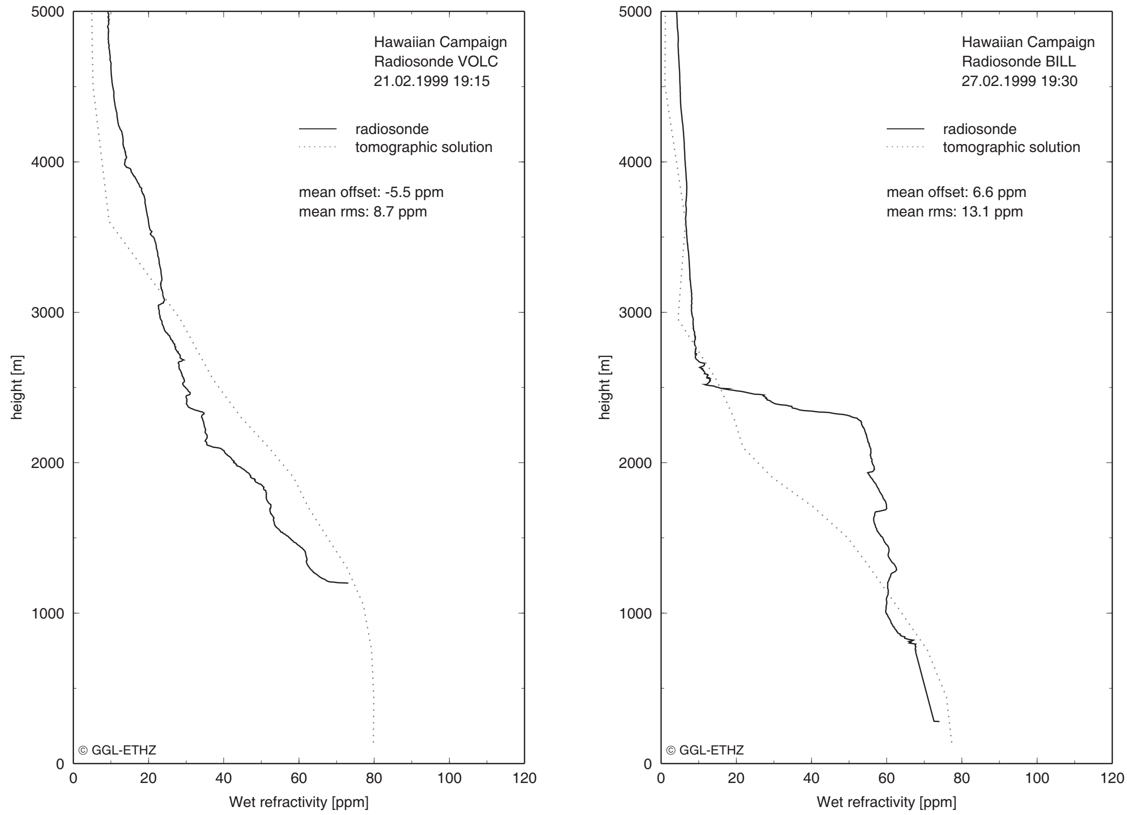

Figure 5.21.: Comparison of tomographic solutions using real GPS data with radiosondes. The figure on the left panel fits the regular refractivity field above the station Volcano Village quit satisfactorily. The rapid change of refractivity on the right panel at 2500 m height at station BILL is not detected.

The resulting solutions are compared with the respective radiosonde profiles (Figure 5.21). In order to obtain realistic measures for the error of the solution, rms values from comparisons with radiosonde data have been calculated and are given in Figure 5.21. The radiosonde profile at station VOLC (left subfigure) is a nearly consistently decreasing exponential function as used in the first simulations. The tomographic solution shows a good agreement. The statistical parameters mean offset and mean rms are satisfactory. The radiosonde profile at station BILL (right subfigure) shows a rapid refractivity change at the height of 2500 m. The tomographic solution is unable to reproduce this behavior because of the smoothing effect of the inter-voxel constraints. A detailed investigation of all 16 radiosonde profiles confirms this behavior. While consistently decreasing atmospheric conditions are reproduced satisfactorily, the detection of rapid changes in height is critical.

To reduce the smoothing effect, the influence of inter-voxel constraints must be minimized in favor of real atmospheric a priori observations. Using COMEDIE, ground meteorological measurements are interpolated at each GPS station. This data is introduced as a priori information into the tomographic analysis. The information is down-weighted by a factor of 20^2 compared to the observations and up-weighted compared to the inter-voxel constraints by a factor of 3. Figure 5.22 shows two representative samples. In the case of a consistently decreasing refractivity profile (station VOLC, left subfigure), a priori meteorological ground measurements do not strongly affect the solution. In the case of a rapid change in the refractivity field (right subfigure), the improvement of the tomographic solution is very significant. The mean rms could nearly be reduced by a factor 2 in this case. This behavior is characteristic for all analyzed profiles. However, the fact, that ground meteorological measurements do not match radiosonde data very well (Section 5.5.2) leads us to the conclusion that the improvement of accuracy could be even better. All investigated refractivity profiles are shown in Appendix C. The tomographic solution without and with a priori ground measurements is displayed in each case in the same figure.

5.8. Discussion

A tomographic software package for the determination of the height resolution in the refractivity field based on double-difference GPS phase observations has been successfully developed. Introducing double-differences in contrast to slant delays reduces the number of observations. However, the advantage is, that the satellite and receiver clock errors are already eliminated in advance. Various simulations confirm the feasibility of this approach. They show good results also in the presence of white noise, provided additional constraints are introduced.

The analysis of real data of the Hawaiian campaign shows an overall good accuracy. However, due to the necessary inter-voxel constraints the model is unable to properly account for all irregularities. They are smoothed out. Meteorological a priori information improves the results significantly. Therewith, additional important information is provided and allows to down-weight ordinary inter-voxel constraints. Statistical comparisons to radiosonde profiles reveal an accuracy of around 10 ppm for the wet refractivity.

However, the special conditions on the Hawaiian Island have to be kept in mind. The distribution of stations from the sea level to a height of over 4000 m is exceptional

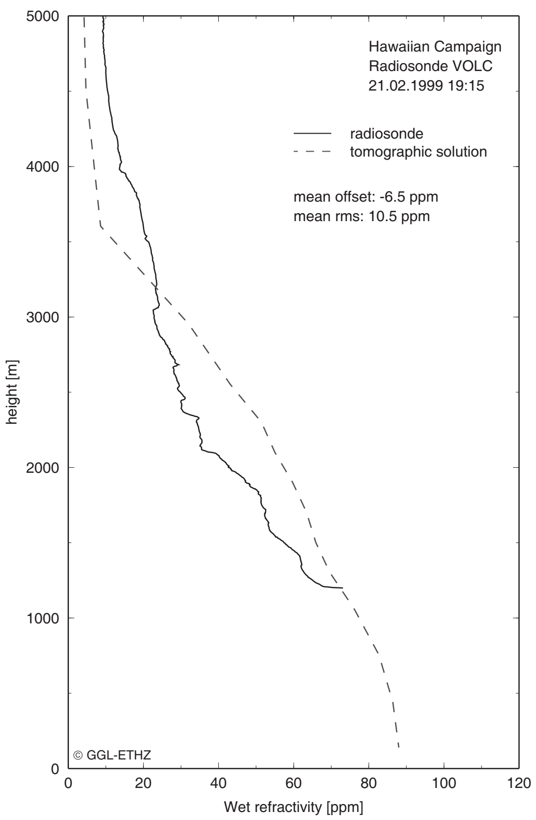

Figure 5.22.: Comparison of tomographic solutions using real GPS data with radiosondes. Compared to the analysis in Figure 5.21, ground meteorological data are introduced as a priori values in the tomographic processing. On the left panel, the regular refractivity field above the station VOLC can be reproduced accurately by the tomographic solution. Even the rapid change of refractivity on the right panel at 2500 m height at station BILL is detected by the tomographic solution.

and results in an excellent height distribution for testing methods of tomography. But the Hawaiian climatic and weather conditions induce most irregular humidity distribution and corresponding refractivity fields. Applying the tomographic method on other GPS networks allows to compare and verify the present conclusions. Such an investigation based on the AGNES network in Switzerland is presented in the following chapter.

Currently, water vapor measurements are mainly acquired with radiosondes. Due to the high costs, the spatial and temporal resolution of radiosonde launchings is relatively low. Using GPS tomography, a high temporal and spatial density of the water vapor is provided at low costs. Another promising approach represents the radio occultation measurements from low Earth orbiting satellites. During the occultation, GPS limb sounding measurements are obtained and vertical profiles of the atmospheric refractivity can be determined (Ware et al., 1996). However, accurate profiles can be achieved from 40 to about 5 km height. Currently, in the lower troposphere the GPS tomography is assumably the more accurate technique.

6. Comparisons of Refractivity Determination Methods

6.1. Introduction

This research study investigates several approaches to determine the refractivity in the atmosphere. In this section, the various methods are compared with each other using a dedicated set of data. The potential and limits of the methods are discussed. The analyses are separated in two parts:

- Integrated total zenith path delays
- 3D wet refractivity distribution in the troposphere and its temporal behavior

For the purpose of independent validation, several measurements, such as radiosondes as well as data of a numerical weather model are available.

6.2. Experiment Description

Switzerland has been chosen as area of investigation. This area is especially suited because of the dense GPS permanent network AGNES which is covering the entire Swiss territory. An automated near real-time processing is providing hourly means of zenith total delays. Furthermore, the height distribution of the GPS stations from 400 m to 3600 m is well-balanced. For further information on the AGNES network and its spatial distribution of the GPS stations we refer to Section 4.3.1.

In addition, pressure, temperature and humidity data from the automated meteorological network (ANETZ) are used (Section 3.3.2) as well as radiosonde data (Section 3.3.3).

As investigation period, the days 3-10 of November, 2002 have been chosen. Some rapid weather changes occurred during this period. After heavy rainfall in the morning of November 3, bright intervals interrupted the rainfall in the afternoon. During the next two days, wet air reached Switzerland continuously and caused further rainfall. Only the southern part of Switzerland was sunny. On November 6, continental dry air predominated and lead to a sunny day in the whole country. On the next day, wet air arrived and caused rainfall in the afternoon in the northern part of Switzerland. A belt of high pressure allowed sunshine on November 8 and in the morning of November 9. New rainfall appeared on the same afternoon (SFDRS, 2002).

In the investigations, the water vapor retrievals of COMEDIE, COITROPA and AWATOS are compared with each other. Additionally, GPS estimated path delays, data of radiosondes and a numerical weather model are used for the analyses.

6.3. The Alpine Model (aLMo) in Switzerland

The Alpine Model aLMo is the Swiss implementation of the non-hydrostatic local weather model called COSMO (Consortium of small scale modeling). The model is operational at MeteoSwiss since April 2001. It consists of 385x325 grid points with a horizontal grid spacing of around 7 km. 45 levels are used in the vertical. The prognostic variables are air pressure p, temperature T, cartesian wind components, specific humidity Q_v and liquid water content. Two 72 hours forecasts are calculated daily. However, for the investigations in this study, only the data of the assimilation cycles are used, which represent the best possible state of the atmosphere as viewed by aLMo. For a detailed description of the COSMO model and the Swiss aLMo implementation we refer to Doms and Schättler (2003).

The main idea using aLMo is to compare the tomographic solutions that will be described in Chapter 6.5. According to the choice of the tomographic voxel model and the time resolution, 8 x 5 meteorological profiles are available within a time interval of one hour. Considering the investigation time of one week, a total of 7680 profiles results. Each profile consists of 45 vertical layers with a resolution depending on the height extending from below 100 m (lower troposphere) to around 2000 m.

The aLMo variables have to be transformed to wet refractivity. Based on the coherence of path delay and precipitable water vapor (2.42), the following relation can be written (including (2.18) and (2.35)):

$$10^{-6} \cdot \int N_{wet} ds = \kappa' \cdot \int \rho_w ds \tag{6.1}$$

$$N_{wet} = \kappa' \cdot 10^6 \cdot \rho_w \tag{6.2}$$

The equation of state for ideal gas can be used to express the mass density of air ρ_a:

$$\rho_a = \frac{p}{R_a \cdot T_v} \tag{6.3}$$

where:

$$\begin{array}{rll} T_v = & T \cdot (1 + 0.378\frac{e}{p}) & : \text{virtual temperature} \\ R_a = & 287 Jkg^{-1}K^{-1} & : \text{specific gas constant for dry air} \\ e & & : \text{water vapor pressure} \end{array}$$

Introducing the specific humidity Q_v

$$Q_v = \frac{\rho_w}{\rho_a} \tag{6.4}$$

we finally get the refractivity N_{wet} as:

$$N_{wet} \quad = \quad \kappa' \cdot 10^6 \cdot Q_v \cdot \frac{p}{R_a \cdot T \cdot (1 + 0.378\frac{e}{p})} \tag{6.5}$$

Additionally, the dry refractivity is retrieved by aLMo using relation (2.19) and the total refractivity is calculated (2.17). Latter is then integrated along the zenith direction (2.18) to obtain the zenith total path delay Δ^{PD}. It is used as independent comparison of the other methods of zenith path delay determination (Chapter 6.4). As the comparisons are made at the AGNES stations, the aLMo solutions are interpolated using COITROPA.

6.4. Integrated Zenith Path Delay Comparisons

The determination of integrated zenith wet path delays is important on the one hand to correct the tropospheric error in GPS measurements and on the other hand to continuously monitor the variation of the total water vapor amount in the troposphere. In the following study, the GPS-estimated total path delays of the AGNES processing are taken as reference values. These are compared with:

- COITROPA solution: Interpolation of GPS-estimated total path delays of the AGNES stations (cross-correlation method).
- COMEDIE solution: Determination of path delays from meteorological measurements at ground stations (ANETZ) and radiosondes.
- Saastamoinen solution: Determination of path delays using the formula of Saastamoinen (1972) and the current meteorological ground measurements, interpolated with COMEDIE.
- aLMo solution: The vertical refractivity profiles of the numerical weather model are integrated and interpolated using COITROPA.

The comparison is done at the 30 AGNES stations (Figure 4.3). Time series of one week are compared and statistically evaluated.

A strong variation of the refractivity appears due to various weather changes during the investigation period. The end of a period with heavy rainfall on November 3 causes a decrease of the zenith total delay of 10 cm. The path delay was constant on the next two days due to continuous rainfall and wind which balanced the wet air. The sunny and dry day on November 6 leads to another distinct decrease of the path delay. Because of new continuous rainfall in the following days, the amount of water vapor is increasing again to the level prevailing on the previous days.

The comparison of all 30 AGNES stations during the investigated period shows an overall good agreement. For example, plots of the stations STGA, SANB and DAVO are given in Figures 6.1, 6.2 and 6.3. The excellent fit of the COITROPA solution with the AGNES data is clearly visible. The solution using the aLMo data, interpolated applying COITROPA, fits only marginally less accurately. Also the COMEDIE solution fits the AGNES data. However, COMEDIE is unable to reproduce short-time variations. Even the Saastamoinen solution shows an overall good agreement with AGNES. Though, large discrepancies are visible on November 3 and 9.

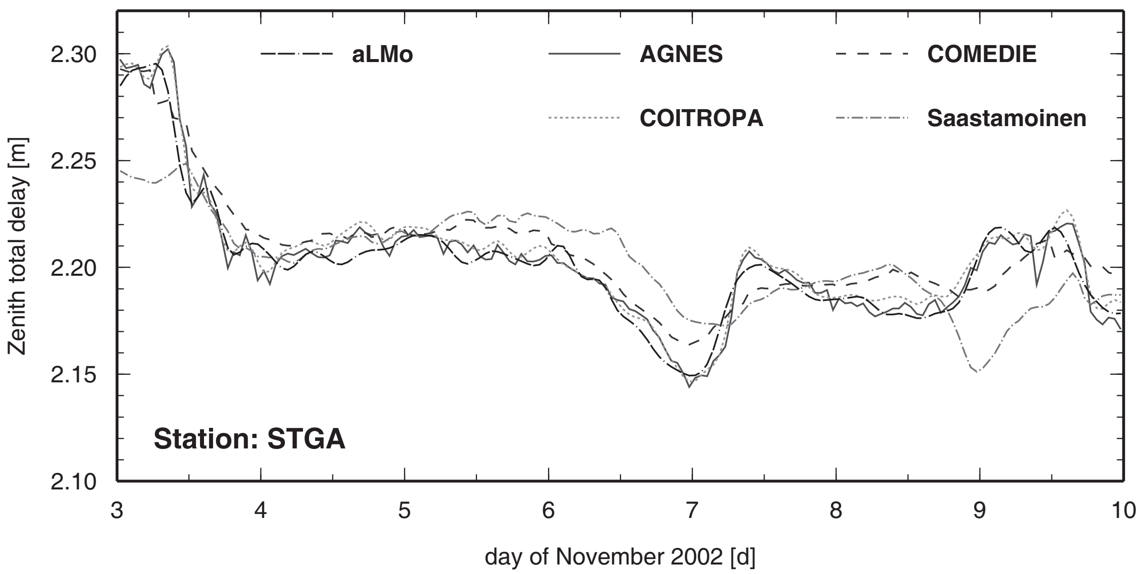

Figure 6.1.: Zenith total delays at AGNES station St. Gallen (STGA). The plot represents a typical situation for a station in the Swiss Mittelland. The best fit of the AGNES curve is obtained by the aLMo and the COITROPA solution, followed by the COMEDIE solution. The Saastamoinen solution displays the largest deviation.

A statistical evaluation with respect to the AGNES solution is provided in Table 6.1. The mean of the analysis of all 30 AGNES stations during one week is shown.

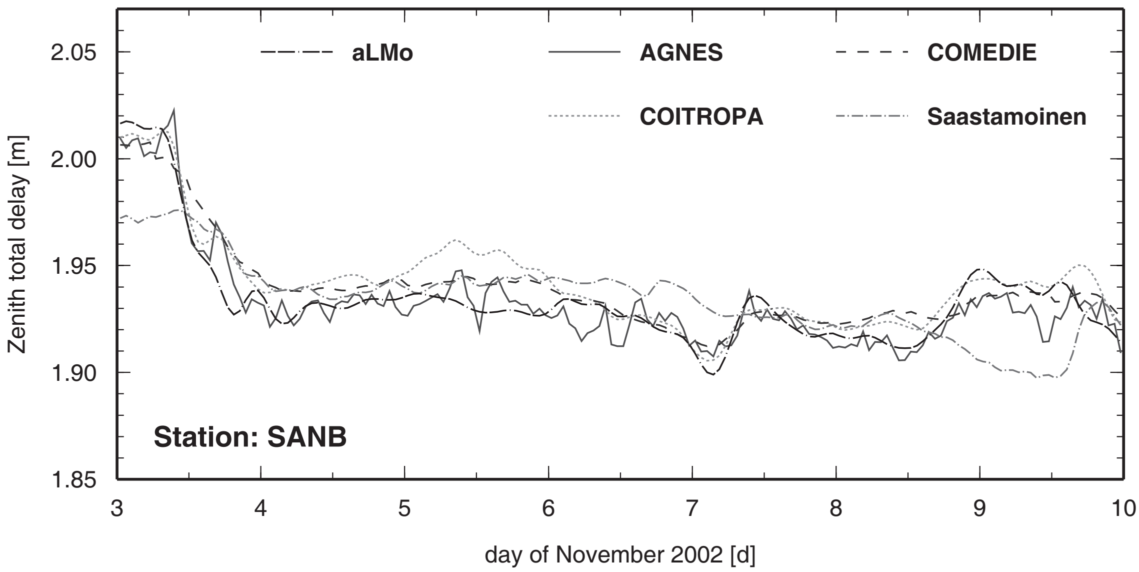

Figure 6.2.: Zenith total delays at AGNES station San Bernardino (SANB). The plot shows a situation, where the COMEDIE solution fits the AGNES solution better than the COITROPA solution. Nearby meteorological stations account for an accurate modeling of the atmospheric conditions with COMEDIE, whereas the COITROPA solution has to include mainly AGNES stations at locations with a different atmospheric behavior. This fact is confirmed considering the aLMo solution which is interpolated also with COITROPA but fits the AGNES solution even more accurately than the COMEDIE solution.

Figure 6.4 displays the rms values of the individual AGNES stations according to their station height.

In general, the COITROPA solution is the most accurate method followed by aLMo and COMEDIE. Saastamoinen shows the biggest rms values. However, considering the fact, that only ground meteorological measurements are used, this method is amazingly accurate. Due to the small mean offset of all four methods, the standard deviation σ does not differ much from the rms.

Figure 6.4 allows some detailed statements:

- A decrease of the rms with the station height can be seen in the case of the Saastamoinen solution. This effect correlates with the decrease of the integrated total path delay with height.
- The rms of the COMEDIE solution shows a small decrease with the station height as well. The rms in the Swiss Mittelland ranges between 10-20 mm and decreases to less than 10 mm in the Alpine area.

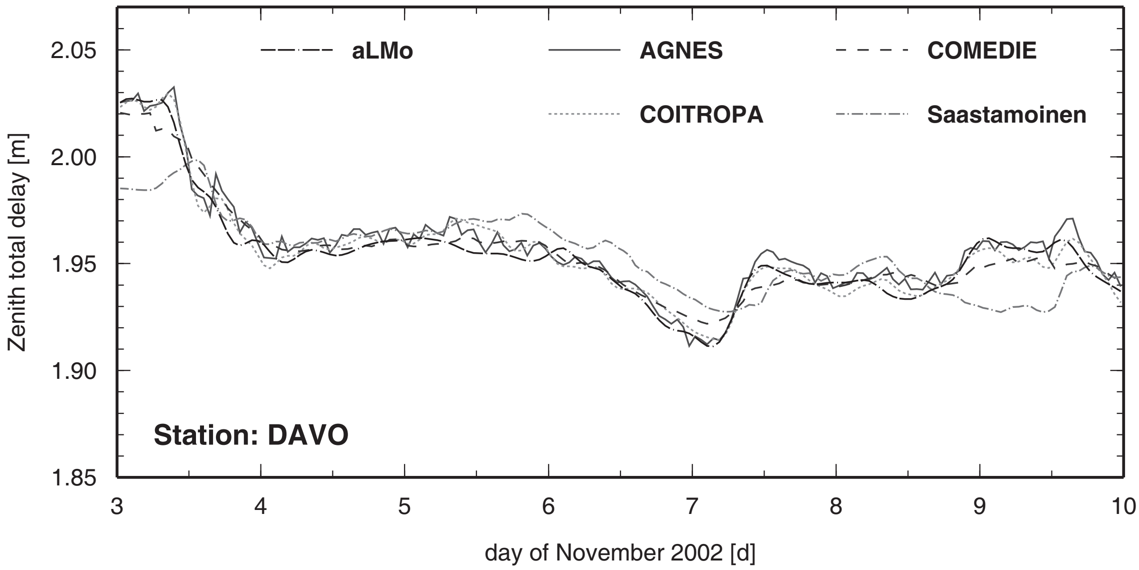

Figure 6.3.: Zenith total delays at AGNES station Davos (DAVO). The plot represents a typical situation for a station in the Swiss Alps. Because of the sufficient coverage of surrounding GPS stations with the same atmospheric conditions, the COITROPA solution shows the smallest deviation from the AGNES solution, closely followed by the aLMo solution. The differences to the COMEDIE solution are slightly larger. Again, the Saastamoinen solution has the largest differences.

[mm]	COITROPA	COMEDIE	Saastamoinen	aLMo
mean offset	-0.0	-4.6	1.7	1.2
mean rms	6.8	12.8	22.8	9.4
mean σ	5.5	11.5	22.3	8.7

Table 6.1.: Numerical values of the statistical analysis. The mean offset describes the mean of the deviations from the reference data set. The mean rms corresponds to the mean of all rms values of the GPS stations. The mean σ represents the mean deviation after removing the offset. The rms values characterize the accuracy of the methods chosen. While COITROPA and aLMo allow an accuracy of normally better than 10 mm, the COMEDIE rms is slightly larger and the Saastamoinen solution is settled at around 25 mm.

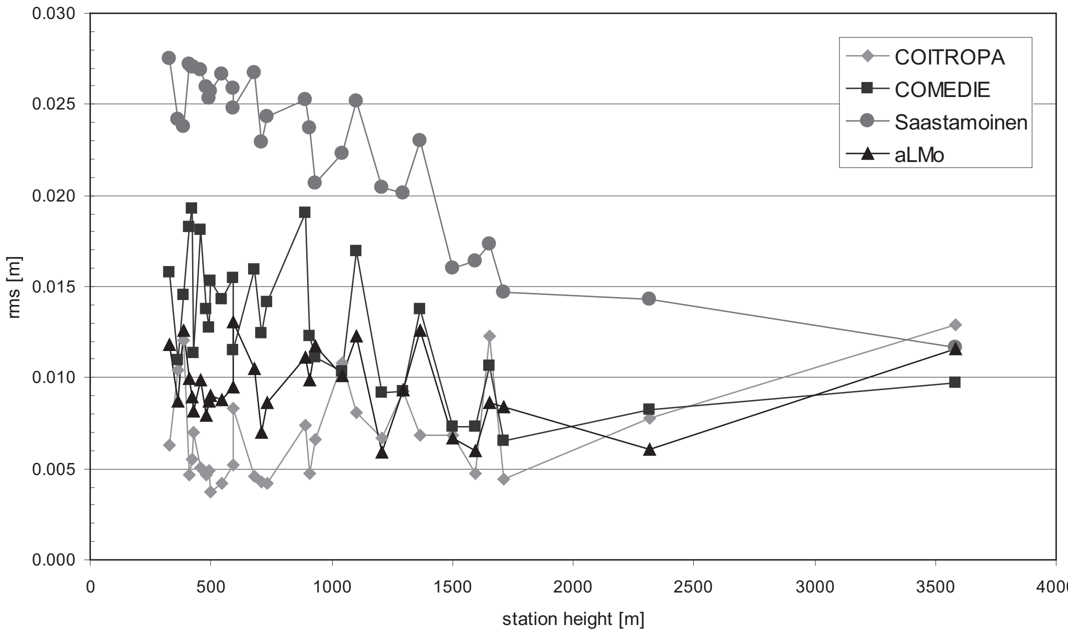

Figure 6.4.: Statistical evaluation of the three methods COITROPA, COMEDIE and Saastamoinen in comparison with the GPS estimated total zenith path delays from AGNES. Furthermore, the solution using the aLMo data interpolated with COITROPA is included. The plot shows the rms versus the station height. While the rms values stay approximately constant in the COITROPA, COMEDIE and aLMo solutions, the Saastamoinen solution becomes more accurate with increasing station height.

- The rms of the COITROPA solution does not show a correlation with station height. It is mostly smaller than 10 mm. Only five stations exceed this value: STAB, LOMO, PFAN, SANB and JUJO. The station heights reach from 366 m (STAB) to 3584 m (JUJO). The reason for the high rms values for these stations is found in the geometry of the AGNES network:
  - The station JUJO is the highest station in the AGNES network (more than 3500 m). Therefore, it cannot be regarded as an *interpolation* from the other AGNES stations but rather as some kind of an *extrapolation*.
  - The stations LOMO and STAB are located in the Ticino. They are the only stations in this topographic layer and in this meteorological condition. Moreover, the other surrounding stations are located in the Alps with a different meteorological behavior.
  - A similar reason applies to the station SANB which is located in the Swiss Alps ($\sim$ 1750 m high). No nearby GPS station with the same height level is available.

  - The station PFAN is located in Austria at about 1000 m station height. Due to the AGNES network configuration, it has to be looked upon as an extrapolation which explains the relatively high rms.

- The rms of the aLMo solution is absolutely independent of the station height. Keeping in mind that the aLMo data are interpolated using COITROPA, the rms consists of the error of the original aLMo model and the error of COITROPA. Therefore, it can be expected, that the fit of the aLMo solution to the AGNES data can be even more accurate.

In summary, it can be concluded that the COITROPA method achieves the best accuracy. However, it has to be ensured that the desired point can be interpolated with surrounding GPS stations at the same topographic level and with the same meteorological behavior. Otherwise, or if not enough GPS estimated path delays are available, a reasonably accurate zenith path delay can be determined with COMEDIE. If only ground meteorological data are available, the Saastamoinen method can be used to calculate path delays, though a reduction in accuracy has to be accepted.

Using data of aLMo is a successful approach as well. An increase in accuracy is expected, if the refractivity values are interpolated directly in the numerical weather model. Applying this approach, equally accurate and reliable results are obtained as by using the COITROPA approach. However, the processing and interpolation of a numerical weather model is complex, time-consuming and expensive. For practical applications, therefore, this method cannot be recommended.

6.5. Comparisons of Water Vapor Profiles

6.5.1. Experimental Setup

Vertically high-resolved water vapor data give valuable information of the air flow in the troposphere, in particular as far as its continuous variation is concerned. This chapter investigates the potential and limits of estimating the 3-dimensional water vapor distribution and its temporal behavior using GPS tomography.

A voxel model above the Swiss territory was chosen with 6 x 3 core voxels plus 22 outer voxels horizontally, and 16 layers up to 15'000 m. The layer thickness reaches from 300 m in the lower troposphere to several thousand meters in the stratosphere. Figure 6.5 shows the voxel model and the distribution of the AGNES stations. A near real-time processing of the GPS data is providing hourly means of zenith delays. The data of the meteorological network of MeteoSwiss (ANETZ) are used to decompose the GPS total delay into the dry and wet part. Combining the wet delays with double difference residuals and the geometrical information of double-differences, allows the reconstruction of the double-difference slant delays. These are introduced directly into the tomographic inversion.

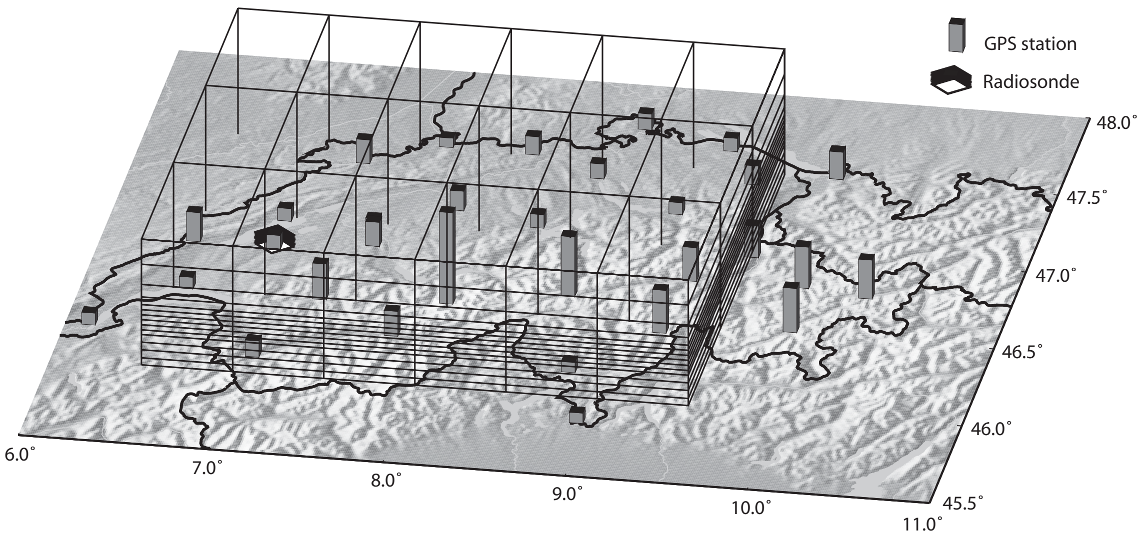

Figure 6.5.: 3D view of the tomographic voxel model above the Swiss territory. The complete model consists of 16 layers up to 15'000 m (the figure shows layers up to 5000 m). Each layer contains 6 voxels in longitude and 3 voxels in latitude (spacing 0.5°) plus 22 outer voxels (not shown on the picture). The GPS stations of the permanent AGNES processing are shown as gray columns according to their station height. The 4 stations in the east of Switzerland are taken into consideration by the outer voxels. Radiosondes are launched from the radiosonde station Payerne, shown as a black cuboid.

According to the investigations of the Hawaiian campaign (Chapter 5.8), additional constraints are necessary to achieve an appropriate result. The following comparisons contain four solutions applying different constraints:

- AWATOS Correlation: This solution contains inter-voxel constraints between all voxels as described in Chapter 5.4.5. The constraints are down-weighted compared to the double-difference observations by a factor of 50^2 (regularization factor $= \frac{1}{2500}$).
- AWATOS AGNES: In addition to the inter-voxel constraints, this solution contains a priori refractivity data. The wet refractivity has been calculated at each location of an AGNES station, and introduced into the equation system. This solution is based on the concept, that only a small additional effort is necessary to perform meteorological measurements at GPS stations. Like the inter-voxel constraints, the a priori meteorological constraints are down-weighted by a factor of 50^2 compared to the observations.
- AWATOS ANETZ: In contrast to the solution AWATOS AGNES, this estimation introduces one a priori refractivity value for each voxel lower than 2000 m.

The refractivity values are interpolated using the ANETZ data and COMEDIE. The border value of 2000 m has been chosen, as COMEDIE is able to interpolate ANETZ data sufficiently accurately up to this height. These constraints are down-weighted by a factor of 20^2 (regularization factor $\frac{1}{400}$).

- AWATOS aLMo: This investigation contains a priori wet refractivity obtained from the aLMo model. For each aLMo profile, the refractivity value of the lowest height is introduced in the respective voxel. This results in one a priori value for each voxel column. The constraints are introduced with a regularization factor of $\frac{1}{900}$.

In addition, an a priori wet refractivity of zero is assigned to the uppermost layer (8'000-15'000 m height) of all solutions, with a regularization factor of $\frac{1}{900}$.

For comparison, independent determinations of the vertical profiles have been generated:

- aLMo solution: Hourly profiles of the aLMo model of MeteoSwiss are directly used for comparison.
- COMEDIE solution: Using the ANETZ data and radiosondes, COMEDIE allows to estimate the wet refractivity for each voxel (Chapter 3). The values are calculated with a sampling rate of one hour.
- Radiosonde: Radiosondes are launched usually twice or four times a day from the radiosonde station Payerne. A total of 22 launches have been carried out during the time of investigation.

Figure 6.6 shows the tomographic voxel model in the Swiss area. Furthermore, the locations of the independent vertical refractivity profiles (aLMo and COMEDIE) are shown as well as the radiosonde station Payerne.

6.5.2. A Priori Network Design Analysis

Evaluating the matrices of the cofactors, the network geometry can be investigated. Figure 6.7 shows a cross section of the square root of cofactors of the four tomographic solutions. The use of the covariance function only leads to a profile with an accuracy increasing with the height. If a priori refractivity values are introduced, a significant increase of the accuracy is visible, but only locally. The voxels with a priori refractivity information are evident in the figures. Furthermore, a priori refractivity allows to strengthen the whole equation system and, therefore, to increase the accuracy of the whole voxel model. As the amount of a priori refractivity is high in the solution AWATOS ANETZ, this solution should attain the best accuracy.

To determine the accuracy of the profiles, the arithmetic mean of all square roots of cofactors along each profile are calculated. Figure 6.8 shows two time series of the

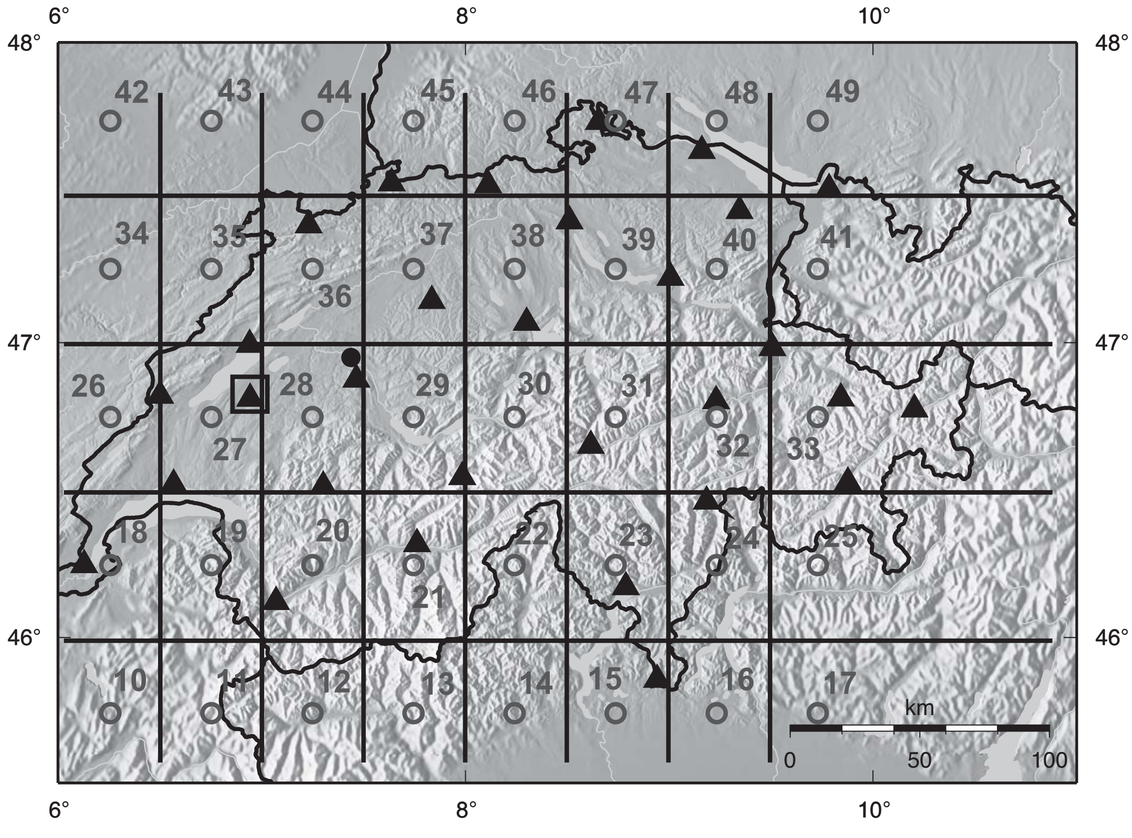

Figure 6.6.: Area of investigation with 30 AGNES stations (triangle) and a further GPS station (dots) included. The voxel model is indicated in black. For the purpose of comparison, radiosonde data of Payerne (black square) are used as well as vertical refractivity profiles from aLMo and COMEDIE at the voxel centers (circlet). The profiles are numbered.

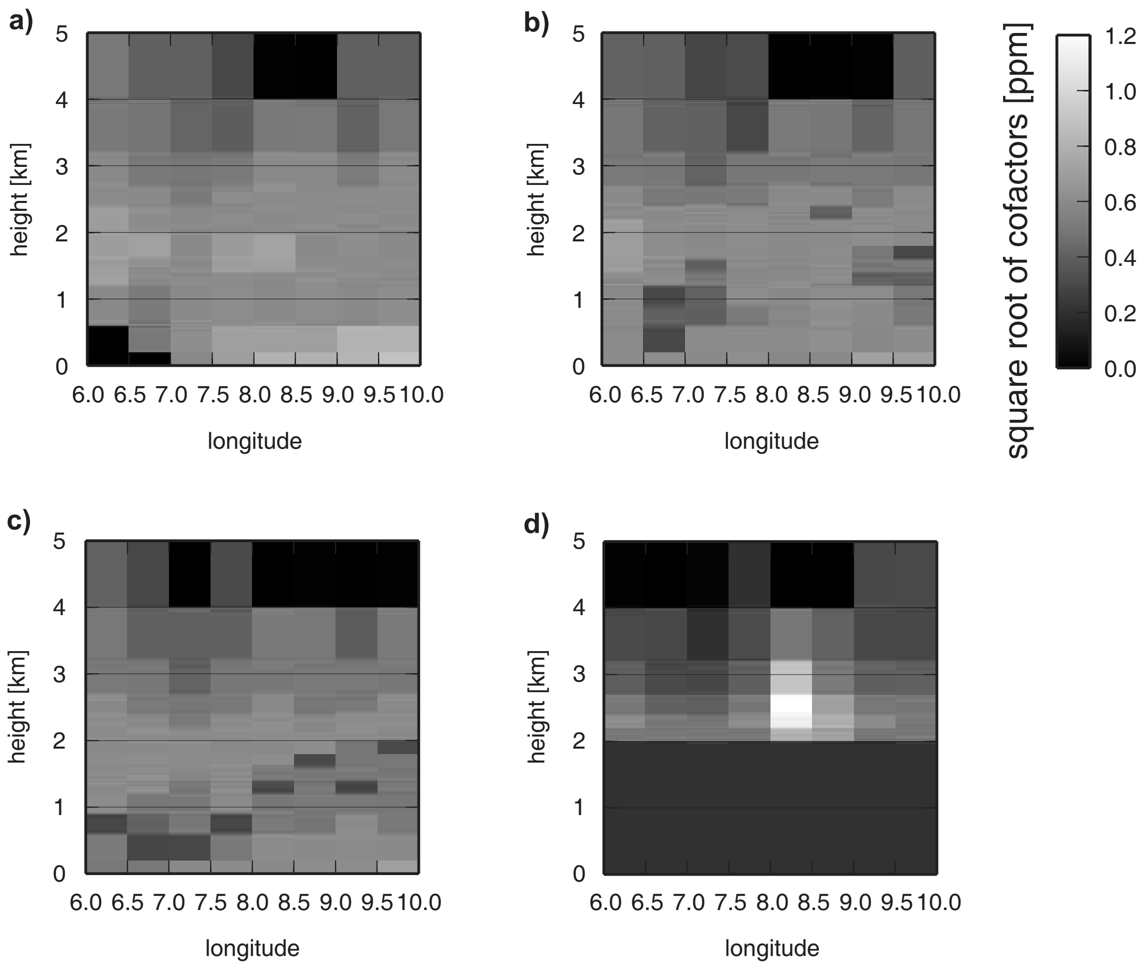

Figure 6.7.: Cross section of the square root of cofactors at latitude 46.75°. The two top layers (5-8km and 8-15km height) are not shown in the figures. (a) represents the solution AWATOS Correlation, (b) AWATOS AGNES, (c) AWATOS aLMo and (d) AWATOS ANETZ. It is seen, that, if only covariance observations are used, the accuracy is increasing with height. If a priori refractivity is introduced, the accuracy increases locally. In panel (b), the locations of the AGNES stations are clearly visible: Payerne, 549 m, Neuchatel, 505 m, EPF Lausanne, 460 m and Sainte-Croix, 1155 m (second column on the left), Bern, 627 m and Zimmerwald, 956 m (third column), Jungfraujoch, 3635 m (fourth column), Andermatt, 2368 m (sixth column), Falera, 1344 m (seventh column) and Sargans, 1265 m, Davos, 1646 m, Samedan, 1759 m and Ardez, 1547 m (eighth column). Considering the aLMo solution (panel c), it is obvious, that each column includes one a priori refractivity value. As every voxel up to 2000 m in the solution AWATOS ANETZ (panel d) includes one a priori refractivity value, this part is generally better determined. The white area in panel (d) indicates values of the square root of cofactors exceeding the range of the scale bar.

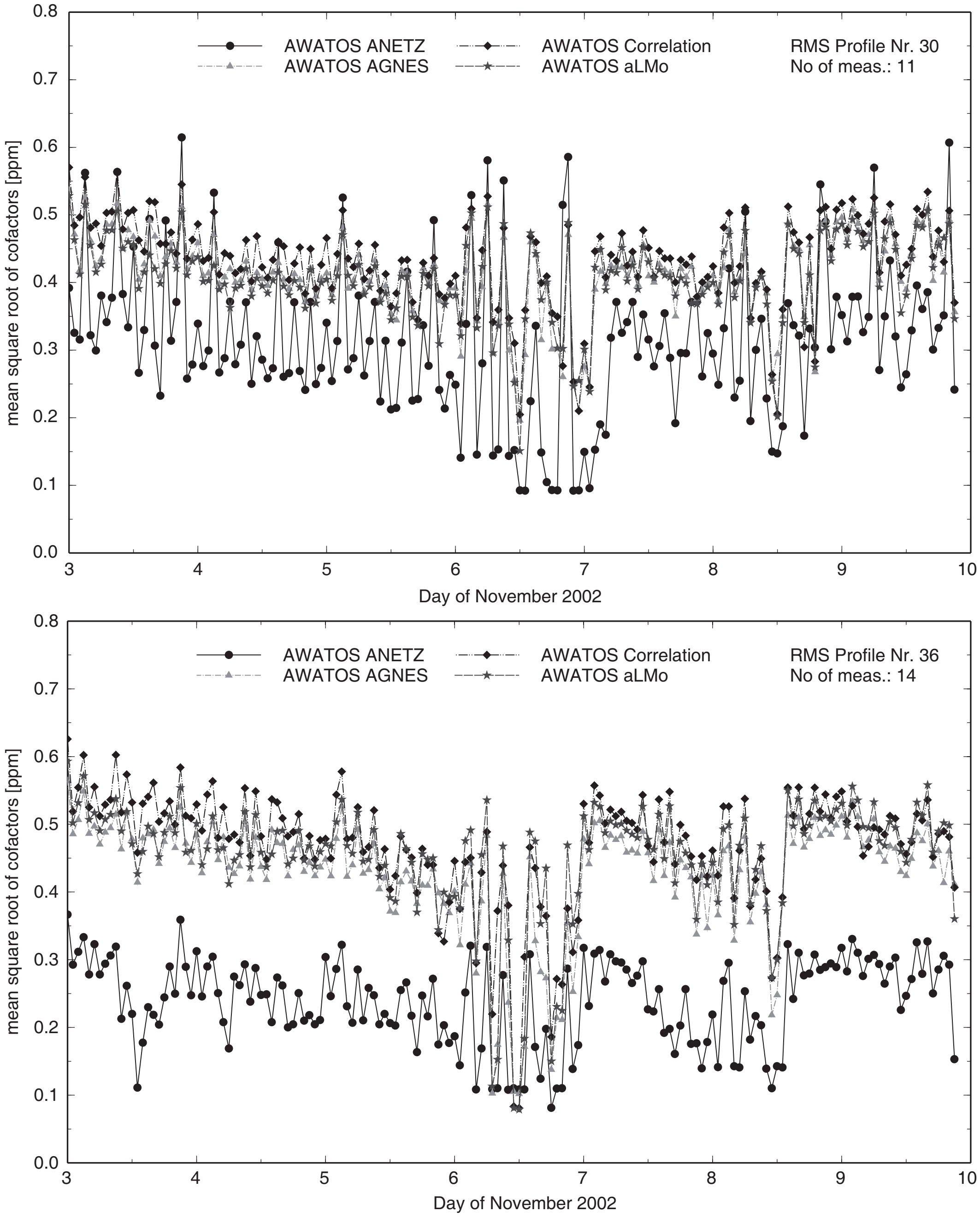

Figure 6.8.: Time series of the mean of the square root of cofactors along the profiles during the investigation time. The solutions AWATOS Correlation, AWATOS AGNES and AWATOS aLMo show a similar accuracy. AWATOS ANETZ is generally more accurate. In profile 36, the ground height is lower than in profile 30. Therefore, a larger amount of voxels with a priori refractivity is included which decreases the error. On November 6, large variations and momentary improvements of the accuracy of the solutions AWATOS Correlation, AWATOS AGNES and AWATOS aLMo are visible. The reason for this behavior has not been clearly identified.

square root of cofactors. Generally, the solution AWATOS ANETZ is more accurate than the other three solutions due to the fact that the tomographic equation system is well-determined with a priori refractivity data. The time series of the arithmetic mean of all profiles are given in Figure 6.9. Again, the solution AWATOS ANETZ exhibits the best accuracy, the other three solutions are similarly accurate.

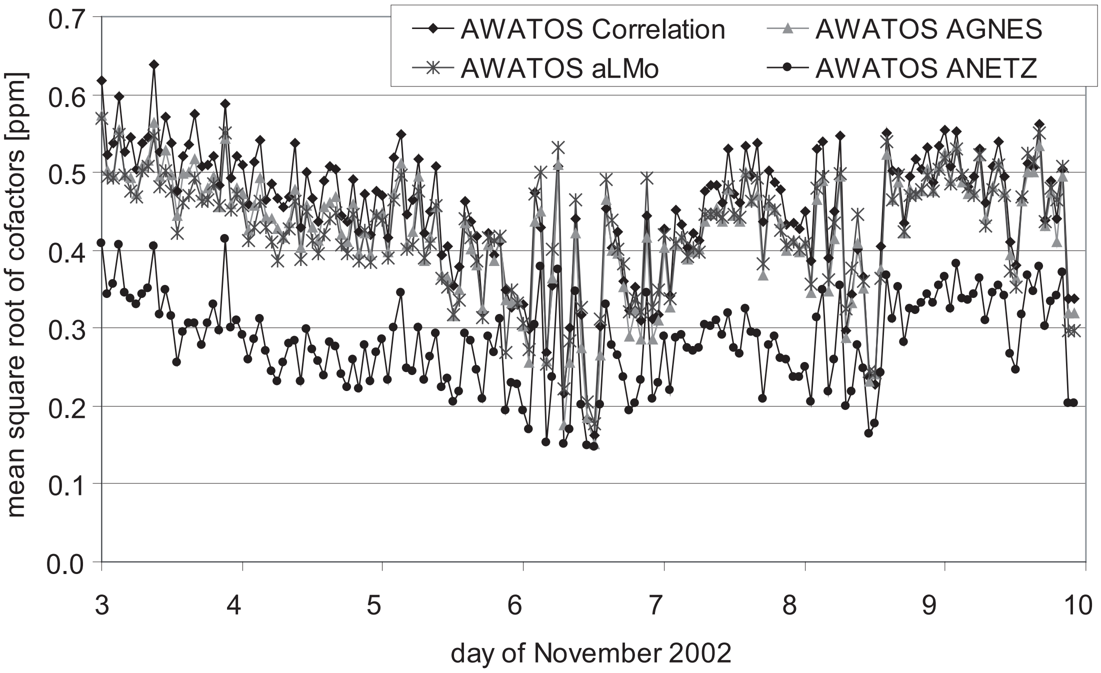

Figure 6.9.: Time series of the mean of the square root of cofactors of all profiles. AWATOS ANETZ shows the best accuracy, followed by the other three tomographic solutions, which are quite similar. Large variations are visible on November 6.

For the solutions AWATOS Correlation, AWATOS AGNES and AWATOS aLMo, all three plots (Figure 6.8 and 6.9) show large jumps on November 6. The reason for this behavior has not been clearly identified. One cause could be attributed to the forming of the double differences by the GPS processing software. The measurements of the AGNES network are processed using the Bernese GPS Software (Beutler et al., 2001) and the *OBS-MAX* strategy to form baselines. This means, that the baselines are selected yielding the maximum number of observations. Considering, that satellites are occasionally not available, the selection of baselines can change hourly and could cause a variation of the mean square root of cofactors.

The total number of ray traces, indeed, stays approximately constant (Figure 6.10). The periodicity of one day of the GPS space segment is roughly reproduced.

Looking at each profile separately, Figure 6.11 shows a contour map of the mean of the square root cofactors for each of the 40 profiles collected during the seven days.

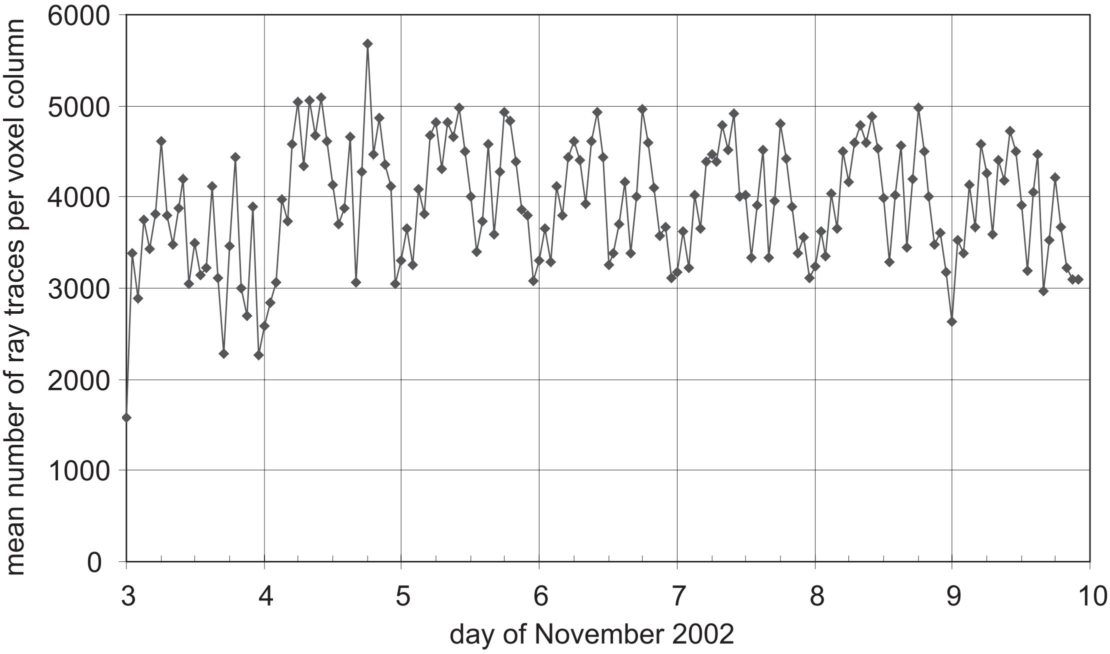

Figure 6.10.: Time series of the mean number of ray traces through the voxels along the profiles. A daily periodicity is clearly visible which is explained by the GPS space segment constellation.

The solution AWATOS ANETZ has generally the best accuracy, except for some few outliers. The solutions AWATOS aLMo and AGNES have a similar accuracy, and the accuracy of AWATOS Correlation is constantly a little worse.

6.5.3. Error Budget

To estimate the accuracy of the tomographic determination, the a posteriori variance of unit weight was calculated. Figure 6.12 shows the behavior during the evaluation time. A strong variation is visible. It is assumed, that the meteorological conditions in the atmosphere influences the accuracy of the tomographic determination. Compared to the prevailing weather situation, the heavy rainfall seems to be coupled with the large jump on November 3. The high level of a posteriori weighting unit appears during a large decrease of water vapor which leads to a sunny period on November 6 and the ensuing rapid increase of wet air. Finally, the increase of the a posteriori variance of unit weight on November 9 coincides with new heavy rainfall.

The a posteriori variances of the refractivity values are given by the diagonal elements of the a posteriori covariance matrices. A mean a posteriori standard deviation has been calculated for each refractivity profile. Table 6.2 shows the statistical evaluation of different groups of profiles. No relevant differences between the individual

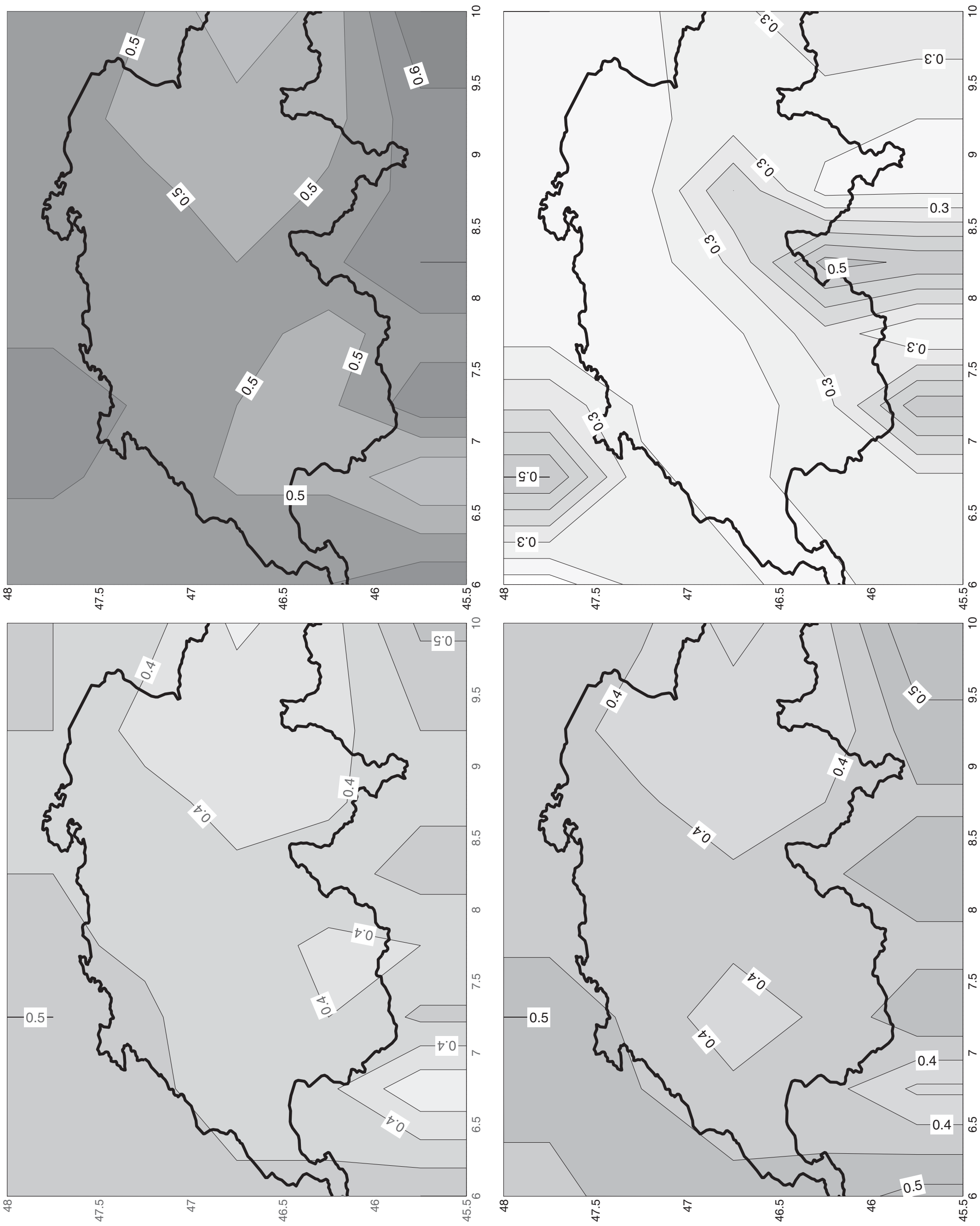

Figure 6.11.: Mean of the square root of cofactors of the individual profiles along the investigation time of seven days of AWATOS aLMo (bottom left), AWATOS Correlation (top left), AWATOS AGNES (bottom right) and AWATOS ANETZ (top right). The figure shows contour maps with an interval of 0.5 ppm (refractivity units). The larger the square root, the darker the color. The overall accuracy is comparable to the figures given above showing the time series: The solution AWATOS ANETZ shows the best accuracy, followed by AWATOS AGNES and AWATOS aLMo. AWATOS Correlation, indeed, is a little worse than the other solutions.

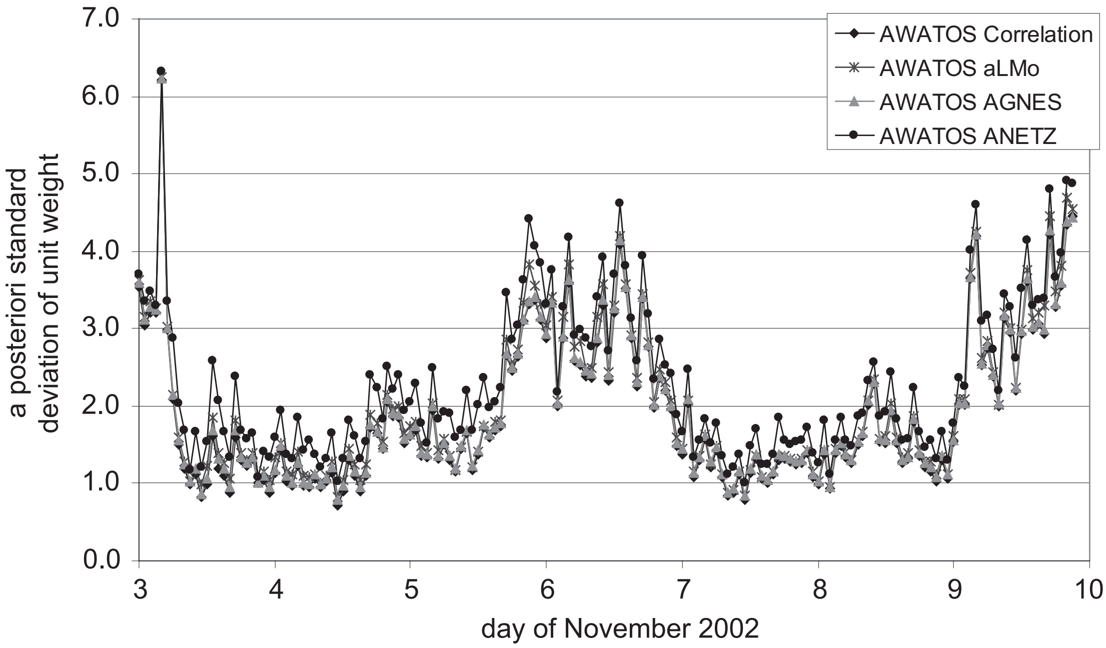

Figure 6.12.: A posteriori standard deviation of unit weight of the tomographic solutions during the investigation time. A significant variation is visible during this seven days. It is suggested, that the variation is caused by the weather situation.

[ppm]	AWATOS Correlation	AWATOS AGNES	AWATOS aLMo	AWATOS ANETZ
all profiles	0.84	0.81	0.85	0.65
all border profiles	0.86	0.84	0.88	0.67
western border p.	0.85	0.87	0.92	0.57
core profiles	0.81	0.77	0.81	0.63
inner core profiles	0.80	0.75	0.80	0.66

Table 6.2.: Statistical analysis of the a posteriori standard deviations of refractivity values. An a posteriori mean standard deviation of each profile has been calculated based on the standard deviations of the 16 refractivity values of each voxel column. The statistics contains the analysis of the hourly profiles within the investigation period (at 168 time points). The profiles are divided into several groups of 4 (inner core) - 40 (all) profiles. However, the mean a posteriori standard deviations of the individual groups do not differ substantially. Considering the individual tomographic solutions, AWATOS Correlation, AWATOS AGNES and AWATOS aLMo have a similar precision, whereas AWATOS ANETZ is more precise.

groups of profiles are visible. The solutions AWATOS Correlation and AWATOS aLMo have a similar precision, AWATOS AGNES is slightly more precise. The best results are obtained with AWATOS ANETZ.

6.5.4. Profile Evaluations

The vertical refractivity profiles of the tomographic solutions are compared with aLMo profiles, radiosonde launchings and COMEDIE profiles. The degree of agreement of the individual profiles is varying. Figure 6.13 (left panel) shows a profile with a homogeneous decrease of the refractivity with height. All solutions match the aLMo solution. An rms between 2.5 ppm (refractivity units) for the solution AWATOS ANETZ to 5.7 ppm (AWATOS Correlation) is achieved. However, this profile is pretty easy to estimate if a covariance function is applied. The example in Figure 6.13 (right panel) has a rapid refractivity change at around 1800 m height. This behavior cannot easily be captured by a covariance function and, therefore, the reproduction requires reliable GPS measurements; in particular for the solution AWATOS Correlation, which contains only double-difference observations and a covariance function. All solutions fit the numerical weather model determination well, an rms of 2.3 (AWATOS ANETZ) up to 6.2 ppm (AWATOS aLMo) was obtained. GPS tomography has the potential to estimate the 3-dimensional water vapor refractivity in the atmosphere.

But not all profiles show such an accurate result. In Figure 6.14 (left panel), particularly the wet refractivity of the solution AWATOS Correlation is under-estimated in the first 1000 m height. The rms increases to 4.9 ppm (AWATOS ANETZ) and to 9.2 ppm (AWATOS Correlation). In the right panel of the same figure, an under-estimation of the tomographic solutions in the first 5000 m height is visible. Only the solution AWATOS ANETZ fits the aLMo solution as long as the solution is constrained by meteorological ground measurements. The mean rms for this profile is 6.6 ppm (AWATOS ANETZ) up to 10.2 ppm (AWATOS AGNES).

The COMEDIE solution is not independent of the aLMo solution. In part, the same input data is introduced in both models. However, in the higher troposphere, COMEDIE follows an atmospheric standard model. If inversions or other irregularities are present (Figure 6.14), an offset to aLMo appears. The radiosonde profiles, whose data are assimilated to the weather model as well, fit accurately to aLMo most of the time, on the order of 2-3 ppm. Rarely, rapid refractivity changes, which are recorded by the radiosondes, are not reproduced with aLMo. The statistical evaluation of the four profiles is given in Table 6.3. For illustration, a couple of representative refractivity profiles of the tomographic and independent solutions are shown in Appendix D.

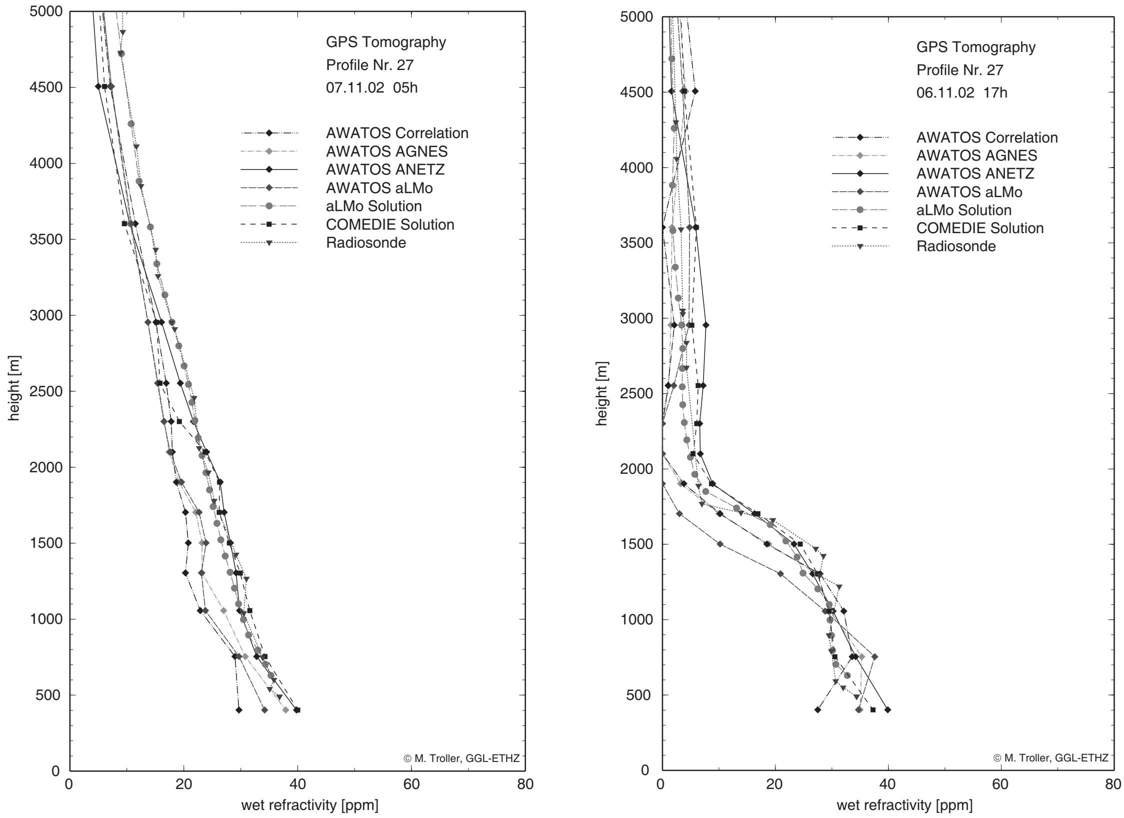

Figure 6.13.: Wet refractivity profiles of four different tomographic solutions, a solution using COMEDIE, a refractivity profile obtained by a radiosonde launching at the station Payerne and data of the numerical weather model aLMo. The left panel shows a profile with a homogeneous decrease of the refractivity with height. All solutions match accurately together on the order of 10 ppm. The right panel shows a profile with a rapid refractivity change at 1800 m height. Again, all solutions fit on the order of 10 ppm.

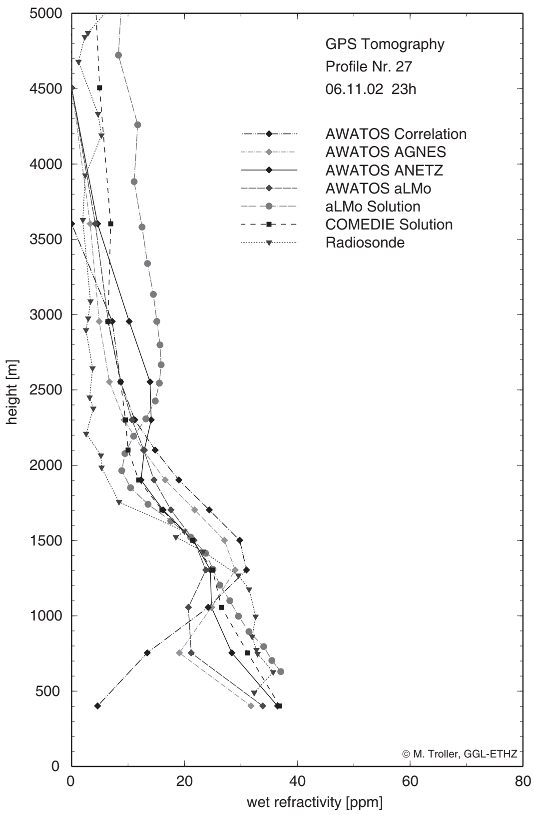

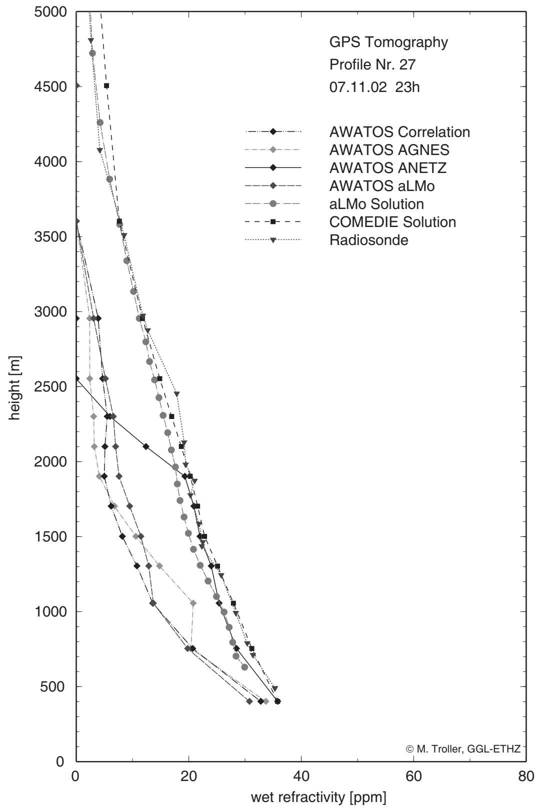

Figure 6.14.: Wet refractivity profiles of four different tomographic solutions, a solution using COMEDIE, a refractivity profile obtained by a radiosonde launching at the station Payerne and data of the numerical weather model aLMo. The left panel shows a profile with an inhomogeneous decrease of the refractivity with height. The wet refractivity of AWATOS Correlation is under-estimated in the first 1000 m height. Also the other three tomographic solutions as well as the radiosonde profile show differences to the aLMo solution. The right panel shows a profile, where the refractivity of all tomographic solutions is under-estimated. Only the solution AWATOS ANETZ fits the aLMo solution as long as ground meteorological constraints are used (up to 2000 m height).

[ppm]	COMEDIE	AWATOS Correlation	AWATOS AGNES	AWATOS aLMo	AWATOS ANETZ
Date: 06.11.02 17h (Figure 6.13, right subfigure)					
mean offset	1.1	-1.5	-1.6	-2.9	1.4
mean rms	1.7	3.4	3.3	6.2	2.3
mean σ	1.3	3.1	2.9	5.5	1.8
Date: 06.11.02 23h (Figure 6.14, right subfigure)					
mean offset	-3.2	-3.0	-3.6	-4.5	-3.0
mean rms	4.4	9.2	7.8	7.0	4.9
mean σ	3.0	8.7	6.9	5.3	3.8
Date: 07.11.02 05h (Figure 6.13, left subfigure)					
mean offset	-1.7	-5.2	-4.6	-4.7	-1.6
mean rms	3.0	5.7	5.0	5.1	2.5
mean σ	2.4	2.4	1.9	2.0	2.0
Date: 07.11.02 23h (Figure 6.14, left subfigure)					
mean offset	0.9	-9.2	-8.8	-8.2	-3.8
mean rms	1.3	10.2	10.0	9.0	6.6
mean σ	1.0	4.4	4.7	3.7	5.3

Table 6.3.: Statistical analysis of the tomographic profiles and the COMEDIE solution shown in Figures 6.13 and 6.14. The values are evaluated compared to the aLMo profiles. The accuracy of the different profiles varies significantly. Of all tomographic solutions, AWATOS ANETZ has the smallest differences to aLMo.

6.5.5. Statistical Comparisons

All 40 profile locations have been statistically evaluated and compared to the aLMo model during the experiment term of seven days (168 estimated time points per profile). Depending on the profile location the rms level ranges between 5 - 10 ppm (refractivity unit) but outliers can reach up to 20 ppm. Figure 6.15 gives two examples of statistical time series. The top panel shows a profile located in the center of the voxel model. The rms is relatively small, only few outliers are visible. The time series on the panel below with a profile of the north-western part of Switzerland, shows a similar rms level, but three periods with a higher mean rms, namely on November 3, 6 and 9. The overall comparison shows a similar rms behavior of all tomographic solutions, even though the characteristics of the outliers differ. Therefore, we expect, that the temporal behavior of the rms is correlated with the actual weather situation.

An evaluation of the time series of all 40 profiles has been performed. Figure 6.16 (upper panel) shows the time series of the mean rms of all profiles. It is clearly seen, that the rms of the solution AWATOS ANETZ is generally smaller than that

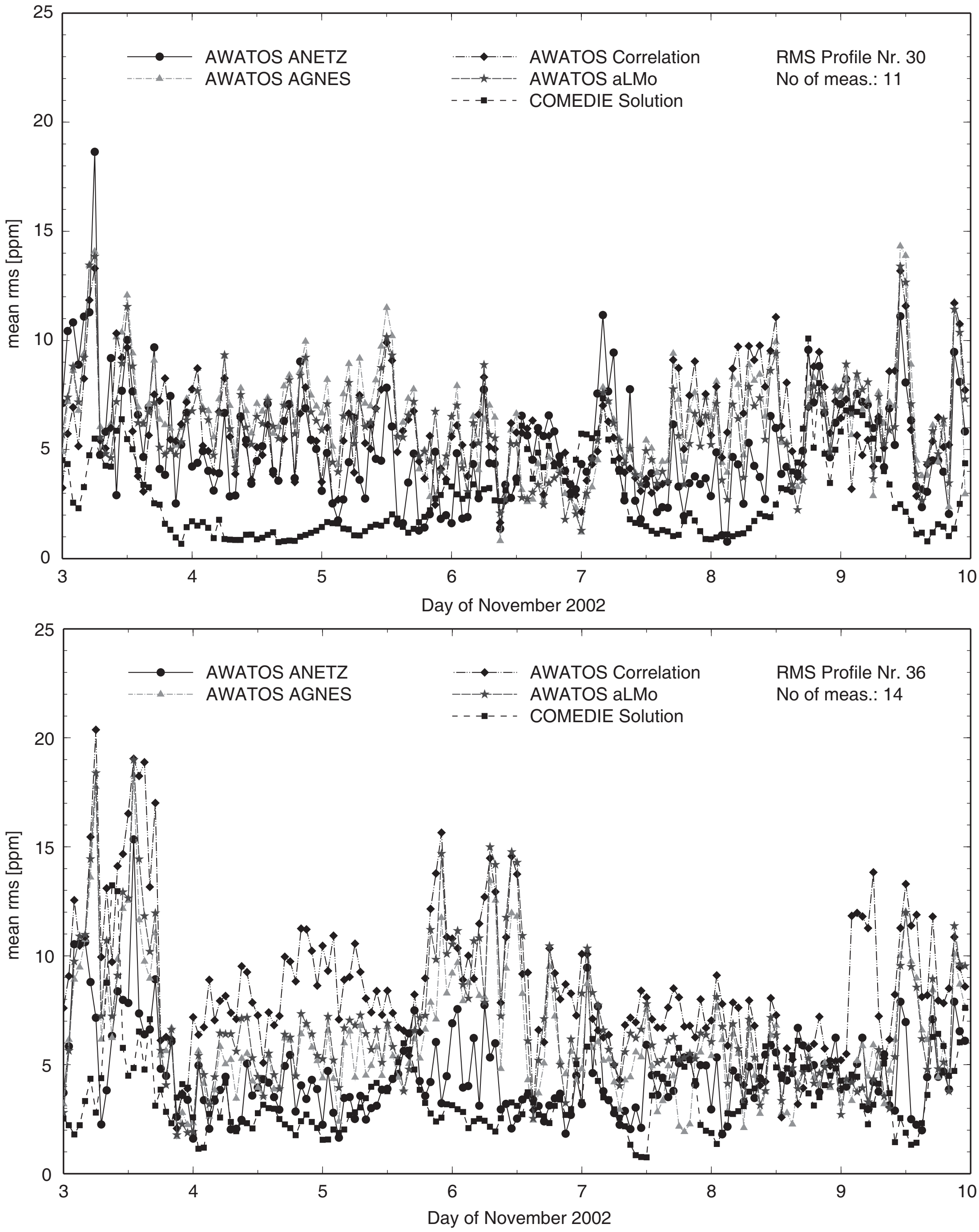

Figure 6.15.: Time series of the mean rms of two refractivity profiles compared to aLMo. The above panel represents the situation of profile nr. 30 (central Switzerland). The rms of all four AWATOS determinations is approximately on the same level, the COMEDIE rms is somewhat smaller. Two obvious jumps are visible, one in the morning of November 3, and the other at noon on November 9. The lower panel shows the profile nr. 36 in the north-western part of Switzerland. The rms level is generally higher. Three periods with outliers are visible, on the 3, 6 and 9 of November.

of the other solutions. However, a correlation between the different tomographic solutions is obvious and, again, three outlier regions are found. Comparing with the prevailing weather situation, the outlier in the morning of November 3 can be explained with the humidity change due to heavy rain in the morning and bright intervals in the afternoon. The outlier period of November 6 corresponds to a rapid decrease of humidity. Finally, the outlier of November 9 in the morning coincides with anew increase of humidity (change from sunny weather in the morning to rain in the afternoon). In contrast to the tomographic solutions, the rms of the COMEDIE time series does not show the same behavior nor the same outliers.

The mean offset (Figure 6.16, lower panel) shows a significant difference between the tomographic solutions and aLMo. The water vapor is often underestimated during the investigation period. Large jumps appear at the same time as the outliers in the rms time series.

To quantify the accuracy of the different profile locations, the mean rms of the complete time series of each profile was determined and compared to each other. Figure 6.17 shows a contour map of the mean rms of each profile compared to the aLMo data. Obviously, the highest rms is present for the north-western most profiles. For the solution AWATOS Correlation, the accuracy is varying in Switzerland, whereas it is approximately constant for the solution AWATOS ANETZ. The COMEDIE solution acts completely different. The rms is dependent on the number of ANETZ stations in the profile area. Therefore, the profile in the south of Domodossola has the highest rms, together with the most north-western profile. No ANETZ stations are located in this areas.

Considering the mean offset (Figure 6.18), again, the COMEDIE solution shows a different behavior than the tomographic solutions. COMEDIE has a small positive offset compared to the aLMo data. The tomographic solutions AWATOS ANETZ has a small negative offset, AWATOS aLMo and AWATOS AGNES have a relatively large negative offset compared to aLMo.

Table 6.4 shows the statistical comparison of all 7680 evaluated profiles. The interpretation of Figure 6.17 and 6.18 is confirmed. Again, it is obvious, that the COMEDIE solution is more accurate than the tomographic solutions. The solution AWATOS ANETZ is the most accurate of the tomographic solutions with a relatively small mean offset. The other three tomographic solutions are similar. A relatively large mean offset of 4 ppm points at a systematic effect. The tomography is more accurate if meteorological a priori data are used.

The assumption of different rms levels depending on the profile location is also confirmed (Table 6.4). Obviously, the western border profiles have the worst accuracy. However, the border voxels are only present to allow the use of all double-difference observations, even if they reach outside the voxel model. Thus, it is obvious, that outer voxels cannot be used. Considering only the core profiles, a small improvement of the accuracy is realized. When looking at only the four, most inner core voxel, we do not see the rms improve substantially.

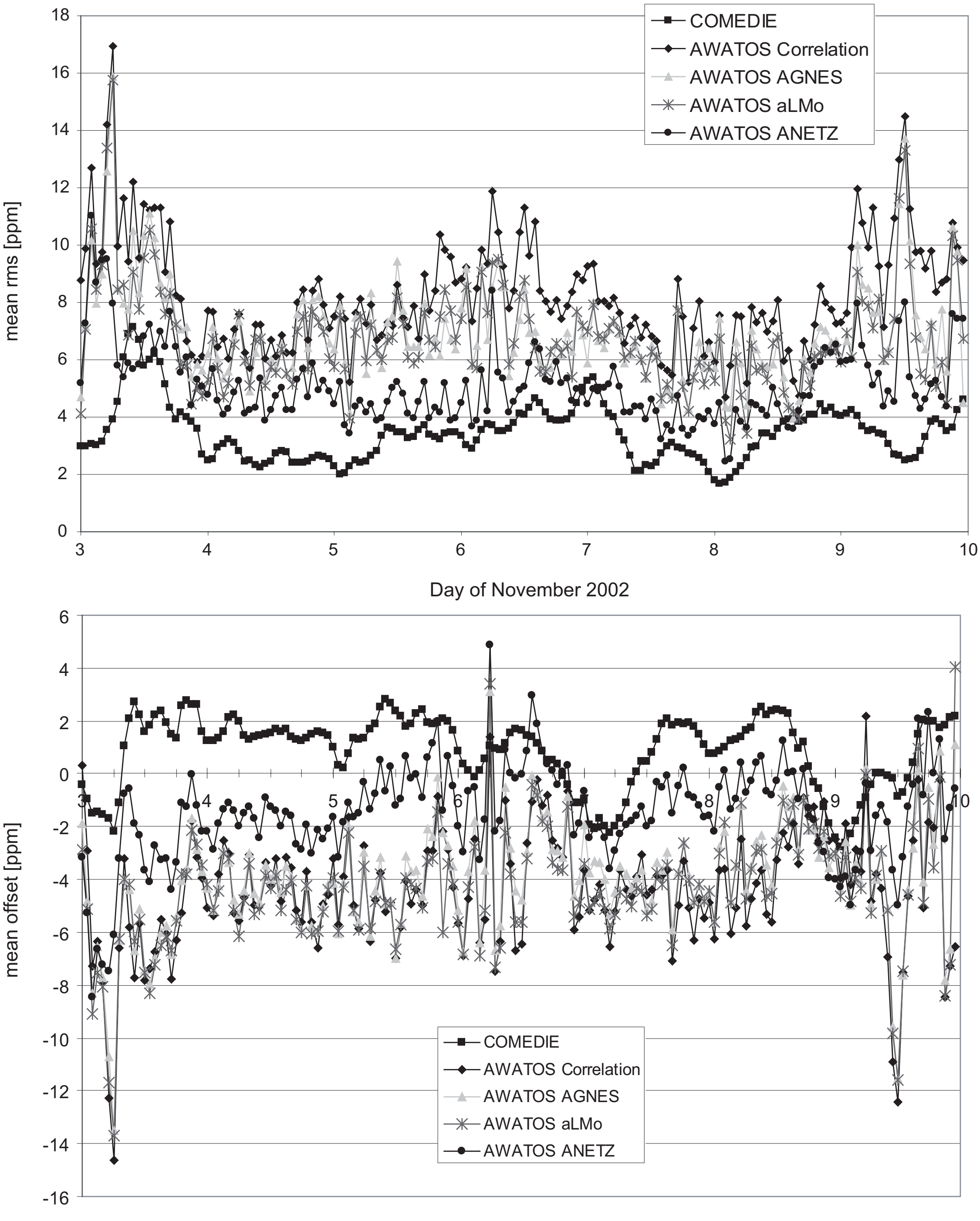

Figure 6.16.: Time series of the mean rms of all 40 profiles compared to aLMo (upper panel). Overall, the COMEDIE solution has the smallest rms, followed by the AWATOS ANETZ solution. The other three solutions AWATOS aLMo, AWATOS AGNES and AWATOS Correlation have a similar rms level. Outliers are visible for all tomographic solutions on November 3, 6 and 9. The lower panel shows the mean offset to aLMo. The COMEDIE solution fits aLMO, whereas the tomographic determinations have a significant offset compared to aLMo. Strong jumps correlate with strong outliers of the mean rms.

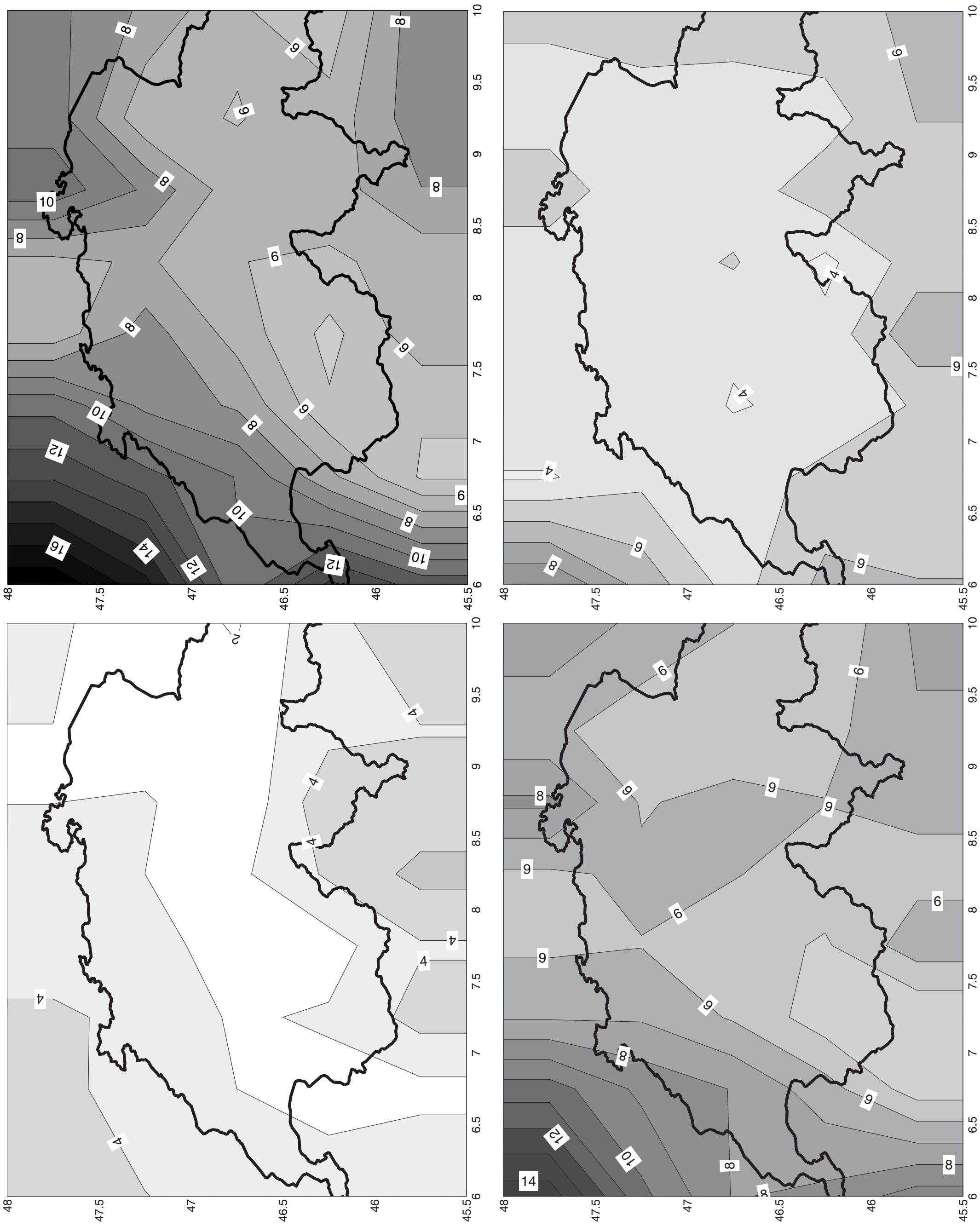

Figure 6.17.: Mean rms of the individual refractivity profiles of AWATOS aLMo (bottom right), COMEDIE (bottom left), AWATOS ANETZ (top right) and AWATOS Correlation (top left) compared to aLMo. The figure shows contour maps with an interval of 1 ppm (refractivity units), whereas each second interval is labeled. The larger the rms, the darker the color. In general, the north-western profiles have the highest rms in all tomographic solutions. Considering AWATOS Correlation, the rms is varying in Switzerland and reaches a minimum in the south-western part of Switzerland. In contrast, the solution AWATOS ANETZ has a similar rms in whole Switzerland. The COMEDIE solution, as independent method, shows a different behavior.

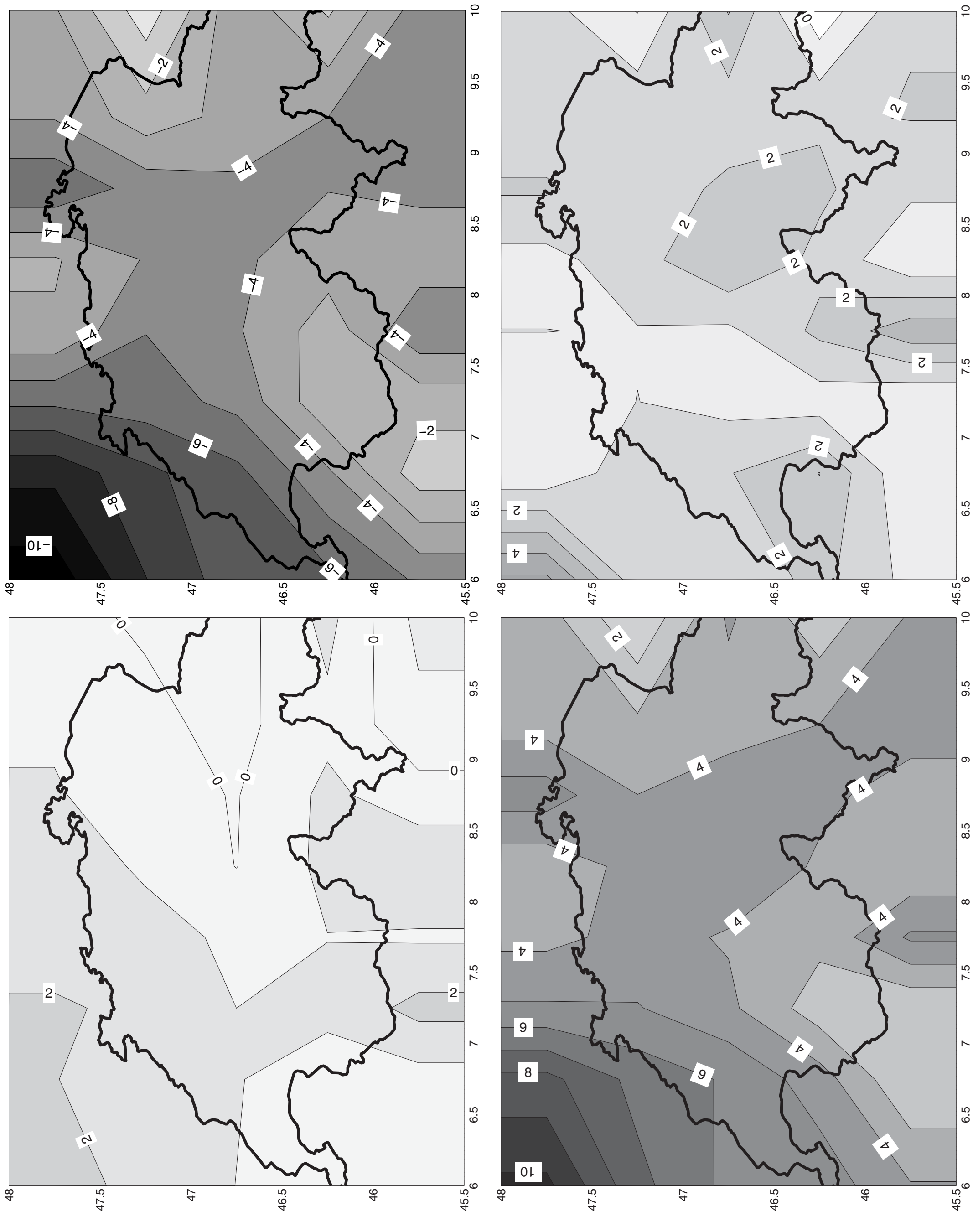

Figure 6.18.: Mean offset of the individual refractivity profiles of AWATOS aLMo (bottom right), COMEDIE (bottom left), AWATOS ANETZ (top right) and AWATOS Correlation (top left) compared to aLMo. The figure shows contour maps with an interval of 1 ppm (refractivity units), whereas each second interval is labeled. The larger the mean offset, the darker the color. The solutions AWATOS Correlation and AWATOS aLMo show a similar behavior. The solution AWATOS ANETZ has smaller offset in the whole area. Again, COMEDIE shows a different behavior compared to the tomographic solutions.

[ppm]	COMEDIE	AWATOS Correlation	AWATOS AGNES	AWATOS aLMo	AWATOS ANETZ
mean offset	0.9	-4.4	-4.0	-4.4	-1.5
mean rms:					
all profiles	3.4	8.3	7.0	6.7	5.1
all border profiles	3.7	9.2	7.6	7.3	5.6
western border p.	4.0	13.6	11.3	10.1	6.5
core profiles	3.1	7.2	6.2	6.1	4.5
inner core profiles	2.6	6.7	6.0	5.9	4.4

Table 6.4.: Numerical values of the statistical analysis. The mean offset describes the mean of the deviation from the aLMo data set. The mean rms corresponds to the mean of all rms values of all profiles. The profiles are divided into several groups of profiles with a similar rms level. The lowest accuracy is obtained for the profiles of the western outer voxels, followed by all outer voxel profiles. Overall, the core voxel profiles are slightly more accurate. No significant improvement can be seen if only the four, most inner core voxels are considered.

The mean offsets of the tomographic solutions often lead to smaller wet path delays compared to aLMo. Figure 6.19 shows two examples of wet path delay comparisons at the station Payerne (PAYE) and St.Gallen (STGA). It is obvious, that the input data in the tomographic processing, the AGNES time series, fits the aLMo solution accurately. At station STGA a slight systematic underestimation of the wet path delay determined with the tomographic method is visible. At station PAYE, the refractivity is underestimated systematically. This is caused during the tomographic processing. However, the reason for this systematic effect is not clear yet.

6.5.6. Discussion

The application of the tomographic approach in the area of Switzerland has been successfully performed. AGNES is a GPS permanent network dedicated to tomography. However, due to the geometrical limitations of the number of GPS satellites and receivers, some voxels are over-determined, other voxels are under-determined. Therefore, additional information is necessary to achieve a reliable result. It is verified, that meteorological a priori data significantly improve the tomographic inversion. If a priori values are introduced on several layers, the result becomes more accurate than if only few a priori values are assimilated.

A network design analysis allows to check the suitability of the GPS network and the individual profiles. It is shown, that all profiles reach a similar a priori precision. Time series of the mean of ray traces of the profiles show a daily periodicity. This behavior is given by the GPS satellite constellation. No periodicity is seen in the

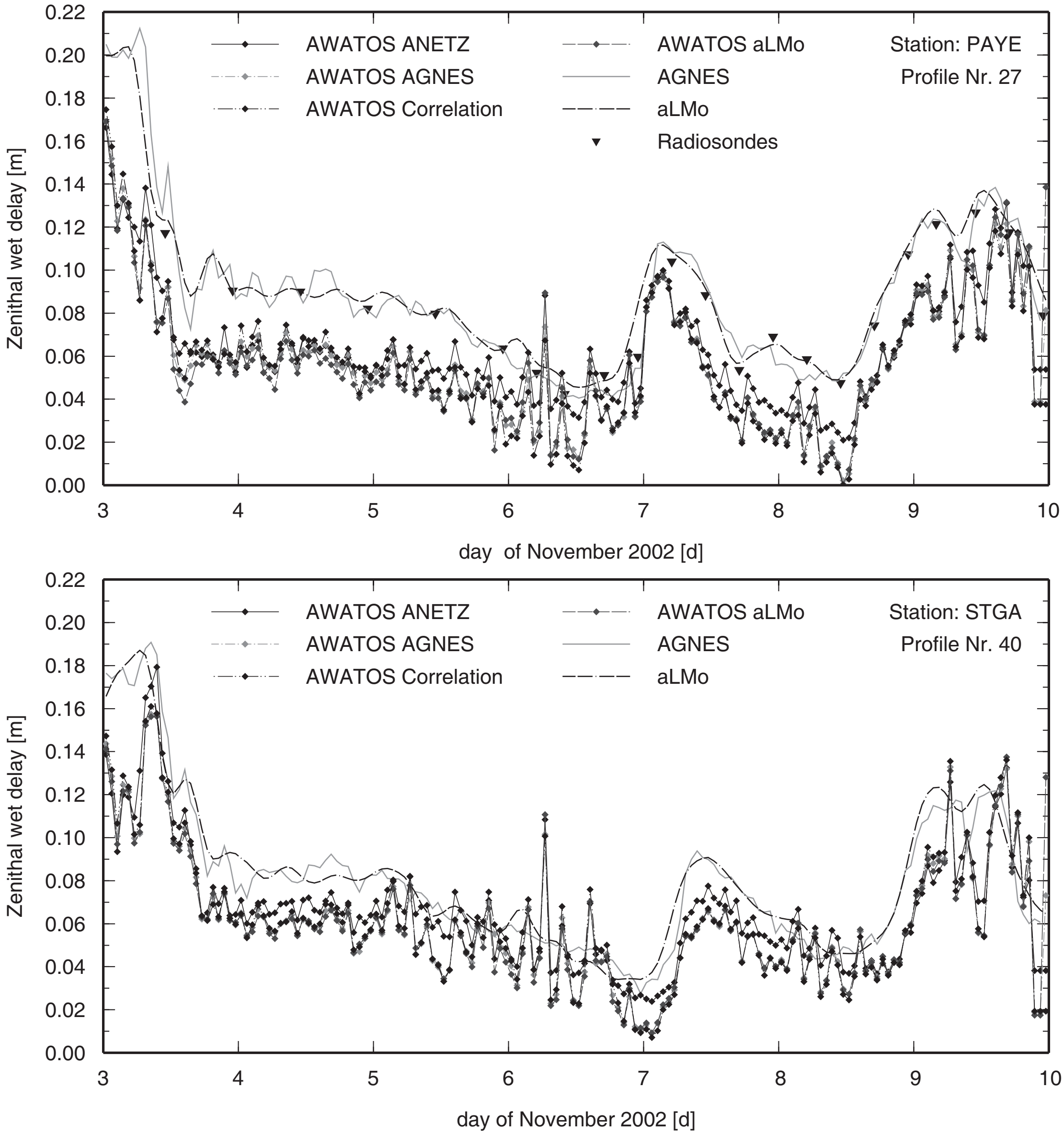

Figure 6.19.: Examples of integrated zenith wet path delay of the four tomographic solutions at the two stations PAYE and STGA. In addition, path delays derived from GPS (AGNES), aLMo and radiosondes (only station PAYE) are shown. The GPS-derived path delays (AGNES) fits the aLMo and radiosonde data accurately. The tomographic solutions at station STGA slightly underestimate the wet path delay. At station PAYE, the wet path delay is underestimated systematically.

time series of the mean square root of the cofactors. The values are approximately constant during the investigation time, but large jumps appear on November 6. The mean square root of the cofactors of each profile results, apart from some few outliers, in a similar precision of the profiles, assuming that the same tomographic solution is chosen. However, as the border voxels are open, they contain also rays to stations from far abroad, which are used for the stabilization of the GPS processing. The meteorological conditions in these areas can differ. Therefore, the border profiles cannot be considered as precise. These voxels are only used, to allow the assimilation of double-difference observations which are not completely located within the area of the voxel model.

Analyzing the time series of profiles (Figure 6.9) and the individual profile examination (Figure 6.11), similar differences in precision between the tomographic solutions are seen. AWATOS ANETZ has the most precise result, followed by AWATOS aLMo and AWATOS AGNES. AWATOS Correlation is slightly less precise. The a posteriori covariance matrices of the tomographic adjustment allow to calculate the a posteriori standard deviations of the tomographic profiles. A precision between 0.65 and 0.85 ppm (refractivity unit) was achieved, depending on the type of additional information in the tomographic inversion. Again, the solution AWATOS ANETZ attains the most precise results, the other three solutions are similarly precise. The differences in precision of the tomographic solutions relative to each other seem to be realistic, however, the absolute value of this inner consistency is probably too small.

A total of 7680 profiles of the numerical weather model aLMo is used to compare the tomographic determinations with independent data. A statistical accuracy of around 5.1 to 8.3 ppm (refractivity unit) was achieved. Compared to the precision of the a posteriori standard deviation values, a difference of around a factor of eight remains. The difference of the accuracy of the individual tomographic solutions is similar to the precision of the a posteriori evaluation, except to the solution AWATOS aLMo, which has a better accuracy in the comparison. aLMo data are used in the solution AWATOS aLMo. Therefore, this comparison is not independent.

The time series of the profiles compared with aLMo (Figures 6.15 and 6.16) differ from the plots of the matrices of cofactors (Figures 6.8 and 6.9). The difference is caused by the meteorological variation of the troposphere. A correlation between the a posteriori standard deviation of unit weight and the mean rms of the tomographic solutions was verified. The strongest correlation is obtained with the solution AWATOS Correlation ($R^2 = 0.27$), only a slight correlation was achieved with the solution AWATOS AGNES ($R^2 = 0.10$).

Considering the individual profiles, significant differences in accuracy are visible (Table 6.4). Generally, the western border profiles are less accurate than the other profiles. This is most likely caused by the open outer voxels. Moreover, as the differences of the border profiles compared to western border profiles are not significantly, considering the precision of the a posteriori evaluation, errors may have been caused also by the numerical weather model aLMo. As regards the core voxels, the accuracy is similar for all profiles if the solution AWATOS ANETZ is considered. Applying one of the other three solutions, the rms differs, and generally the western profiles are less accurate than the eastern ones.

A mean offset of the tomographic solutions compared to aLMo exists. Consequently, the offset also appears in the wet path delays (Figure 6.19). The tomographic input data, GPS estimated path delays of AGNES, do not show this offset. Consequently, the offset must be caused by the tomographic processing. However, the reason for this offset is not clear yet.

The COMEDIE solution fits aLMo mostly accurate. However, COMEDIE is also a kind of simple weather model and the input data are partially the same, as used in the aLMo model. COMEDIE fits aLMo in the lower 2000 m usually precisely, beyond, COMEDIE follows the atmospheric standard model. Therefore, if inversions or other irregularities are present in the higher troposphere, the errors become larger.

7. Conclusions and Outlook

The GPS technology was primarily developed for navigation applications. However, it is also a powerful technique for several other purposes. One of the promising fields of application is the so-called GPS meteorology, promoted due to the high temporal resolution of GPS measurements. As a remote sensing technique, only few GPS receivers are necessary to cover the whole atmosphere. Accurate tropospheric GPS-estimated path delays are obtained from permanent GPS networks and from GPS campaigns with long observation periods. The delays are estimated to correct the tropospheric effect on GPS measurements as well as to determine the integrated amount of water vapor in the troposphere. Short-term measurements do not allow to estimate reliable path delays. Therefore, the tropospheric effect has to be corrected with independent methods in this case.

One possibility is to use meteorological measurements. The software package COMEDIE is determining the spatial and temporal variation of the refractivity in the troposphere based on ground meteorological and radiosonde data. In this work, COMEDIE was successfully enhanced and improved. The extension of the temperature function from the troposphere to the layer above the tropopause contributes considerably to the stability of the equation system. The improvement of the covariance function allows a more precise consideration of the few measurements in the higher troposphere, and again, contributes substantially to the stability of the troposphere refractivity estimates. Several investigations were carried out in Switzerland. A dense network of meteorological ground stations as well as the availability of radiosonde data from Switzerland and its neighborhood allowed to use a dense set of meteorological data. The interpolation of meteorological data (cross-correlation method) showed accurate results for temperature and pressure and confirmed the feasibility of a collocation approach. However, in the complex layers near the tropopause, the temperature modeling is only partly satisfactory. The interpolation of water vapor is accurate, but the short-term variation of water vapor in the atmosphere can only partially be reproduced. Comparisons of COMEDIE path delays with GPS-estimated path delays of the permanent network AGNES were performed. It is shown that the use of a dedicated covariance function improves the accuracy substantially. The rms of the COMEDIE determination compared to GPS-estimated path delays depends on the season. Because of the small amount of water vapor in the dry winter air, the rms is usually smaller than one centimeter. In summer time, the large varying amount of water vapor in the wet air raises the rms to above two centimeters. Usually, path delays are over-estimated by COMEDIE. The statistical investigation of the mean offset resulted again in a seasonal variation. Its value ranges from below one centimeter in winter time up to two centimeters in the summer. In addition, a slight correlation of the offset with the station height was found. Correcting this effect, the rms is improved by about 25%.

Another possibility to determine tropospheric path delays is to use GPS-estimated path delays of permanent networks. Within this work, the software package COITROPA was developed, which collocates and interpolates GPS-estimated tropospheric path delays. Investigations have been performed with the Swiss national GPS network AGNES. The permanent GPS measurements guarantee for an accurate determination of GPS-estimated path delays. Cross-correlations over several years show an increase in accuracy with the growing number of GPS stations. With the actual AGNES configuration of 30 GPS receivers, an rms of 0.5 cm can be expected for stations in the Swiss Alpine foreland. For the mountainous area, the rms is on the order of one centimeter. Additionally, an annual periodicity of the rms was found with a maximum in summer. Contrary to the COMEDIE approach, tropospheric path delays determined with COITROPA are not independent of GPS measurements. However, the COITROPA solutions are usually more accurate than the COMEDIE solutions.

Tropospheric path delays are an important error source in GPS measurements. However, they can also be used as valuable information for meteorology. In the frame of the comparison experiment (Chapter 6), data of the numerical weather model aLMo were compared with GPS-estimated path delays and solutions obtained from COMEDIE and COITROPA. The statistical evaluation showed a good agreement, in particular with GPS-estimated path delays. The overall rms is smaller than one centimeter.

In contrast to the integrated amount of water vapor, a major challenge is to determine the spatial information and temporal variation of water vapor. The software package AWATOS was developed to process GPS-estimated path delays applying a tomographic approach. Vertical profiles of water vapor in a high spatial and temporal resolution can be obtained. Unfortunately, the geometry can only be influenced to a minor degree. GPS stations have to be placed at the surface, and the number and orbits of the satellites are given. Therefore, the tomographic approach leads usually to a partially over- and partially under-determined problem. Simulations applying the geometry of the Hawaiian campaign show, that the over-estimated voxels can be determined using the technique of singular value decomposition (SVD). However, as soon as the observations are introduced with a noise level, the results become less reliable. Applying a reasonable noise level of 5 mm, additional information is necessary to strengthen the equation system and to achieve an accurate result. In the present work, mainly two types of additional information are used: inter-voxel constraints and meteorological a priori information. Latter improve the results significantly. However, measurement systems to obtain such information must be in operation in the area considered. Simulations showed, that, also inter-voxel constraints improve the results and lead to an over-estimated equation system. However, irregularities, such as rapid refractivity changes or inversions tend to be smoothed out.

An investigation of the tomographic approach was performed on the basis of a dedicated field campaign on the big island of Hawaii. This area fits tomographic requirements in particular, as the topography has large height differences in a small geographic area. The vertical water vapor profiles show an overall agreement compared to radiosonde profiles. An accuracy of around 10 ppm (wet refractivity unit) was reached. However, deficiencies are still existing, in particular, in the case of rapid refractivity changes.

An extensive study of GPS tomography has been performed in the area of Switzerland using the dense national GPS permanent network AGNES. This set-up represents a realistic scenario for the implementation of GPS tomography. The evaluation of the matrices of cofactors points out the principle applicability of the GPS network and the voxel model. A similar precision is expected for all profiles chosen in this study. Furthermore, the time series of the mean square root of cofactors per profile show a constant precision during the investigation time. The tomographic solutions, however, differ in precision: The solution with only covariance information gets the least precise result. With the additional amount of meteorological observations, the determination becomes more precise. The error budget of all solutions is correlated with the state of the atmosphere. The precision decreases, if the meteorological conditions change significantly. A precision of the tomographic processing of around 0.7 ppm (wet refractivity unit) was achieved for the mean of all profiles. The comparison of the tomographic solutions with the numerical weather model aLMo allows an additional independent accuracy determination. The statistical investigation yielded approximately eight times less accurate values than the a posteriori evaluation. However, these results seem to be more realistic. The relation between the individual solutions are similar for both types of assessment.

The field experiments showed the principle feasibility of GPS tomography to determine the spatial distribution of water vapor and its temporal variation. The first main step is to conduct an accurate GPS processing and to prepare reliable data for the tomographic adjustment. Afterwards, the meteorological and topographic situation of the area under investigation should be carefully studied. Dedicated meteorological constraints are necessary for an accurate result. So far, because of the necessary inter-voxel constraints, deficiencies still remain. The amount of water-vapor is generally under-estimated. Depending on the applied constraints, an offset in the refractivity profile of about 1-4 ppm results.

Recapitulating, one of the main limiting factor for the high-precision GPS technique is represented by tropospheric path delays in short-time measurements. This causes a deficiency in the height component. Furthermore, in the near future, several navigational applications depend on an accurate determination of the third dimension as well. The investigated methods contribute substantially to this issue. As the number and density of GPS permanent networks will increase in the near future, the method implemented in COITROPA will allow to provide accurate tropospheric path delay corrections in many regions. In areas without GPS networks, but with permanent meteorological measurements, the method of COMEDIE can provide corrections, though, a slight loss of accuracy has to be taken into account. For an operational handling, the supply of the path delay correction in real-time poses a challenge. A possible product could be a map of the condition of the troposphere covering a large region such as a continent, updated in hourly intervals.

As an additional application of COMEDIE, the determination of path delays could be extended from the zenith direction to pointed delays with arbitrary elevation angles. This would allow the estimation of horizontal gradients, which could represent useful information for several applications, such as GPS tomography.

Currently, GPS meteorology is a growing field of research for atmospheric and meteorological sciences, as well as for climatology. Long-term time series of the total amount of water vapor with a high spatial and temporal resolution can be provided with little expenses. A combination of the data obtained by the individual GPS networks, provides a powerful data set over large areas. Moreover, the vertical resolution of water vapor allows numerous additional insights, such as insights into global and regional airflow and chemical processes in the atmosphere. GPS tomography has the potential to provide this data in a 3D spatial and at high temporal resolution. Because of the limited number of GPS satellites and receivers, usually, the equation system is partially underdetermined. Future research has to investigate, whether additional observations can be assimilated. One possibility would be to introduce data retrieved from other measurement techniques such as solar spectrometry or microwave radiometry. Latter has the advantage, that pointed delays can be measured in every azimuth and elevation angle with direct view in the sky, and, that a scan of the whole atmosphere of one location can be processed in a few minutes. Furthermore, improvements can be achieved by introducing additional constraints, tailored to the particular observation area given. For example, height-dependent weighting of the constraints could be considered, or, information about horizontal gradients obtained by an expanded version of COMEDIE.

The spatial resolution of water vapor is mainly dependent on the density of GPS stations. Simulations would allow to quantify this aspect. In the framework of a recently started Swiss National Science Foundation project (SNF), the tomographic method is investigated in a small-scale area in the mountainous part of Switzerland.

A further challenge is to provide four-dimensional water vapor data in near real-time. Instead of precise satellite orbits, only predicted ones could be introduced in the GPS processing. Furthermore, the tomographic input data has to be prepared in a short time. Such a development could serve as an early warning system for thunderstorms. It would also allow to assimilate GPS data in numerical weather models and to improve meteorological forecasts, in local areas, in particular.

In conclusion, several methods to determine the water vapor in the troposphere were investigated. As a result it can be stated, that the estimation using a GPS processing software still represents the most accurate method to determine path delays. Embedding short-time measurements in permanent GPS networks, is equally or more accurate, than correcting measurements with path delays derived from COMEDIE or COITROPA. Therefore, usually, latter is not recommended as it is also more complex. Only in areas without GPS networks, COMEDIE contributes substantially to an accurate GPS determination. GPS meteorology, indeed, is a promising field of application. COITROPA is an accurate technique to interpolate GPS-estimated path delays to determine the spatial distribution of the total amount of water vapor in the troposphere. The estimation of the vertical resolution of water vapor using AWATOS, in fact, is not yet applicable. The principle feasibility is shown in this work. However, the required accuracy and reliability was not achieved so far. Further investigations in terms of constraints are necessary, in combination with meteorological sciences.

Bibliography

Askne, J. and Nordius, H. (1987). Estimation of tropospheric delay for microwaves from surface weather data. *Radio Science*, 22(3):379–386.

BADC (2002). British atmospheric data center (BADC), Natural Environment Research Council (NERC), http://badc.nerc.ac.uk/data/radiosglobe/radhelp.html.

Berg, H. (1948). *Allgemeine Meteorologie: Einführung in die Physik der Atmosphäre.* Dümmlers Verlag Bonn.

Beutler, G., Bock, H., Brockmann, E., Dach, R., Fridez, P., Gurtner, W., Hugentobler, U., Ineichen, D., Johnson, J., Meindl, M., Mervart, L., Rothacher, M., Schaer, S., Springer, T., and Weber, R. (2001). Bernese GPS software version 4.2, edited by U. Hugentobler, S. Schaer and P. Fridez. Astronomical Institute, University of Berne.

Bevis, M., Businger, S., Herring, T., Rocken, C., Anthes, R., and Ware, R. (1992). GPS meteorology: Remote sensing of atmospheric water vapor using the global positioning system. *J. of Geophysical Research*, 97(D14):15787–15801.

Bock, O., Tarniewicz, J., Thom, C., Pelon, J., and Kasser, M. (2001). Study of external path delay correction techniques for high accuracy height determination with GPS. *Physics and Chemistry of the Earth, Part A*, 26(3):165–171.

Boudouris, G. (1963). On the index of refraction of air, the absorption and dispersion of centimeter waves by gases. *J. of Research of the National Bureau of Standards-D.Radio Propagation*, 67D(6):631–684.

Brockmann, E., Guerova, G., and Troller, M. (2001). Swiss activities in combining GPS with meteorology. In *Torres, J.A. and Hornik, H. (Eds.): Subcommission for the European Reference Frame (EUREF), Dubrovnik, Publication 10.*

Brockmann, E., Ineichen, D., and Troller, M. (2003). Using interpolated zenith total delays from the swiss permanent GPS network agnes with time delays of 2 weeks up to 10 minutes. *Geophysical Research Abstracts*, 5.

Brockmann, E. and Troller, M. (2002). GPS meteorology in the swiss alps: Interpolation accuracy for different alpine areas and near real-time results. In *Exploitation of Ground-Based GPS for Meteorology, COST Action 716 Workshop, GeoForschungsZentrum Potsdam, January 28-29.*

Brockmann, E. and Wiget, A. (2001). LAC analysis center report. EUREF permanent networks: 3rd local analysis center workshop 31 may - 1 june 2001. In *Reports on Geodesy, No. 3(58)*, TB01-14, Swisstopo.

Bronstein, I., Semendjajew, K., Musiol, G., and Mühlig, H. (1993). *Taschenbuch der Mathematik*. Verlag Harri Deutsch, 1. Auflage.

Chao, C. (1973). A new method to predict wet zenith range refraction from surface measurements of meteorological parameters. *DSN Progress Report, JPL Pasadena, California, 15 April 1973*, No. 32-1526, Vol. XIV:33–41.

Chaperon, F. and Elmiger, A. (1995). *Geodätische Messtechnik - Vermessungskunde*. Institute of Geodesy and Photogrammetry, ETH Zürich.

Davis, J., Herring, T., Shapiro, I., Rogers, A., and Elgered, G. (1985). Geodesy by radio interferometry: Effects of atmospheric modeling errors on estimates of baseline length. *Radio Science*, 20(6):1593–1607.

Doms, G. and Schättler, U. (eds.) (2003). Newsletter No. 3, February 2003. Technical Report, COSMO (Consortium for Small-Scale Modelling).

Eckert, V., Cocard, M., and Geiger, A. (1992). COMEDIE (collocation of meteorological data for interpolation and estimation of tropospheric pathdelays, Teil I: Konzepte, Teil II: Resultate. Technical Report 194, ETH Zürich.

Elgered, G. (1993). *Atmospheric Remote Sensing by Microwave Radiometry*, chapter Tropospheric Radio-Path Delay from Ground-based Microwave Radiometry, pages 215–258. John Wiley and Sons, Inc.

Emardson, T. and Derks, H. (2000). On the relation between the wet delay and the integrated precipitable water vapour in the european atmosphere. *Meteorological Applications*, 7:61–68.

Essen, L. and Froome, K. (1951). The refractive indices and dielectric constants of air and its principal constituents at 24,000 mc/s. *Proceedings of the Royal Society B*, 64:862–875.

Flores, A. (1999). *Atmospheric Tomography Using Satellite Radio Signals*. PhD thesis, Institute d'Estudis Espacials de Catalunya, Barcelona.

Flores, A., Ruffini, G., and Rius, A. (2000). 4d tropospheric tomography using GPS slant wet delays. *Ann. Geophysicae*, 18:223–234.

Geiger, A. (1987). Einfluss richtungsabhängiger Fehler bei Satellitenmessungen. Technical Report 130, ETH Zürich.

Goff, J. (1965). Saturation pressure of water on the new kelvin scale. *Humidity and Moisture*, 3, A. Wexler, Ed. Reinhold:189–192.

Goff, J. and Gratch, S. (1946). Low pressure properties of water from -160° to 212°F. *Trans. ASHVE*, 52:95–121.

Guerova, G., Brockmann, E., Quiby, J., Schubiger, F., and Matzler, C. (2003). Validation of NWP mesoscale models with swiss GPS network AGNES. *J. of Applied Meteorology*, 42(1):141–150.

Haase, J., Calais, E., Talaya, J., Rius, A., Vespe, F., Santangelo, R., Huang, X.-Y., Davila, J., Ge, M., Cucurull, L., Flores, A., Sciarretta, C., Pacione, R., Boccolari, M., Pugnaghi, S., Vedel, H., Mogensen, K., Yang, X., and Garate, J. (2001). The contribution of the MAGIC project to the COST 716 objectives of assessing the operational potential of ground-based GPS meteorology on an international scale. *Physics and Chemistry of the Earth (A)*, 26(6-8):433–437.

Hann, J. (1901). *Lehrbuch der Meteorologie.* Tauchnitz, Leipzig.

Hartmann, G. and Leitinger, R. (1984). Range errors due to ionospheric and tropospheric effects for signal frequencies above 100 MHz. *Bull. Géod.*, 58:109–136.

Herring, T. (1992). Modeling atmospheric delays in the analysis of space geodetic data. In *Symposium on Refraction of Transatmospheric Signals in Geodesy, edited by J.C. de Munck and T.A.Th Spoelstra, The Netherlands, 19-22 May, Netherlands Geodetic Commission, Publications on Geodesy, Delft*, 36:157–164.

Hirahara, K. (2000). Local GPS tropospheric tomography. *Earth Planets Space*, 52:935–939.

Hirter, H. (1998). Mehrdimensionale Interpolation von meteorologischen Feldern zur Berechnung der Brechungsbedingungen in der Geodäsie. Institut für Geodäsie und Photogrammetrie, Mitteilungen Nr. 64, ETH Zürich.

HMP243 (1996). Transmitter operating manual. Vaisala.

Hofmann-Wellenhof, B., Lichtenegger, H., and Collins, J. (2001). *GPS Theory and Practice.* Springer, Wien, New York.

Hopfield, H. (1969). Two-quartic tropospheric refractivity profile for correcting satellite data. *J. of Geophysical Research*, 74(18):4487–4499.

Hopfield, H. (1971). Tropospheric effect on electromagnetically measured range: Prediction from surface weather data. *Radio Science*, 6(3):357–367.

Ichikawa, R., Kasahara, M., Mannoji, N., and Naito, I. (1995). Estimations of atmospheric excess path delay based on three-dimensional numerical prediction model data. *J. of Geod. Soc. Japan*, 41:379–408.

Ifadis, I. (1986). The atmospheric delay of radio waves: Modelling the elevation dependence on a global scale. Technical Report No 38L, Licentiate Thesis, Chalmers University of Technology.

Ifadis, I. (1987). Contribution to the study of the atmospheric refraction, on radio waves used in modern geodetic techniques in long distance measurements. Technical Report Vol. IA.6, Thesis Report, School of Engineering, Faculty of Civil Engineering, Thessaloniki.

Ifadis, I. (2000). A new approach to mapping the atmospheric effect for GPS observations. *Earth Planets Space*, 52:703–708.

Kaplan, E. (1996). *(ed.), Understanding GPS: principles and applications.* Artech House Publishers, Boston, London.

King, R. and Bock, Y. (1999). Documentation for the GAMIT GPS analysis software. Mass. Inst. Tech. and Scripps Inst. Oceanography.

Kruse, L. (2001). Spatial and temporal distribution of atmospheric water vapor using space geodetic techniques. Geodätisch-geophysikalische Arbeiten in der Schweiz, Volume 61, Schweizerische Geodätische Kommision.

MacDonald, A., Xie, Y., and Ware, R. (2002). Diagnosis of three-dimensional water vapor using a GPS network. *Monthly Weather Review*, 130(2):386–397.

Marini, J. W. (1972). Correction of satellite tracking data for an arbitrary tropospheric profile. *Radio Science*, 7(2):223–231.

Mendes, V.B. (1999). *Modeling the neutral-atmosphere propagation delay in radiometric space techniques.* PhD dissertation, University of New Brunswick.

Menke, W. (1989). *Geophysical Data Analysis: Discrete Inverse Theory*, volume 45 of *International Geophysics Series.* Academic Press.

Mervart, L. (1995). Ambiguity resolution techniques in geodetic and geodynamic applications of the global positioning system. Geodätisch-geophysikalische Arbeiten in der Schweiz, Volume 53, Schweizerische Geodätische Kommision.

Moritz, H. (1973). *Least-Squares Collocation.* PhD thesis, DGK, Bayrische Akademie der Wissenschaften. Reihe AA: Theoretische Geodäsie, Heft Nr. 75.

Niell, A. (1996). Global mapping functions for the atmospheric delay at radio wavelengths. *J. of Geophysical Research*, 101(B2):3227–3246.

Owens, J. (1967). Optical refractive index of air: Dependence on pressure, temperature and composition. *Appl. optics*, 6(1):51–59.

PG.net (2004). Physicalgeography.net, glossary of terms, precipitable water, http://www.physicalgeography.net/glossary.html.

Press, W., Teukolsky, S., Vetterling, W., and Flannery, B. (1994). *Numerical Recipes in C.* Cambridge University Press.

Richner, H., Joss, J., and Ruppert, P. (1996). A water hypsometer utilizing high-precision thermocouples. *J. of Atmospheric and Oceanic Technology*, 13:175–182.

Richner, H., Rieker, J., and Ruppert, P. (1999). Die Auswertung von Radiosondendaten. In *Richner, H. and v. Hünerbein, S. (eds.): Grundlagen aerologischer Messungen speziell mittels der Schweizer Sonde SRS 400, Veröffentlichungen der SMA-Meteo Schweiz*, Nr. 61.

Richner, H. and Viatte, P. (1995). The hydrostatic equation in the evaluation algorithm for radiosonde data. *J. of Atmospheric and Oceanic Technology*, 12:649–656.

Rothacher, M. (1992). Orbits of satellite systems in space geodesy. Geodätisch-geophysikalische Arbeiten in der Schweiz, Volume 46, Schweizerische Geodätische Kommision.

Saastamoinen, J. (1972). Atmospheric correction for the troposphere and stratosphere in radio ranging of satellites. In *Henriksen, S.W.; Mancini, A.; Chovitz, B.H. (ed.): The use of artificial satellites for geodesy, Geophys. Monogr. Ser., AGU*, 15:247–251.

Saastamoinen, J. (1973). Contribution to the theory of atmospheric refraction. *Bull. Geod.*, 105:279–298; 106:388–397, 107:13–34.

Santschi, W., Brockmann, E., and Signer, T. (2000). Verdichtung GPS-Netz in den Kantonen Graubünden und Tessin. Technical report, TB00-39, Bundesamt für Landestopographie, Publication in prep.

Seeber, G. (1993). *Satellite Geodesy.* de Gruyter, Berlin.

Seko, H., Shimada, S., Nakamura, H., and Kato, T. (2000). Three-dimensional distribution of water vapor estimated from tropospheric delay of GPS data in a mesoscale precipitation system of the baiu front. *Earth Planets Space*, 52:927–933.

SFDRS (2002). SFDRS Sendungen - METEO - Archiv - Das Wetterarchiv. http://www.sfdrs.ch/system/frames/highlights/meteo/index.php.

Sierk, B. (2001). Solar spectrometry for determination of tropospheric water vapor. Geodätisch-geophysikalische Arbeiten in der Schweiz, Volume 62, Schweizerische Geodätische Kommision.

SMA (1985). Charakteristiken der ANETZ-Daten. In *Beiträge zum ANETZ-Daten Kolloquium vom 17. April 1985 in Zürich.*, page 56. Schweizerische Meteorologische Anstalt Zürich.

Smith, E. and Weintraub, S. (1953). The constants in the equation for atmospheric refractive index at radio frequencies. *Proc. of the I.R.E.*, 41:1035–1037.

Somieski, A., Bürki, B., Cocard, M., Geiger, A., and Kahle, H.-G. (2002). Water vapor remote sensing techniques- water vapor radiometry and solar spectrometry. *Geophysical Research Abstracts*, 4.

Somieski, A., Bürki, B., Kahle, H.-G., Becker-Ross, H., Florek, S., and Okruss, M. (2003). Geodetic mobile solar spectrometry: Description of the new spectrometer gemoss and first measurements. *Geophysical Research Abstracts*, 5.

Thayer, G. (1974). An improved equation for the radio refractive index of air. *Radio Science*, 9(10):803–807.

Troller, M., Bürki, B., Cocard, M., Geiger, A., and Kahle, H.-G. (2002a). 3d refractivity field from GPS double difference tomography. *Geophysical Research Letters*, 29(24):2149–2152.

Troller, M. and Brockmann, E. (2001). COMEDIE-Modellierung für die Kampagne GRTI00 - Vergleiche verschiedener Atmosphärenmodellierungen. TB(B) 01-20, Wiss. Report, Bundesamt für Landestopographie.

Troller, M. and Brockmann, E. (2002). Troposphäreninterpolation aus AGNES; Benutzeranleitung und Resultate anhand der GPS Verdichtungsmessungen 2001. TB(B) 02-25, Wiss. Report, Bundesamt für Landestopographie.

Troller, M., Brockmann, E., Cocard, M., and Geiger, A. (2002b). GPS derived pathdelays versus four-dimensional meteorological modelling. In *Exploitation of Ground-Based GPS for Meteorology, COST Action 716 Workshop, GeoForschungsZentrum Potsdam, January 28-29*.

Troller, M., Brockmann, E., and Geiger, A. (2003). Estimation of spatial and temporal path delays based on the permanent GPS network in Switzerland. *Geophysical Research Abstracts.*, 5.

Troller, M., Cocard, M., and Geiger, A. (2000). Modellierung 4 dimensionaler Refraktionsfelder zur Berechnung von Weglängen-Korrekturen bei Satellitenmessungen. In *Simulation raumbezogener Prozesse: Methoden und Anwendungen*, 9,*IfGI prints*.

U. S. Standard Atmosphere (1962). *U. S. Standard Atmosphere 1962: ICAO Standard atmosphere to 20 kilometers - proposed ICAO extension to 32 kilometers - Tables and data to 700 kilometers*. US Government Printing Office, Washington DC.

Ware, R., Alber, C., Rocken, C., and Solheim, F. (1997). Sensing integrated water vapor along GPS ray paths. *Geophysical Research Letters*, 24(4):417–420.

Ware, R., Rocken, C., Solheim, F., Exner, M., Schreiner, W., Anthes, R., Feng, D., Herman, B., Gorbunov, M., Sokolovskiy, S., Hardy, K., Kuo, Y., Zou, X., Trenberth, K., Meehan, T., Melbourne, W., and Businger, S. (1996). GPS sounding of the atmosphere from low earth orbit: Preliminary results. *Bulletin of the American Meteorological Society*, 77(1):19–40.

Webb, F. and Zumberge, J. (1997). An introduction to the GIPSY/OASIS II. JPL Publication, D-11088.

Wehrli, J. (1986). Räumliche Interpolation des Druckfeldes aus Messungen des ANETZ unter Verwendung vereinfachten Krigings. Diplomarbeit, LAPETH, ETH Zürich.

Wirth, B. (1990). Höhensysteme, Schwerepotentiale und Niveauflächen: Systematische Untersuchungen zur zukünftigen terrestrischen und GPS-gestützten Höhenbestimmung in der Schweiz. Geodätisch-geophysikalische Arbeiten in der Schweiz, Volume 42, Schweizerische Geodätische Kommision.

Zuev, V. (1974). *Propagation of visible and infrared radiation in the atmosphere.* Wiley, New York.

Zuev, V. and Komarov, V. (1987). *Statistical models of the temperature and gaseous components of the atmosphere.* D. Reidel Publishing Company.

A. Saastamoinen Formula

A.1. Tabulated Standard Values of Correction Factors

Standard values of correction factor B:

station height above sea level	B [mbar]	station height above sea level	B [mbar]
0 km	1.156	2 km	0.874
0.5 km	1.079	2.5 km	0.813
1 km	1.006	3 km	0.757
1.5 km	0.938	4 km	0.654
2 km	0.874	5 km	0.563

Correction Term δ_R in meters:

apparent zenith distance	station height above sea level							
	0 km	0.5 km	1 km	1.5 km	2 km	3 km	4 km	5 km
60°00’	0.003	0.003	0.002	0.002	0.002	0.002	0.001	0.001
66°00’	0.006	0.006	0.005	0.005	0.004	0.003	0.003	0.002
70°00’	0.012	0.011	0.010	0.009	0.008	0.006	0.005	0.004
73°00’	0.020	0.018	0.017	0.015	0.013	0.011	0.009	0.007
75°00’	0.031	0.028	0.025	0.023	0.021	0.017	0.014	0.011
76°00’	0.039	0.035	0.032	0.029	0.026	0.021	0.017	0.014
77°00’	0.050	0.045	0.041	0.037	0.033	0.027	0.022	0.018
78°00’	0.065	0.059	0.054	0.049	0.044	0.036	0.030	0.024
78°30’	0.075	0.068	0.062	0.056	0.051	0.042	0.034	0.028
79°00’	0.087	0.079	0.072	0.065	0.059	0.049	0.040	0.033
79°30’	0.102	0.093	0.085	0.077	0.070	0.058	0.047	0.039
79°45’	0.111	0.101	0.092	0.083	0.076	0.063	0.052	0.043
80°00’	0.121	0.110	0.100	0.091	0.083	0.068	0.056	0.047

A.2. Derivation of the Formulas for the Dry and Wet Path Delay

Saastamoinen (1972) presented a simplified formula to calculate the total path delay. Only ground meteorological data of pressure, temperature and water vapor pressure are necessary to achieve a relatively accurate result. For calculating the dry path delay, usually, humidity is set to zero. However, this procedure provides just partially accurate solutions. In the following, the precise formulas for dry and wet path delay are derived.

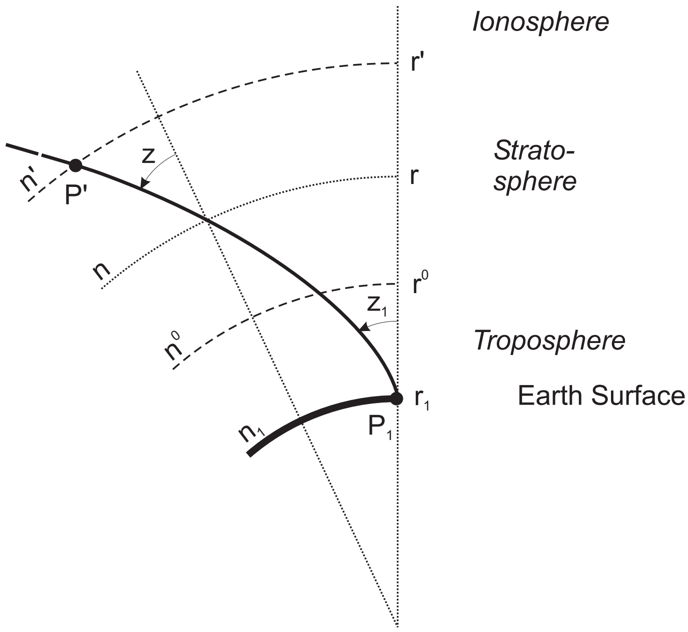

Figure A.1.: Illustration of an electromagnetic ray path in a spherically layered atmosphere (according to Saastamoinen, 1972).

Based on the relation between the refractivity and distance (Figure A.1, (2.8) and Saastamoinen, 1972)

$$\Delta^{PD} = \int (n-1)ds \tag{A.1}$$

and introducing the zenith distance z, it results:

$$\Delta^{PD} = \int_{r_1}^{r'} (n-1)cos^{-1}zdr \tag{A.2}$$

z depends upon the refractive index according to the law of refraction:

$$nrsinz = n_1r_1sinz_1 = const \tag{A.3}$$

It is therefore necessary to find an integrable expression for $cos^{-1}z$.
Setting y to:

$$y = \frac{nr}{n_1r_1} = \frac{sinz_1}{sinz} \tag{A.4}$$

and introducing the relation:

$$sin^2z_1 + cos^2z_1 = 1 \tag{A.5}$$

sin^2z_1 can be substituted:

$$y^2\frac{sin^2z}{cos^2z_1} = \frac{1}{cos^2z_1} - 1 \tag{A.6}$$

It results:

$$sin^2z = \frac{\frac{1}{cos^2z_1} - 1}{\frac{y^2}{cos^2z_1}} \tag{A.7}$$

$$cos^2z = \frac{\frac{y^2}{cos^2z1} - \frac{1}{cos^2z_1} + 1}{\frac{y^2}{cos^2z_1}} \tag{A.8}$$

$$cos^{-1}z = \frac{y}{cosz_1} \cdot \left(1 + \frac{y^2-1}{cos^2z_1}\right)^{-\frac{1}{2}} \tag{A.9}$$

$$= \frac{y}{cosz_1} - \frac{y(y^2-1)}{2cos^3z_1} + ... \tag{A.10}$$

Considering that:

$$y \sim \frac{r}{r_1} = 1 + \frac{1}{r_1}(r - r_1) \tag{A.11}$$

and

$$y(y^2-1) \quad \sim \quad \frac{2}{r_1}(r-r_1) \tag{A.12}$$

a first approximation for $cosz$ results:

$$\frac{1}{cosz} \quad = \quad \frac{1}{cosz_1} - \frac{1}{r_1 cosz_1}(r-r_1) - \frac{1}{r_1} \cdot \left(\frac{r-r_1}{cos^3 z_1} + ... \right. \tag{A.13}$$

$$= \quad \frac{1}{cosz_1} - \frac{1}{r_1} \cdot \left(\frac{1}{cos^3 z_1} - \frac{1}{cosz_1}\right)(r-r_1) + ... \tag{A.14}$$

Consequently Δ^{PD} becomes:

$$\Delta^{PD} \quad = \quad \frac{1}{cosz_1} \cdot \int_{r_1}^{r'} (n-1)dr - \frac{1}{r_1}\left(\frac{1}{cos^3 z_1} - \frac{1}{cosz_1}\right) \cdot \int_{r_1}^{r'} (n-1)(r-r_1)dr + \delta_R \tag{A.15}$$

The range correction is expressed by two atmospheric integrals. The subsequent terms of the binomial expansion are summarized in a so-called range correction term δ_R displayed in Table A.1 (Saastamoinen, 1972). In the following, the two integrals are determined.

a.) Derivation of $\int(n-1)dr$

The atmosphere can be divided into dry air and water vapor components, as stated by the perfect gas law:

$$\rho_{dry} = \frac{p-e}{R_L T} \text{ and } \rho_{wet} = \frac{e}{R_W T} \tag{A.16}$$

where:

$R_L = \; 287 Jkg^{-1}K^{-1}$: specific gas constant for air
$R_W = \; 461.5 Jkg^{-1}K^{-1}$: specific gas constant for water vapor

The total atmospheric gas corresponds to the addition of the dry and wet component:

$$\int \rho dr = \int \rho_{dry} dr + \int \rho_{wet} dr \tag{A.17}$$

$$= \frac{1}{R_L} \int \frac{p-e}{T} dr + \frac{1}{R_W} \int \frac{e}{T} dr = \frac{p_1}{g} \tag{A.18}$$

p_1 represents the pressure value at point P_1 on the earth's surface. g is the local value of gravity at the centroid of the atmospheric column.

The refractivity of moist air for electromagnetic radiation can be written as (Saastamoinen, 1972):

$$(n-1) \cdot 10^6 = \frac{(n_0-1)T_0}{p_0} \cdot \frac{p-e}{T} - c_w \frac{e}{T} + c_w' \frac{e}{T^2} + \frac{(n_0-1)T_0}{p_0} \cdot \frac{e}{T} \tag{A.19}$$

n_0 is the refractive index of dry air at pressure p_0 and temperature T_0. c_w and c_w' are constants. A first expression for the integral we are looking for can be written as follows:

$$\begin{aligned} 10^6 \cdot \int (n-1) dr &= \frac{(n_0-1)T_0}{p_0} \int \frac{p-e}{T} dr - c_w \int \frac{e}{T} dr \\ &\quad + c_w' \int \frac{e}{T^2} dr + \frac{(n_0-1)T_0}{p_0} \cdot \int \frac{e}{T} dr \end{aligned} \tag{A.20}$$

To reduce the complexity of the formula, abbreviations are introduced:

$$\begin{aligned} \text{For (A.20): } k_1 &= \frac{(n_0-1)T_0}{p_0} \\ k_2 &= \frac{(n_0-1)T_0}{p_0} - c_w \\ k_3 &= c_w' \\ \text{For (A.18): } k_4 &= \frac{1}{R_L} \\ k_5 &= \frac{1}{R_w} \end{aligned}$$

Subsequently, (A.20) can be rewritten and divided in a dry and wet part:

$$10^6 \cdot \int (n-1)dr = \underbrace{k_1 \int \frac{p-e}{T} dr}_{d_{dry}} + \underbrace{k_2 \int \frac{e}{T} dr + k_3 \int \frac{e}{T^2} dr}_{d_{wet}} \tag{A.21}$$

That means, that the dry part of the integral $\int (n-1)dr$ can be separated:

$$\left| \int (n-1)dr \right|_{dry} = d_{dry} = k_1 \int \frac{p-e}{T} dr \cdot 10^{-6} \tag{A.22}$$

(A.18) can be rewritten and separated as well:

$$\frac{p_1}{g} = m_T = \underbrace{k_4 \int \frac{p-e}{T} dr}_{m_{dry}} + \underbrace{k_5 \int \frac{e}{T} dr}_{m_{wet}} \tag{A.23}$$

Resulting for d_{dry}:

$$d_{dry} = \frac{k_1}{k_4} \cdot (m_T - m_{wet}) \cdot 10^{-6} = \frac{k_1}{k_4}(\frac{p_1}{g} - k_5 \int \frac{e}{T} dr) \cdot 10^{-6} \tag{A.24}$$

Saastamoinen (1972) derived:

$$\int \frac{e}{T} dr = \frac{R_L}{4g} e_1 = k_6 e_1 \tag{A.25}$$

where e_1 is the water vapor pressure at point P_1 on the Earth's surface and:

$$k_6 = \frac{R_L}{4g}$$

The dry part (A.24) can now be simplified to:

$$d_{dry} = \left(\frac{k_1}{k_4 g} p_1 - \frac{k_1 k_5 k_6}{k_4} e_1 \right) \cdot 10^{-6} \tag{A.26}$$

The coefficients can be written numerically (Saastamoinen, 1972):

$$\begin{aligned}
k_1 &= \frac{(n_0-1)T_0}{p_o} = 77.624 \\
k_4 &= \frac{1}{R} = \frac{1}{287} = 0.003484 \\
k_5 &= \frac{1}{R_w} = \frac{1}{461.5} = 0.002167 \\
k_6 &= \frac{R}{4g} = \frac{287}{4 \cdot 9.784} = 7.31397
\end{aligned}$$

The dry equation can be further shortened to:

$$d_{dry} = a_{dry}p_1 - b_{dry}e_1 \tag{A.27}$$

$$\tag{A.28}$$

using the numerical values:

$$\begin{aligned}
a_{dry} &= 0.002277 \\
b_{dry} &= 0.000354
\end{aligned}$$

Finally, the dry part we are looking for, is given by:

$$\left| \int (n-1)dr \right|_{dry} = d_{dry} = 0.002277p_1 - 0.000354e_1 \tag{A.29}$$

b.) Derivation of $\int(n-1)(r-r_1)dr$

This integral has been derived by Saastamoinen (1972) as follows:

$$\int (n-1)(r-r_1)dr = \frac{R_L^2}{g^2} \cdot \left[\frac{(n_1-1)T_1^2 - \frac{R_L\beta}{g}(n^0-1)T^{0^2}}{1-\frac{R_L\beta}{g}} \right] \tag{A.30}$$

n^0 is the refractive index at the tropopause, T^0 the corresponding temperature and p^0 the pressure and β the vertical gradient of temperature in the troposphere.

Using the equations (Saastamoinen, 1972):

$$p = p_1 \left(\frac{T}{T_1}\right)^{-\frac{g}{R_L \beta}} \tag{A.31}$$

$$(n-1) = (n_1 - 1)\left(\frac{T}{T_1}\right)^{-\frac{g}{R_L \beta}-1} \tag{A.32}$$

it follows:

$$\frac{n_1 - 1}{n-1} = \frac{p_1}{p} \cdot \frac{T}{T_1} \tag{A.33}$$

(A.30) can be rewritten:

$$\int (n-1)(r-r_1)dr = \frac{(n_0 - 1)R_L^2 T_0}{p_0 g^2} \cdot \left[\frac{p_1 T_1 - \frac{R_L \beta}{g} p^0 T^0}{1 - \frac{R_L \beta}{g}}\right] \tag{A.34}$$

$$= a_{dry} \cdot \frac{R_L}{g} \cdot \left[\frac{p_1 T_1 - \frac{R_L \beta}{g} p^0 T^0}{1 - \frac{R_L \beta}{g}}\right] \tag{A.35}$$

To decompose in the dry and wet part, p has to be substituted to $(p-e)+e$:

$$\int (n-1)(r-r_1)dr = a_{dry} \cdot \frac{R_L}{g} \cdot \left[\frac{(p_1 - e_1)T_1 + e_1 T_1 - \frac{R_L \beta}{g}(p^0 - e^0)T^0 + e^0 T^0}{1 - \frac{R_L \beta}{g}}\right] \tag{A.36}$$

The water vapor pressure at the tropopause can be approximated by $e^0 \cong 0$:

$$\int (n-1)(r-r_1)dr = a_{dry} \cdot \frac{R_L}{g} \cdot \left[\frac{(p_1 - e_1)T_1 + e_1 T_1 - \frac{R_L \beta}{g} p^0 T^0}{1 - \frac{R_L \beta}{g}}\right] \tag{A.37}$$

The integral can now be decomposed in a dry and wet part:

$$\left| \int (n-1)(r-r_1)dr \right|_{dry} = a_{dry} \cdot \frac{R_L}{g} \cdot \left[\frac{(p_1 - e_1)T_1 - \frac{R_L \beta}{g} p^0 T^0}{1 - \frac{R_L \beta}{g}}\right] \tag{A.38}$$

$$= a_{dry} \cdot r_1 \cdot B_{dry} \tag{A.39}$$

$$\left| \int (n-1)(r-r_1)dr \right|_{wet} = a_{dry} \cdot \frac{R_L}{g} \cdot \left[\frac{e_1 T_1}{1 - \frac{R_L \beta}{g}}\right] \tag{A.40}$$

$$= a_{dry} \cdot r_1 \cdot B_{wet} \tag{A.41}$$

where:

$B = B_{dry} + B_{wet}$: effect of the spherical curvature of the atmospheric layers

The coefficient B is displayed in Table A.1. It can be decomposed in B_{dry} ($\sim 99\%$) and B_{wet} ($\sim 1\%$). Numerical tests show, that the coefficient is maximal 4 mm at zenith distance $= 80°$, usually smaller than 1 mm (for zenith distance $\leq 75°$). Keeping these conditions in mind, the following approximation is acceptable:

$$\begin{aligned} B_{dry} &= B \\ B_{wet} &= 0 \end{aligned}$$

The same situation applies to the correction quantity δ_R. To be accurate, the total correction has to be decomposed in a dry and wet part. However, the correction is fairly small. If the zenith distance $\leq 80°$, the following simplification is acceptable:

$$\begin{aligned} \delta_{R,dry} &= \delta_R \\ \delta_{R,wet} &= 0 \end{aligned}$$

Finally, the two integrals in (A.15) can now be substituted by (A.29) and (A.39) to achieve the dry path delay Δ^{PD}_{dry}:

$$\begin{aligned} \Delta^{PD}_{dry} &= \frac{1}{cos z_1} \cdot \left| \int_{r_1}^{r'} (n-1) dr \right|_{dry} \\ &\quad - \frac{1}{r_1} \left(\frac{1}{cos^3 z_1} - \frac{1}{cos z_1} \right) \cdot \left| \int_{r_1}^{r'} (n-1)(r - r_1) dr \right|_{dry} + \delta_{R,dry} \quad \text{(A.42)} \\ &= \frac{1}{cos z_1} \cdot (a_{dry} p_1 - b_{dry} e_1) - \frac{1}{cos z_1} \cdot a_{dry} \cdot B \cdot tan^2 z_1 + \delta_R \quad \text{(A.43)} \end{aligned}$$

The dry part of the atmospheric correction can now be written in its final numerical form.

$$\Delta^{PD}_{dry} = 0.002277 \cdot \frac{1}{cos z_1} \cdot \left(p_1 - 0.155471 e_1 - B \cdot tan^2 z_1 \right) + \delta_R \quad \text{(A.44)}$$

The wet part of the atmospheric refractivity corresponds to the subtraction of the dry part from the total amount:

$$\Delta_{wet}^{PD} = \Delta_{total}^{PD} - \Delta_{dry}^{PD} \tag{A.45}$$

where:

$$\Delta_{total}^{PD} = \tfrac{0.002277}{cosz_1}\big(p_1 + (\tfrac{1255}{T_1} + 0.05)e_1 - Btan^2 z_1\big) + \delta_R \quad \text{(Saastamoinen, 1972)}$$

$$\Delta_{dry}^{PD} = \tfrac{0.002277}{cosz_1}\big(p_1 - 0.155471e_1 - Btan^2 z_1\big) + \delta_R \quad \text{(relation A.44)}$$

Finally we obtain:

$$\Delta_{wet}^{PD} = \frac{0.002277}{cosz_1}\left(\frac{1255}{T_1} + 0.205471\right) \cdot e_1 \tag{A.46}$$

B. Statistical Issues

Hereafter, the statistical tools used in this work for the comparison of different results are given in details. Usually, a dedicated data series was chosen as reference. However, sometimes, no reference data set was obvious and therefore, the mean of all data series was selected as reference.

The *offset* of the data series compared to the reference was calculated as follows:

$$\textit{offset} \text{ of data set } a\text{:} \quad \overline{d}_a = \frac{\sum_{i=1}^{n} d_{i,a}}{n} \tag{B.1}$$

where:

$d_{i,a}$: difference between value i of data set a and reference value i

n : total number of data values

The *rms* (root mean square) of the data series is obtained:

$$rms \quad \text{of data set a} = \sqrt{\frac{1}{n} \cdot \sum_{i=1}^{n} d_{i,a}^2} \tag{B.2}$$

Contrary to the *rms*, the sigma value represents the standard deviation of the data series from the estimated offset (B.1):

$$\sigma \quad \text{of data set a} = \sqrt{\frac{1}{n-1} \cdot \sum_{i=1}^{n} (d_{i,a} - \overline{d}_a)^2} \tag{B.3}$$

C. Refractivity Profiles of the Hawaiian Campaign

The following figures show refractivity profiles of all radiosondes launched during the Hawaiian campaign. They are compared with the tomographic solutions discussed in Section 5.7. The tomographic solution 1 (dotted line) illustrates the tomographic analysis applying a covariance function. The tomographic solution 2 (dashed line) shows the solution with additional ground meteorological a priori values. Moreover, both solutions contain a small a priori refractivity constraint of zero in the uppermost layer (8'000-15'000 m height).

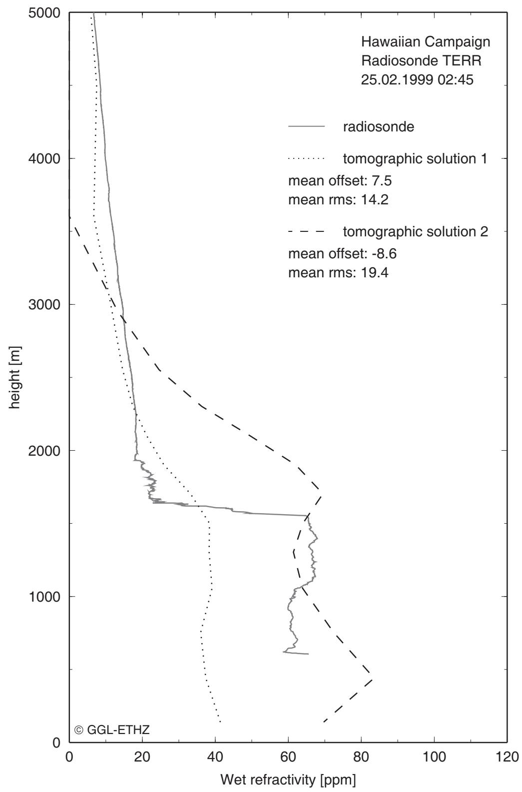

Figure C.1.: Refractivity profile above station TERR. A large inhomogeneity is detected at 1600 m height.

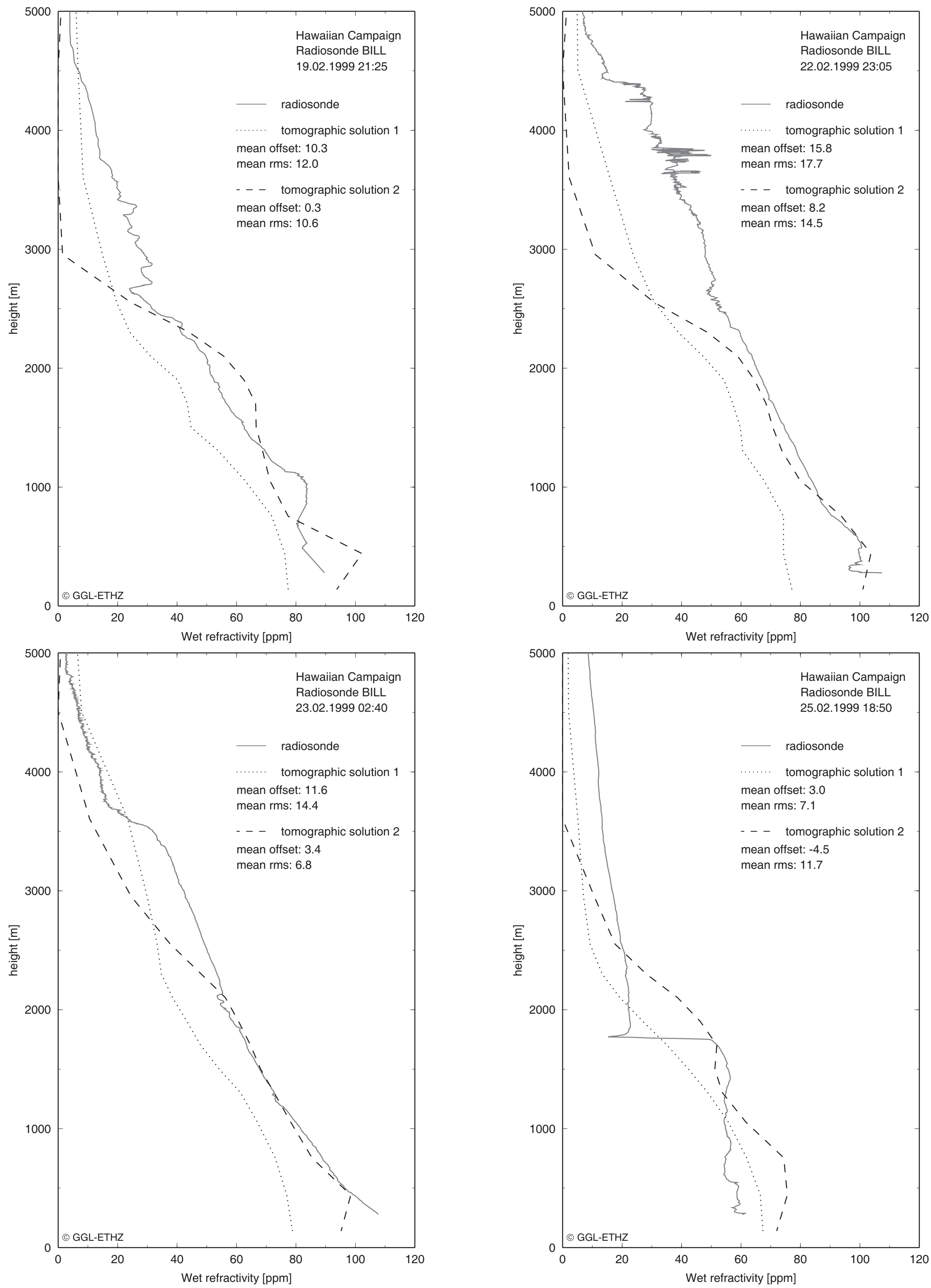

Figure C.2.: Refractivity profiles above station BILL (continued on Figure C.3). A large profile variation is visible in time.

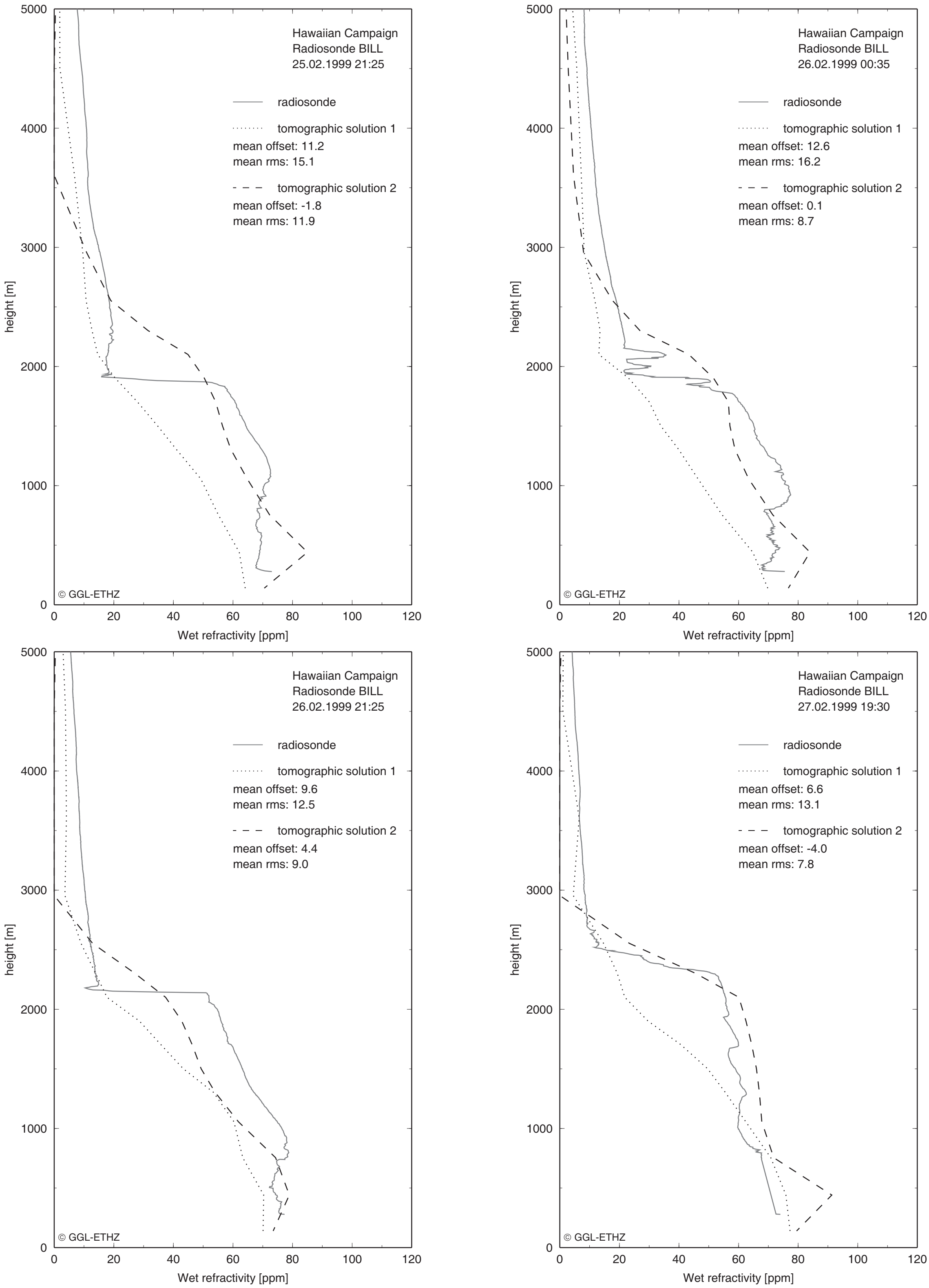

Figure C.3.: Refractivity profiles above station BILL (continuation of Figure C.2).

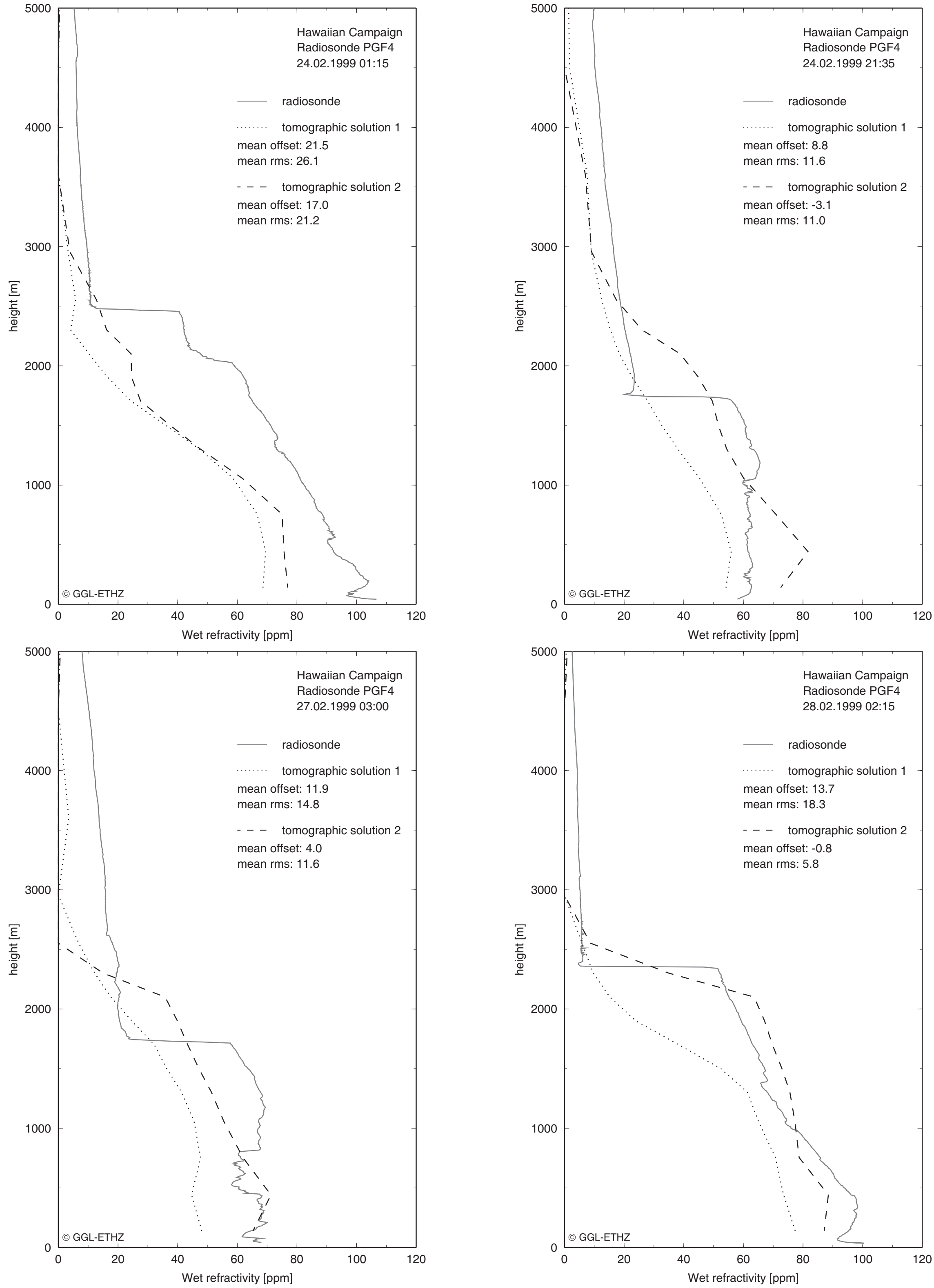

Figure C.4.: Refractivity profiles above station PGF4. During the time, the large inhomogeneity is varying in height.

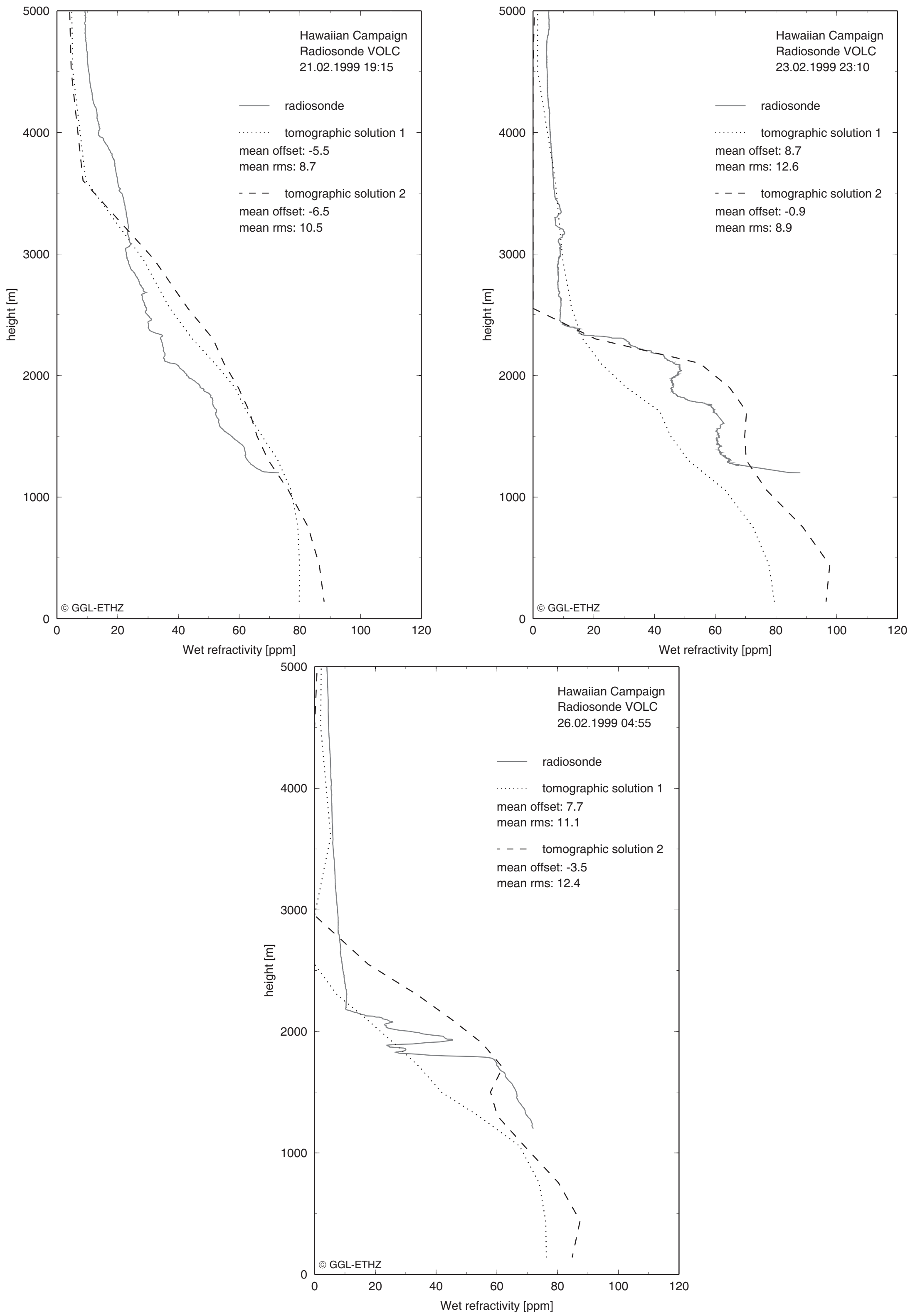

Figure C.5.: Refractivity profiles above station VOLC.

D. Refractivity Profiles based on the AGNES Network

In the following figures, a selection of the 7680 investigated refractivity profiles are shown. The tomographic solutions are compared to the refractivity profiles of the numerical weather model aLMo, COMEDIE, and, where applicable, radiosondes. The input data is described in detail in Section 6.5. The location of the profiles is displayed in Figure 6.6.

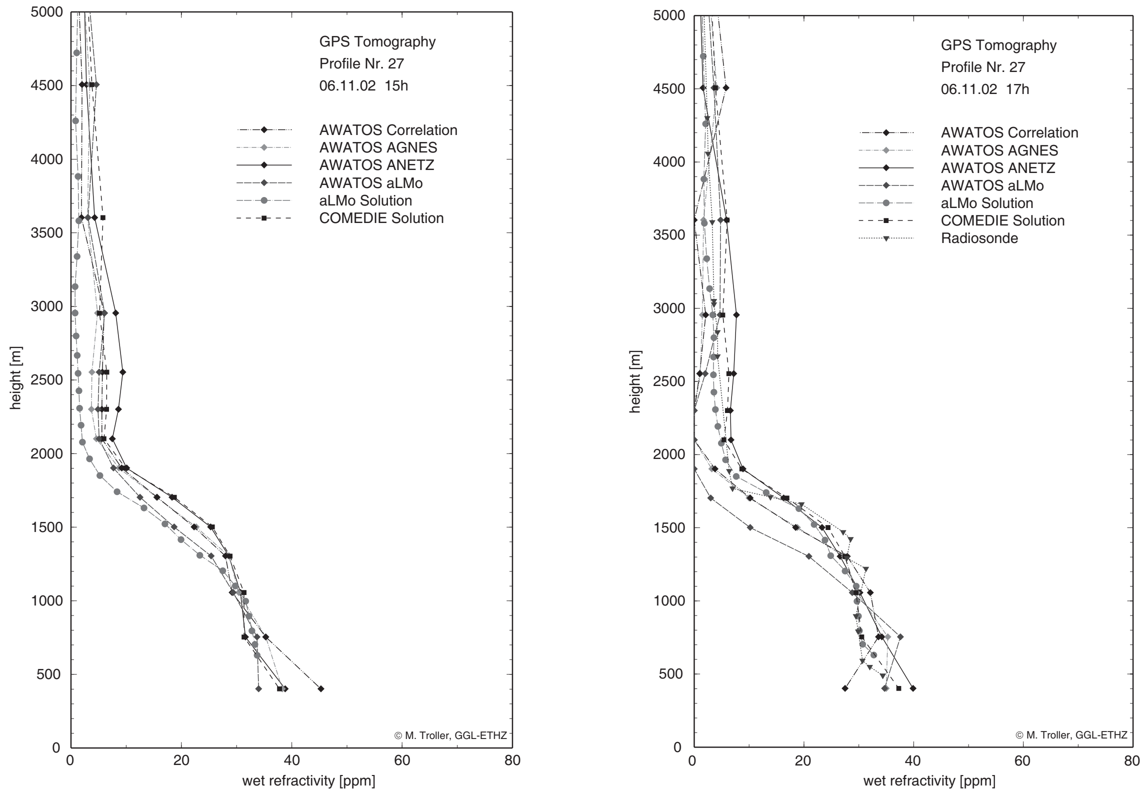

Figure D.1.: Refractivity characteristics during eight hours on profile no. 27 (continued in Figure D.2). A rapid decrease of refractivity appears at 1000-2000 m height. The agreement of the tomographic solutions with aLMo is varying in time.

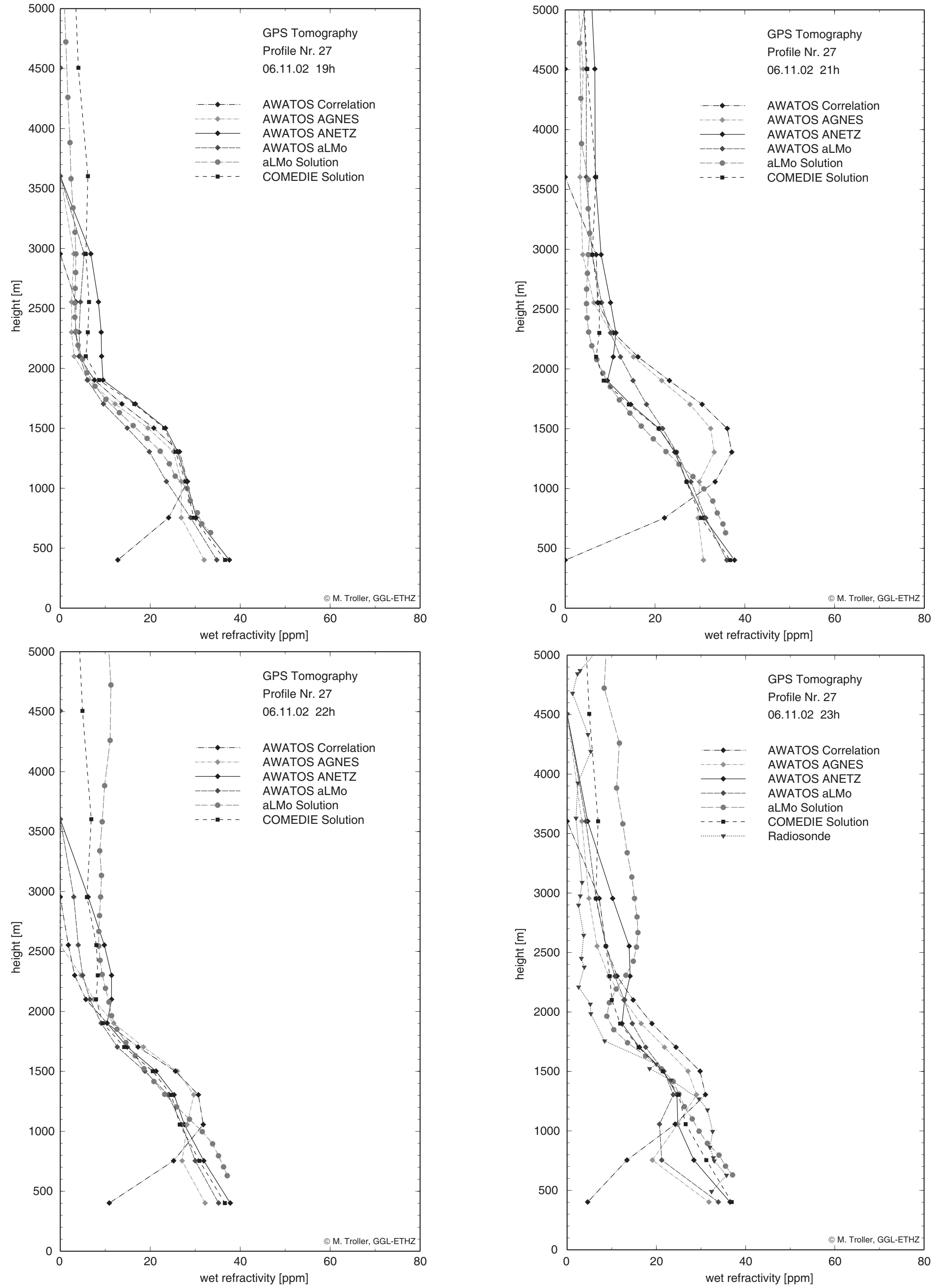

Figure D.2.: Continuation of Figure D.1.

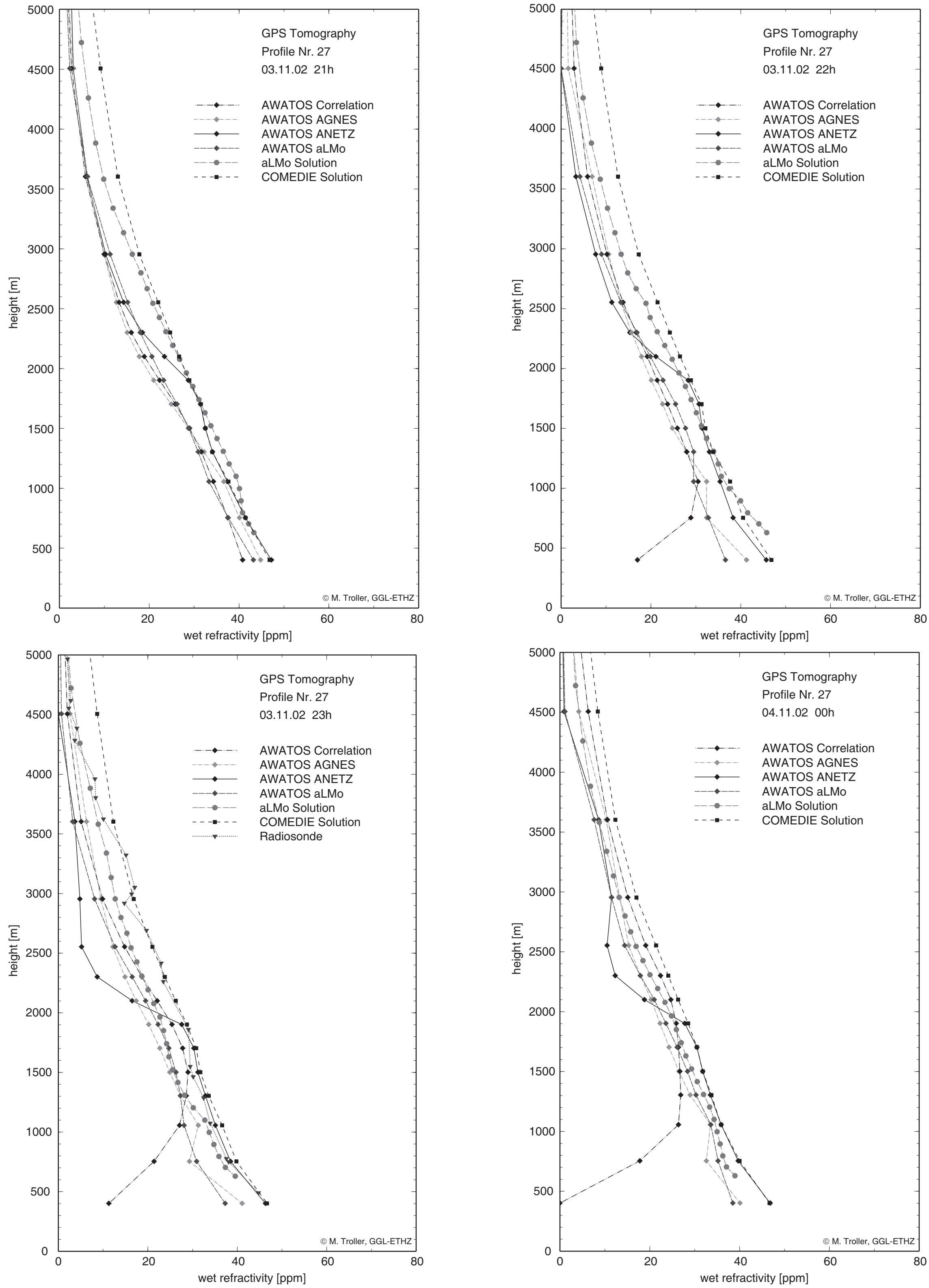

Figure D.3.: Example of a homogeneous refractivity distribution in the atmosphere. The figure shows the situation during three hours. The tomographic solutions fit aLMo usually accurate.

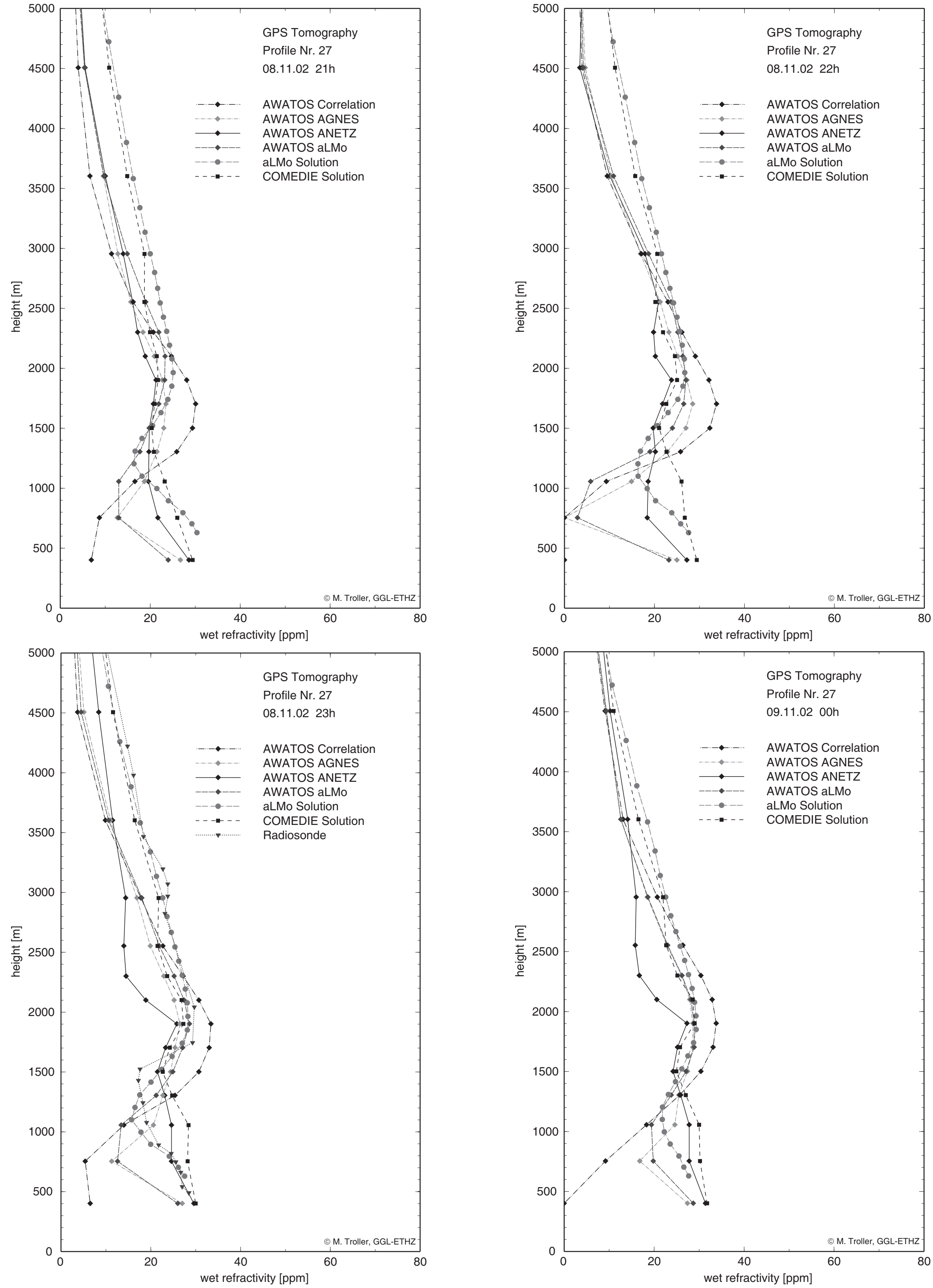

Figure D.4.: Example of an atmospheric inversion during three hours. The solution AWATOS Correlation, in particular, reproduces the aLMo profile only partially.

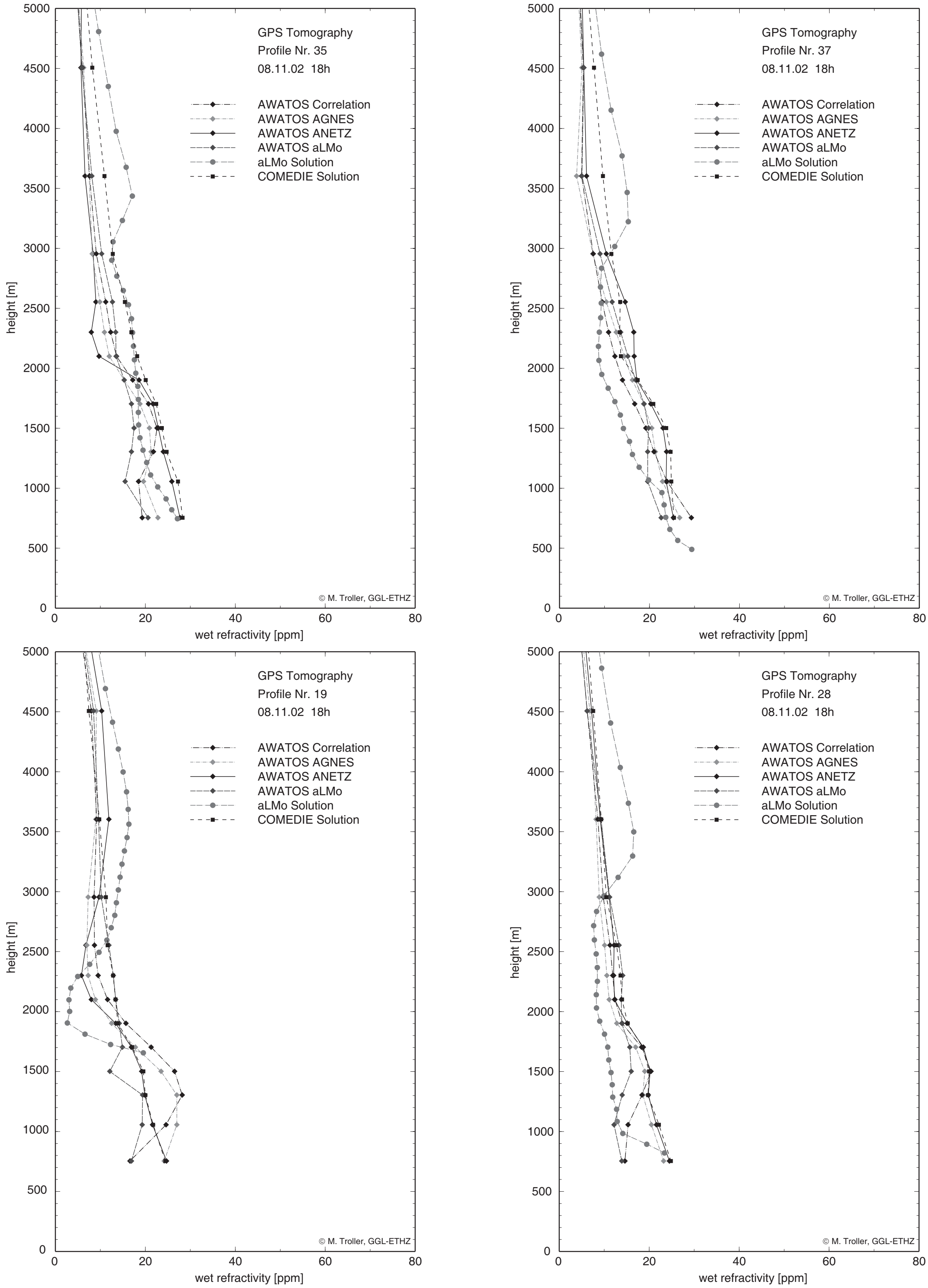

Figure D.5.: The refractivity variation in Switzerland on November 8, 6 pm is shown. Eastern profiles are given in Figure D.6. Partially, an atmospheric inversion becomes apparent. Consequently, the tomographic solutions agree with aLMo only partially.

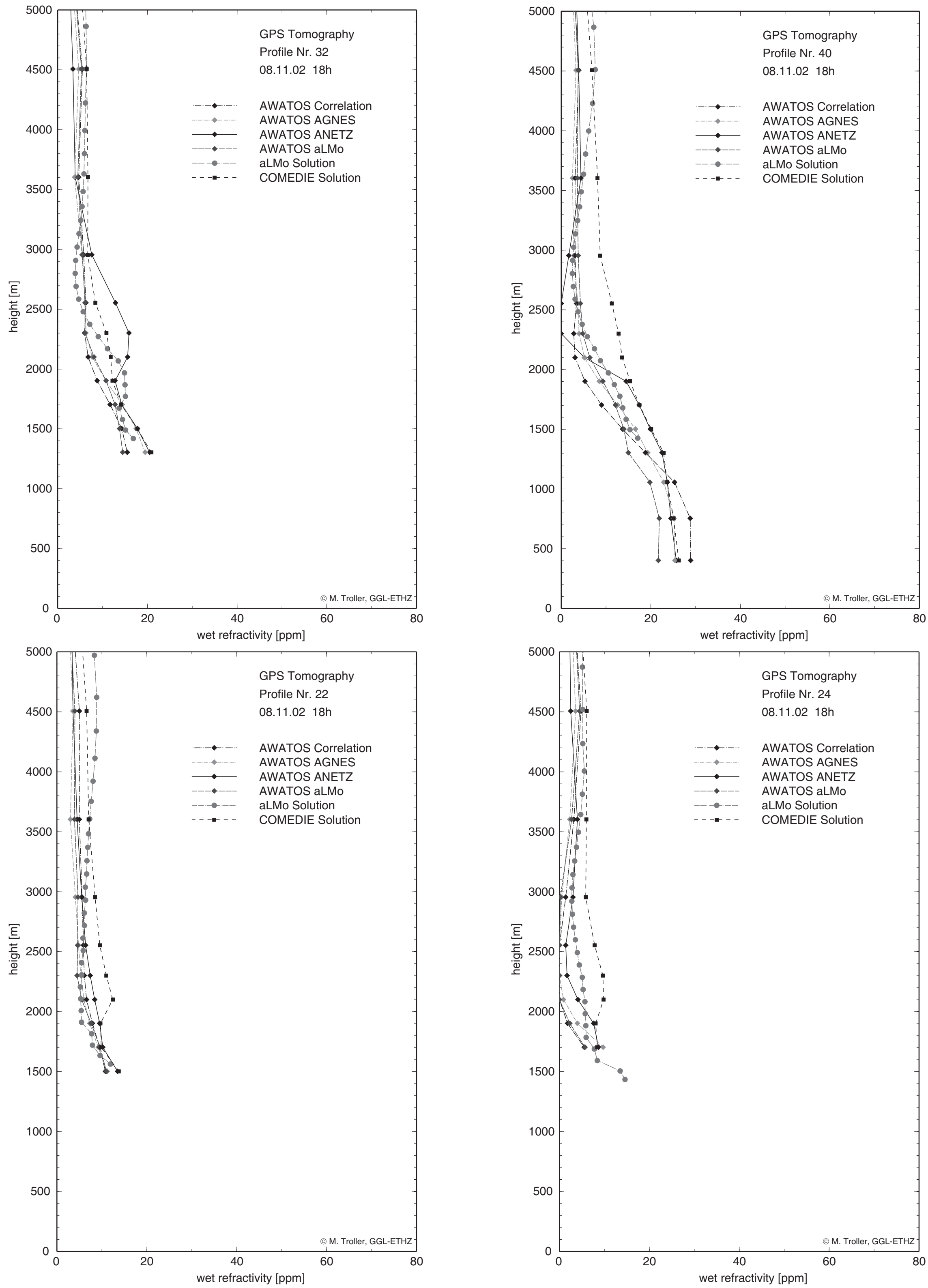

Figure D.6.: Continuation of Figure D.5.

“Geodätisch-geophysikalische Arbeiten in der Schweiz”

(Fortsetzung der Publikationsreihe ”Astronomisch-geodätische Arbeiten in der Schweiz”)
der Schweizerischen Geodätischen Kommission (ab Bd. 46):

46 1993 Orbits of Satellite Systems in Space Geodesy. M. Rothacher. 243 Seiten.

47 1993 NFP 20. Beitrag der Geodäsie zur geologischen Tiefenstruktur und Alpendynamik. H.-G. Kahle (Hrsg.) Autoren: I. Bauersima, G. Beutler, B. Bürki, M. Cocard, A. Geiger, E. Gubler, W. Gurtner, H.-G. Kahle, U. Marti, B. Mattli, M. Rothacher, Th. Schildknecht, D. Schneider, A. Wiget, B. Wirth. 153 Seiten plus 90 Seiten Anhang.

48 1994 Ionosphere and Geodetic Satellite Systems: Permanent GPS Tracking Data for Modelling and Monitoring: Urs Wild, 155 Seiten.

49 1994 Optical Astrometry of Fast Moving Objects using CCD Detectors: Thomas Schildknecht, 200 Seiten.

50 1995 Geodätische Alpentraverse Gotthard: A. Elmiger, R. Köchle, A. Ryf und F. Chaperon. 214 Seiten.

51 1995 Dreidimensionales Testnetz Turtmann 1985-1993, Teil II (GPS-Netz). F. Jeanrichard (Hrsg.) Autoren: G. Beutler, A. Geiger, M. Rothacher, Stefan Schaer, D. Schneider, A. Wiget, 173 Seiten.

52 1995 High Precision GPS Processing in Kinematic Mode: M. Cocard. 139 Seiten.

53 1995 Ambiguity Resolution Techniques in Geodetic and Geodynamic Applications of the Global Positioning System. L. Mervart. 155 Seiten.

54 1997 SG 95: Das neue Schweregrundnetz der Schweiz: F. Arnet und E. Klingelé. 37 Seiten.

55 1997 Combination of Solutions for Geodetic and Geodynamic Applications of the Global Positioning System (GPS). Elmar Brockmann, 211 Seiten.

56 1997 Geoid der Schweiz 1997. Urs Marti, 140 Seiten.

57 1998 Astrometry and Satellite Orbits: Theoretical Considerations and Typical Applications. Urs Hugentobler, 209 Seiten.

58 1998 Systematic Investigations of Error- and System-Modelling of Satellite Based Flight Approaches and Landings in Switzerland. Maurizio Scaramuzza, 165 Seiten.

59 1999 Mapping and Predicting the Earth’s Ionosphere Using the Global Positioning System. Stefan Schaer, 205 Seiten.

60 2000 Modeling and Validating Orbits and Clocks Using the Global Positioning System. Timon Anton Springer, 154 Seiten.

61 2001 Spatial and Temporal Distribution of Atmospheric Water Vapor using Space Geodetic Techniques. Lars Peter Kruse, 128 Seiten.

62 2001 Solar Spectrometry for Determination of Tropospheric Water Vapor. Bernd Sierk, 212 Seiten.

63 2001 Analysis of refraction influences in geodesy using image processing and turbulence models. Philipp Flach, 175 Seiten.

64 2003 INS/GPS Integration for Pedestrian Navigation. V. Gabaglio, 161 Seiten.

65 2003 Efficient Methods for Determining Precise Orbits of Low Earth Orbiters Using the Global Positioning System. Heike Bock, 214 Seiten.

66 2003 Capteurs et Algorithmes pour la Localisation Autonome en Mode Pédestre. Quentin Ladetto, 121 Seiten.

67 2004 GPS based Determination of the Integrated and Spatially Distributed Water Vapor in the Troposphere. Marc Troller, 172 Seiten.